

**Hydrogen-Diesel Dual Fuel Combustion Characterization for an Internal
Combustion Engine**

by

Jakub Tyler McNally

A thesis submitted in partial fulfillment of the requirements for the degree of

Master of Science

Department of Mechanical Engineering
University of Alberta

© Jakub Tyler McNally, 2024

Abstract

Hydrogen as a fuel has the potential to reduce tailpipe carbon dioxide emissions of vehicles to near-zero, while also allowing for the generation of a hydrogen-based economy and lowering humanity's dependence upon oil. Hydrogen-diesel dual fuel combustion, where hydrogen and diesel are combusted together within a diesel engine, allows for application of hydrogen combustion technology with current technologies. Offsetting diesel consumption with hydrogen can significantly reduce CO₂ emissions, and allow for cleaner emissions engines with current-day technology. However, the dual-fuel combustion process is more complex than standard compression ignition or spark ignition combustion. To understand diesel-hydrogen dual fuel combustion, testing of various operating points with varied operating parameters must be conducted. This thesis outlines the modification and hydrogen dual-fuel testing of a Cummins QSB 4.5 L engine. The engine was modified to have port hydrogen injection into Cylinder 1 with a custom controller software implementation. Cylinder pressure and engine-out emissions were measured while running both hydrogen-diesel and pure diesel. The engine was run with a load ranging between 4.5 bar IMEP and 12.5 bar IMEP, equivalent to approximately 70 percent of the engine's maximum load. Hydrogen was injected into the engine with a fuel energy fraction of up to 92 percent. For most tests, a dual-diesel injection strategy was used, with the pilot timing advance being changed to facilitate earlier hydrogen combustion timings. Intake manifold pressure was varied to approximate turbocharged operation. It was found that increasing hydrogen replacement caused greater engine-out NO_x compared to pure diesel for almost all load cases, and hydrogen caused a greater fraction of NO₂

in the exhaust stream. Engine-out CO₂ was able to be reduced by up to 89 percent, and engine-out particulate was reduced up to 97 percent. At operating points with a sufficient hydrogen mixture fraction, the engine efficiency was equivalent or greater than that while running pure diesel. Low hydrogen replacement amounts resulted in no premixed flame propagation, limiting engine efficiency and increased unburnt hydrogen emissions at lower loads. High hydrogen replacement was observed to cause more rapid combustion along with higher cylinder pressures compared to pure diesel combustion, limiting the maximum hydrogen replacement.

Preface

The results presented in this thesis are the original work of Jakub McNally. The funding from this research is from the CFREF Future Energy program at University of Alberta and NSERC Grant RGPIN-2022-03411.

I have presented sections of the work seen in Chapter 5 at the 2022 Canadian Society for Mechanical Engineering Conference, and the 2023 Combustion Institute Canadian Section meeting. I have also presented an overview of the Chapter 5 results at the Canadian Hydrogen Convention as a poster.

1. J. McNally, D. Gordon, A. Norouzi, M. Shahbakhti, and C. R. Koch, “Experimental Study of Hydrogen-Diesel Dual Fuel Engine Characterization,” Canadian Society for Mechanical Engineering Conference, 2022.
2. J. McNally, D. Gordon, E. Sperling, M. Shahbakhti, and C. R. Koch, “Performance and Emission Investigation of Hydrogen Diesel Dual Fuel Combustion,” Combustion Institute Canadian Section Meeting, 2023.
3. J. McNally, E. Sperling, D. Gordon, M. Shahbakhti, and C. R. Koch, “Hydrogen Diesel Dual Fuel Engine Efficiency and Emission Characterization,” Canadian Hydrogen Convention, 2023.

Acknowledgements

I would like to express my thanks and gratitude towards my Supervisor Dr. Charles Robert (Bob) Koch for his feedback, patience and support through the completion of my M.Sc. His academic and personal knowledge have been of great importance to my work and life throughout my M.Sc. program at the University of Alberta. His opportunity to connect me with local businesses for further applications of my gained knowledge is greatly appreciated.

I also need to acknowledge my colleagues within my research group for the majority of my degree and the University of Alberta (Armin and Alex) for their support, encouragement, and always-helpful knowledge and demeanor. I would also like to thank newer members of the lab group (Ed, Javad) who pushed me to explain and document my experiment apparatus. I would also like to provide special thanks to David Gordon for his immense help and knowledge in regards to the hardware and software setup of the engine dyno cell. Without his hard work, I would not have been able to accomplish near as much as I have in the pursuit of my M.Sc.

Finally, I acknowledge my parents (Simona and Lawrence), who have supported me through the pursuit of my degree. Without their encouragement, I would not have been able to complete my studies.

Table of Contents

1	Introduction	1
1.1	Motivation	1
1.2	Problem Statement	2
1.3	Thesis Organization	2
1.4	Contributions	3
2	Background	4
2.1	Hydrogen in Engines	4
2.2	Combustion of Hydrogen	5
2.2.1	Dual Fuel Combustion Process	7
2.2.2	Injection Methods	7
2.2.3	Emissions and Efficiency	10
2.2.4	Hydrogen Slip and Its Mitigation	13
2.2.5	Aftertreatment of Hydrogen Engines	14
3	Experimental Setup	16
3.1	Engine Assembly	16
3.1.1	Hydrogen Injection Strategy	17
3.1.2	Modifications to Engine Assembly	20
3.1.3	Manifold Air Conditioning	22
3.1.4	Hydrogen Delivery System	24
3.1.5	Diesel Fuel System	28
3.2	Injection Strategy	29
3.2.1	Engine Feedback Sensors	30
3.2.2	In-Cylinder Pressure sensors	32
3.2.3	Emissions measurement	33
3.2.4	Engine torque and speed	34
3.2.5	Cooling water and oil supply	35
3.3	Engine Control	35

3.3.1	Reverse Engineering of Injector Energization Profile	36
3.3.2	Reverse Engineering of Cummins Controller	38
3.4	Data collection	38
3.5	Testing Procedure	40
4	Combustion Analysis	42
4.1	Governing Equations of Combustion	42
4.1.1	In-Cylinder Energy Conservation	42
4.1.2	Cylinder Gas Properties	47
4.2	Mass Flows	47
4.2.1	Diesel Injector Injection Model Calibration	48
4.2.2	Hydrogen Flow Model	50
4.2.3	Engine Airflow Overview	51
4.2.4	Exhaust Gas Diesel Injection Model	54
4.2.5	Fuel Energies and Combustion Efficiencies	58
4.3	Cylinder Pressure Analysis	59
4.3.1	Preprocessing of Cylinder Pressure Data	60
4.3.2	Pressure Trace Analysis	63
4.3.3	Calculation of Heat Release	65
4.3.4	Calculation of Emissions	66
4.4	Error Analysis	68
5	Steady-State Results	70
5.1	Structure of Chapter	70
5.2	Overview of Steady-State Tests	70
5.3	Testing Schema	72
5.4	List of Conventional Dual-Fuel Combustion Tests	72
5.4.1	Summary of Test Results	87
5.5	Cylinder Pressures	87
5.6	Engine Efficiency	94
5.6.1	Combustion Efficiencies	97
5.7	Engine Emissions	102
5.7.1	NO _x emissions	102
5.7.2	CO ₂ Emissions	105
5.7.3	Particulate Emissions	108
5.7.4	CO Emissions	110
5.7.5	Unburnt Hydrocarbon Emissions	112

5.8	Heat Release	114
5.8.1	Exhaust Temperatures	120
5.9	Best-Case Comparison	121
6	Conclusion	129
6.1	Steady State Dual-Fuel Operation	129
6.2	Future Work	130
	Bibliography	133
	Appendix A: Engine Operation Procedures	149
A.1	Operating Manual for 4.5L Cummins Engine	149
A.1.1	PPE Required	149
A.1.2	Safety Rules	149
A.1.3	Startup Procedure	150
A.1.4	If running with Boosted Intake Pressures	153
A.1.5	If running with hydrogen	155
A.1.6	Shutdown Procedure	155
	Appendix B: Complete Selection of Steady-State Testing Results Figures	157
B.1	Injector Cup Design	157
	Appendix C: Testing List	159
C.1	Testing List and their Relation to Files	159
	Appendix D: Selection of Steady-State Testing Results Figures	168
D.1	Figures from Steady-State Testing Results	168
D.1.1	Cylinder Pressure Traces	168
D.1.2	Cylinder Pressure Heat Release Rate Traces	171

List of Tables

2.1	Comparison between perspective energy sources in the heavy-duty market.	4
2.2	Comparison between injection methods.	9
3.1	Cummins QSB 4.5 Tier 3 parameters, as tested	18
3.2	Properties of the HANA H2200 port injector [84]	28
3.3	Omega FMA-1611A hydrogen mass flow meter properties [86].	31
3.4	Hydrogen exhaust concentration sensor specifications	32
3.5	Properties of cylinder pressure sensors and amplifiers	33
3.6	Accuracy of the FTIR emissions measurement system for selected gases.	34
3.7	Accuracy of the PPS-M emissions measurement system [87].	34
3.8	Rapid prototyping ECU Specifications	37
3.9	Diesel Injector Energization Profile	37
3.10	NI data acquisition system specifications [88]	39
3.11	Injection parameters used for baseline testing of engine.	41
4.1	DOI-injected diesel mass test parameters	48
4.2	Calculated repeatability of relevant primary sensors on engine.	69
5.1	List of all conventional dual-fuel combustion tests. Test names appended with a “S” note cases where a single diesel injection was used to maximize H ₂ replacement.	74
C.1	List of all conventional dual-fuel combustion tests correlated to their file number.	159

List of Figures

2.1	Diagram of the entrainment and ignition process in a dual-fuel hydrogen diesel engine [40].	8
3.1	Image of the tested engine.	17
3.2	Image of the exhaust side of the tested engine.	19
3.3	Image of the populated holes bored into the head for intake port temperature monitoring and hydrogen injector installation with mounted items.	20
3.4	Top-down sectional view of the intake and exhaust runners cast in the head.	21
3.5	Exhaust manifold routing schematic.	22
3.6	Process diagram of the intake air system that provides pressure from building air.	23
3.7	Image of the intake collector where building air is regulated to engine intake pressure.	24
3.8	Image of the hydrogen gas cabinet.	25
3.9	Process diagram of the hydrogen delivery system.	25
3.10	Injection Scheme for testing.	29
3.11	Sensors on the engine.	30
4.1	Injector nozzle area with a single diesel injection over varied durations of injection for the measured injection mass and Cummins models.	50
4.2	Hydrogen injector nozzle area over varied durations of injection for data-relevant injection durations.	51
4.3	Combined volumetric efficiency over various pressures and hydrogen addition amounts.	53
4.4	Comparison of the two injection models under double-diesel injection conditions.	57
4.5	Comparison between filtered and unfiltered cylinder pressure traces for a 1350 J H ₂ test (test G-25).	62

4.6	Comparison of heat release between filtered and unfiltered ensemble average cylinder pressure traces for test G-25.	62
5.1	600-cycle ensemble average of cylinder pressure traces from Bin A at an injection advance of -12.9 CAD pilot injection.	88
5.2	600-cycle ensemble average of cylinder pressure traces from Bin G at an injection advance of -11.1 CAD pilot injection advance.	89
5.3	600-cycle ensemble average of cylinder pressure traces from Bin H at an injection advance of -12.9 CAD pilot injection advance.	90
5.4	Maximum and minimum cylinder pressure traces from selected Bin E trials.	91
5.5	MPPRR for the Bin F trials.	91
5.6	CoV of IMEPg for the Bin A trials.	93
5.7	CoV of IMEPg for the Bin H trials.	93
5.8	Gross engine efficiency of the Bin A trials.	94
5.9	Gross engine efficiency of the Bin H trials.	95
5.10	Gross engine efficiency of the Bin A trials plotted against the cylinder hydrogen-air equivalence ratio, including pure diesel trials.	95
5.11	H ₂ combustion efficiency of the Bin A trials.	98
5.12	H ₂ combustion efficiency of the Bin H trials.	98
5.13	Diesel combustion efficiency of the Bin F trials.	100
5.14	Overall combustion efficiency of the Bin F trials.	101
5.15	NO _x output for the Bin C trials, with EPA Tier 3 Offroad Standard threshold.	102
5.16	NO _x output for the Bin F trials, with EPA Tier 3 Offroad Standard threshold.	103
5.17	NO/NO _x molar ratio from the Bin H trials.	104
5.18	CO ₂ output for the Bin C trials.	106
5.19	CO ₂ output for the Bin G trials.	107
5.20	Particulate output for the Bin C trials, with EPA Tier 4 Offroad Standard threshold.	109
5.21	Particulate emissions output per Joule of diesel for the Bin C trials. Max H ₂ trials are run with a single diesel injection.	109
5.22	CO output for the Bin C trials.	111
5.23	Ratio of CO to CO ₂ output for the Bin G trials.	111
5.24	NMHC output for the Bin A trials,, with EPA Tier 4 Offroad Standard threshold.	112

5.25	NMHC output for the Bin F trials.	113
5.26	Heat release rate traces for Bin A.	115
5.27	Heat release rate traces for Bin C.	115
5.28	CA ₁₀ for the Bin F trials.	116
5.29	CA ₅₀ for the Bin F trials.	117
5.30	CA ₉₀ for the Bin F trials.	117
5.31	MFB ₁₀₋₉₀ for the Bin F trials.	118
5.32	Engine exhaust port gas temperatures for the Bin A trials.	120
5.33	Highest hydrogen fractions achieved in trials.	123
5.34	Comparison between the best efficiencies for dual-fuel and diesel operation in trials.	124
5.35	CO ₂ reduction for the highest hydrogen fraction trials.	125
5.36	Particulate reduction for the highest hydrogen fraction trials.	126
5.37	Comparison between the CO ₂ emissions for dual-fuel and diesel operation in trials.	126
5.38	Comparison between the particulate emissions for dual-fuel and diesel operation in trials.	127
5.39	Comparison between the NO _x emissions for dual-fuel and diesel operation in trials.	127
5.40	Comparison between the overall combustion efficiencies for dual-fuel and diesel operation in trials.	128
B.1	Injector cup schematic.	158
D.1	600-cycle ensemble average of cylinder pressure traces from Bin A at an injection advance of -11.1 CAD pilot injection advance.	168
D.2	600-cycle ensemble average of cylinder pressure traces from Bin B at an injection advance of -9.3 CAD pilot injection advance.	169
D.3	600-cycle ensemble average of cylinder pressure traces from Bin C at an injection advance of -11.1 CAD pilot injection advance.	169
D.4	600-cycle ensemble average of cylinder pressure traces from Bin D at an injection advance of -11.1 CAD pilot injection advance.	170
D.5	600-cycle ensemble average of cylinder pressure traces from Bin E at an injection advance of -16.5 CAD pilot injection advance.	170
D.6	600-cycle ensemble average of cylinder pressure traces from Bin F at an injection advance of -9.3 CAD pilot injection advance.	171
D.7	600-cycle ensemble average of cylinder pressure traces from Bin G at an injection advance of -9.3 CAD pilot injection advance.	171

D.8	600-cycle ensemble average of cylinder pressure traces from Bin H at an injection advance of -11.1 CAD pilot injection advance.	172
D.9	Heat release rate traces for Bin A.	172
D.10	Heat release rate traces for Bin B.	173
D.11	Heat release rate traces for Bin C.	173
D.12	Heat release rate traces for Bin D.	174
D.13	Heat release rate traces for Bin E.	174
D.14	Heat release rate traces for Bin F.	175
D.15	Heat release rate traces for Bin G.	175
D.16	Heat release rate traces for Bin H.	176

List of Symbols

Constants

κ_B	Boltzmann Constant.	$1.380649E - 23 J/K$
R	Ideal Gas Constant.	$8.314 J/(Kmol)$

Latin

CR	Cylinder Compression Ratio
HCR	Hydrogen-to-Carbon Molar Ratio
A_p	Piston Wall Area
A_w	Cylinder Wall Area
A_{inj}	Injector Orifice Area
C	Concentration of Species
c_p	Constant-Pressure Specific Heat Capacity
c_v	Constant-Volume Specific Heat Capacity
D_{cyl}	Cylinder Bore Diameter
E	Energy
h_w	Cylinder Wall Heat Transfer Coefficient
l_r	Cylinder Rod Length
l_{hg}	Headgasket Thickness
l_{prot}	Piston Protrusion Height
l_{st}	Cylinder Stroke Length
M	Molar Mass of Species
m	Mass
N	Number
n	Mols of Species

P_{cyl}	Cylinder Pressure
P_{rail}	Diesel Rail Pressure
Q_b	Cylinder Wall Heat Transfer
Q_b	Heat Release of Combustion
T_g	Cylinder Gas Temperature
T_w	Cylinder Wall Temperature
T_{cyl}	Cylinder Temperature
U	Internal Energy
u	Specific Internal Energy
v_p	Piston Velocity
V_{cyl}	Cylinder Volume
V_s	Cylinder Swept Volume
W	Work
x_{wp}	Cylinder Wrist Pin x-Position
$y_{wp,max}$	Cylinder Wrist Pin Maximum y-Position
y_{wp}	Cylinder Wrist Pin y-Position

Greek

α	Convective Heat Transfer Coefficient
α_w	Cylinder Wall Absorptivity
α_{inj}	Injector Flow Coefficient
χ	Replacement Fraction
ϵ_g	Cylinder Gas Emissivity
η	Efficiency
κ	Ratio of Specific Heat Capacities
λ	Engine Air-Fuel Stoichiometric-Normalized Ratio
ω_{crk}	Crankshaft Rotation Speed
ϕ	Engine Fuel-Air Stoichiometric-Normalized Ratio
ρ	Density
Θ	Specific Emissions Output
θ	Engine Crank Angle

Abbreviations

AFR Air-fuel mass ratio.

aTDC After top dead center, in reference to crankshaft angle.

BDC Bottom dead center.

bTDC Before top dead center, in reference to crankshaft angle.

CA Crank angle.

CA10 Crank angle of 10% mass burned.

CA50 Crank angle of 50% mass burned.

CA90 Crank angle of 90% mass burned.

CI Compression ignition.

CO Carbon monoxide.

CO₂ Carbon dioxide.

CoV Coefficient of variance.

DOC Diesel oxidation catalyst.

DOI Duration of injection.

DPF Diesel particulate filter.

ECU Engine control unit.

EGR Exhaust gas recirculation.

EOC End of Combustion.

EVC Exhaust valve closure.

EVO Exhaust valve opening.

H₂O Water.

HCCI Homogeneous charge compression ignition.

HCR Hydrogen-to-carbon atomic ratio of a fuel.

HHV Higher Heating Value.

IMEP Indicated mean effective pressure.

IMEPg Gross indicated mean effective pressure.

LHV Lower Heating Value.

LTC Low temperature combustion.

LUT Look-up table.

M Molar mass of a species.

M2P Time between the end of the main injection and start of the post injection.

MABX dSPACE MicroAutoBox II.

N₂ Nitrogen.

N₂O Nitrous oxide, an oxide of nitrogen.

NMHC Non-methane hydrocarbon.

NO Nitrogen monoxide, an oxide of nitrogen.

NO₂ Nitrogen dioxide, an oxide of nitrogen.

NO_x Oxides of nitrogen.

O₂ Oxygen.

P2M Time between the end of the pilot injection and start of the main injection.

PCCI Premixed charge compression ignition.

PLB Premixed lean burn.

RCCI Reactivity controlled compression ignition.

RPM Revolutions per minute.

SCR Selective catalytic reduction.

SI Spark ignition.

SOC Start of combustion.

SOI Start of injection.

TBI Throttle body injection.

TDC Top dead center.

uH₂ Unburnt hydrogen, in reference to exhaust gases.

uHC Unburnt hydrocarbons, in reference to exhaust gases.

VE Volumetric efficiency.

Chapter 1

Introduction

1.1 Motivation

Many governments around the world are pledging for reduced or net zero carbon dioxide output by 2050 [1]. In the realm of transport, the methods to meet this have widened from only internal combustion engines to battery electric power and fuel-cell powered vehicles [2–4]. While all these methods allow for the reduction of tailpipe CO₂ emissions to near-zero, the relative energy and power density of each method causes a significant gap in use cases. Battery-based vehicles will likely be applicable in the light-duty segment, however the high energy usage in the heavy-duty segment may require other fuels such as hydrogen for efficient usage of vehicle volume and mass, especially with long-distance transport [5, 6]. Hydrogen is a fuel that can reduce the carbon output at the site of its consumption to zero, meaning that only fuel producers would have to focus on avoiding carbon emissions by process design or carbon capture.

At this time, little vehicular fueling infrastructure for hydrogen exists in North America outside of California [7, 8]. There is also a significant gap between current hydrogen production and the possible demand if wide scale vehicle adoption occurs [9]. This lack of infrastructure in many areas creates a severe issue for perspective adopters: hydrogen vehicles may provide lower tailpipe emissions, but without an economic supply of fuel there is no reason for most users to adopt them. Dual fuel

presents a solution to this problem: a vehicle can be run purely on conventional fuels or on a blend of both hydrogen and conventional fuel when hydrogen is available and economic to operate with. This helps to tide over the initial adoption period, and allow for the demand of hydrogen to grow based on consumer demand and consumer capital.

In the case of heavy-duty diesel-hydrogen dual fuel engines, they could run partially on hydrogen, reducing their tailpipe carbon dioxide emissions. Depending upon the ratio of hydrogen, interim climate goals (such as Canada's 2030 carbon emissions reduction targets [10]) could be achieved with existing vehicles and largely existing technologies. This would present a low-cost pathway to decarbonization, which may make widespread adoption more likely, thus causing more emissions reduction. It may even be possible to run dual-fuel hydrogen diesel on largely unmodified diesel engines, making the retrofits of engines possible instead of the purchase of a new vehicle.

There are some barriers to hydrogen-diesel dual fuel beyond the availability of hydrogen. A large dataset for hydrogen diesel dual-fuel with a wide load range and varied injection parameters has not been published. Having a large dataset would help to identify patterns in how the dual fuel combustion effects efficiency, performance, and emissions over the whole load spectrum. A large dataset would also allow for better modeling of perspective vehicle performance with simulated drive cycles.

1.2 Problem Statement

The objective of this thesis and the research presented therein is to provide combustion and emissions data and characterization of a combustion engine running on a hydrogen-diesel dual-fuel blend, with a wide range of operating conditions.

1.3 Thesis Organization

The structure of this thesis is as follows:

Chapter 2 examines the background information needed in this work. Previous works involving hydrogen-diesel dual fuel combustion, hydrogen combustion, engine emissions and combustion methods. Hydrogen's usage as a fuel is also explored and compared to conventional fuels.

Chapter 3 contains information related to the physical setup of the test engine, engine controller implementation, design of the hydrogen injection system and injection test procedure. It also contains information on all relevant sensors and data capture systems used.

Chapter 4 provides information related to the analysis of the combustion and emissions produced from the engine. Formulae used for the analysis of data are also provided in this chapter.

Chapter 5 contains results and analysis related to steady-state operation of the engine while running pure diesel and hydrogen-diesel dual fuel.

Chapter 6 concludes the thesis, with a summarization of the of the results found and a discussion of areas of possible future work.

1.4 Contributions

The major contributions of this work are as follows:

- Collection of a wide-range dataset of hydrogen-diesel dual fuel engine performance and emissions with varied injection parameters, intake pressures, hydrogen replacement and loads
- Characterization of the impact of hydrogen on the conventional diesel combustion process

Chapter 2

Background

2.1 Hydrogen in Engines

The usage of hydrogen as an engine fuel has been explored since the De Rivaz engine in 1806 [11], and holds promise in reducing carbon dioxide emissions [12]. Hydrogen is a gaseous fuel that is characterized by its low density and wide flammability range. Currently, hydrogen is being investigated as a fuel and energy carrier in a zero-emissions economy [9, 13], where hydrogen could be burned as a fuel at endpoints without causing CO₂ emissions. To better understand the fuel-relevant properties of hydrogen, some of the properties of hydrogen fuel as compared to diesel, CNG, and LiFePO₄ batteries are present in Table 2.1.

Many methods of using hydrogen in engines have been studied. The oldest is spark

Table 2.1: Comparison between perspective energy sources in the heavy-duty market.

Fuel	LHV (MJ/kg)	Energy Density (MJ/L)	Tailpipe CO ₂ (g CO ₂ /MJ LHV)
Diesel	42.83 [14]	35.87 [14]	74.9 [14]
H ₂ (350 bar)	119.64 [14]	2.83 [15]	0
H ₂ (700 bar)	119.64	4.75 [15]	0
LH ₂	119.64	8.66 [15]	0
CNG (250 bar)	47.14 [14]	9.71 [14]	56.3 [14]
LiFePO ₄	0.50 [16]	0.76 [16]	0

ignition of a pre-mixed charge [11] and this is still studied today [17]. Hydrogen can be injected directly into the combustion chamber as a gas [18] or cryogenic liquid [19]. When directly injected into the combustion chamber, it can burn as either premixed or stratified charge ignited by a diesel pilot [18], or as a jet which can be ignited by pilot fuel [20] or hot surface igniter [21]. HCCI combustion has also been studied [22].

2.2 Combustion of Hydrogen

Hydrogen is characterized by its high flammability range and high flame speed at near-stoichiometric mixtures, making it an excellent fuel for pursuing premixed-lean-burn (PLB) combustion. PLB has significant advantages in engine efficiency and NO_x reduction over conventional stoichiometric ($\lambda = 1$) premixed combustion [23]. When ignited by a spark, λ , the stoichiometric ratio of air to fuel for hydrogen, is often in the range of $1 \leq \lambda \leq 5$ [24], meaning that up to 5 times the required air for stoichiometric combustion can be introduced into the cylinder and premixed flame propagation can still occur.

As hydrogen is usually introduced as a premixed fuel, engine knock is a concern. Knock is a process where combustion occurs abnormally, and pressure waves are generated within the cylinder [25]. Knock occurs due to the auto-ignition of end-gas in the engine cylinder before the premixed flame front can reach it [25]. Depending on the temperature, temperature gradient and energy content of this end gas, the knock produced from autoignition can range from mild to engine failure [25, 26]. Knock also increases the heat rejection through the cylinder walls (up to 2.5x greater at higher knock intensities [27]), causing higher engine temperatures, and lower engine efficiencies due to heat loss from the cylinder. Knock can be detected via either measurement of the in-cylinder pressure, engine block vibration, or exhaust temperature [26].

High end-gas temperatures (and thus high in-cylinder temperatures) increase the risk of knock [26]. In general, as load increases, the in-cylinder temperatures increase

due to increasing heat release. Cylinder temperatures can be reduced by combustion phasing (late ignition results in lower end-gas temperatures [25, 28]) but the engine thermal efficiency reduces, The compression ratio of the engine is a dominant factor in the in-cylinder temperatures [26]. However, reducing the engine’s compression ratio would have a negative effect on the mixing-controlled diesel combustion [29].

Introduction of exhaust gas recirculation (EGR) can also reduce the chance of knocking. The burnt gas and inert components of EGR have a radical-quenching effect [30, 31], which can help to neutralize combustion-inducing radicals throughout the cylinder — particularly in areas where the flamefront has not reached yet to avoid or delay knock.

Preignition is also a concern when combusting hydrogen [32, 33]. Despite hydrogen’s octane rating of exceeding 120 RON under lean conditions that other fuels would not support [34], when hydrogen is combusted at stoichiometric conditions it has a very low octane number of 63 RON [34]. This high reliance of hydrogen on the mixture conditions for knock resistance means that in high-compression engines, hydrogen may have to be run at very lean mixture ratios [35, 36], which significantly limits power density due to the high ratios of excess air required for non-knocking operation. At higher engine compression ratios, knock intensity at the same operating points increases greatly [37]. In diesel engines, with very high compression ratios (ranging between 17:1 and 21:1, generally), this compression ratio limitation results in lower load ceilings [12].

Similar to its low octane when approaching stoichiometric conditions, hydrogen has a minimum ignition energy value of only 0.034 mJ/mm when using a spark igniter at stoichiometric conditions [38], and overall approximately 10% that of similar hydrocarbon mixtures [12]. This translates into a very low activation energy for combustion. Preignition can cause higher-than expected cylinder pressures due to advanced combustion phasing. However, preignition is not the same as end-gas knock, which requires the hydrogen flamefront to not have consumed the end-gas

before autoignition can occur [12]. Because of hydrogen’s high flame speed, knock is less likely than conventional fuels such as gasoline [12]. This can be explained as a preignited flamefront being able to quickly traverse the cylinder before the hydrogen end-gas can autoignite. However, this does not avoid the higher cylinder pressures and temperatures associated with preignition, nor does it guarantee that a thermal run-away situation will not occur with successive preignition cycles leading to knock [12].

2.2.1 Dual Fuel Combustion Process

Diesel-Hydrogen dual fuel combusts in a method that shares similarities to both premixed and nonpremixed combustion, however these are phased together resulting in overlapping combustion methods and differing optimal conditions. Due to the large differences in the optimal excess air ratios for these methods, often low-load conditions result in low thermal efficiencies while running dual fuel [39].

Figure 2.1 shows the stages of combustion that would occur in a dual-fuel combustion cycle with rich enough lambda to support a premixed flame. As the premixed hydrogen air-fuel ratio becomes closer to stoichiometric, the hydrogen flame is able to travel closer to the cylinder walls before extinction, reducing hydrogen slip [33]. The lean boundary for ignition is expanded due to an increasing reaction rate as load (and cylinder temperature) increases [33].

2.2.2 Injection Methods

In an engine, hydrogen can be introduced either upstream of the intake manifold (throttle-body injection, TBI), into the intake runners (port injection, PI) or directly into the cylinder (direct injection, DI). Table 2.2 compares these methods in both complexity and cost. From a load and combustion strategy standpoint, DI is very attractive due to its high load ceiling. Hydrogen DI is also able to increase knock thresholds via delaying injection into the compression stroke. The injection event can

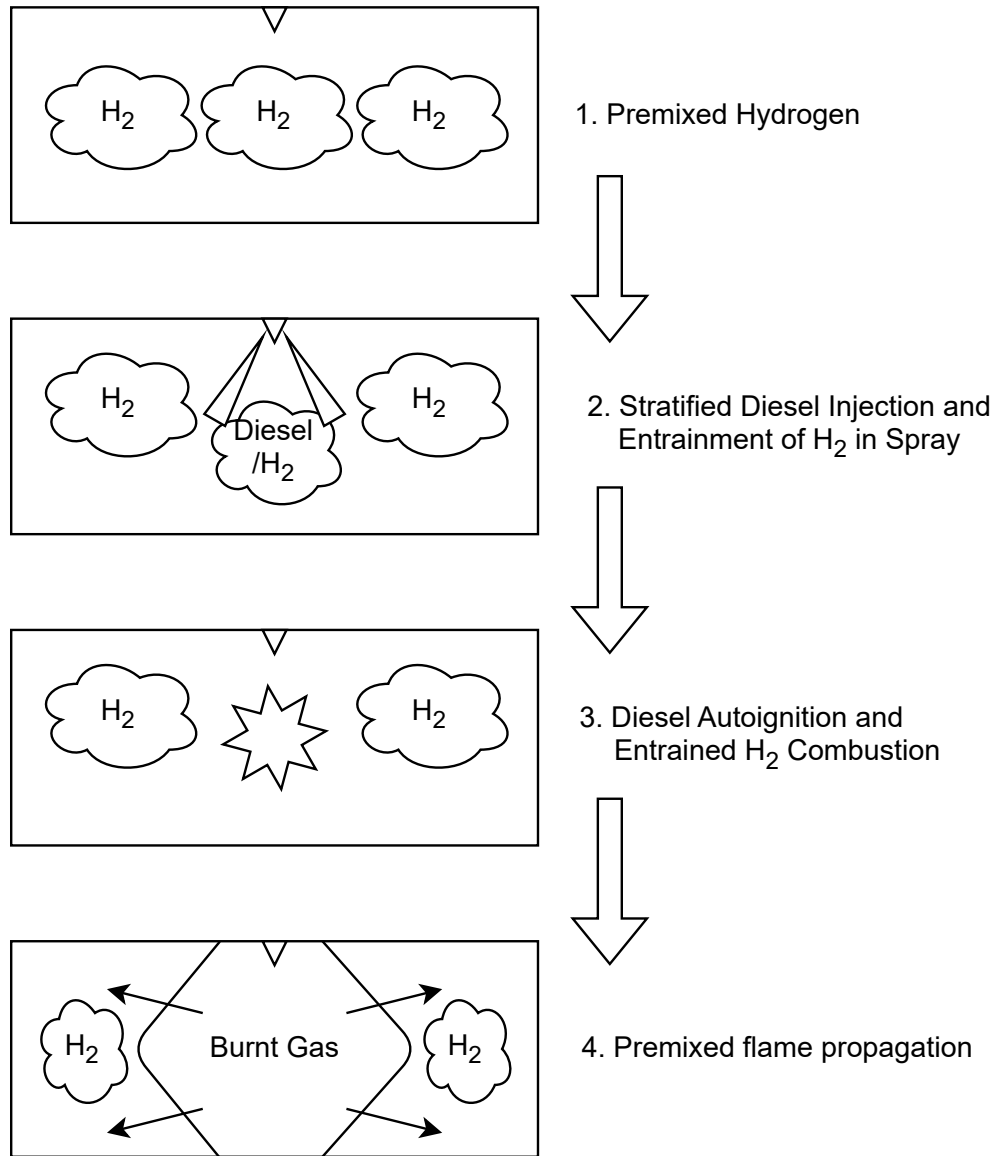


Figure 2.1: Diagram of the entrainment and ignition process in a dual-fuel hydrogen diesel engine [40].

Table 2.2: Comparison between injection methods.

Parameter	TBI	PI	DI
Maximum Load	Low	Low	High
Knock Threshold	Low	Low	High
Injection Pressure	< 16 bar	< 16 bar	> 60 bar
Injector Count	≥ 1	1 per cylinder	1 per cylinder
Combustion Methods	Premixed	Premixed	Premixed, Stratified, Diffusion
Cylinder Balancing	No	Yes	Yes
Cost	Low	Medium	High
Control Complexity	Low	Medium	High

also be significantly delayed into the compression stroke (or even expansion stroke) to adjust the hydrogen mixing/in-cylinder gas temperature and create a stratified hydrogen charge. Some energy can also be recovered from the injection and expansion of the compressed hydrogen into the cylinder. Liu et. al. have experimented with a hydrogen-diesel duel fuel DI engine which was capable of up to a 13.3% improvement in indicated efficiency over pure diesel operation, and were able to produce a hydrogen diffusion flame by delaying hydrogen injection into the expansion stroke [18]. However, direct injection gas injectors suitable for production vehicles have had limited development. Additionally, an onboard compressor is required to allow operation when the hydrogen tank pressure is lower than the requested injection pressure. This significantly increases the complexity and implementation costs for mobile applications.

Non-DI solutions have a significant downside of displacing air from the intake stream (and replacing said air with the injected hydrogen). This reduces the peak power density of the engine without using forced induction [12]. Injection of gas before the cylinder could also result in flammable or potentially explosive atmospheres occurring in the manifold, resulting in backfiring and potentially dangerous engine

operation [41]. However, due to the lower operating pressure of the injectors, no gas compressor would be required for operation. Additionally, only limited stratification can be achieved with non-DI injection, especially without specialized engine port design [42–44]. This limits combustion strategies.

Port gas injection has had significant development with CNG and LPG fuels in the European and Asian markets [45]. Existing port injection control strategies that exist for conventional fuels could be leveraged for hydrogen control [46], reducing system development costs. Port injection strategies in gasoline engines have been implemented for decades to control cylinder balancing, fuelling targets, and knock avoidance [47]. Importantly, injection timing can be adjusted with port-injected operation, which can help to alleviate backfiring of the engine [41].

Throttle body injection (TBI) is a low-cost implementation of hydrogen injection, which can use as little as a single injector to feed an entire engine’s fuel supply, or in some cases a simple valve. This simplicity limits the amount of control and can create operation limitations. The single injection point requires good mixing to occur for even mixture distribution [48], and optimal combustion to occur in all engine cylinders.

2.2.3 Emissions and Efficiency

As hydrogen gas has no carbon component, it is an attractive fuel for reducing tailpipe carbon oxide emissions to near-zero. CO presents immediate health hazards in parts-per-million quantities, while CO₂ has negative environmental effects in regards to the greenhouse effect. Hydrogen combustion does not produce particulates, meaning that the only particulate production in a hydrogen engine would be from the cylinder oil film [49–51]. Hydrogen also produces no unburnt hydrocarbons, reducing the unburnt hydrocarbon (uHC) output of a dual-fuel engine. Hydrogen itself is not a controlled emission, and its only negative greenhouse effect is indirect by scavenging OH- radicals that would otherwise be used to break down atmospheric methane [52].

In a dual-fuel engine, the benefits to uHC, particulate, and CO₂ emissions reduction remains, with the amount dependent upon the hydrogen replacement fraction and operating point [53].

Hydrogen-diesel dual fuel is known to increase the NO_x output of the engine at medium and high loads compared to diesel, and to offer a similar NO_x output compared to diesel at low loads [47, 54]. This NO_x increase is partly driven by an increased conversion rate of NO to NO₂, driven by a radical mechanism involving unburnt hydrogen [55], which can easily be alleviated by existing aftertreatment technologies [56]. However, the major contributing factor to higher NO_x is higher cylinder pressures (and thus in-cylinder temperatures), which is driven by the premixed combustion process. NO_x production is known to increase following an exponential relationship when cylinder temperatures exceed 1800 K [57], with the Zeldovich mechanism becoming dominant and further increasing NO_x production beyond 2300 K [58]. Premixed combustion results in higher cylinder pressures than mixing-controlled combustion at the same compression ratio, as the cylinder pressure cannot be shaped in-cycle by rate control of the fuel injection. EGR can be used to reduce NO_x output by reducing combustion speed (and thus temperatures) [59] and quenching hydrogen-related combustion radicals responsible for nitrogen oxidation [60].

Engine efficiency in pure hydrogen (SI) applications is known to be greater than the equivalent gasoline engine efficiency [61, 62], which is mainly driven by hydrogen's high flame speeds and lean burn capability. However, maximum power output is reduced due to the displacement of air from the intake stream and concerns with abnormal combustion causing engine damage at near-stoichiometric conditions with hydrogen [32]. This difference in power output can be alleviated by using forced induction and increasing the intake air pressure to account for the higher air consumption required, however this requires greater engine complexity, and more robust components to handle higher cylinder pressures.

In dual fuel applications, the engine efficiency is often reported as being less than

pure diesel at low loads and equivalent or better than diesel at high loads for port injection studies [47]. The reasons for this relate to lean mixtures of hydrogen at low loads due to a lack of throttling of the air intake, and colder cylinder conditions. This results in lower combustion efficiencies of hydrogen. Running at an engine load of 2.1 bar BMEP in a heavy duty engine, approximately 80% hydrogen combustion efficiency was reported due to failure to support a vigorous premixed flame [63]. Combustion efficiency was improved dramatically at higher engine loads. EGR has been used to increase the combustion efficiency of the premixed hydrogen. A sensitivity analysis at 3 bar BMEP engine load found a strong correlation between increased EGR rate and improved hydrogen combustion efficiency [39], at a cost of increased particulate generation. A similar improvement in efficiency with increased EGR rate at 6 bar BMEP load was also reported, but with a lower magnitude of improvement [64].

Hydrogen-diesel dual fuel has been explored extensively in literature for both port and direct hydrogen injection, where the diesel serves as an ignition source for a hydrogen premixed flame. Both strategies show significant reductions in CO₂ output, and increased NO_x production at higher engine loads. For load conditions of 6 bar BMEP and higher, an increase in NO_x emissions positively scaling with load and hydrogen replacement ratio was reported [33, 65]. High exhaust gas recirculation (EGR) concentrations were able to decrease NO_x output to be comparable to pure diesel operation with a particulate formation penalty. Engine efficiency was also found to decrease at low loads and power outputs due to increasing hydrogen slip. A similar impact of EGR on NO_x trends was reported, where increasing EGR rates allowed for a 35% decrease in NO_x emissions versus zero EGR flow [59].

Port fuel hydrogen substitution is usually limited by maximum pressure rise rate and end-gas knock [66]. Direct injection allows for the extension of knock limits and to allow stratification of the hydrogen mixture. 90% energy replacement of hydrogen using direct injection with a peak 57.2% indicated efficiency has been accomplished [18], at a cost of high NO_x emissions.

Low temperature combustion (LTC) has also been accomplished with hydrogen, however with a limited load and engine speed range and at high compression ratios [67–69]. Diesel-hydrogen LTC has also been accomplished with similar constraints [70].

2.2.4 Hydrogen Slip and Its Mitigation

With hydrogen fuel, the presence of unburnt fuel surviving the combustion cycle and escaping in the exhaust stream (hydrogen slip) can occur at low loads and lean mixtures [40, 63]. Hydrogen slip is driven by load and mixture richness [40, 63]. Low-load operating points have lower in-cylinder temperatures, which results in slower combustion rates and lower propagation speed of the hydrogen flame throughout the cylinder [33, 39]. A low flame speed means a longer combustion duration, which when progressing late into the expansion stroke can result in temperatures too low to maintain vigorous combustion [40]. Having a lean mixture also reduces the flame speed, resulting in a similar increase in slip with very lean mixtures [40]. However, there are methods to mitigate hydrogen slip.

Increased EGR rates can have a positive effect on engine efficiency at lower load operating points (at approximately 8 bar IMEP and lower) where the bulk cylinder temperatures are lower due to less combustion heat released per cycle [64]. Improvements in engine efficiency are accomplished by reduced hydrogen slip due to higher temperatures and supporting more vigorous premixed flame propagation. Increased EGR fraction at these loads additionally improves NO_x emissions, and lowers the maximum cylinder pressure rise rate [64]. However, particulate emissions rise with increasing EGR fraction due to its negative effect on the soot oxidation process [64]. This can be mitigated by further increasing the hydrogen fuel energy fraction, however this strategy may not be viable at all operating points.

Premixed hydrogen combustion with λ close to stoichiometric improves flame speed and can also reduce hydrogen slip [40]. This can be accomplished by either decreas-

ing the mass of air in the cylinder (throttled) or increasing the mass of the hydrogen injection. While throttling the intake air is an effective strategy for many engine operating points, throttling introduces an efficiency penalty by increasing the pumping losses of the engine [71]. Depending on the operating point, this efficiency penalty may be greater than the efficiency gained from more vigorous combustion. Increasing the hydrogen injection mass requires a reduction in diesel injection mass in order to retain the same power output. This may not be possible at high hydrogen replacement rates due to the minimum possible injection duration from the diesel injector. Additionally, high replacement values of hydrogen may run into the knock limit of the engine, which limits further increases to the hydrogen injection mass.

Changes in the diesel injection strategy can also help to mitigate hydrogen slip. Entrainment (effectively the volume of the cylinder that is within the diesel spray) can be improved by increasing diesel injection pressure, which improves the diesel spray atomization and penetration into the cylinder [72].

2.2.5 Aftertreatment of Hydrogen Engines

Due to the lean mixtures that hydrogen burns at, the traditional 3-way catalyst is ineffective at emissions reduction in a hydrogen engine under most operating conditions. Instead, lean-operating catalysts such as the urea-SCR catalysts developed for diesel engines must be used [56]. There is evidence that usage of hydrogen with a traditional urea-based SCR system may improve its efficiency and conversion rate of NO_x , along with increasing resistance to catalyst poisoning [73]. This would be advantageous in dual-fuel conversions, as it could help alleviate the higher engine-out NO_x as compared to pure diesel operation without increasing urea usage or requiring larger catalyst surfaces. Hydrogen has also been found to increase the ratio of NO_2 to NO_x in the exhaust stream under certain conditions [74], which would further improve traditional SCR conversion efficiency [75, 76]. Purpose-built dual fuel vehicles could also take advantage of these factors by having a SCR system with reduced size,

lowering costs. In these vehicles, catalyst chemistry could also be changed to different types with higher hydrogen reactivity [77].

However, there has been research into purely hydrogen-based SCR aftertreatment systems, which use hydrogen as the reducing gas itself instead of an additional injected compound [78, 79]. This method has an advantage over traditional urea-based SCR systems, as an additional chemical is no longer required, and depending on implementation may also simplify the dosing system to only use the engine fuel injectors.

Hydrogen also appears to have a positive impact on diesel oxidation catalyst effectiveness [80, 81], reducing light-off temperature. In a dual-fuel setup, this would allow for greater oxidation of UHC and CO emissions, especially at low exhaust temperatures/loads, where DOCs suffer reduced performance [76]. A reduced light-off temperature would also mean that the diesel injection strategy would be able to use less fuel during post injection, which could be used to improve engine efficiency.

DPF regeneration can also be effected by hydrogen content. This can allow for lower temperature regeneration cycles, improving DPF substrate lifespan [82]. Regeneration temperature is lowered due to a lower light-off temperature provided by free hydrogen in the exhaust stream [82]. Additionally, passive regeneration of the DPF may become possible at low engine exhaust temperatures/loads in dual-fuel setups due to hydrogen slip [76].

Chapter 3

Experimental Setup

3.1 Engine Assembly

The experimental results reported in this thesis are performed on an inline four cylinder Cummins QSB 4.5 Tier 3 diesel engine located at the University of Alberta engine lab. The engine meets the previous United States EPA emissions standards (EPA Tier 3 Offroad), which were in effect from 2006 to 2014. This engine is a turbocharged after-cooled direct-injected diesel engine without external aftertreatment or exhaust gas recirculation (EGR). The engine is designed for an off road application such as a pump or stationary generator, with a reduced peak power output to ensure long service life (as compared to the on-road variants of the engine). The architecture of the engine is cam-in-block, and a single camshaft controls both intake and exhaust valve lift. No camshaft angle phasing or variable valve lift system is implemented on this engine. Diesel fuel is pressurized by a on-board electronically controlled high pressure fuel pump, and delivered through a high-pressure common fuel rail to the injectors. These injectors are solenoid-type injectors and are electronically controlled. The fuel system is return-style, meaning that some fuel flows through the injectors and returns to the fuel storage tank to ensure proper cooling of the injectors. Fuel is also returned from the pump before compression in order to control the diesel fuel rail pressure. Coolant temperature is controlled by a wax-thermostat element which adjusts how much coolant bypasses the heat exchanger. The engine, as tested, is

pictured in Figures 3.1 and 3.2. More parameters of the engine are available in Table 3.1.

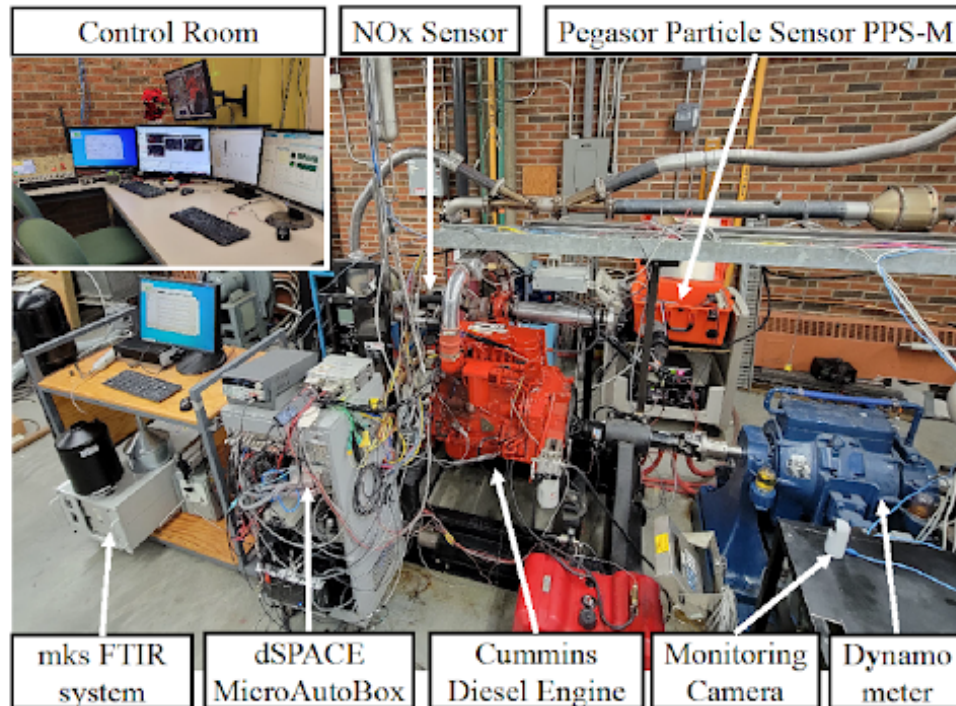


Figure 3.1: Image of the tested engine.

3.1.1 Hydrogen Injection Strategy

To better represent the conversion of an existing engine, the selected hydrogen injection strategy was port injection. This allows for lower gas pressures immediately before injection, and for an increased mixing and diffusion time for hydrogen as compared to a direct injection setup. Direct injection (DI) would require an addition set of holes being drilled into the combustion chamber, which was not possible without intersecting the valvetrain components. There are also significantly more port gas injectors commercially available than direct gas injectors, allowing for a better selection of injectors that meet high volumetric flow requirements. However, there are some combustion disadvantages of port injection such as a lower knock limit [83] and lower engine volumetric efficiency due to hydrogen displacing air from the intake gas

Table 3.1: Cummins QSB 4.5 Tier 3 parameters, as tested

Parameter	Value
Total Displacement	4.460 L
Number of Cylinders	4
Bore	107 mm
Stroke	124 mm
Connecting Rod Length	192 mm
Compression ratio	17.2:1
Piston Protrusion	0.43 mm
Headgasket Thickness	1.6 mm
Valve train	Pushrod
No. of valves (In/Ex)	2/2
No. of Camshafts	1
Max. valve lift (In/Ex)	8 mm/8 mm
Valve angle (In/Ex)	0°/0°
Valve diameter (In/Ex)	33 mm/33 mm
Combustion Chamber Type	Bowl in Piston
Injection Type	Direct
Injection Pressure	300 bar - 1500 bar
Spray Angle	124°
Injector Holes	8 Holes
Injection Plane	Single
Injector Actuation	Solenoid



Figure 3.2: Image of the exhaust side of the tested engine.

stream. Usage of port injection also rules out stratified combustion strategies with hydrogen.

Only cylinder 1 runs in a hydrogen-diesel dual fuel configuration, while cylinders 2 through 4 run on pure diesel. This reduces hydrogen gas usage, deemed necessary as to minimize high-pressure high-capacity tanks in University of Alberta engine lab. Standard K-tanks were used to supply hydrogen, which contain a nominal hydrogen mass of 570 g each. To ensure that hydrogen was only flowing into cylinder 1, the injection timing of the port injector was limited to a 90-degree span during the intake stroke of cylinder 1. These limits were verified while measuring all the engines cylinder pressures simultaneously to ensure that cylinders 2 through 4 did not experience an increase in gas pressure due to the presence of hydrogen.

Running one cylinder with hydrogen and the other cylinders with diesel allows for some of the multi-cylinder dynamics of the engine to be preserved. This includes in-cycle crank acceleration from the other cylinder's compression and expansion events, along with intake manifold gas-scavenging phenomena.

3.1.2 Modifications to Engine Assembly

To allow for the measurement of in-cylinder pressure, the intake charge temperature, and the injection of hydrogen, 6 holes were drilled into the engine cylinder head. Four of these holes were drilled directly into the cylinders of the engine. These holes were sleeved and sealed with o-rings as they crossed both coolant and oil passages inside of the cylinder head. A tap was manufactured for each of these cylinder head holes to allow for the engine to retain compression if a cylinder pressure transducer was not being used. Two additional holes were made in the non-shared intake runner of cylinder 1, one for measurement of the gas charge temperature with a thermocouple and one to mount the port gas injector, as detailed in Figure 3.3. Two existing holes in the engine were also rebored to accept a thermocouple to measure intake air temperature at the mouth of the manifold and air pressure with a high-speed sensor.



Figure 3.3: Image of the populated holes bored into the head for intake port temperature monitoring and hydrogen injector installation with mounted items.

Each of the engine cylinders are fed by 2 separate intake runners, meaning that 5 intake runners are cast into the cylinder head instead of a single runner per cylinder. The central 3 runners are shared between their respective cylinders, while the outer

runners supply only a single cylinder, detailed in Figure 3.4. This setup precludes being able to isolate cylinder 1's intake parts from cylinder 2's intake ports. Each cylinder has a single dedicated exhaust runner. To create a greater injection window for port hydrogen into cylinder 1, the gas injector was mounted to inject into cylinder 1's non-shared intake runner. This mounting location was originally where a frost plug was located on the engine, allowing for the injector and mounting solution to minimally impact the cross-sectional area of the intake runner.

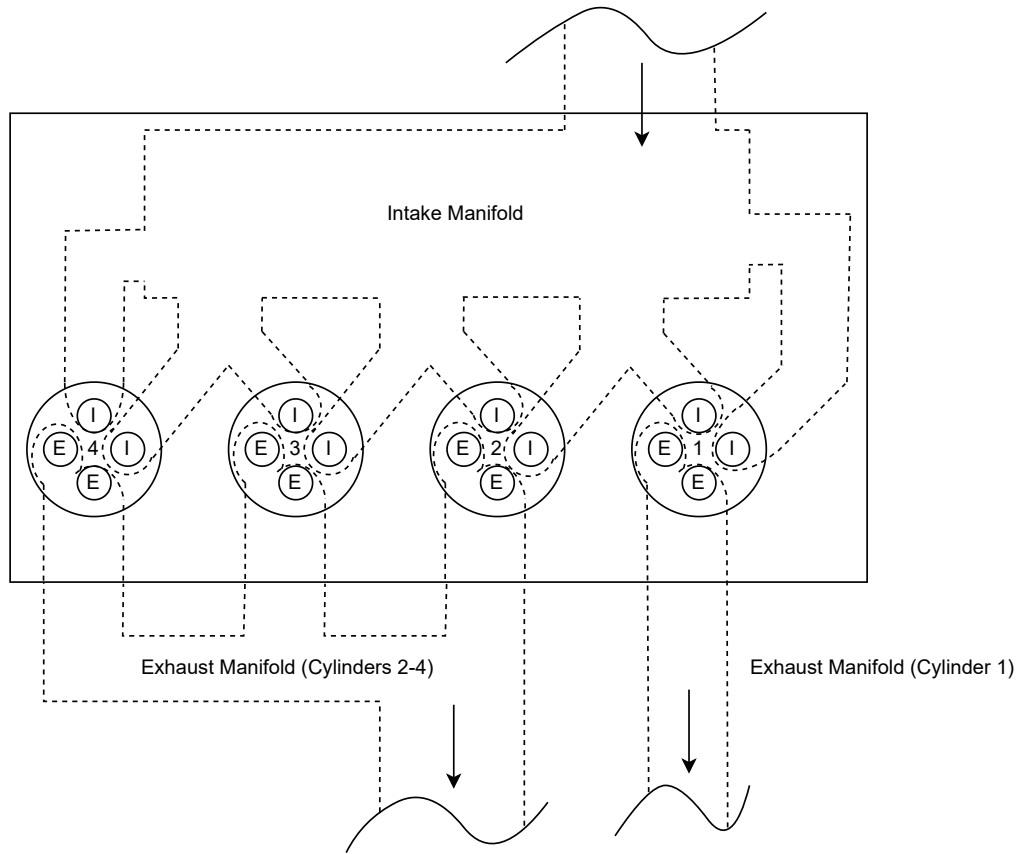


Figure 3.4: Top-down sectional view of the intake and exhaust runners cast in the head.

The exhaust manifold was split in order to measure exhaust gases purely from cylinder 1. Cylinders 2 through 4 were routed into a common collector then through the turbine inlet of the turbocharger, as per the production engine configuration. The turbocharger turbine outlet then went to the ventilation system. Cylinder 1's exhaust

was routed through a 1.5 m length of pipe, then into the common ventilation system with the other cylinder’s exhaust stream (Figure 3.5). This long length ensures that no backflow of gas from cylinders 2 through 4 can reach the cylinder 1 exhaust gas instrumentation.

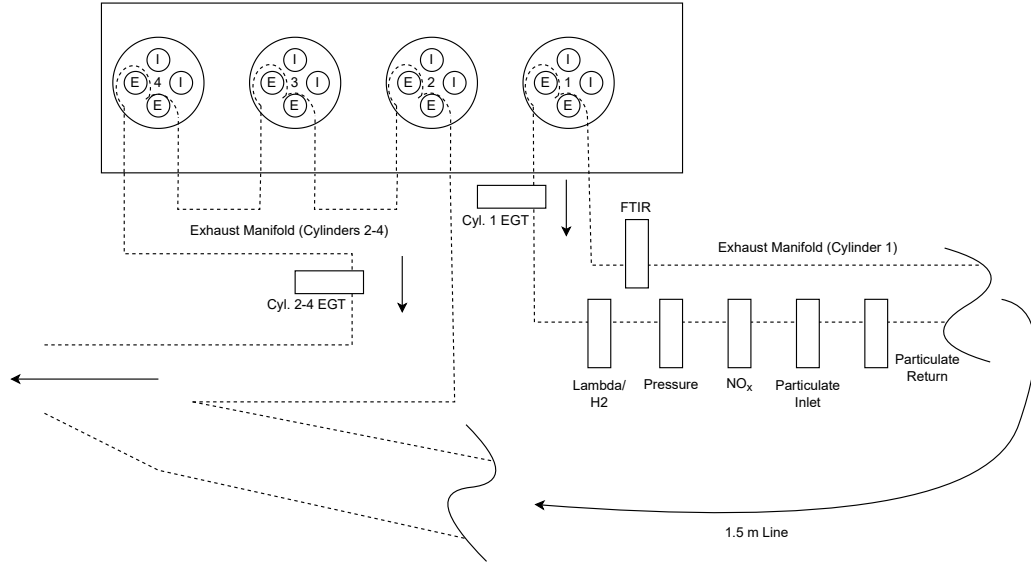


Figure 3.5: Exhaust manifold routing schematic.

The engine’s alternator was removed to eliminate the transient load it would produce while charging the battery. The battery is only used for cranking the engine, and is charged by a battery tender from building power. The power required to drive the engine electronics is supplied from a Sorensen DCS 55-55 power supply with an auxiliary 5V source for sensors provided by a Keithley 2231A-30-3 DC power supply.

3.1.3 Manifold Air Conditioning

Due to the splitting of the exhaust manifold and reduction of mass flow, the turbocharger was unable to develop boost pressure beyond 30 kPa, resulting in non-representative performance. To supply boost pressure, regulated building air was used to pressurize the air in the engine intake manifold. The building air is dried, resulting in minimal water intake under boosted operation. The manifold pressure of the engine is set by manually changing the regulator output pressures. This setup is

sufficient to supply 2 bar absolute intake pressure to the engine at an engine speed of 2500 RPM. No temperature control is present on building air setup, as the air temperature post-regulation is approximately room temperature at the manifold (19-25 degrees Celsius depending on pressure). The setup also features a gate valve and a vacuum valve to allow for operation at ambient and sub-ambient pressures, and to assist with ease of starting the engine. A process diagram of this intake setup is present in Figure 3.6, and an image of the intake manifold collector is in Figure 3.7.

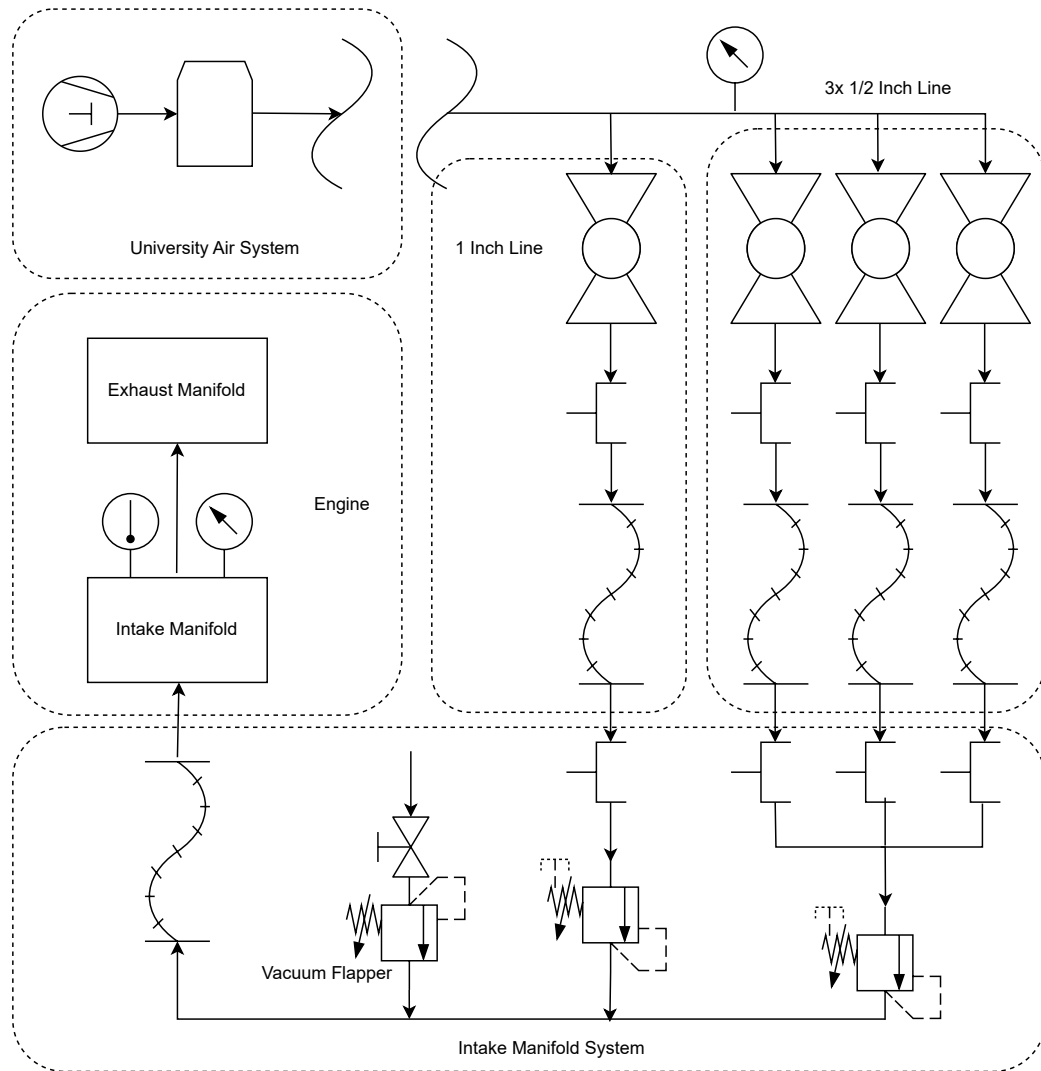


Figure 3.6: Process diagram of the intake air system that provides pressure from building air.

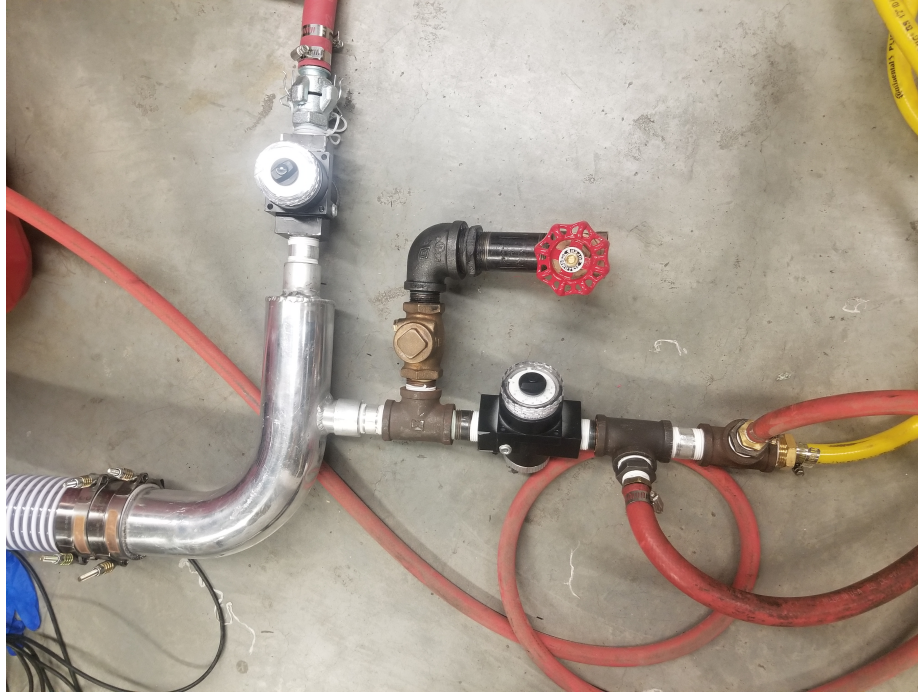


Figure 3.7: Image of the intake collector where building air is regulated to engine intake pressure.

3.1.4 Hydrogen Delivery System

To safely deliver hydrogen from the storage tank to the engine manifold, a low pressure drop system was designed to transport the gas from a gas cabinet. An image of the gas cabinet with installed hardware is available in Figure 3.8. The system is designed to flow up to 15 L/s of H_2 at a pressure drop of less than 0.5 bar. To resist hydrogen embrittlement, all components of the system exposed to hydrogen gas are made of 316 alloy stainless steel or 6061-T6 aluminum alloy, or are otherwise rated for hydrogen usage. Component connections are accomplished by swage and SAE-ORB fittings, with a pair of NPT type fittings immediately post-regulator. Swage and SAE-ORB fittings reduce the risk of leaks as compared to an NPT fitting, as both do not require additional teflon sealants. NPT fittings are sealed with a combination of PTFE tape and TF-15 liquid PTFE sealant. The system is checked before each run with a flammable gas detector to determine if there is a leak. A process diagram of the delivery system is available in Figure 3.9.



Figure 3.8: Image of the hydrogen gas cabinet.

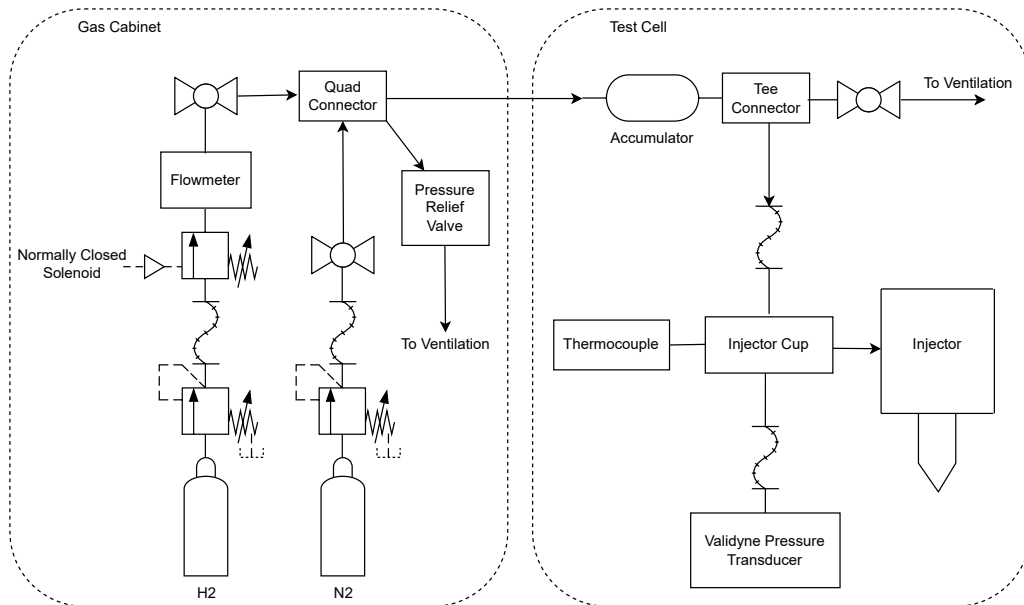


Figure 3.9: Process diagram of the hydrogen delivery system.

The hydrogen source is a Praxair hydrogen K-tank (nominal pressure 2000 psi, 99.50% purity), which is regulated by a Praxair PRS40865000-CGA single-stage high flow hydrogen rated stainless steel pressure regulator. This regulator is set to supply hydrogen at a static pressure of 8.3 bar gauge. The active cylinder is stored in a gas cabinet to safely remove any emissions from the regulator vent.

Four main safeties are present in the hydrogen delivery system. The first safety is the usage of a normally-closed solenoid in the hydrogen line immediately post-regulator. This solenoid is driven by 4 inputs that all must be enabled to allow for hydrogen flow. Two of these are toggle switches for hydrogen flow, one which is present inside the test cell and one which is present inside the control room. This allows for a person in the test cell to disable the flow of hydrogen while they are in the room. The third toggle is provided by the engine controller: only enabling hydrogen flow if there is a demand for hydrogen injection in the controller and if an engine safety-state has not been triggered. The safety states include engine knock, rapid hydrogen pressure loss (if a hydrogen delivery line ruptures) and hydrogen line pressure being less than 1 bar above manifold pressure. The fourth toggle is actuated by a Honeywell E3Point hydrogen detector mounted near the ceiling of the test cell, which closes the solenoid and activate an alarm if hydrogen content in the test cell atmosphere exceeds 5% of the lower flammability limit.

The second safety is an emergency overpressure vent present in the gas cabinet where the hydrogen tank is stored. This vent is designed to open if the post-regulated pressure exceeds 250 psi, consistent with diaphragm failure in the pressure regulator. All components of the delivery system are burst rated to over 250 psi, avoiding further damage to the system in this case.

The third safety is a Swagelok manually operated ball valve present on the hydrogen line, pressure rated to tank pressures, allowing for the lockout of hydrogen flow to the rest of the system. Another ball valve present on a teed line near the engine allows for de-energization of the entire system when shutting down testing or having to

service the injection system. This de-energization vent leads into an explosion-proof ventilation system.

The fourth safety is a nitrogen pressurization-purge system, which runs off a nitrogen cylinder on a system that can be isolated from the hydrogen line with a manually operated ball valve. Usage of the nitrogen purge system during H₂ cylinder changeover allows for the atmosphere inside of the hydrogen delivery system to never enter the hydrogen flammability region. Every time the hydrogen bottle is changed, the delivery system is pressurized and purged twice with nitrogen. The purge line connects into an explosion-proof ventilation system.

An accumulator is used in the system close to the injector. This accumulator has a volume of 3.79 L, and is used to reduce pressure fluctuations due to the rapid switching of the hydrogen injector coupled with the high volumetric flow per injection event. Using an accumulator improves the system pressure stability, pressure regulator lifespan and allows for more consistent flow through the injector, along with more accurate flow measurement from the hydrogen mass flow meter.

The hydrogen port injector is a HANA H2200A, a natural gas port injector with the suggested manufacturer application being industrial engines with a cylinder volume of approximately 2.5 L and up [84]. As hydrogen has less than 30% the volumetric energy density as CNG, the injector flow rates are adequate for running a single 1.12 L cylinder. The list of specifications for the injector are in Table 3.2. This injector is a side-feed injector, meaning that hydrogen gas is introduced into the side of the injector body close to the injection tip. This necessitated the design and manufacture of an injector cup to control gas flow and allow the injector to retain a gas seal in operation. For ease of manufacture, the injector cup was constructed from 6061-T6 aluminum alloy. A schematic of the cup is available in Appendix B. The hydrogen temperature and pressure was measured at the elbow of the injector cup through a measurement port.

A stainless steel flexible line is used at the end-stage of the system between the

injector cup and the engine. This line reduces the stress on the fixed tubing and limits the transmission of vibrations through the delivery system. Without running a flex line, metal fatigue from the movement of the engine could occur at a rapid rate in the piping system, possibly leading to line failure.

Table 3.2: Properties of the HANA H2200 port injector [84]

Property	Value
Maximum Flow Rate	850 SLPM (CNG)
Maximum Rail Pressure	9 bar
Opening Time	1.4 ms
Closing Time	1.4 ms
Driver	Peak and Hold

3.1.5 Diesel Fuel System

All diesel fuel used in this work is Canadian CAN/CGSB-3.517 Type B ultra low sulfur diesel, used for off-road applications. Specifications of this fuel are assumed to meet CAN/CGSB-3.517 [85]. The diesel fuel system is a common rail return-style, where some diesel fuel is cycled through the high and low pressure sides of the circuit and returns to the fuel tank without being injected into the combustion chamber. The temperature of the diesel fuel is uncontrolled in this experiment, but the temperature of the fuel exiting the return line is monitored. A steady-state temperature of approximately 45°C above ambient is usually reached by the fuel during testing. A water separator and fuel filter are present in the circuit. The high-pressure region of the diesel injection system is fed by an electronically-controlled Bosch CP3S3 gear-driven fuel pump (part number 0 445 020 122 LW). The fuel injectors are Bosch CRIN 1-16 solenoid-actuated direct injectors (part number 0 445 120 231), without needle lift measurement. The high pressure fuel pump is fed by a generic low-pressure electric fuel pump to prevent cavitation at high fueling rates.

3.2 Injection Strategy

A diagram of the injection strategy is present in Figure 3.10. The hydrogen injection mass was varied in steps, along with the pilot to main advance (P2M). Each test targeted a certain load (based on the gross indicated mean effective pressure of the cycle) at a certain intake manifold pressure (MAP). To maintain the load target with the varied hydrogen injection mass, the diesel injection mass was modified. A double-injection strategy for the diesel was used, with a constant 0.23 ms pilot injection duration and a varied duration main injection. At very high hydrogen injection masses, the diesel main injection duration was reduced to zero to further decrease diesel usage. The start of injection of the main diesel injection (MSOI) was held at TDC (0 CAD) for all trials.

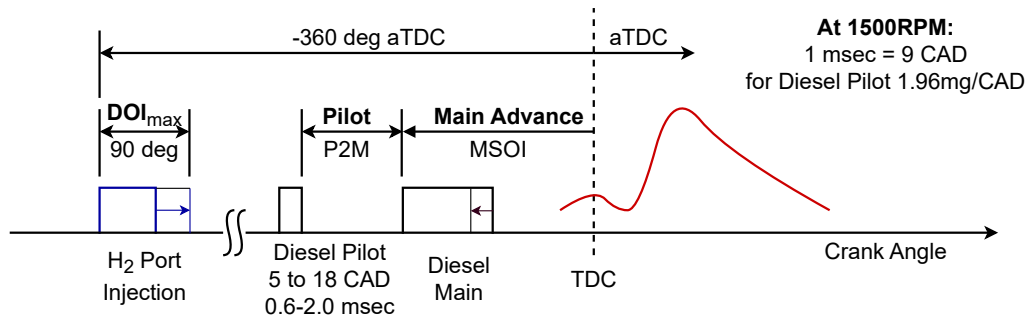


Figure 3.10: Injection Scheme for testing.

Hydrogen is delivered to the cylinder by a single port injection per cycle. The start of injection is held at -360 CAD, or the beginning of the intake stroke. This allows for hydrogen to not be regurgitated out of the cylinder as compared to a late injection time. As the hydrogen injection duration increases, the end of injection (EOI) becomes later in the cycle, but never beyond an equivalent of a 90 CAD duration (10 ms at 1500 rpm).

3.2.1 Engine Feedback Sensors

A diagram of the engine sensors and their readers is present in Figure 3.11. Two systems are used to measure the crankshaft angle. A multiplexed 3600 pulse per revolution (PPR) and 1 PPR optical gate encoder is used for high-resolution measurement of engine crank angle during operation. Low resolution measurement of the crankshaft angle is accomplished by two production Bosch 2872277 magnetic hall-effect sensors originally installed on the engine, which measure crankshaft and camshaft rotation. The tone wheel for the crankshaft is a 60-2 tooth type, and the camshaft tone wheel is a 6 pulse type. The camshaft sensor is used for the initial angle acquisition while the crankshaft sensor is used to determine the low-resolution crankshaft angle while running.

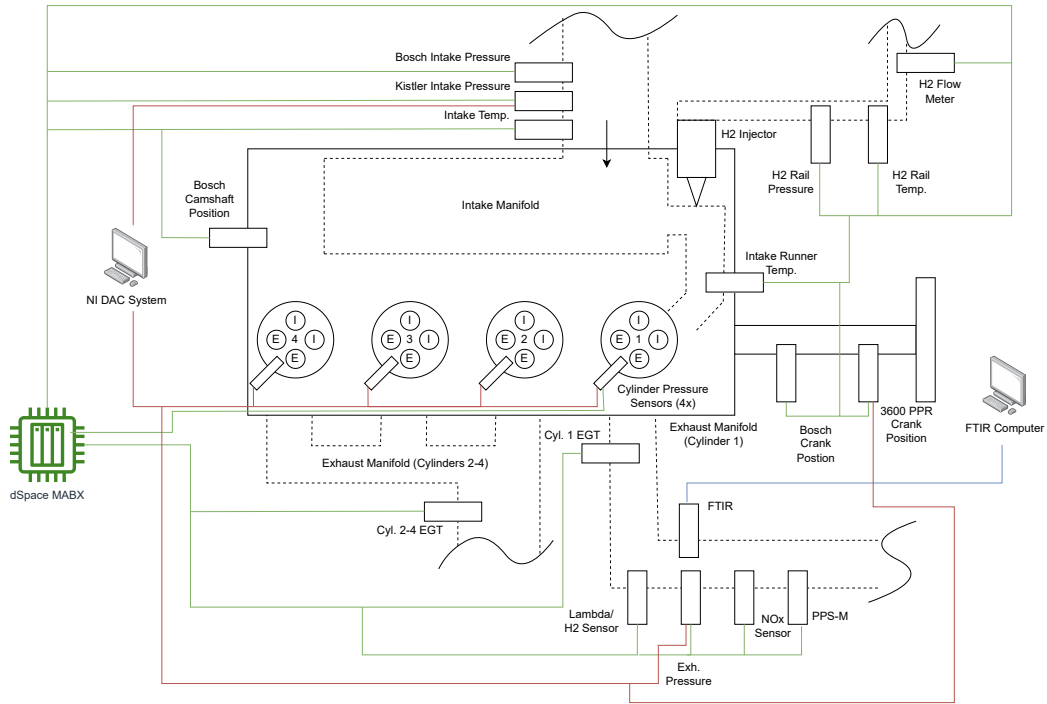


Figure 3.11: Sensors on the engine.

Intake gas flow parameters are measured by 7 sensors. Intake manifold pressure is measured by a Bosch 4921322 production pressure sensor, with the offset calibrated to atmospheric conditions. A high-speed, high-accuracy Kistler 4011A piezo-resistive

sensor was also used to measure intake air pressures simultaneously. The temperatures of the gas streams at the hydrogen rail, intake manifold, and cylinder 1 intake runner after hydrogen injection are all sensed by OMEGA type-K immersion probe thermocouples. Hydrogen mass flow is measured by an Omega FMA-1611A mass flow meter. The specifications of this meter are available in Table 3.3. Hydrogen pressure is measured by a Validyne DP15 transducer with a Validyne CD15 Wheatstone bridge amplifier.

Table 3.3: Omega FMA-1611A hydrogen mass flow meter properties [86].

Property	Value
Maximum Flow	250 SLPM
Maximum Temperature	50°C
Accuracy	±0.8%
Measurement Element	Laminar Flow

The coolant temperature of the engine is monitored by an OMEGA type-K immersion probe thermocouple. The diesel fuel rail return temperature is also measured by an OMEGA type-K thermocouple. The diesel rail pressure itself is measured by a Bosch 5297640 production sensor.

The exhaust temperature of cylinder 1 is measured by an Omega type-K armored thermocouple located in the gas stream. The exhaust temperature of cylinder 2 through 4 post turbine outlet are measured by an Omega type-K armored thermocouple located in the gas stream. The exhaust pressure is measured by a water-cooled Kistler 4049B piezo-resistive sensor.

NO_x concentration in the exhaust stream is measured by an ECM NOxCANt measurement module with a calibrated NO_x sensor that broadcasts its output over controller area network (CANBUS). This NO_x sensor was used for the purposes of rapid feedback during operation.

Oxygen concentration in the exhaust stream is measured by an ECM Lambda-

CANp measurement module with a calibrated NTK 24302 wideband lambda sensor connected to a CANBUS interface. This sensor is able to output the estimated lambda of the exhaust stream, oxygen concentration, and the cell pumping currents.

Hydrogen concentration in the exhaust stream is measured by a Neoxid Group NEO951A exhaust hydrogen concentration sensor, connected to the CANBUS interface. This sensor is used to measure the hydrogen slip in the exhaust stream. The specifications of this sensor is available in Table 3.4.

Table 3.4: Hydrogen exhaust concentration sensor specifications

Parameter	Specification
Sensing Limits	
H ₂ Concentration Range	0 - 5 vol.%
Accuracy	± 0.5 vol.%
H ₂ Detection Limit	< 0.5 vol.%
Response Time t_{90}	< 10 s
Resolution	100 ppm
Sampling Time	100 ms
Cross Sensitivities	O ₂ , CO
Operating Conditions	
Temperature Range	-40°C - 400°C
Pressure Range	95 - 105 kPa
Humidity Range	0 - 95 %
Heater Voltage	24 V

3.2.2 In-Cylinder Pressure sensors

The in-cylinder pressure in cylinder 1 is measured using a using a Kistler 6124A piezo-capacitive pressure transducer that is mounted between the exhaust valves. Cylinders 2 through 4 use a Kistler 6125C piezocapacitive pressure transducer mounted between the exhaust valves to measure pressure. The transducer mounted in cylinder 1 fea-

tures a higher maximum pressure than other sensors. In case of a severe engine knock event, this would allow the sensor to not be damaged. Severe knock in cylinders 2 through 4 was not considered in sensor selection due to the lack of hydrogen addition and the usage of production diesel injection tables for cylinders 2 through 4. The intake manifold pressure is used to reference the in-cylinder pressure at intake valve closure. To convert the output from the cylinder pressure transducers to a voltage, two Kistler charge amplifiers are used. Each charge amplifier channel and pressure transducer are calibrated as a pair to reduce the amount of measurement error and to correct for sensor aging characteristics. The specifications of the sensors and amplifiers are available in Table 3.5;

Table 3.5: Properties of cylinder pressure sensors and amplifiers

Cylinder	Model	Type	Sensitivity (pC/bar)	ω_o (kHz)	Calibration (bar/V)
1	Kistler 6124A	Piezocapactive	-29.98	≥ 65	19.701
2	Kistler 6125C	Piezocapactive	-33	≥ 70	20.596
3	Kistler 6125C	Piezocapactive	-33	≥ 70	20.482
4	Kistler 6125C	Piezocapactive	-33	≥ 70	20.858

3.2.3 Emissions measurement

An emission measurement system is used to determine the exhaust gas composition. Three measurement devices are used, an MKS 2030 FTIR, an NO_x Sensor, and a Pegasor PPS-M. The FTIR provides measurements of unburnt hydrocarbons, water, carbon monoxide, carbon dioxide, NO, NO₂ and N₂O, and an IR spectrum that can be resolved into most other polar chemical species. This unit has slow measurement speeds, making it useful only for steady-state measurements. A Denso NO_x sensor/ECM NO_x sensor CAN interface is used to determine NO_x and oxygen concentration. This sensor has a quick response, allowing for it to be used in transient measurements and feedback control. The final measurement device is a Pegasor PPS-

M , used for measuring the mass of soot in a volume of the exhaust stream. The specifications of the MKS FTIR emission measurement system is provided in Table 3.6, and the specifications of the Pegasor PPS-M are in Table 3.7.

Table 3.6: Accuracy of the FTIR emissions measurement system for selected gases.

Gas	Maximum	Detection level	Resolution	Accuracy
NO _x	10000 ppm	0.1 ppm	0.1 ppm	1% of reading
uHC	5%	0.04 ppm	0.1 ppm	1% of reading
CO (low)	2500 ppm	0.1ppm	0.1ppm	1% of reading
CO (high)	10%	0.1%	0.1%	1% of reading
CO ₂	18%	0.1%	0.1%	1% of reading
H2O	25%	0.1%	0.1%	1% of reading

Table 3.7: Accuracy of the PPS-M emissions measurement system [87].

	Parameter	Specification
Pegasor PPS-M		
	Particle Concentration Range	1 $\mu\text{g}/\text{m}^3$ - 290 mg/m^3
	Minimum Particle Size	10 nm
	Sample Temperature	200°C
	Sample Rate	100 Hz
	SNR	100 dB

3.2.4 Engine torque and speed

The dynamometer controller is set to run in a speed-controlling mode for this work. The engine speed is regulated to a set value supplied from the engine controller and the torque produced by the engine is measured using a Dyne Systems 1014W Eddy Current dynamometer with an integrated load cell.

3.2.5 Cooling water and oil supply

The engine coolant is run through a flat plate heat exchanger which is connected to the city water. This allows for controlled heat rejection from the engine cooling jacket during operation. The engine coolant temperature is controlled by a wax thermostat unchanged from the stock configuration, resulting in an engine coolant temperature ranging between 83 °C and 87 °C when the engine is at operating temperature.

Oil heat rejection is accomplished by an internal oil cooler within the engine block. This flat plate heat exchanger allows the transfer of heat between the engine coolant and the engine oil, resulting in the engine oil temperature being closely coupled to coolant temperature. The oil pressure is controlled by a crankshaft-driven oil pump with no variable displacement features. The oil used in this experiment is Shell Rotella T4 SAE 15W-40, an engine oil weight recommended by the manufacturer.

3.3 Engine Control

The engine control stack consists of a dSPACE hardware stack and a Raspberry PI 3 external processor. A dSPACE 1401 Micro Autobox II (MABX) was used to control the engine when tested. This controller is paired with a dSPACE 1513 Rapidpro, a power-electronics control unit that is used to send and receive high-power signals from the engine sensors and actuators. Combined, these two devices fulfil the roll of a production engine control unit (ECU), managing fuel pressure and fuel injection. A dSPACE 1514 field programmable gate array (FPGA) is present as a daughter board to the 1401, which is used to provide control updates every tenth of a crank angle degree. In this thesis, it is configured to calculate the maximum cylinder pressure rise rate per cycle, the maximum cylinder pressure per cycle and cylinder 1 IMEP. These parameters are used for feedback control and as an emergency stop in case of a cylinder pressure parameter overrun. Overrun of these parameters results in the MABX commanding a known safe value for diesel fuel injection while temporarily

suspending hydrogen injection. The specifications of the control stack is given in Table 3.8.

The control software for the engine is designed in MATLAB Simulink with some functions provided by in-built dSPACE libraries. The controller flow of the MABX software differs from the production software flow by having two diesel injection algorithms that are run in parallel, one for cylinder 1 and one for cylinders 2 through 4. This allows cylinder 1's diesel injection parameters to be modified while running hydrogen without affecting the operation of the other cylinders, which run at a steady-state operating point. Up to 3 separate diesel injection events per cycle are implemented in the software. A separate hydrogen injection function is also run in parallel. A moving average of the engine speed and the hydrogen mass flow rate is used to calculate how much hydrogen is injected per cycle. The MSOI angle, pilot advance, injection durations and diesel fuel pressure can all be separately adjusted by the user.

3.3.1 Reverse Engineering of Injector Energization Profile

Solenoid injectors use high initial current flows in order to quickly raise the injector needle and allow for multiple injection events per engine cycle. However, continual usage of this high current draw mode would result in the overheating of the injector solenoid and damage to the device. As such, engine controllers use multiple current flows and voltages, depending on the progression of the needle lift. The current and voltage limits of the injector were found via analysis of the injector electrical lines while running the production controller at high diesel injection durations. The voltage of the injectors was determined using an oscilloscope and the amperage was measured using a high-speed current clamp. Three energization profiles of the injector were identified, corresponding to the initial injector needle lift, end-stage needle lift, and needle steady state. The properties of these states is available in Table 3.9.

Table 3.8: Rapid prototyping ECU Specifications

	Parameter	Specification	
Processor	dSPACE [®] 1401	IBM PPC-750GL	
	Speed	900 MHz	
	Memory	16 MB main memory	
I/O Board	dSPACE [®] 1513		
	Analog input	24 Parallel channels	
	Resolution	16 bit	
	Sampling frequency	1 Msps	
	Analog input	32 Multiplexed channels	
	Resolution	16 bit	
	Sampling frequency	200 Ksps	
	Analog output	12 Channels	
	Digital input	40 Channels	
	Digital output	40 Channels	
	FPGA	dSPACE [®] 1514	Xilinx [®] Kintex-7
		Flip-flops	407600
Lookup table		203800	
Memory lookup table		64000	
Block RAM		445	
Digital signal processing		840	
I/O		478	

Table 3.9: Diesel Injector Energization Profile

Needle Position	Start Time (us)	Max Voltage (V)	Mean Current (A)
Closed	0	58	20.8
Opening	80	14.4	18.1
Full Open	435	14.4	12.8

3.3.2 Reverse Engineering of Cummins Controller

To determine the baseline operating points for the engine, allow for easier startups, and to determine the control scheme of the diesel injection, the production engine controller's injection and fuel pressure software has been reverse engineered. Cummins CALTERM software was used to extract fueling tables/parameters directly from the ECU software, and to collect low-speed data about the controller's internal states while operating for verification. Reverse engineering of the engine software was accomplished by partial disassembly of the software binary in IDA. This revealed functions in software to designed to counteract pressure waves in the injection rail with multiple injection events per cycle, which were used to calibrate the injector functions.

Verification of the implemented version of the reverse engineered software on the dSPACE controller was accomplished by the comparison of the controller values at 6 operating points. The high-speed injector current profile measured by a current clamp was also compared between implementations to check if the dSPACE injector driver was comparable to the production driver.

3.4 Data collection

Data collection for offline analysis is accomplished by 3 computers running at various collection rates. High speed data (updated every tenth of a degree) is collected by an NI PCIe-6351 data acquisition system which is housed in a dedicated logging computer. The specifications of the NI system are available in Table 3.10. The computer runs a MATLAB script to enable the data acquisition card and record a specified number of cycles. To synchronize the data between the MABX and the NI system, the NI card sends a pulse (CAS) to the MABX when recording is triggered. The start and end of measurement by the high-speed system is triggered by the 1 PPR output from the high-resolution encoder. Triggering of the individual measurements is accomplished by the 3600 PPR high-speed encoder mounted to the engine crankshaft.

Table 3.10: NI data acquisition system specifications [88]

Parameter	Specification
Channels	8 Differential/16 Single
Resolution	16 bit
Sample Rate	1.25 MS/s
Input Voltage	± 10 V
Absolute Accuracy	$\pm 1520 \mu\text{V}$

Low speed data from the engine controller and sensors is recorded by a computer running the dSPACE ControlDesk software. The low speed data is used to determine the mean value and standard deviation of the measured channels in offline analysis. ControlDesk allows for the collection of data directly from the MABX over Ethernet at a sampling rate of 100 Hz, and storage in a MATLAB database file. FPGA data is also extracted via ControlDesk, but at the same limited sample rate. Note that because they are used for feedback control, emissions data from the NO_x sensor and the Pegasor soot measurement system are collected by the MABX and recorded in ControlDesk.

Emissions data from the FTIR is collected by the third computer. FTIR data is collected using a proprietary program called MG2000, which provides emissions sampling data at a sample rate of 10 Hz. The program works by using “recipes,” which are files that contain spectral output for certain species under infrared light. These recipes are used by the FTIR to convert the spectra to species concentration. The selected comparison IR spectra/recipe used in the software was Diesel-C1 Extended. The gas concentrations of the species present in this recipe are recorded locally, along with the spectral measurements. MG2000 outputs concentration data in a proprietary format, which is processed by a python script to convert it into a comma-separated-value file for further analysis. During steady-state operation, the CSV file is manually trimmed if necessary due to the FTIR’s slow settling time (30-60 seconds). The

acquisition of the FTIR data is manually triggered, and is not aligned to the other datasets via CAS.

3.5 Testing Procedure

For steady-state load tests, the engine was first started following the procedure in Appendix A then allowed to warm up to a coolant temperature of 85°C under mild load at a crank speed of 1500 rpm. Once this temperature had been achieved, a baseline measurement was taken for every day to track the consistency of the measurement. This baseline consisted of setting the diesel injection rate of the engine to the parameters outlined in Table 3.11, and collecting data from the MABX, emissions systems and high-speed cylinder pressure acquisition. The data outputs were then analyzed for integrity and consistency with previous results. The intake pressure would then be adjusted to the pressure at the testpoint, and the injection strategy would be followed in order to meet the engine load at the testpoint. Once this load was reached, the FTIR would be engaged, and after stability in the measurement was confirmed 600 cycles of engine operation were recorded.

For transient step tests two operating points would be programmed, and the engine would be allowed to settle to steady-state operation at the first point. Settling was determined by stability in the FTIR output. Measurement was then started, and the engine would be stepped and allowed to settle at the second operating point before suspending measurement.

Table 3.11: Injection parameters used for baseline testing of engine.

Parameter	Specification
Intake Pressure	1.0 bar (building air)
Diesel Pilot Duration	0.25 ms
Diesel Main Duration	0.45 ms
Diesel Post Duration	0 ms
Diesel Rail Pressure	900 bar
Diesel Main Injection Timing	-3 CAD
Diesel P2M	800 μ s
Diesel M2P	800 μ s

Chapter 4

Combustion Analysis

4.1 Governing Equations of Combustion

In order to adequately model the combustion process of the dual-fuel engine, the relevant governing equations of the physical system must be determined. Assumptions made at this step will affect the accuracy of the analysis.

4.1.1 In-Cylinder Energy Conservation

In this analysis, the volume of the cylinder is treated as the control volume, with mass only able to enter or leave the volume via flow through the valves or through direct injection of fuel. The cylinder is assumed to be quasi-static system at each step, with a globally uniform temperature and pressure. The phase of the mixture is assumed to be purely gaseous (all injected fuel immediately vaporizes). The in-cylinder energy conservation, neglecting kinetic energy of the fuel and gases is [89]:

$$\frac{dQ_b}{d\theta} = \frac{dU}{d\theta} + P\frac{dV}{d\theta} + \frac{dQ_w}{d\theta} + \sum_i h_i \frac{dm_i}{d\theta} \quad (4.1)$$

where $dQ_b/d\theta$ is the rate of heat release from the combustion of the mixture, $dU/d\theta$ the rate of change in internal energy, $PdV/d\theta$ is work of the system, $dQ_w/d\theta$ the wall heat transfer, and $h_i dm_i/d\theta$ the rate of change of energy due to mass flow in or out of the cylinder. The internal energy of the gases in the cylinder is defined by the molar content of the cylinder, and the bulk pressure and temperature of the cylinder. In order to simplify Equation 4.1, the sensible enthalpy, h_s , of the fuel is assumed to

be approximately zero. This is because of the relatively low magnitude of the mass of the diesel injection that occurs relative to the mass of the gas present within the cylinder. The internal energy of the trapped gas, U , is the product of the specific internal energy u or and the mass m of the charge. Via partial differentiation, U becomes:

$$\frac{dU}{d\theta} = m \frac{du}{d\theta} + u \frac{dm}{d\theta} \quad (4.2)$$

The specific internal energy has a dependence upon the temperature (T), pressure (P), and content of the cylinder charge (air-fuel ratio, λ). Via the chain rule, partial differentiation of u yields:

$$\frac{du}{d\theta} = \left[\frac{\partial u}{\partial P} \frac{\partial P}{\partial \theta} \right]_{T,\lambda} + \left[\frac{\partial u}{\partial T} \frac{\partial T}{\partial \theta} \right]_{P,\lambda} + \left[\frac{\partial u}{\partial \lambda} \frac{\partial \lambda}{\partial \theta} \right]_{T,P} \quad (4.3)$$

where, m is the mass of the gas in the control volume, T is the bulk temperature of gas in the volume and c_v is the constant volume specific heat of the gas mixture (which must be calculated based on the species and conditions). The equation is simplified by assuming the ideal gas law holds, neglecting the impact of the change in pressure on internal energy ($\partial u / \partial P \approx 0$) and the impact of λ on internal energy ($\partial u / \partial \lambda \approx 0$) [90]. This results in the change in specific internal energy being defined as:

$$\frac{du}{d\theta} = c_v \frac{dT}{d\theta} \quad (4.4)$$

The above simplification allows for Equation 4.1 to be simplified as follows:

$$\frac{dQ_b}{d\theta} = mc_v \frac{dT}{d\theta} + \frac{dW}{d\theta} + \frac{dQ_w}{d\theta} \quad (4.5)$$

The average cylinder gas temperature, $T(\theta)$, can be obtained via rearrangement of Equation 4.5:

$$\frac{dT}{d\theta} = \frac{-\frac{dQ_b}{d\theta} + \frac{dW}{d\theta} + \frac{dQ_w}{d\theta}}{mc_v} \quad (4.6)$$

The crank angle based heat release rate can be found by combining Equation 4.5, the crank angle resolved cylinder pressure trace ($P(\theta)$), the ideal gas law, neglecting enthalpy flow, and assuming semi-perfect gas behaviour ($R = c_p - c_v$ and $\kappa = \frac{c_p}{c_v}$ as per Heywood, resulting in [89]:

$$\frac{dQ_b}{d\theta} = -\frac{1}{\kappa - 1}V(\theta)\frac{dP(\theta)}{d\theta} - \frac{\kappa}{\kappa - 1}P(\theta)\frac{dV(\theta)}{d\theta} + \frac{dQ_w}{d\theta} \quad (4.7)$$

Where, $V(\theta)$ is the crank-resolved instantaneous cylinder volume, $P(\theta)$ is the measured instantaneous cylinder pressure and Q_w is the heat loss of the cylinder gases to the cylinder wall. During heat release, the engine valves are closed, so the mass transferred over the valves is zero. Further simplifications include neglecting mass flows due to blow-by, assuming ideal gas state and constant gas composition, and a non-changing mixture gas constant ($dR/d\theta = 0$). The effects of mass flow due to direct injection of diesel fuel were disregarded as the magnitude of the sensible enthalpy flow of the diesel fuel is small as compared to the internal energy of the cylinder gases [89].

Heat losses to the walls of the combustion chamber happen through both convection and radiation. The emissivity of a mixture is correlated with the concentration of CO₂ and water vapour in the mixture [91], while the absorbtivity is correlated to the materials of the cylinder wall. Cylinder wall heat loss is:

$$\frac{dQ_w}{d\theta} = h_w \frac{dt}{d\theta} A_w (T_g - T_w) + \sigma \frac{dt}{d\theta} A_w (\varepsilon_g T_g^4 - \alpha_w T_w^4) \quad (4.8)$$

where h_w is the wall heat transfer coefficient of the engine cylinder, A_w is the area of the engine cylinder exposed to the gas mixture, T_g is the temperature of the gas, T_w is the average cylinder wall temperature, σ is the Boltzmann constant, ε_g is the emissivity of the gas mixture, and α_w is the absorptivity of the cylinder wall.

To simplify Equation 4.8, the radiation heat transfer is incorporated into the convective heat transfer coefficient α :

$$\frac{dQ_w}{d\theta} = \alpha(\theta)A_w(\theta)(T_w - T(\theta)) \quad (4.9)$$

Where, $A(\theta)$ is the instantaneous exposed wall area of the combustion chamber, T_w is the average wall temperature, and $T(\theta)$ is the instantaneous spatially averaged gas temperature. The wall temperature is assumed to be constant for a specific engine load and speed, and was selected per load point in order for the total heat release to be equal to the calculated combustion fraction energy.

The exposed wall area of the cylinder, $A(\theta)$, can be found from the geometry of the cylinder. The initial step for solving for cylinder wall area is to find the piston wristpin position as a function of crank angle as this is fixed in relation to the piston deck:

$$y_{wp}(\theta) = \sqrt{l_r^2 - (x_{wp} - \sin(\theta)\frac{l_{st}}{2})^2} + \cos\theta\frac{l_{st}}{2} \quad (4.10)$$

Where, y_{wp} is the height of the piston wristpin in the cylinder, x_{wp} is the lateral position of the piston wristpin in the cylinder (constrained to a single value by piston wristpin offset) and l_{st} is the stroke of the cylinder. To find the volume of the cylinder as a function of crank angle, the minimum cylinder volume (volume at top dead center) must be known. This can be found with knowledge of the engine's compression ratio:

$$V_{cyl,min} = \frac{V_s}{CR - 1} \quad (4.11)$$

Where, V_s is the swept volume of the cylinder (commonly referred to as the displacement of the cylinder) and CR is the compression ratio of the engine. Now, the volume of the cylinder can be found using the knowledge of the wristpin position, and knowing that at the wristpin's peak position the cylinder volume is at its minimum:

$$V_{cyl}(\theta) = V_{cyl,min} + \pi\frac{D_{cyl}^2}{2}(y_{wp,max} - y_{wp}(\theta)) \quad (4.12)$$

Where, $V_{\text{cyl,min}}$ is the minimum cylinder volume, D_{cyl} is the cylinder bore and $y_{\text{wp,max}}$ is the maximum height of the wristpin in the cylinder.

The exposed wall area of the cylinder can also be found from the wristpin position. Note that in order to find the exposed area, knowledge of the cylinder's combustion chamber geometry must be known. This includes the piston bowl and head exposed area, as they are fixed constants throughout the cycle and cannot be determined through other means. The diesel cylinder head was approximated as a flat plane due to the flat geometry of the head, and the piston bowl was modeled based upon measurements taken. The crevice area of the piston near the rings was neglected. The instantaneous exposed cylinder area is:

$$A_{\text{cyl}}(\theta) = \pi \frac{D_{\text{cyl}}^2}{2} + \pi D_{\text{cyl}}(l_{\text{hg}} - l_{\text{prot}} + y_{\text{wp,max}} - y_{\text{wp}}(\theta)) + A_p \quad (4.13)$$

Where, l_{hg} is the headgasket thickness, l_{prot} is the piston protrusion from the cylinder head deck at top dead center and A_p is the exposed area of the piston.

A widely accepted method of calculation the heat transfer coefficient is the Woschni relationship [92]. This correlation is known to underestimate wall heat loss at low loads. To alleviate this, a revised approach using the cylinder volume as the characteristic length is used [93]:

$$\alpha(\theta) = 130V_{\text{cyl}}^{-0.06}P_{\text{cyl}}^{0.8}T_{\text{cyl}}^{-0.4}(v_p + 1.4)^{0.8} \quad (4.14)$$

This correlation is commonly used for diesel engines. However, in previous work this correlation has been used for dual-fuel CNG-diesel engines [94, 95], thus its adoption here due to the the similar combustion processes. The piston speed v_p is calculated as a function of crank angle:

$$v_{\text{cyl}}(\theta) = \frac{\frac{l_{\text{st}}}{2} \cos(\theta)(x_{\text{wp}} - \frac{l_{\text{st}}}{2} \sin \theta)\omega_{\text{crk}}}{\sqrt{l_r^2 - (x_{\text{wp}} - \frac{l_{\text{st}}}{2} \sin \theta)^2 - \frac{l_{\text{st}}}{2}}} \quad (4.15)$$

Where, ω_{crk} is the rotational speed of the engine’s crankshaft. The overall heat release can then be found via integration of Equation 4.7 over the period of heat release in the cylinder:

$$Q_b(\theta) = \int_{\theta_{\text{SOC}}}^{\theta_{\text{EOC}}} dQ_b(\theta) \quad (4.16)$$

The bounds on the start and end of integration are tied to the start and end of combustion (SOC and EOC, respectively). Due to combustion only being able to start after the pilot injection of diesel, the start of combustion is taken to be the angle of the SOI of the pilot. The end of combustion is found iteratively. In the cases where the heat release rate is found to approach zero before the exhaust valves open, the end of combustion is taken as the angle where the heat release derivative becomes equal to zero relative to its noise. In the cases where the heat release rate is not found to reach zero before the exhaust valves open, the end of combustion is taken as the angle of exhaust valve opening.

4.1.2 Cylinder Gas Properties

In order to evaluate the value of κ , gas density, and cylinder gas temperature, CANTERA was used. CANTERA is an open-source software suite for solving chemical kinetics, thermodynamics, and transport problems [96]. The selected gas model within CANTERA was dodecane-reitz, which uses a combination of the NASA gas polynomials and ideal gas laws in order to determine the gas properties of the mixture. The value of κ for each measurement point was estimated as the mean value of the κ of the air-hydrogen gas mixture immediately before combustion and the κ of the exhaust gas mixture at the exhaust temperature.

4.2 Mass Flows

To determine the amount of energy moving in and out of the cylinder, the internal gas temperatures and phenomena related to the in-cylinder pressure, it is crucial to

have accurate metering of fuel and air mass inputs. The following section describes how these values were achieved.

4.2.1 Diesel Injector Injection Model Calibration

Because the engine is run on a passive dynamometer, it must supply sufficient torque to overcome the friction of its components and the load of accessories such as the fuel and oil pumps. To do with sufficiently low vibration, all 4 cylinders must be firing. Additionally, the fuel tank return flow of a single injector cannot be measured with the cylinder head geometry and measurement of diesel flow at pressures up to 16 MPa would present extreme difficulties in selecting a fuel flow meter. Therefore, a model of the injector was developed to create a single diesel injection per cycle calibration. Weighing of the fuel tank during operation requires a high amount of cycles (≈ 3000) to obtain a measurement with an injected mass error of $\leq 2\%$. For the initial calibration of the diesel injection without running any hydrogen this was used.

To verify the accuracy of the stock injection curve with a single injection case, the rail fuel pressure was held constant and the injection parameters were set:

Table 4.1: DOI-injected diesel mass test parameters

Engine Speed (rpm)	Fuel Pressure (bar)	Number of In- jections	SOI (de- gATDC)	DOI (msec)
1500	993.4	1	220	0 - 1.06

Injection was set to begin and end during the exhaust stroke in order to minimize the effects of variable cylinder pressure over the combustion duration. Both cylinders 1 and 3 were set to the same injection parameters in order to reduce the number of cycles required for low-error measurements. The diesel fuel tank mass was measured with a scale with a 5-gram resolution over at least 7500 cycles per test point in order to

develop a relationship between the injection duration and injected mass. To compare the results due to differing fuel temperatures and densities, a fitted injection model is used [89, 97]:

$$m_{\text{fuel}} = \text{DOI} \alpha_{\text{inj}} A_{\text{inj}} \sqrt{2\rho_{\text{fuel}}(P_{\text{rail}} - P_{\text{cyl}})} \quad (4.17)$$

Where, DOI is the duration of the injection event, A_{inj} is the maximum orifice area and ρ_{fuel} is the fuel density. The flow coefficient α_{inj} is taken as a function of DOI to model the non-linear behavior during the opening and closing of the injector. The pressure differential between the fuel rail (P_{rail}) and cylinder ($-P_{\text{cyl}}$), was calculated as an average over to total injection period. Fuel density was modeled based on the measured fuel temperature and rail pressure with the following modified Tait equation [98]:

$$\rho_{\text{fuel}} = \frac{\rho_o(T)}{1 - C \log \frac{P_{\text{fuel}} + B(T)}{0.1 + B(T)}} \quad (4.18)$$

Where, $\rho_o(T)$ is a fitted polynomial of the diesel density at ambient pressure over various temperatures, $B(T)$ is a fitted polynomial relating the diesel temperature and pressure, and C is a correcting factor. The Cummins pilot injection, Cummins main injection and measured DOI curves at equal fuel rail pressures is present in Figure 4.1.

Of note is the overestimation of injector area at DOI of approximately 0.55 ms, and the underestimation of injector area in the 0.15 ms to 0.20 ms region. However, it can be seen that the Cummins curve is in agreement with the measured data elsewhere. It was also determined from this curve that the stock controller curves were based on a constant cylinder pressure of 1 bar. Because of this, a pressure correction factor for the diesel injection was developed based on Equation 4.17:

$$m_{\text{corr}} = m_{\text{fuel}} \frac{\sqrt{2\rho_{\text{fuel}}(P_{\text{rail}} - P_{\text{cyl}})}}{\sqrt{2\rho_{o,\text{fuel}}P_{\text{fuel}}}} \quad (4.19)$$

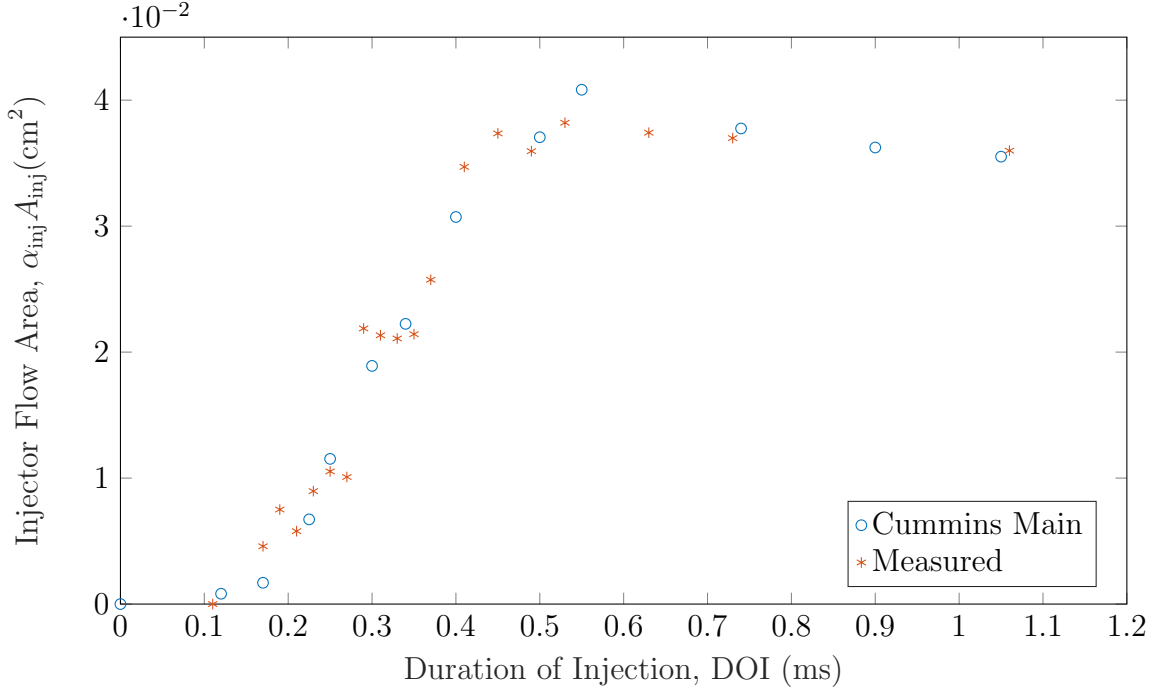


Figure 4.1: Injector nozzle area with a single diesel injection over varied durations of injection for the measured injection mass and Cummins models.

Where, m_{corr} is the corrected fuel mass and $\rho_{o,\text{fuel}}$ is the nominal fuel density assuming a temperature of 293.15 K.

The injection model was used to determine the flow of diesel into the cylinder in cases where a single diesel injection per cycle occurred and to estimate the pilot injection mass when multiple injection events occurred.

4.2.2 Hydrogen Flow Model

The mass flow meter used for measuring the hydrogen flow presents its results as a continuous flow. Thus, it is required to convert the flow into an amount of mass delivered per cycle. The mass flow of hydrogen into cylinder 1 at steady state was converted into a fueling per stroke with:

$$m_{\text{H2,cycle}} = \frac{2\dot{m}_{\text{H2}}}{\omega_{\text{crk}}} \quad (4.20)$$

Where, $m_{\text{H2,cycle}}$ is the delivered hydrogen mass per cylinder cycle, \dot{m}_{H2} is the mass flow rate reported by the flow meter and ω_{crk} is the crankshaft speed. The gas flowing

through the mass flow meter was assumed to be pure hydrogen, as the overall purity is guaranteed to be $> 99.95\%$ [99].

The hydrogen injector was modeled by fitting steady-state hydrogen fueling per stroke values at various injection durations to equation 4.17. A fit to this data is present in Figure 4.2. Note that this model was only used during transient operation, and during steady state operation only Equation 4.20 was used for analysis with data supplied from the low-error hydrogen flow meter.

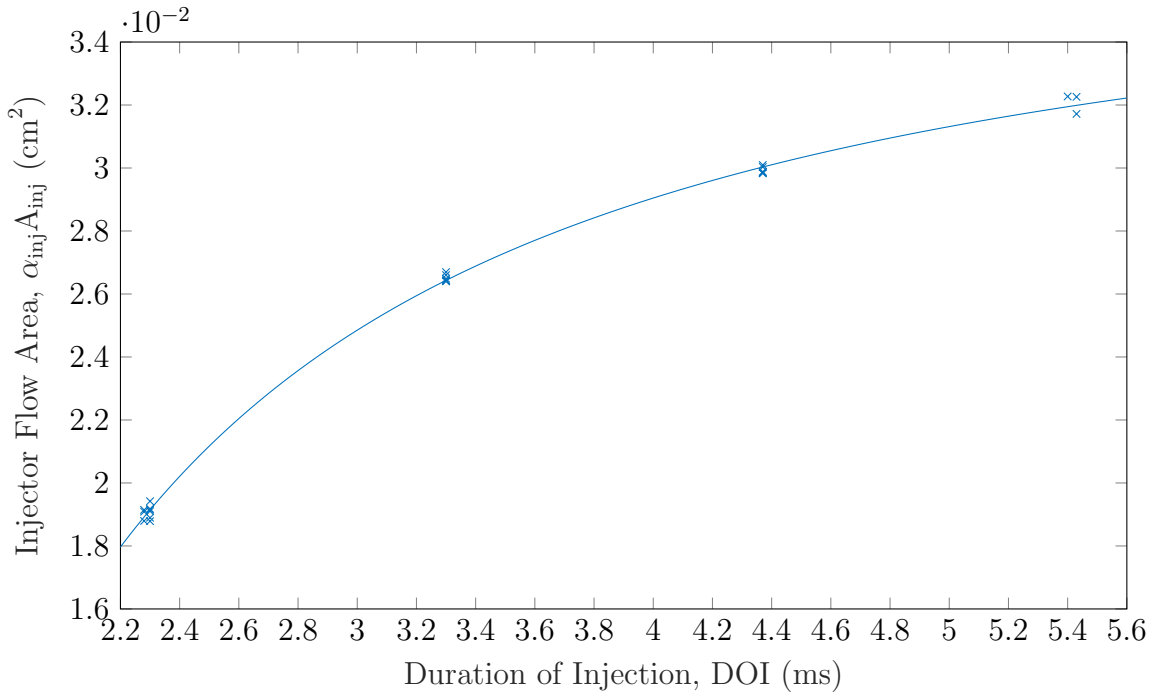


Figure 4.2: Hydrogen injector nozzle area over varied durations of injection for data-relevant injection durations.

4.2.3 Engine Airflow Overview

As only cylinder 1 of the engine is studied, the intake airflow of cylinder 1 must be determined. Due to manifold design, the air flow is not equally split between cylinders, and a calibration approach was used to model the flow through cylinder 1, coupled with verification by directly measuring engine volumetric efficiency under no-injection conditions. As there multiple gas streams injected into the manifold, the

volumetric efficiency definition was split to describe the air and hydrogen volumetric efficiencies separately as a fraction of the combined volumetric efficiency:

$$\eta_c = \eta_a + \eta_{H_2} \quad (4.21)$$

Where, η_c is the combined volumetric efficiency, η_a is the air volumetric efficiency, and η_{H_2} is the hydrogen volumetric efficiency.

The air volumetric efficiency is based upon the measured density of the air in the intake manifold, which is calculated using the manifold temperature and pressure along with ideal gas law. The air intake to the engine was assumed to be humidity-free due to the dried compressed air used. The air volumetric efficiency is defined from manifold conditions as follows:

$$\eta_a = \frac{V_{air}}{V_s} = \frac{m_{air}}{\rho_{air,int} V_s} = \frac{m_{air} R_{air} T_{air,int}}{P_{int} V_s} \quad (4.22)$$

Because hydrogen is injected into the manifold as a gas, it has an impact on volumetric efficiency by displacing air. Hydrogen's volumetric efficiency (η_{H_2}) was calculated using Equation 4.22 using the average intake pressure for the gas pressure but using the hydrogen fuel rail gas temperature instead of the intake air temperature. As hydrogen has an inverted Joule-Thomson coefficient as compared to most gases near standard conditions, the gas experiences a temperature rise as it passes through the injector (a throttle) on the manifold [100]. However, due to the low pressure differential of approximately 8 bar between the injector rail and the intake, this warming effect is limited, and the hydrogen temperature in the intake was assumed to be equal to that of the injection rail temperature.

The model for air flow was based upon the combined volumetric efficiency definition. The combined volumetric efficiency was calibrated based upon intake MAP and the volume of hydrogen injected per stroke into the manifold. Figure 4.3 shows the results of this calibration. Hydrogen injection was found to negatively impact

the combined volumetric efficiency in a manner that was stable regardless of injection duration. The change in η_c as hydrogen introduced is likely due to the rapid expansion of the hydrogen in the manifold after injection as its pressure drops, which transiently slows the gas velocity through the intake runner.

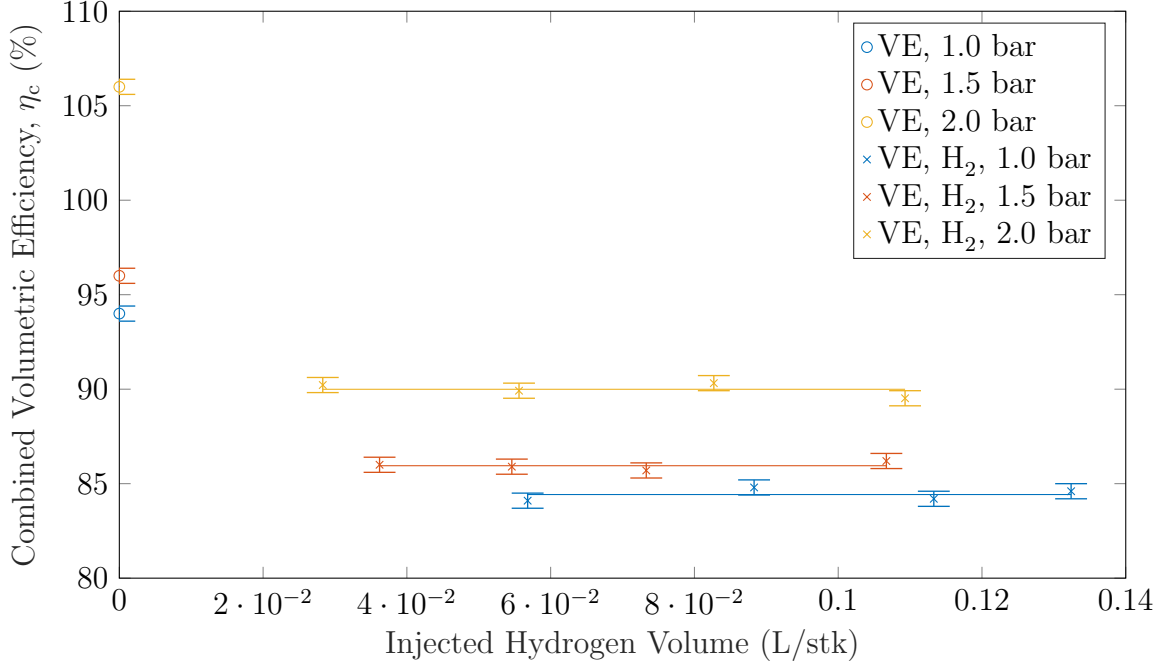


Figure 4.3: Combined volumetric efficiency over various pressures and hydrogen addition amounts.

To find the air intake of the cylinder 1 from the interpolated combined volumetric efficiency and hydrogen injection volume, Equations 4.21 and 4.22 can be arranged to find the inducted air mass from the combined volumetric efficiency:

$$m_{\text{air}} = \frac{\eta_c V_s - V_{\text{H}_2}}{\rho_{\text{air, int}}} \quad (4.23)$$

This formula was used to find the injected diesel mass when using the exhaust gas model and to determine the mass of the emissions produced from the engine from the concentrations found by the sensors.

4.2.4 Exhaust Gas Diesel Injection Model

When the single diesel injection model was extrapolated to twin injections per cycle, a large deviation in the estimated and actual injection masses was noted, likely due to the transient pressure waves generated in the fuel rail during injection. A higher fuel pressure not only creates a higher differential pressure driving injector flow, but also effects the opening and closing durations of the injector by working against the preload of the injector seating spring. As injector needle lift was not measured, an exhaust-gas composition based model was used for multiple diesel injection cycles.

Exhaust gas concentrations were provided by the FTIR. This method was based upon a chemical species balance accounting for CO, NO, and H₂O combustion products. Diesel is modeled as a single carbon molecule with an amount of hydrogen based on the molar hydrogen to carbon ratio (HCR) of the diesel fuel. Due to the high combustion fraction in most trials, diesel is assumed to completely combust in this model. In order to determine the amount of unburnt hydrogen in the exhaust, the model also splits the hydrogen and diesel production of water during combustion. This model is described below:

$$n_{\text{NO,exh}} = n_{\text{tot,exh}} c_{\text{NO,exh}} \quad (4.24)$$

$$n_{\text{NO}_2,\text{exh}} = n_{\text{tot,exh}} c_{\text{NO}_2,\text{exh}} \quad (4.25)$$

$$n_{\text{CO,exh}} = n_{\text{tot,exh}} c_{\text{CO,exh}} \quad (4.26)$$

$$n_{\text{H}_2\text{O,exh}} = n_{\text{tot,exh}} c_{\text{H}_2\text{O,exh}} \quad (4.27)$$

$$n_{\text{O}_2,\text{exh}} = n_{\text{tot,exh}} c_{\text{O}_2,\text{exh}} \quad (4.28)$$

$$n_{\text{diesel}} = n_{\text{CO}_2,\text{exh}} + n_{\text{CO,exh}} \quad (4.29)$$

$$n_{\text{H}_2\text{O,exh}} = n_{\text{H}_2\text{O,exh,diesel}} + n_{\text{H}_2\text{O,exh,H}_2} \quad (4.30)$$

$$\begin{aligned} n_{\text{O}_2,\text{int}} = n_{\text{O}_2,\text{exh}} + n_{\text{CO}_2,\text{exh}} + \frac{n_{\text{CO,exh}}}{2} + \frac{n_{\text{H}_2\text{O,exh}}}{2} \\ + \frac{n_{\text{NO,exh}}}{2} + n_{\text{NO}_2,\text{exh}} \end{aligned} \quad (4.31)$$

$$n_{\text{H}_2,\text{int}} = n_{\text{H}_2,\text{exh}} + n_{\text{H}_2\text{O,exh,H}_2} \quad (4.32)$$

$$n_{\text{H}_2\text{O,exh,diesel}} = \frac{\text{HCR}}{2} n_{\text{diesel,b}} \quad (4.33)$$

$$n_{\text{N}_2,\text{int}} = n_{\text{N}_2,\text{exh}} + \frac{n_{\text{NO,exh}}}{2} + \frac{n_{\text{NO}_2,\text{exh}}}{2} \quad (4.34)$$

$$\begin{aligned} n_{\text{tot,exh}} = n_{\text{CO}_2,\text{exh}} + n_{\text{CO,exh}} + n_{\text{H}_2\text{O,exh}} + n_{\text{O}_2,\text{exh}} + n_{\text{H}_2,\text{exh}} \\ + n_{\text{N}_2,\text{exh}} + n_{\text{NO,exh}} + n_{\text{NO}_2,\text{exh}} \end{aligned} \quad (4.35)$$

$$n_{\text{N}_2,\text{int}} = 3.76 n_{\text{O}_2,\text{int}} \quad (4.36)$$

Where, n is the amount of moles of a species and c is the concentration of a species. Subscript exh refers to the exhaust stream, int the intake stream, b to the combusted fuel, ub to the uncombusted fuel. For pure diesel combustion, the model was slightly modified to not include hydrogen-related variables or exhaust water measurement:

$$n_{\text{NO,exh}} = n_{\text{tot,exh}} c_{\text{NO,exh}} \quad (4.37)$$

$$n_{\text{NO}_2,\text{exh}} = n_{\text{tot,exh}} c_{\text{NO}_2,\text{exh}} \quad (4.38)$$

$$n_{\text{CO,exh}} = n_{\text{tot,exh}} c_{\text{CO,exh}} \quad (4.39)$$

$$n_{\text{O}_2,\text{exh}} = n_{\text{tot,exh}} c_{\text{O}_2,\text{exh}} \quad (4.40)$$

$$n_{\text{diesel}} = n_{\text{CO}_2,\text{exh}} + n_{\text{CO,exh}} \quad (4.41)$$

$$n_{\text{O}_2,\text{int}} = n_{\text{O}_2,\text{exh}} + n_{\text{CO}_2,\text{exh}} + \frac{n_{\text{CO,exh}}}{2} + \frac{n_{\text{H}_2\text{O,exh}}}{2} + \frac{n_{\text{NO,exh}}}{2} + n_{\text{NO}_2,\text{exh}} \quad (4.42)$$

$$n_{\text{H}_2\text{O,exh}} = \frac{\text{HCR}}{2} n_{\text{diesel,b}} \quad (4.43)$$

$$n_{\text{N}_2,\text{int}} = n_{\text{N}_2,\text{exh}} + \frac{n_{\text{NO,exh}}}{2} + \frac{n_{\text{NO}_2,\text{exh}}}{2} \quad (4.44)$$

$$n_{\text{tot,exh}} = n_{\text{CO}_2,\text{exh}} + n_{\text{CO,exh}} + n_{\text{H}_2\text{O,exh}} + n_{\text{O}_2,\text{exh}} \\ + n_{\text{N}_2,\text{exh}} + n_{\text{NO,exh}} + n_{\text{NO}_2,\text{exh}} \quad (4.45)$$

$$n_{\text{N}_2,\text{int}} = 3.76 n_{\text{O}_2,\text{int}} \quad (4.46)$$

HCR was calibrated based upon the exhaust gas concentrations while running pure diesel combustion trials. Because the exact ratio of hydrogen to carbon in diesel is variable based on the refinery inputs, it was calibrated on a per-refuel basis. The HCR was observed to be a value of 1.91. HCR is calculated as follows:

$$\text{HCR} = \frac{2c_{\text{H}_2\text{O}}}{c_{\text{CO}} + c_{\text{CO}_2}} \quad (4.47)$$

To determine the mass of air ingested into the cylinder, the mass of diesel was converted to a molar amount using the HCR value. Diesel was assumed to consist purely of carbon and hydrogen for this analysis due to the usage of ultra low sulfur diesel. The diesel mass equation is given:

$$m_{\text{diesel,inj}} = n_{\text{diesel,inj}}(M_{\text{C}} + \text{HCR}M_{\text{H}}) \quad (4.48)$$

Where, M_{C} is the molar mass of carbon, and M_{H} is the molar mass of hydrogen.

The volume of exhaust produced per cycle can also be determined from the model, provided that the exhaust temperature and pressure are known:

$$V_{\text{exh}} = \frac{n_{\text{total,exh}}RT_{\text{exh}}}{P_{\text{exh}}} \quad (4.49)$$

To determine the mass of the pilot injection with multiple injections, the single injection model was used. The estimated mass from the single injection model was then subtracted from the injected mass of the feedback model to determine the mass of the main injection.

The output of the multi-injection model as compared to using the single-injection model twice per cycle can be seen in Figure 4.4. The exhaust gas model can be seen to have better predictive performance than repeating the single injection model, especially at lower injection masses.

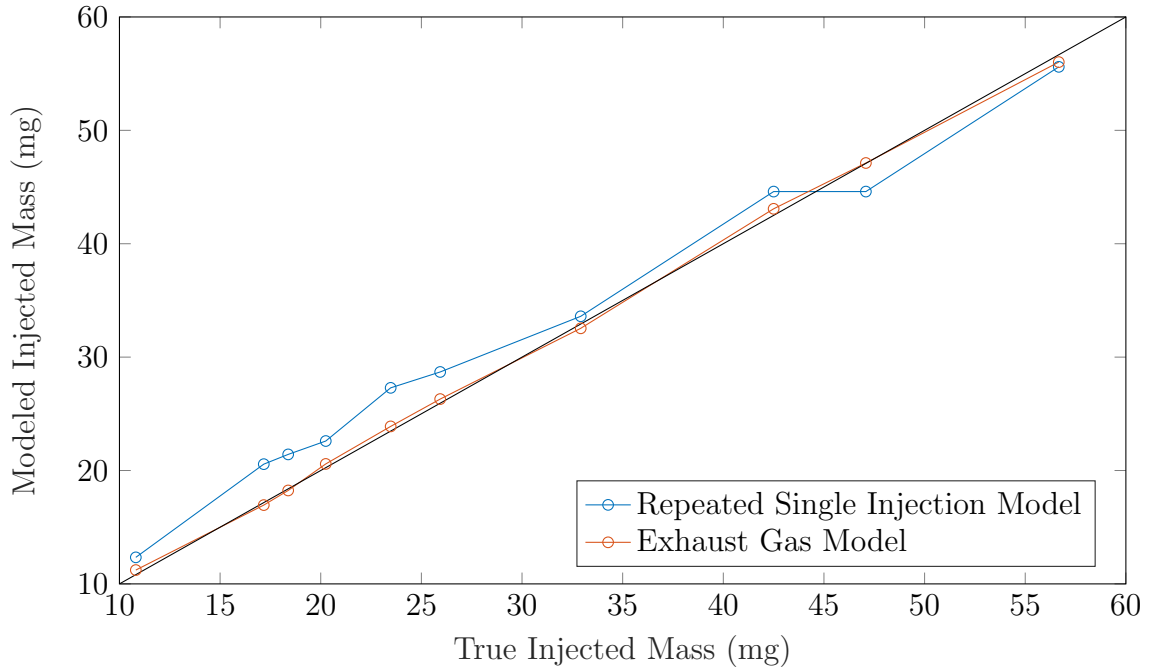


Figure 4.4: Comparison of the two injection models under double-diesel injection conditions.

4.2.5 Fuel Energies and Combustion Efficiencies

The inputted mass of diesel and hydrogen were converted into the fuel energy per cycle by multiplication with their lower heating values. The usage of a per cycle-based time unit instead of a direct unit of time was chosen in order to decouple the energy flow rate from the engine speed:

$$E_{\text{cycle,H2}} = m_{\text{cycle,H2}} \text{LHV}_{\text{H2}} \quad (4.50)$$

$$E_{\text{cycle,diesel}} = m_{\text{cycle,diesel}} \text{LHV}_{\text{diesel}} \quad (4.51)$$

Where, LHV_{H2} was taken as 119.64 MJ/kg and $\text{LHV}_{\text{diesel}}$ was taken as 42.83 MJ/kg [14]. These fuel energy values were not verified with the selected test fuels, but the Transportation Energy Data Book used gives suggested values for North American fuels.

The ratio of hydrogen replacement of diesel was taken as the fraction of the total cycle fuel energy that was supplied by hydrogen:

$$\chi_{\text{H2}} = \frac{E_{\text{cycle,H2}}}{E_{\text{cycle,H2}} + E_{\text{cycle,diesel}}} \quad (4.52)$$

The hydrogen combustion efficiency was taken from the ratio of the chemical potential energy of the unburnt hydrogen to total input hydrogen gas, as per:

$$\eta_{\text{comb,H2}} = 1 - \frac{E_{\text{H2,exh}}}{E_{\text{H2,int}}} \quad (4.53)$$

where, E is the chemical potential energy (defined here as the lower heating value) of the species. Separation of the combustion efficiencies of both diesel and hydrogen was able to be accomplished due to the FTIR's measurement of only carbon-containing species in its reported C1 FID-equivalent hydrocarbon emissions. Fugitive hydrogen emissions were assumed to only be caused by incomplete combustion of hydrogen, and hydrogenation of carbon-containing compounds was assumed not to occur in

significant quantities due to the lack of residence time within the cylinder and a suitable catalyst such as platinum [101]. Note that with a richer fuel-air mixture, incomplete combustion of diesel produces hydrogen [102], however due to the low concentrations produced the production of hydrogen gas from diesel was neglected in the analysis. The diesel combustion efficiency was calculated from the ratio of the chemical potential energy of the unburnt hydrocarbons and CO in the exhaust stream and the chemical potential energy of the input diesel fuel. The diesel combustion efficiency is given below:

$$\eta_{\text{comb,diesel}} = 1 - \frac{E_{\text{uHC,exh}} + E_{\text{CO,exh}}}{E_{\text{diesel,int}}} = 1 - \frac{n_{\text{uHC,exh}} \text{LHV}_{\text{CH}_4,\text{molar}} + n_{\text{CO,exh}} \text{LHV}_{\text{CO,molar}}}{E_{\text{diesel,int}}} \quad (4.54)$$

where, E is the chemical potential energy (defined here as the lower heating value) of the species. The overall combustion efficiency was calculated based on enthalpy of the inputted fuels and the enthalpy of the uncombusted exhaust products, as per:

$$\eta_{\text{comb,overall}} = 1 - \frac{E_{\text{uHC,exh}} + E_{\text{CO,exh}} + E_{\text{H}_2,\text{exh}}}{E_{\text{diesel,int}} + E_{\text{H}_2,\text{int}}} \quad (4.55)$$

These combustion efficiencies allow for the completeness of the combustion process to be quantified, and to analyze both the diesel and hydrogen combustion efficiencies separately to examine their relationship.

4.3 Cylinder Pressure Analysis

Direct measurement of an engine's cylinder pressure is a crucial tool for analysis. Cylinder pressure measurement allows for the determination of the temperature within the cylinder during the combustion cycle, along with measurements of combustion roughness and efficiency.

4.3.1 Preprocessing of Cylinder Pressure Data

In order to correct for the cycle-to-cycle drift of the in-cylinder pressure sensors, the cylinder 1 sensor is referenced to the average exhaust manifold pressure over a period from 220 CAD through 320 CAD during each cycle [103]. Exhaust pressure referencing was chosen due to the separated exhaust manifold. Using the intake manifold pressure referencing would result in pressure waves from other cylinders causing inaccuracies in the pressure at intake valve closure [104], along with inaccuracies due to the intake manifold's tuned nature [103]. The separated exhaust manifold is untuned, thus avoiding inaccuracies associated with pressure-wave based tuning. Cylinders 2 through 4 are referenced using a variable polytropic coefficient method [104]. This method was not chosen for usage on cylinder 1 due to transient noise issues that would occur with the cylinder's pressure sensor. Pressure referencing is described by:

$$P_{\text{cyl}} = P_{\text{cyl,raw}} - \frac{\sum_{n=220}^{320} P_{\text{cyl,raw}}(n)}{\sum_{n=220}^{320} 1} + \frac{\sum_{n=220}^{320} P_{\text{exh}}(n)}{\sum_{n=220}^{320} 1} \quad (4.56)$$

Where P_{cyl} is the corrected absolute cylinder pressure, $P_{\text{cyl,raw}}$ is the measured cylinder pressure and P_{exh} is the exhaust manifold pressure. In order to reduce high-frequency noise associated with the valvetrain, injectors, and fuel pump, filtering was used. To filter the cylinder pressure, a fourth-order Butterworth lowpass filter was used. A stopband for frequencies greater than 4000 Hz was selected in order to reduce noise from other engine accessories such as the fuel pump, valves, and injectors. This filter was applied using a zero-phase shift method, and was applied over the whole captured dataset of cylinder pressures. To analyze the average combustion cycle, an ensemble average of the filtered cylinder pressure measurements for each test point was then taken. 600 cycles per measurement point was used.

Despite the initial filtering, noise was found to have an effect in the heat release rate analysis. Severe noise is relatively common in compression ignition engines due to the production of acoustic waves within the cylinder during combustion coupled with only having a single pressure sensor to determine the cylinder pressure [105]. In

order to alleviate the noise in the heat release rate, further filtering was used [106]. Filtering allows the damping of the acoustic noise, and to reduce its effect on the calculated heat release rate.

For the heat release calculations, the cylinder pressure trace was filtered using a zero phase shift Butterworth low-pass filter with a cutoff frequency band starting at 3300 Hz and ending at 3800 Hz. This cutoff frequency was found to be able to significantly reduce the noise during heat release with a minimal impact on the overall pressure curve shape. To provide another estimate of an appropriate cutoff frequency, a noise-based cutoff frequency selection algorithm was used [107]. This algorithm suggested a minimum cutoff frequency of 4400 Hz to 4600 Hz across all test cases, which resulted in acceptable cylinder pressure traces but unacceptable noise in the heat release rate traces. Implementation of a similar algorithm on a diesel-CNG engine in a previous work [108] showed that diesel-CNG combustion resulted in lower frequency noise than pure diesel combustion, which helps to explain why the suggested cutoff frequency still resulted in high amounts of noise. Figure 4.5 shows the effect of the cutoff frequencies on a pressure trace with dual-fuel operation. Figure 4.6 shows the effect of the filtering on the instantaneous heat release trace.

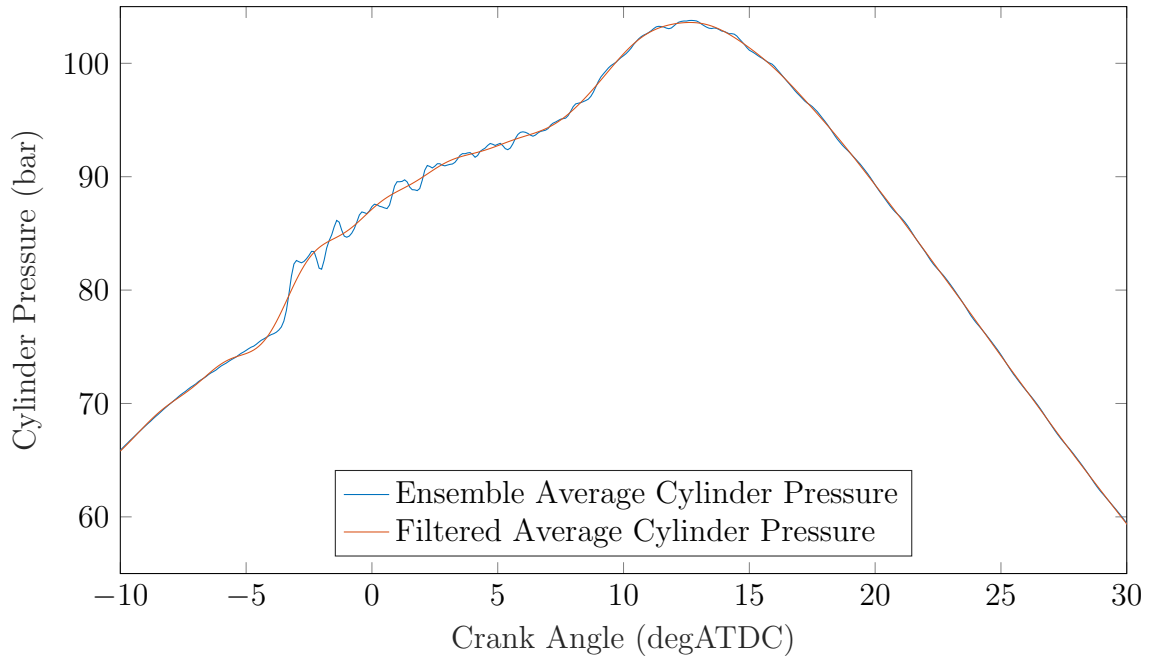


Figure 4.5: Comparison between filtered and unfiltered cylinder pressure traces for a 1350 J H₂ test (test G-25).

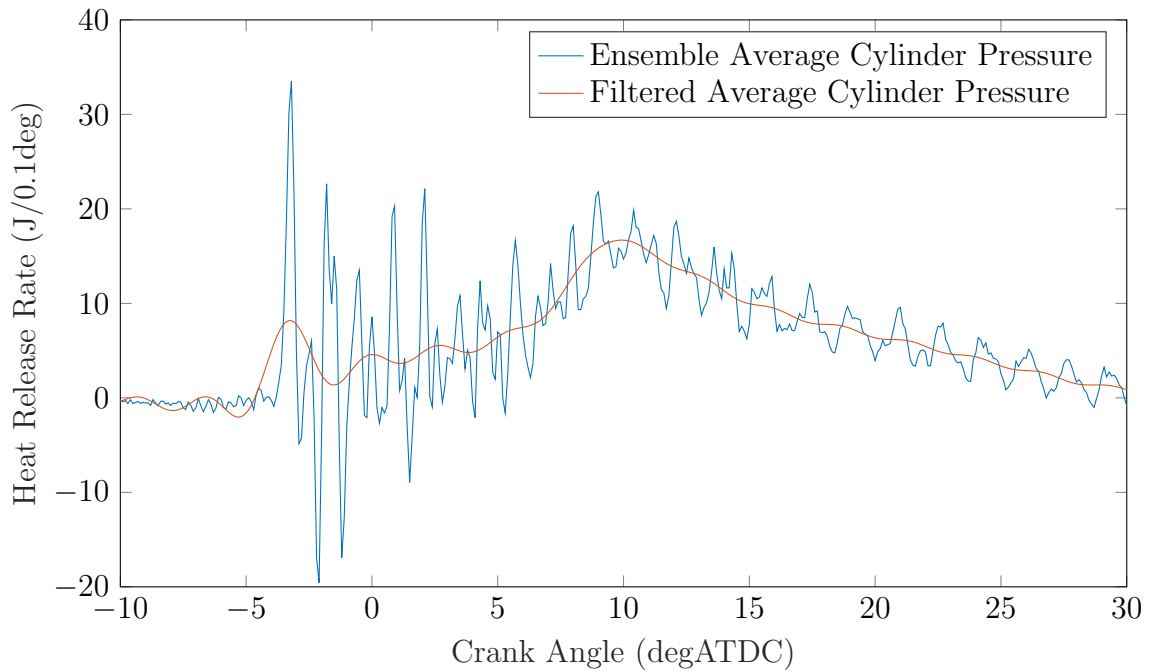


Figure 4.6: Comparison of heat release between filtered and unfiltered ensemble average cylinder pressure traces for test G-25.

4.3.2 Pressure Trace Analysis

To compare the engine performance both in a cycle-to-cycle manner and as an average for comparison between operating points, the net indicated mean effective pressure (IMEP) for each respective cylinder was calculated. Net IMEP (IMEP_n) is a measurement of the average cylinder pressure acting on the piston to produce work over the whole engine cycle [109]. As such, it can be related to both the engine torque and the engine displacement. The integration bounds for net IMEP were set to start at the beginning of the intake stroke (-360 CAD) and at the end of the exhaust stroke (359.9 CAD) for a cycle in order to couple a particular cycle's gas exchange process to its compression and expansion strokes. Net IMEP was separately calculated for every engine cycle from the cylinder pressure with:

$$\text{IMEP}_n = \frac{1}{V_s} \int_{-360\text{CAD}}^{359.9\text{CAD}} P_{\text{cyl}}(\theta) dV \quad (4.57)$$

It is important to note that due to the engine's supercharged-like nature, an increase in intake pressure would result in a significant increase in IMEP for the same fueling due to positive work being extracted over the gas exchange cycles. This is because as the intake pressure increases, the exhaust pressure does not increase in the same rate as with turbocharged aspiration. In order to compensate for this, gross IMEP (IMEP_g) was used to compare data over various intake manifold pressures. Gross IMEP is a measurement of IMEP that has the integration bounds only between the beginning of the compression stroke and end of the expansion stroke instead of the whole cycle. This significantly reduces the effect of differing intake and exhaust gas exchange pressures on the reported IMEP [110]. The equation for gross IMEP is as follows:

$$\text{IMEP}_g = \frac{1}{V_s} \int_{-180\text{CAD}}^{180\text{CAD}} P_{\text{cyl}}(\theta) dV \quad (4.58)$$

The crank angle dataset has a resolution of 0.1 CAD in order to reduce systematic

error from measurement [111]. This means that IMEP was integrated over a discrete dataset. In order to reduce inaccuracy from integration, a center-weighted method was used. This center-weighted method was used for the calculation of both $IMEP_n$ and $IMEP_g$, with differing summing bounds. Note that this method requires taking a single sample from both the previous and subsequent engine cycles. To allow for the sample to take place on all engine cycles, a single cycle was trimmed from all measurements to provide the bounding points for the first and last cycles of the measurement set.

$$IMEP_n = \frac{1}{V_s} \sum_{\theta=-360}^{359.9} P_{cyl}(\theta)(V(\theta+h) - V(\theta-h)) \quad (4.59)$$

Where, h is the minimum step size of the crank angle, in this case 0.1 CAD. To determine the cycle-to-cycle variation, the coefficient of variance (CoV), a normalized standard deviation of the IMEP, was calculated:

$$IMEP_{CoV} = \frac{\sigma_{IMEP}}{\mu_{IMEP}} \quad (4.60)$$

Where, σ is in reference to the standard deviation of a dataset and μ is the average of a dataset. IMEP is also closely related to the amount of energy extracted as work from the cylinder system. This can be used to find the indicated work from $IMEP_n$, which is the work produced from the cycle before frictional losses of the engine take place. The gross work can be found in the same manner using $IMEP_g$, however this is only a measurement of the work produced over the compression and expansion strokes. The indicated work of the cylinder was determined from IMEP by Equation 4.61.

$$W_g = IMEP_g V_s \quad (4.61)$$

The maximum cylinder pressure and maximum pressure rise rates (MPRR) were also analyzed. These parameters were both calculated online by the MABX FPGA

module and offline for the purpose of analysis. During online operation, MPRR was found to be reported to be significantly higher than the true value. This is likely due to a filter design in-FPGA that is optimized for SI combustion and not diesel combustion. This limited the true MPRR values to relatively low magnitudes. Both maximum cylinder pressure and its rise rate were calculated on a cycle-to-cycle basis. The pressure rise rate was calculated per-cycle on the raw pressure traces using a 1-degree moving interval. This was done in order to mediate the high-noise combustion noise diesel creates, especially the noise at high sampling rates.

$$\frac{dP_{\text{cyl}}}{d\theta} = P_{\text{cyl}}(\theta + 10h) - P_{\text{cyl}}(\theta) \quad (4.62)$$

4.3.3 Calculation of Heat Release

The heat release of the fuel in the cylinder was calculated using Equation 4.7. The integration was bounded from the angle of the start of the pilot diesel injection to the angle of exhaust valve opening. A forwards-weighted first order method was used to discretely integrate the cylinder pressure and cylinder volume.

To account for the mass flow of diesel during injection, the injection events were modeled as square-wave pulses that lasted from the SOI to the EOI. These pulses were modeled as enthalpy flows of n-dodecane, with the mass of n-dodecane being set equal to the mass of diesel injection. The injected mass was assumed to be a liquid that evaporated on the same crank angle as the injection event. This modeling approach is similar to Mattson et al.'s approach in a multizone model [112]. During the compression and expansion strokes the enthalpy flow in and out of the cylinder was modeled as:

$$h \frac{dm}{d\theta} = (h_{fg} + c_{\text{fuel}}(T_{\text{vap}} - T_{\text{inj}}) + c_{p,\text{fuel}}(T_{\text{cyl}} - T_{\text{vap}})) \frac{dm}{d\theta} \quad (4.63)$$

Where, h_{fg} is the enthalpy of vaporization of the fuel, T_{vap} is the vaporization temperature of the fuel, $c_{p,\text{fuel}}$ is the constant pressure specific heat of the vaporized

fuel, and c_{fuel} is the specific heat of the liquid fuel.

The crank angle of cumulative heat release (CA) is the crank angle where a given fraction of fuel is burned (ie. CA_{50} is the crank angle at which 50% of the fuel has combusted. Due to the low fraction of combusted fuel in some trials, the total heat release for the purposes of CA calculation was normalized to the combusted fuel energy instead of the total fuel energy. This was done in order to make sure each measurement had a set of CA values to compare to other measurements with. The method of calculating the exact angle of CA was accomplished using a search algorithm to determine the crank angle that had the nearest value to the desired CA fraction.

The mass fraction burned interval (MFB) is the duration taken to combust a fraction of fuel. A shorter MFB duration means that combustion occurred quicker, suggesting higher efficiency. MFB_{10-90} is of particular interest as the 10%-90% burn interval contains the majority of combustion and should also remove the beginning phase of combustion where flame propagation is slower due to lower turbulence [113]. Mass fraction burned is presented in the unit of crank angle degrees (CAD) between the two crank angles at which the lower and upper angles of cumulative heat release are reached.

4.3.4 Calculation of Emissions

The concentration of gaseous emissions from the exhaust stream were determined via FTIR measurement. However, in order to turn these concentrations into masses and ratings to compare operating points, the mass of emissions produced for each analyzed species had to be determined:

$$m_{\text{species}} = M_{\text{species}} n_{\text{total,exh}} c_{\text{species}} \quad (4.64)$$

In the case of NO_x emissions, the concentrations of the three NO_x species (NO , NO_2 and N_2O) and their molar masses were summed in order to determine the emissions

mass:

$$m_{\text{NO}_x} = (M_{\text{NO}}c_{\text{NO,exh}} + M_{\text{NO}_2}c_{\text{NO}_2,\text{exh}} + M_{\text{N}_2\text{O}}c_{\text{N}_2\text{O,exh}})n_{\text{total,exh}} \quad (4.65)$$

In the case of unburnt hydrocarbon mass, the molar mass of methane is used to represent the molar mass of C1 hydrocarbons. This is then combined with the C1 FID-equivalent unburnt hydrocarbon output given by the FTIR to yield a mass of unburnt hydrocarbons:

$$m_{\text{uHC}} = M_{\text{CH}_4}n_{\text{total,exh}}c_{\text{uHC,exh}} \quad (4.66)$$

Note that the FTIR is only capable of reporting partially combusted and uncombusted species of gas with at least one carbon molecule. In the case of particulate emissions, the PPS-M gives measurements in terms of a density per unit volume of gas. The volume of exhaust gas produced per cycle had to be combined with the soot density to determine the mass of soot produced:

$$m_{\text{soot}} = \rho_{\text{soot}}V_{\text{exh}} \quad (4.67)$$

To determine the specific emissions produced per unit of energy, the mass of the emissions produced is normalized using the gross indicated work over the test period, in order to be compared in terms of a g/kWh rating:

$$\Theta = \frac{m_{\text{test}}}{W_g N_{\text{test}}} \quad (4.68)$$

Where, m_{species} is the mass of the emissions produced per test, N_{test} is the number of engine cycles in the test and Θ is the specific mass of the emissions produced per unit of work. In this work, Θ was standardized to the gross indicated work of the gases in the engine cylinder.

4.4 Error Analysis

In this thesis, error is reported with a 95% confidence interval for random (non-bias) error in measurement. The student's t-test was used to determine an appropriate value to scale the standard deviation of measurement to create a confidence interval for said measurement. Bias error was not measured due to the lack of applicable measurement standards that could be used with all equipment (ie. in-cylinder pressure bias error). The confidence interval is reported with the following formula:

$$CI_{95, \text{ sample}} = \zeta_{\alpha/2} \frac{\sigma}{\sqrt{n-1}} \quad (4.69)$$

where, $\zeta_{\alpha/2}$ is the student's t-test value for a 95% confidence interval (1.96), σ is the standard deviation of the measurement set, and n is the number of samples within the measurement set. The propagation of error was calculated using the exact formula for the propagation of error:

$$\sigma_x^2 = \left(\frac{\delta x}{\delta a}\right)^2 \sigma_a^2 + \left(\frac{\delta x}{\delta b}\right)^2 \sigma_b^2 + \dots \quad (4.70)$$

This formula was then applied to the previous formulas outlines in this section as appropriate in order to propagate error. Error was only propagated for random error, not bias error. Repeatability of measurement was estimated using repeated measurement of a single operating point over multiple days. 12 total measurements were taken for this testpoint. Repeatability was calculated with a 95% confidence interval using Equation 4.69. The testpoint had a consistent operating point as per Table 3.11. Pure diesel was chosen for the operating point due to both the cost of hydrogen, and the repeatability and bias error specifications being available for the hydrogen mass flow meter (and the meter being within the calibration period of 1 year). Note that this was not a perfect test of repeatability – environmental conditions such as ambient pressure, temperature and humidity could not be controlled for, and could conceivably cause measurement deviation in the emissions equipment by

changing the local air density and oxygen partial pressures. The repeatability for each of the measurements is listed in Table 4.2.

Table 4.2: Calculated repeatability of relevant primary sensors on engine.

Parameter	Repeatability
Exhaust Oxygen Concentration	$\pm 0.03\%$
FTIR CO ₂ Concentration	$\pm 0.1\%$
FTIR CO Concentration	$\pm 18ppm$
FTIR uHC Concentration	$\pm 9ppm$
FTIR NO _x Concentration	$\pm 10ppm$
Engine Gross IMEP	$\pm 0.02bar$

Chapter 5

Steady-State Results

5.1 Structure of Chapter

The structure of this chapter is separated into 4 main parts. Firstly, the boundaries and testing scheme used for the testing structure are defined and explored. Secondly, the test results are presented in Table 5.1. Thirdly, the individual sensed data from all of these tests (ie. NO_x concentration and CA_{50}) is explored, and trends related to hydrogen replacement and hydrogen air-fuel ratio are explored and related to literature results. Finally, a selection of optimal operating points is chosen, and the performance is compared to pure diesel operation and emissions output differences are assessed.

5.2 Overview of Steady-State Tests

The main driving parameters of the steady state tests was to find the maximum possible CO_2 emissions reduction possible while running hydrogen, and the most efficient operating points to combust hydrogen. These parameters are driven by two main factors: the push for CO_2 reduction in future emissions standards and the relative difficulty of storing large masses of hydrogen on-vehicle. This means that both the magnitude of the reduction and the most optimal usage of hydrogen to attain this reduction were the primary investigated parameters. In order to find operating points that maximized these parameters, the impact on other emissions

(such as NO_x) were neglected. The only other parameters that limited search points were the maximum cylinder pressure and the maximum cylinder pressure rise rate, which were both kept under 150 bar and 10 bar/CAD, respectively, to reduce the probability of engine damage.

Steady-state tests were taken at discrete operating points with a specified total fuel cycle energy (J/stk) and a specified H_2 fuel energy (ranging from 0% to 92% of the total cycle fuel energy). The engine load and engine intake pressures were held constant throughout each trial set, with an engine speed of 1500 rpm. The injection timing and duration for the diesel injection was adjusted through these tests, with one or two diesel injection pulses per cycle, depending on the load scenario. With two pulses, the diesel injection strategy was to have a low-mass pilot injection (≈ 3 mg), and a high-mass main injection. When using two injections, the main injection was set to begin at TDC (0 CAD), while the pilot injection angle was varied. In cases with only a single injection (the pilot injection), no injection of diesel at TDC occurred. Multiple-pilot injection strategies were not pursued during hydrogen testing due to a lack of data on the engine's operation while running a multi-pilot strategy (the Cummins engine was only programmed with a double-injection strategy). Because of a lack of this data, the safe operating parameters for multi-pilot operation were not known. Creating an injection scheme for running pure-diesel multi-pilot injection to compare to was considered out-of-scope for the work of this thesis. Additionally, initial testing showed that with a second, earlier pilot injection, the maximum pressure rise rate in-cylinder was significantly higher than with a single pilot, and knocking occurred during combustion while running hydrogen-diesel dual fuel, similar to single pilot injection dual fuel trials where the pilot injection was advanced significantly.

The double diesel injection strategy was used in the higher-diesel mass cases as a pilot injection reduces the pressure rise rate due to the large main diesel injection [114], which can allow for lower peak combustion temperatures and lower NO_x output [115]. When hydrogen was added to the cylinder, the pilot injection also served to

begin the ignition process of the premixed hydrogen, which has a long ignition delay due to its octane number of 120 RON at $\lambda = 2$ [116]. As such, varying the diesel pilot angle can have a significant effect on engine performance by advancing or retarding the combustion timing of the hydrogen mixture.

5.3 Testing Schema

All of the tests taken were done at steady-state operating conditions in order to allow for large statistical sets for analysis. Tests were grouped into “Bins”, where the engine load and engine intake manifold absolute pressure (IMAP) were held constant. This approach was taken in order to explore the effects of varied hydrogen replacement on each operating point in a granular manner, instead of finding a single high-performing operating point and not having non-optimal operating points to explore trends in results that varied with hydrogen replacement. CA_{50} was not directly controlled for as online heat release models were found to differ significantly from offline calculated CA_{50} parameters. Additionally, due to the changing diesel load, adjustment of CA_{50} to a significant degree would require advancement of the main injection. This was found to result in significantly increased maximum pressure rise rate. In order to reduce the maximum pressure rise rate, the decision to not advance the main injection was made. In each Bin, while the load was held constant, the hydrogen fuel energy was stepped in units of 450 J. Pilot injection timing was then advanced to either a pre-set limit or the point of knock, which made up the test grid. The diesel injection mass was reduced in order to maintain constant load. Fuel flow, emissions, and cylinder pressure were measured in order to present the results.

5.4 List of Conventional Dual-Fuel Combustion Tests

All test points were taken at an engine speed of 1500 RPM and a main diesel start of injection timing of 0 CAD. The pilot injection of diesel was held at 0.23 ms for all tests.

The pilot injection angle, hydrogen energy fraction, load target and intake manifold pressure were all varied to build the dataset. The pilot advance was increased until either the point of knock, ringing, a maximum pressure rise rate limit, or where a significant number of preignition cycles were observed. The hydrogen energy fraction was pursued in steps, where an injected hydrogen energy was selected for multiple tests then the diesel injection was varied to meet the load target. While most tests used a double diesel injection strategy, some high-replacement tests used only the pilot diesel injection to further reduce diesel usage. The tests are separated into lettered Bins based upon their targeted loads and intake manifold pressures. Table 5.1 contains the list of test points undergone during conventional dual-fuel combustion, which are correlated to their file numbers in Appendix C. Appendix C also contains CO and NMHC emissions data. The cylinder pressure and heat release traces plotted as figures are available in Appendix D.

Table 5.1: List of all conventional dual-fuel combustion tests. Test names appended with a “S” note cases where a single diesel injection was used to maximize H₂ replacement.

Test	IMEP _g (bar)	IMAP (bar)	H ₂ Energy (J)	H ₂ Ratio (%)	Pilot Angle (CAD)	η_g (%)	η_{H_2} (%)	P_{\max} (bar)	P_{\max} Angle (CAD)	CoV IMEPg (%)	MRRR (bar/CAD)	MFB ₁₀₋₉₀ (CAD)	CA ₁₀ (CAD)	CA ₅₀ (CAD)	NO _x (g/kWh)	CO ₂ (g/kWh)	Soot (mg/kWh)
A-1	4.5	1.0	0	0.0	-7.5	43.1	-	53.4	2.8	1.0	2.8	26.9	9.0	15.9	2.65	606.18	182
A-2	4.5	1.0	0	0.0	-9.3	43.0	-	54.4	1.3	1.5	3.2	25.9	9.1	15.7	2.71	604.52	162
A-3	4.5	1.0	0	0.0	-11.1	43.0	-	54.9	0.3	1.3	3.6	27.3	8.7	15.4	2.81	605.22	172
A-4	4.5	1.0	0	0.0	-12.9	42.8	-	55.1	-0.1	2.2	3.7	26.3	8.7	15.2	2.85	605.62	185
A-5	4.5	1.0	453	29.4	-7.5	37.0	48.7	54.2	3.3	1.8	3.3	33.9	7.3	15.6	3.22	414.81	89
A-6	4.5	1.0	455	30.0	-9.3	37.7	55.2	55.7	2.1	2.3	3.9	31.7	6.0	14.9	3.39	406.28	78
A-7	4.5	1.0	455	31.9	-11.1	40.2	80.5	56.7	1.4	2.2	4.2	31.1	3.7	13.9	3.47	400.46	71
A-8	4.5	1.0	455	33.3	-12.9	41.8	92.8	57.5	1.9	3.6	4.5	32.4	0.0	13.2	3.43	387.31	65
A-9	4.5	1.0	918	71.7	-7.5	44.7	99.3	57.6	10.7	3.3	3.3	21.2	4.6	12.5	3.88	184.55	7.7
A-10	4.5	1.0	918	72.8	-9.3	44.8	98.7	61.1	9.7	2.8	3.8	21.0	2.4	10.6	3.98	169.83	7.3
A-11	4.5	1.0	928	74.1	-11.1	45.0	98.8	64.9	9.1	3.3	4.1	18.8	0.7	8.5	4.23	162.00	7.1
A-12	4.5	1.0	931	75.5	-12.9	45.4	99.6	68.6	8.3	4.2	4.3	16.5	-0.7	6.8	4.52	156.75	6.2

Test	IMEP _g (bar)	IMAP (bar)	H ₂ Energy (J)	H ₂ Ratio (%)	Pilot Angle (CAD)	η_g (%)	η_{H2} (%)	P_{max} (bar)	P_{max} Angle (CAD)	CoV IMEP _g (%)	MRRR (bar/CAD)	MFB ₁₀₋₉₀ (CAD)	CA ₁₀ (CAD)	CA ₅₀ (CAD)	NO _x (g/kWh)	CO ₂ (g/kWh)	Soot (mg/kWh)
A-13S	4.5	1.0	1096	88.8	-7.5	45.8	99.8	62.4	10.5	0.9	4.4	16.6	3.5	9.9	3.73	85.09	4.9
A-14S	4.5	1.0	1084	88.7	-9.3	45.8	99.4	67.1	9.2	1.0	5.0	14.3	1.4	7.6	4.21	83.18	5.3
A-15S	4.5	1.0	1073	88.5	-12.9	45.5	98.1	77.4	8.1	0.9	5.5	10.6	-1.8	3.7	4.98	78.38	5.0
B-1	4.5	1.5	0	0.0	-7.5	46.5	-	81.7	1.1	1.7	4.5	23.0	7.9	14.3	3.39	563.54	97.4
B-2	4.5	1.5	0	0.0	-9.3	46.8	-	82.4	0.0	1.3	5.2	22.7	8.0	14.2	3.47	559.47	99.0
B-3	4.5	1.5	0	0.0	-11.1	46.5	-	82.4	-0.9	1.8	5.6	22.5	7.7	13.8	3.56	562.39	96.9
B-4	4.5	1.5	0	0.0	-12.9	46.6	-	82.4	-0.5	1.9	6.0	22.0	7.8	13.8	3.58	562.32	92.4
B-5	4.5	1.5	460	29.9	-7.5	34.3	23.8	82.5	1.5	2.2	5.1	25.9	6.6	14.2	3.92	389.27	42.0
B-6	4.5	1.5	461	30.3	-9.3	34.6	29.2	83.5	0.3	2.8	5.7	25.5	6.6	13.9	4.21	389.87	39.2
B-7	4.5	1.5	460	32.3	-11.1	37.0	58.5	83.8	-0.5	3.2	6.2	25.7	6.1	13.5	4.38	384.74	37.8
B-8	4.5	1.5	461	33.6	-12.9	37.9	69.0	84.0	-0.1	5.2	6.4	25.3	5.5	13.2	4.52	380.42	33.9
B-9	4.5	1.5	906	60.8	-7.5	35.8	93.9	83.3	1.6	3.4	5.4	29.1	2.2	14.1	4.04	264.87	14.3
B-10	4.5	1.5	908	61.7	-9.3	35.4	94.3	84.3	0.6	5.3	6.0	29.2	0.2	12.8	4.28	261.83	12.8
B-11	4.5	1.5	907	63.3	-11.1	36.0	96.3	85.0	1.0	8.3	6.3	27.8	-1.5	11.3	4.42	252.71	10.5

Test	IMEP _g (bar)	IMAP (bar)	H ₂ Energy (J)	H ₂ Ratio (%)	Pilot Angle (CAD)	η_g (%)	η_{H_2} (%)	P_{max} (bar)	P_{max} Angle (CAD)	CoV IMEP _g (%)	MRRR (bar/CAD)	MFB ₁₀₋₉₀ (CAD)	CA ₁₀ (CAD)	CA ₅₀ (CAD)	NO _x (g/kWh)	CO ₂ (g/kWh)	Soot (mg/kWh)
B-12	4.5	1.5	901	64.0	-12.9	36.4	95.7	86.1	1.1	7.8	6.6	25.6	-2.9	10.0	4.47	248.70	9.7
B-13S	4.5	1.5	1191	89.8	-7.5	39.5	99.5	85.0	2.1	2.9	6.8	34.0	1.4	14.1	3.32	108.79	10.5
B-14S	4.5	1.5	1153	89.5	-9.3	40.1	99.4	86.7	2.2	2.9	7.6	30.5	-0.5	11.4	3.57	105.75	11.4
B-15S	4.5	1.5	1119	89.2	-11.1	40.2	100.2	88.9	2.9	2.5	8.2	25.4	-2.2	8.5	3.97	105.71	8.5
B-16S	4.5	1.5	1113	89.1	-12.9	41.4	98.7	92.2	4.2	2.0	8.5	21.0	-3.7	6.1	4.08	101.45	8.0
C-1	7.5	1.5	0	0.0	-7.5	47.4	-	80.6	1.1	1.0	4.5	22.2	9.9	17.2	3.08	566.12	100
C-2	7.5	1.5	0	0.0	-9.3	47.0	-	81.2	-0.1	0.8	5.1	23.5	9.7	17.3	3.12	566.96	99.5
C-3	7.5	1.5	0	0.0	-11.1	46.7	-	81.3	-1.0	1.0	5.7	23.6	9.3	16.9	3.22	570.08	95.1
C-4	7.5	1.5	0	0.0	-12.9	46.9	-	81.3	-0.5	0.9	6.0	23.6	9.2	16.9	3.22	567.02	90.0
C-5	7.5	1.5	458	22.2	-7.5	41.7	43.6	81.9	1.3	0.8	5.2	27.9	9.2	17.1	3.68	437.17	63.1
C-6	7.5	1.5	458	22.3	-9.3	41.8	47.1	82.8	0.0	1.1	5.9	28.5	8.8	16.9	3.80	435.96	62.6
C-7	7.5	1.5	459	23.2	-11.1	43.3	71.6	83.1	-0.6	1.7	6.5	28.3	8.1	16.3	3.91	433.52	58.6
C-8	7.5	1.5	466	23.6	-12.9	44.1	77.8	83.9	-0.2	2.6	7.2	27.6	7.5	15.8	3.99	421.10	51.9
C-9	7.5	1.5	905	46.0	-12.9	44.4	86.2	86.5	1.6	3.1	7.4	27.1	1.0	12.9	4.53	306.03	23.6

Test	IMEP _g (bar)	IMAP (bar)	H ₂ Energy (J)	H ₂ Ratio (%)	Pilot Angle (CAD)	η_g (%)	η_{H_2} (%)	P_{\max} (bar)	P_{\max} Angle (CAD)	CoV IMEP _g (%)	MRRR (bar/CAD)	MFB ₁₀₋₉₀ (CAD)	CA ₁₀ (CAD)	CA ₅₀ (CAD)	NO _x (g/kWh)	CO ₂ (g/kWh)	Soot (mg/kWh)
C-10	7.5	1.5	899	46.3	-11.1	42.3	82.0	84.2	0.9	2.1	6.5	25.8	3.8	13.9	4.27	301.74	27.0
C-11	7.5	1.5	928	45.2	-9.3	41.6	71.2	82.5	0.8	1.4	6.1	24.9	5.4	14.8	4.06	306.32	32.1
C-12	7.5	1.5	925	45.5	-7.5	42.1	76.9	81.1	1.8	1.4	5.3	24.1	7.0	15.6	3.93	307.28	33.1
C-13	7.5	1.5	1356	73.9	-7.5	45.8	99.9	82.4	4.5	1.8	5.9	25.3	4.0	14.0	3.95	178.93	11.9
C-14	7.5	1.5	1356	72.9	-9.3	45.5	98.3	85.9	7.8	1.7	6.5	25.4	1.7	12.3	4.34	177.38	11.3
C-15	7.5	1.5	1357	74.7	-11.1	46.2	98.8	90.6	8.4	1.9	7.0	24.7	-0.5	10.3	4.56	162.01	11.1
C-16	7.5	1.5	1356	74.7	-12.9	46.8	99.1	96.4	8.3	3.1	7.8	21.8	-2.4	8.2	5.11	162.38	10.6
C-17S	7.5	1.5	1677	92.5	-7.5	46.2	100.1	89.8	8.6	0.8	7.6	23.2	1.7	10.7	3.99	74.39	7.0
C-18S	7.5	1.5	1648	92.4	-9.3	47.1	100.4	97.2	8.0	0.8	8.8	17.8	-0.4	8.0	4.72	74.62	6.9
C-19S	7.5	1.5	1629	92.3	-11.1	47.0	97.7	101.4	7.6	0.6	8.8	16.2	-2.0	6.2	4.82	67.46	6.8
C-20S	7.5	1.5	1621	92.2	-12.9	47.2	98.4	113.7	8.1	0.6	9.3	12.6	-3.6	3.9	5.57	66.98	6.8
D-1	7.5	2.0	0	0.0	-7.5	46.0	-	103.3	0.5	2.2	4.7	22.4	9.3	16.7	3.99	620.11	67.9
D-2	7.5	2.0	0	0.0	-9.3	47.1	-	103.8	-0.6	2.0	5.5	22.7	9.2	16.6	3.94	606.82	67.2
D-3	7.5	2.0	0	0.0	-11.1	46.0	-	103.7	-0.4	1.8	6.2	22.3	9.1	16.3	4.17	619.20	67.1

Test	IMEP _g (bar)	IMAP (bar)	H ₂ Energy (J)	H ₂ Ratio (%)	Pilot Angle (CAD)	η_g (%)	η_{H_2} (%)	P_{\max} (bar)	P_{\max} Angle (CAD)	CoV IMEP _g (%)	MRRR (bar/CAD)	MFB ₁₀₋₉₀ (CAD)	CA ₁₀ (CAD)	CA ₅₀ (CAD)	NO _x (g/kWh)	CO ₂ (g/kWh)	Soot (mg/kWh)
D-4	7.5	2.0	0	0.0	-12.9	46.1	-	103.9	-0.7	2.0	6.6	21.2	8.9	16.0	4.21	617.26	63.9
D-5	7.5	2.0	445	23.2	-7.5	40.6	21.6	101.8	0.6	1.5	5.1	22.9	8.7	15.9	3.87	419.45	35.9
D-6	7.5	2.0	445	23.1	-9.3	41.0	22.6	102.6	-0.5	1.6	5.8	23.5	8.4	16.0	4.01	418.63	36.8
D-7	7.5	2.0	446	23.3	-11.1	41.2	28.4	102.7	-0.4	1.8	6.5	22.7	8.0	15.4	4.19	419.57	36.9
D-8	7.5	2.0	454	24.3	-12.9	41.9	41.0	103.1	-0.6	1.9	7.1	22.9	8.0	15.2	4.30	414.91	35.7
D-9	7.5	2.0	895	44.0	-7.5	38.6	80.4	102.9	1.0	2.1	5.7	26.3	7.8	15.8	4.07	338.87	27.9
D-10	7.5	2.0	909	44.5	-9.3	38.6	78.9	103.9	-0.2	2.2	6.7	26.1	7.3	15.5	4.23	333.70	27.3
D-11	7.5	2.0	910	44.9	-11.1	38.7	79.1	104.5	-0.1	2.2	7.4	26.5	6.4	14.9	4.45	332.62	26.2
D-12	7.5	2.0	903	45.3	-12.9	39.0	82.0	105.1	-0.2	2.1	7.8	26.3	5.9	14.6	4.64	332.73	24.5
D-13S	7.5	2.0	1348	70.8	-9.3	41.1	93.5	104.7	0.6	2.2	7.1	23.9	2.2	13.2	3.75	208.18	13.1
D-14S	7.5	2.0	1349	73.9	-11.1	43.3	100.3	106.4	1.4	2.5	7.8	23.7	-1.0	11.6	3.98	201.70	11.9
D-15S	7.5	2.0	1350	74.9	-12.9	43.0	99.8	108.8	2.3	3.5	8.3	22.2	-2.7	10.1	4.24	200.60	10.9
D-16S	7.5	2.0	1348	75.5	-14.7	44.2	99.3	112.1	3.1	3.5	8.5	21.3	-4.0	8.8	4.35	193.48	10.4
E-1	10.5	1.5	0	0.0	-7.5	45.5	-	82.4	0.9	0.7	4.6	29.4	11.1	19.8	3.18	572.82	80.8

Test	IMEP _g (bar)	IMAP (bar)	H ₂ Energy (J)	H ₂ Ratio (%)	Pilot Angle (CAD)	η_g (%)	η_{H_2} (%)	P_{max} (bar)	P_{max} Angle (CAD)	CoV IMEP _g (%)	MRRR (bar/CAD)	MFB ₁₀₋₉₀ (CAD)	CA ₁₀ (CAD)	CA ₅₀ (CAD)	NO _x (g/kWh)	CO ₂ (g/kWh)	Soot (mg/kWh)
E-2	10.5	1.5	0	0.0	-9.3	45.3	-	82.9	-0.2	0.7	5.2	29.2	11.0	19.8	3.24	573.51	83.9
E-3	10.5	1.5	0	0.0	-11.1	45.2	-	83.0	-0.7	0.7	5.7	29.1	10.5	19.3	3.36	575.27	91.3
E-4	10.5	1.5	0	0.0	-12.9	45.3	-	83.0	-0.4	0.7	6.0	28.8	10.4	19.2	3.37	572.95	84.2
E-5	10.5	1.5	0	0.0	-14.7	45.4	-	82.7	-1.1	0.7	5.9	28.5	10.5	19.3	3.35	573.22	76.7
E-6	10.5	1.5	0	0.0	-16.5	45.5	-	82.3	-0.6	0.6	5.5	28.5	10.3	19.1	3.36	573.66	81.4
E-7	10.5	1.5	0	0.0	-18.3	45.6	-	82.5	-0.7	0.6	5.4	28.5	10.1	19.2	3.29	571.08	75.8
E-8	10.5	1.5	0	0.0	-20.1	45.7	-	83.0	-0.6	0.6	5.4	28.3	9.8	19.1	3.22	569.22	66.1
E-9	10.5	1.5	455	16.9	-7.5	43.0	23.8	83.6	1.2	0.8	5.1	32.0	10.4	19.2	3.40	446.50	76.7
E-10	10.5	1.5	455	16.9	-9.3	43.2	31.9	84.3	-0.0	0.8	5.8	32.2	10.2	19.1	3.47	447.22	76.1
E-11	10.5	1.5	453	17.6	-11.1	44.9	66.2	84.7	-0.4	0.7	6.5	31.8	9.6	18.5	3.57	445.97	76.9
E-12	10.5	1.5	454	17.6	-12.9	45.1	69.0	84.8	-0.1	0.9	6.6	31.4	9.4	18.4	3.59	448.52	76.6
E-13	10.5	1.5	453	17.9	-14.7	45.7	76.6	84.7	-0.5	0.9	6.4	31.1	9.2	18.3	3.52	442.97	73.2
E-14	10.5	1.5	453	17.9	-16.5	45.7	72.7	85.3	0.1	0.7	6.4	30.8	8.5	17.9	3.50	442.07	72.3
E-15	10.5	1.5	456	17.9	-18.3	45.7	70.0	86.0	0.3	0.7	6.2	30.8	7.8	17.8	3.41	438.40	63.5

Test	IMEP _g (bar)	IMAP (bar)	H ₂ Energy (J)	H ₂ Ratio (%)	Pilot Angle (CAD)	η_g (%)	η_{H_2} (%)	P_{\max} (bar)	P_{\max} Angle (CAD)	CoV IMEP _g (%)	MRRR (bar/CAD)	MFB ₁₀₋₉₀ (CAD)	CA ₁₀ (CAD)	CA ₅₀ (CAD)	NO _x (g/kWh)	CO ₂ (g/kWh)	Soot (mg/kWh)
E-16	10.5	1.5	454	17.9	-20.1	45.4	63.3	86.7	0.4	0.7	5.7	30.7	7.2	17.6	3.28	436.49	59.2
E-17	10.5	1.5	921	35.0	-7.5	44.0	71.5	85.1	1.5	0.7	6.0	27.2	8.3	17.0	3.78	341.23	73.9
E-18	10.5	1.5	931	35.7	-9.3	44.2	74.1	85.8	0.9	0.8	6.2	27.0	7.5	16.5	3.81	340.13	76.5
E-19	10.5	1.5	927	36.9	-11.1	45.8	87.3	87.0	2.6	0.7	6.8	27.9	5.9	15.5	4.04	338.47	62.6
E-20	10.5	1.5	925	37.4	-12.9	46.5	91.3	88.8	4.3	0.8	7.3	29.1	3.6	14.8	4.13	334.34	49.5
E-21	10.5	1.5	928	38.5	-14.7	47.9	100.4	91.0	3.7	0.8	7.1	30.8	1.3	14.2	4.10	330.79	45.7
E-22	10.5	1.5	930	39.2	-16.5	47.9	98.3	94.1	4.0	0.7	7.0	31.8	-1.2	13.2	4.04	322.39	35.4
E-23	10.5	1.5	933	38.9	-18.3	47.2	90.8	96.5	3.6	0.6	6.2	32.4	-2.7	12.9	3.80	318.82	31.6
E-24	10.5	1.5	938	39.0	-20.1	47.1	88.8	99.5	3.4	0.5	5.6	32.8	-4.3	12.3	3.57	316.02	28.2
E-25	10.5	1.5	1349	55.9	-7.5	47.2	99.6	88.2	12.9	1.1	6.4	23.9	5.3	14.5	4.59	254.35	25.1
E-26	10.5	1.5	1361	56.9	-9.3	47.6	100.2	91.9	13.1	1.0	7.0	25.0	3.2	13.4	4.85	245.39	20.6
E-27	10.5	1.5	1366	57.5	-11.1	48.1	100.3	96.9	12.5	0.7	7.7	23.4	1.1	12.0	5.32	239.57	14.8
E-28	10.5	1.5	1367	58.6	-12.9	48.3	99.7	101.8	11.8	0.7	7.9	22.1	-0.7	10.6	5.61	229.00	11.1
E-29	10.5	1.5	1365	58.9	-14.7	48.5	100.0	109.0	10.0	0.8	8.0	21.3	-2.6	8.5	5.89	228.62	9.6

Test	IMEP _g (bar)	IMAP (bar)	H ₂ Energy (J)	H ₂ Ratio (%)	Pilot Angle (CAD)	η_g (%)	η_{H_2} (%)	P_{\max} (bar)	P_{\max} Angle (CAD)	CoV IMEP _g (%)	MRRR (bar/CAD)	MFB ₁₀₋₉₀ (CAD)	CA ₁₀ (CAD)	CA ₅₀ (CAD)	NO _x (g/kWh)	CO ₂ (g/kWh)	Soot (mg/kWh)
E-30	10.5	1.5	1363	59.0	-16.5	48.4	99.7	114.7	7.5	1.0	7.9	22.0	-4.4	6.5	5.82	227.74	9.5
F-1	10.5	2.0	0	0.0	-7.5	49.0	-	105.3	0.4	0.6	4.9	23.5	10.4	18.8	3.47	545.82	52.6
F-2	10.5	2.0	0	0.0	-9.3	48.6	-	105.9	-0.6	0.7	5.7	23.3	10.5	18.8	3.54	547.19	49.0
F-3	10.5	2.0	0	0.0	-11.1	48.4	-	105.9	-0.3	0.7	6.3	23.5	10.1	18.3	3.63	547.14	46.7
F-4	10.5	2.0	0	0.0	-12.9	48.2	-	106.0	-0.9	0.8	6.6	23.5	10.1	18.3	3.67	549.83	47.1
F-5	10.5	2.0	0	0.0	-14.7	48.3	-	105.7	-0.6	0.6	6.9	23.2	10.3	18.4	3.64	547.55	44.7
F-6	10.5	2.0	0	0.0	-16.5	48.2	-	105.7	-0.5	0.6	6.9	23.3	10.2	18.4	3.61	548.15	42.8
F-7	10.5	2.0	0	0.0	-18.3	48.3	-	105.6	-0.8	0.6	6.7	23.4	10.2	18.4	3.53	547.85	44.0
F-8	10.5	2.0	0	0.0	-20.1	48.1	-	106.1	-0.3	0.6	6.6	23.3	10.0	18.4	3.49	548.19	43.3
F-9	10.5	2.0	461	18.0	-7.5	43.9	27.3	106.3	0.7	0.7	5.2	26.6	10.0	18.4	3.89	412.64	35.3
F-10	10.5	2.0	460	18.2	-9.3	44.4	35.5	107.0	-0.5	0.8	6.1	26.7	9.8	18.2	4.03	409.51	31.3
F-11	10.5	2.0	453	18.5	-11.1	46.1	66.7	107.4	-0.2	0.9	6.9	26.9	9.4	17.8	4.17	410.71	31.4
F-12	10.5	2.0	456	18.8	-12.9	46.1	69.7	107.5	-0.6	0.9	7.3	26.9	9.2	17.7	4.24	407.80	30.7
F-13	10.5	2.0	459	19.1	-14.7	46.7	75.8	107.4	-0.4	1.1	7.5	26.2	9.2	17.7	4.22	406.11	29.4

Test	IMEP _g (bar)	IMAP (bar)	H ₂ Energy (J)	H ₂ Ratio (%)	Pilot Angle (CAD)	η_g (%)	η_{H_2} (%)	P_{\max} (bar)	P_{\max} Angle (CAD)	CoV IMEP _g (%)	MRRR (bar/CAD)	MFB ₁₀₋₉₀ (CAD)	CA ₁₀ (CAD)	CA ₅₀ (CAD)	NO _x (g/kWh)	CO ₂ (g/kWh)	Soot (mg/kWh)
F-14	10.5	2.0	464	19.2	-16.5	46.2	66.9	107.5	-0.4	0.7	7.4	26.3	9.0	17.6	4.16	404.22	29.4
F-15	10.5	2.0	466	19.2	-18.3	46.0	61.9	107.7	-0.3	0.8	7.2	26.3	8.8	17.5	4.05	404.28	29.2
F-16	10.5	2.0	466	19.0	-20.1	45.7	55.3	108.2	-0.1	0.8	6.7	26.2	8.5	17.4	3.88	403.91	28.7
F-17	10.5	2.0	917	34.6	-7.5	42.4	71.4	107.3	0.9	1.0	5.8	31.0	9.4	18.2	4.03	333.61	27.4
F-18	10.5	2.0	916	34.9	-9.3	42.7	74.5	108.2	-0.3	1.2	6.7	30.5	9.0	17.9	4.14	332.87	26.9
F-19	10.5	2.0	914	36.3	-11.1	44.3	89.7	108.4	0.2	1.2	7.3	30.1	8.3	17.2	4.27	332.52	26.4
F-20	10.5	2.0	914	36.4	-12.9	44.5	89.7	109.3	-0.4	1.1	7.9	29.5	7.8	16.9	4.40	331.38	25.3
F-21	10.5	2.0	914	37.0	-14.7	45.0	91.5	109.3	0.5	1.1	7.9	28.9	7.5	16.6	4.34	326.27	24.2
F-22	10.5	2.0	916	37.1	-16.5	45.3	89.5	110.5	0.2	0.9	8.0	28.6	6.5	16.1	4.34	323.66	23.2
F-23	10.5	2.0	917	37.4	-18.3	45.4	89.0	111.6	0.8	0.9	7.7	28.9	4.8	15.6	4.24	321.65	22.1
F-24	10.5	2.0	1363	54.0	-7.5	44.1	85.7	108.1	1.2	1.4	6.5	23.2	6.8	15.8	4.13	245.56	16.7
F-25	10.5	2.0	1363	54.6	-9.3	44.5	87.6	109.5	1.0	1.3	7.4	23.9	5.2	14.9	4.23	239.62	16.1
F-26	10.5	2.0	1365	56.4	-11.1	46.2	95.3	110.8	1.5	1.4	7.7	23.9	3.6	13.9	4.34	237.08	14.6
F-27	10.5	2.0	1363	57.3	-12.9	47.8	99.1	114.0	3.1	1.8	8.6	24.6	1.0	12.8	4.46	228.15	12.9

Test	IMEP _g (bar)	IMAP (bar)	H ₂ Energy (J)	H ₂ Ratio (%)	Pilot Angle (CAD)	η_g (%)	η_{H_2} (%)	P_{\max} (bar)	P_{\max} Angle (CAD)	CoV IMEP _g (%)	MRRR (bar/CAD)	MFB ₁₀₋₉₀ (CAD)	CA ₁₀ (CAD)	CA ₅₀ (CAD)	NO _x (g/kWh)	CO ₂ (g/kWh)	Soot (mg/kWh)
F-28	10.5	2.0	1369	58.7	-14.7	47.2	97.2	117.1	3.2	2.0	8.4	24.4	-1.1	11.6	4.50	220.37	11.9
F-29	10.5	2.0	1368	58.2	-16.5	47.6	96.5	122.4	4.1	1.3	8.8	24.6	-3.3	10.3	4.70	221.31	11.3
F-30	10.5	2.0	1797	77.8	-7.5	48.4	100.3	108.9	2.2	0.9	7.0	24.7	4.6	14.7	3.66	155.47	10.9
F-31	10.5	2.0	1802	78.4	-9.3	48.5	100.0	112.1	4.8	1.2	7.7	25.6	2.6	13.2	3.85	150.73	10.2
F-32	10.5	2.0	1808	79.6	-11.1	48.1	99.8	116.8	7.6	1.6	8.2	25.1	0.6	11.3	4.11	141.56	9.4
G-1	12.5	1.5	0	0.0	-7.5	44.0	-	83.7	0.8	0.7	5.1	33.0	11.7	21.6	3.31	597.52	106.0
G-2	12.5	1.5	0	0.0	-9.3	43.5	-	84.0	-0.4	0.7	5.4	33.1	11.7	21.6	3.37	600.65	98.3
G-3	12.5	1.5	0	0.0	-11.1	43.5	-	84.1	-0.5	0.8	6.0	33.2	11.2	21.2	3.48	599.81	103.5
G-4	12.5	1.5	0	0.0	-12.9	43.4	-	83.8	-0.6	0.9	5.9	33.1	11.2	21.2	3.48	600.81	111.0
G-5	12.5	1.5	0	0.0	-14.7	43.5	-	83.6	-0.8	0.9	6.0	32.7	11.1	21.0	3.49	597.55	108.0
G-6	12.5	1.5	0	0.0	-16.5	43.6	-	83.5	-0.8	0.7	5.9	32.5	10.8	20.8	3.47	595.24	95.0
G-7	12.5	1.5	0	0.0	-18.3	43.6	-	83.2	-0.5	0.7	5.7	32.5	10.9	20.9	3.36	594.24	93.2
G-8	12.5	1.5	0	0.0	-20.1	43.7	-	83.2	-0.4	0.7	5.1	32.4	10.9	21.0	3.30	593.54	73.3
G-9	12.5	1.5	469	15.1	-7.5	44.3	65.9	84.7	1.1	0.8	5.3	34.7	11.2	20.8	3.28	479.90	107.6

Test	IMEP _g (bar)	IMAP (bar)	H ₂ Energy (J)	H ₂ Ratio (%)	Pilot Angle (CAD)	η_g (%)	η_{H_2} (%)	P_{\max} (bar)	P_{\max} Angle (CAD)	CoV IMEP _g (%)	MRRR (bar/CAD)	MFB ₁₀₋₉₀ (CAD)	CA ₁₀ (CAD)	CA ₅₀ (CAD)	NO _x (g/kWh)	CO ₂ (g/kWh)	Soot (mg/kWh)
G-10	12.5	1.5	457	14.6	-9.3	44.0	68.3	85.4	-0.1	0.8	6.0	34.7	11.0	20.7	3.35	481.58	103.1
G-11	12.5	1.5	464	14.6	-11.1	43.3	56.7	85.8	-0.1	0.9	6.5	34.8	10.4	20.2	3.45	481.95	130.1
G-12	12.5	1.5	475	15.0	-12.9	43.4	58.6	86.3	-0.4	0.9	6.9	34.4	9.9	19.9	3.56	480.38	116.4
G-13	12.5	1.5	476	15.0	-14.7	43.3	54.6	85.8	-0.7	0.8	6.8	34.0	9.8	19.8	3.57	481.40	114.6
G-14	12.5	1.5	473	15.0	-16.5	43.7	62.7	86.2	0.2	0.7	6.6	34.2	9.3	19.6	3.51	480.48	105.0
G-15	12.5	1.5	466	14.8	-18.3	43.5	55.5	86.6	0.3	0.7	6.3	34.1	8.9	19.5	3.41	477.42	100.3
G-16	12.5	1.5	915	30.1	-7.5	45.3	96.3	84.7	1.5	0.8	5.9	31.1	9.4	18.5	3.82	394.68	101.7
G-17	12.5	1.5	915	30.0	-9.3	45.0	94.1	85.5	1.1	0.7	6.4	31.3	8.4	18.0	3.89	391.56	87.4
G-18	12.5	1.5	914	29.7	-11.1	44.7	89.1	87.3	3.0	0.7	7.2	32.1	6.6	17.1	4.11	390.40	80.3
G-19	12.5	1.5	916	30.2	-12.9	45.1	89.4	88.9	5.4	0.7	7.6	32.6	4.6	16.4	4.19	385.00	63.3
G-20	12.5	1.5	914	30.2	-14.7	45.1	88.9	91.1	4.0	0.8	7.4	33.7	2.2	16.0	4.21	383.78	55.7
G-21	12.5	1.5	914	30.8	-16.5	46.0	95.7	93.9	4.3	0.7	7.3	34.2	-0.2	15.3	4.17	381.43	47.9
G-22	12.5	1.5	913	31.2	-18.3	46.3	96.3	96.9	3.6	0.6	6.8	34.8	-2.5	14.7	4.02	374.57	36.2
G-23	12.5	1.5	1358	46.3	-7.5	46.5	99.9	92.2	15.9	0.7	6.6	23.5	5.9	15.2	4.74	297.66	45.4

Test	IMEP _g (bar)	IMAP (bar)	H ₂ Energy (J)	H ₂ Ratio (%)	Pilot Angle (CAD)	η_g (%)	η_{H_2} (%)	P_{\max} (bar)	P_{\max} Angle (CAD)	CoV IMEP _g (%)	MRRR (bar/CAD)	MFB ₁₀₋₉₀ (CAD)	CA ₁₀ (CAD)	CA ₅₀ (CAD)	NO _x (g/kWh)	CO ₂ (g/kWh)	Soot (mg/kWh)
G-24	12.5	1.5	1360	46.5	-9.3	46.8	99.7	97.3	14.7	0.8	7.1	23.5	4.2	13.9	4.98	291.99	27.8
G-25	12.5	1.5	1360	47.3	-11.1	47.1	100.0	104.6	12.3	0.6	7.4	22.6	2.1	11.8	5.36	287.27	14.6
H-1	12.5	2.0	0	0.0	-7.5	47.3	-	105.8	0.3	0.6	4.9	24.4	11.2	20.5	3.47	566.72	31.0
H-2	12.5	2.0	0	0.0	-9.3	46.8	-	106.1	-0.8	0.7	5.7	24.6	11.2	20.5	3.52	565.82	31.8
H-3	12.5	2.0	0	0.0	-11.1	46.7	-	106.0	-0.2	0.7	6.4	24.5	10.7	20.0	3.62	563.58	31.9
H-4	12.5	2.0	0	0.0	-12.9	46.9	-	106.3	-1.0	0.8	7.0	24.3	10.6	19.9	3.67	560.68	32.3
H-5	12.5	2.0	0	0.0	-14.7	47.0	-	105.8	-0.6	0.8	7.1	24.2	10.7	20.0	3.63	557.68	30.3
H-6	12.5	2.0	0	0.0	-16.5	46.9	-	106.0	-0.6	0.7	7.3	24.4	10.5	19.9	3.64	558.26	30.2
H-7	12.5	2.0	0	0.0	-18.3	46.9	-	106.0	-0.8	0.6	7.2	24.3	10.5	20.0	3.59	558.60	29.8
H-8	12.5	2.0	0	0.0	-20.1	46.9	-	105.7	-0.4	0.6	6.6	24.0	10.7	20.1	3.49	557.78	29.3
H-9	12.5	2.0	466	15.9	-7.5	45.8	62.7	106.4	0.5	0.7	5.2	30.5	10.8	20.0	3.93	429.78	25.7
H-10	12.5	2.0	466	16.0	-9.3	46.1	66.1	106.9	-0.6	0.7	6.0	30.6	10.6	19.9	3.96	427.77	25.1
H-11	12.5	2.0	465	16.2	-11.1	46.7	77.9	107.3	-0.2	0.8	6.8	30.2	10.0	19.3	4.09	428.62	25.6
H-12	12.5	2.0	464	15.8	-12.9	45.7	56.5	107.5	-0.8	0.8	7.2	29.2	9.8	19.2	4.08	426.71	25.9

Test	IMEP _g (bar)	IMAP (bar)	H ₂ Energy (J)	H ₂ Ratio (%)	Pilot Angle (CAD)	η_g (%)	η_{H2} (%)	P_{max} (bar)	P_{max} Angle (CAD)	CoV IMEP _g (%)	MRRR (bar/CAD)	MFB ₁₀₋₉₀ (CAD)	CA ₁₀ (CAD)	CA ₅₀ (CAD)	NO _x (g/kWh)	CO ₂ (g/kWh)	Soot (mg/kWh)
H-13	12.5	2.0	464	15.8	-14.7	45.2	44.6	107.2	-0.3	0.7	7.5	28.4	9.7	19.2	4.05	425.35	23.7
H-14	12.5	2.0	465	15.9	-16.5	45.7	50.9	107.6	-0.4	0.7	7.6	28.6	9.5	19.1	3.97	423.22	24.6
H-15	12.5	2.0	473	16.2	-18.3	45.7	49.9	108.2	-0.1	0.7	7.6	27.6	9.2	19.0	3.87	420.06	23.7
H-16	12.5	2.0	472	16.1	-20.1	45.5	45.5	108.7	-0.1	0.6	7.2	27.1	9.0	18.9	3.67	420.34	22.7
H-17	12.5	2.0	913	30.9	-7.5	45.1	79.6	107.1	0.6	0.8	5.6	32.3	10.2	19.4	3.98	350.70	22.5
H-18	12.5	2.0	913	31.0	-9.3	45.4	82.2	107.9	-0.5	0.8	6.4	32.1	9.8	19.2	4.07	350.25	22.2
H-19	12.5	2.0	914	31.5	-11.1	46.3	88.1	108.6	0.2	0.8	7.3	31.4	8.9	18.5	4.21	349.16	22.1
H-20	12.5	2.0	913	31.3	-12.9	45.5	80.9	109.2	-0.2	0.9	7.9	30.1	8.2	18.0	4.34	349.10	21.6
H-21	12.5	2.0	915	31.1	-14.7	45.3	75.9	109.9	0.3	0.9	8.2	28.5	7.5	17.8	4.34	346.70	20.7
H-22	12.5	2.0	917	32.0	-16.5	46.2	84.2	110.6	0.5	0.8	8.2	27.7	6.6	17.3	4.30	341.66	19.7
H-23	12.5	2.0	1352	47.9	-7.5	47.0	90.1	108.4	1.1	0.8	6.4	22.0	7.8	16.6	4.15	265.09	16.6
H-24	12.5	2.0	1354	48.6	-9.3	47.5	92.6	109.2	1.3	0.8	7.1	22.7	6.7	16.0	4.18	262.35	15.9
H-25	12.5	2.0	1357	49.6	-12.9	47.7	94.0	114.6	3.5	0.8	8.7	25.5	1.5	13.8	4.65	256.60	13.4

5.4.1 Summary of Test Results

Throughout the load sweep between 4.5 bar IMEP and 12.5 bar IMEP, 6 major trends were noticed:

1. CO₂ and CO emissions were found to greatly decrease with increasing hydrogen replacement.
2. NO_x production was found to significantly increase with hydrogen replacement as compared to pure diesel operation.
3. An increase in the maximum pressure rise rate and maximum cylinder pressure was found to occur during hydrogen replacement.
4. At hydrogen air-fuel mixtures rich enough to allow premixed combustion, gross efficiency was similar to or better than pure diesel operation.
5. Particulate emissions were significantly reduced with increasing hydrogen replacement.
6. CA₁₀ and CA₅₀ were found to advance with hydrogen replacement, indicating that combustion was phased forwards in the cycle.

These trends will be explored in the following sections.

5.5 Cylinder Pressures

In this section the cylinder pressure and its derived primary metrics (maximum pressure rise rate and CoV IMEP) are explored. The cylinder pressures for the various Bins are given in the Figures 5.1 through 5.3. Within each Figure, the pilot injection advance is kept constant in order to illustrate the effects of hydrogen energy variation on the cylinder pressure curve.

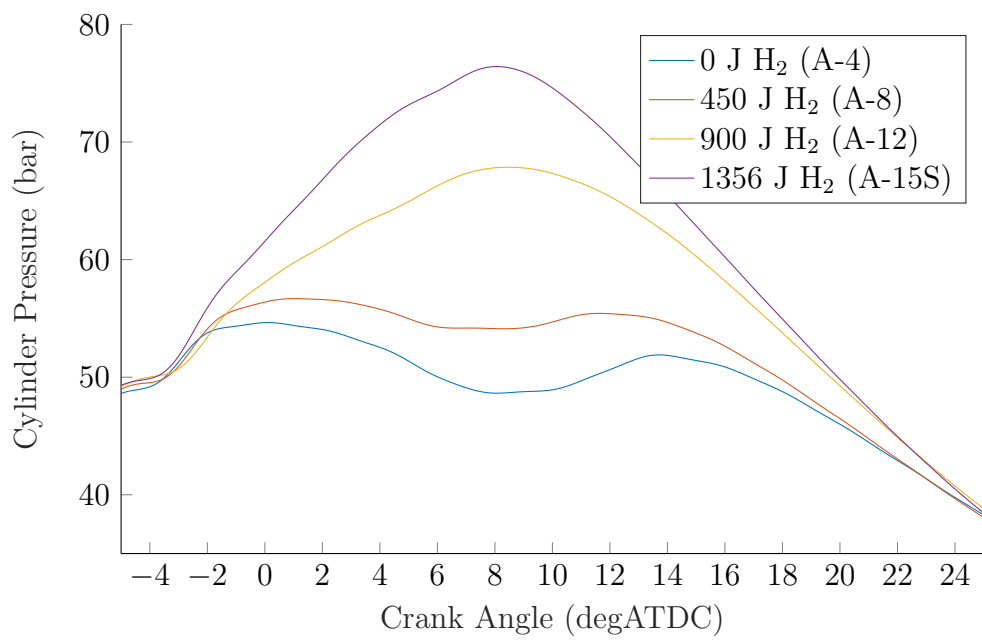


Figure 5.1: 600-cycle ensemble average of cylinder pressure traces from Bin A at an injection advance of -12.9 CAD pilot injection.

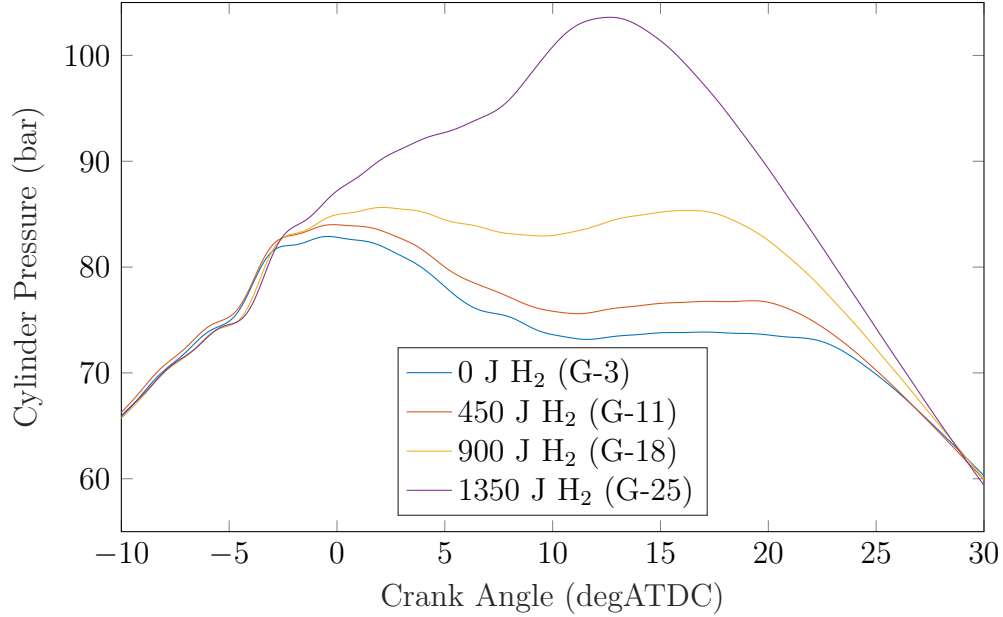


Figure 5.2: 600-cycle ensemble average of cylinder pressure traces from Bin G at an injection advance of -11.1 CAD pilot injection advance.

From Figures 5.1 and 5.3, it is evident that high hydrogen replacement and richer premixed air-fuel ratios result in the pressure trace shape transitioning from features of diffusion flame combustion to premixed flame combustion. This would be consistent with the propagation of a premixed flame with a sufficiently rich hydrogen air-fuel mixture. The start of combustion timing is linked to the ignition of the pilot diesel injection and its timing advance, with higher peak pressures with advanced timing being noticeable with higher hydrogen replacement.

It is evident that the excess air ratio plays a large part in the peak combustion pressure and the overall shape of the combustion trace when combusting hydrogen. For instance, when comparing Bins G (Figure 5.2) and H (Figure 5.3), which ran the same loads, Bin H with the higher intake pressure resulted in hydrogen combustion with significant constant-pressure combustion characteristics. However, Bin G, with the lower intake pressure, resulted in a peaky combustion trace, more similar to premixed-flame combustion.

Different (or oscillating) modes of combustion were not readily observed during the conventional dual-fuel tests. Combustion would generally occur in a similar progression each cycle, with the exception of occasional knock or preignition cycles in some

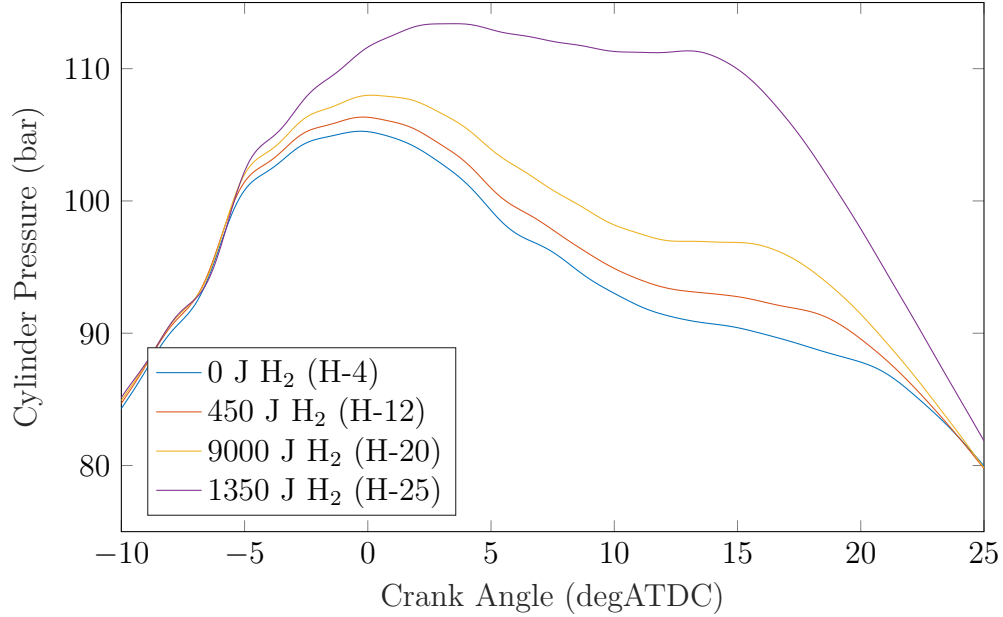


Figure 5.3: 600-cycle ensemble average of cylinder pressure traces from Bin H at an injection advance of -12.9 CAD pilot injection advance.

cases. Figure 5.4 give examples of the mean, minimum and maximum pressure traces that were achieved at certain test points. Higher hydrogen replacement was observed to create larger maximum bounds in cylinder pressure.

An example of the maximum pressure rise rate (MPRR) for the Bins is presented in Figure 5.5. The most notable pattern is a general increase in the MPRR with both increasing hydrogen replacement and increasing pilot injection advance. High MPRR presents a limiting factor on engine operation, as a higher MPRR results in thinner gas boundary layers and greater heat transfer to the cylinder walls [27], which in turn causes hotter and weaker engine components. However, with high injection advances, MPRR can be seen to reverse its increasing trend at a pilot injection advance around -18 CAD. This is likely due to changes within the diesel pilot spray combustion, as the trend occurs in pure diesel trials. Similar results have been reported where in pure-diesel combustion, where if the main injection begins when the pilot injection is burning in a premixed-flame like state, MPRR can decrease [117].

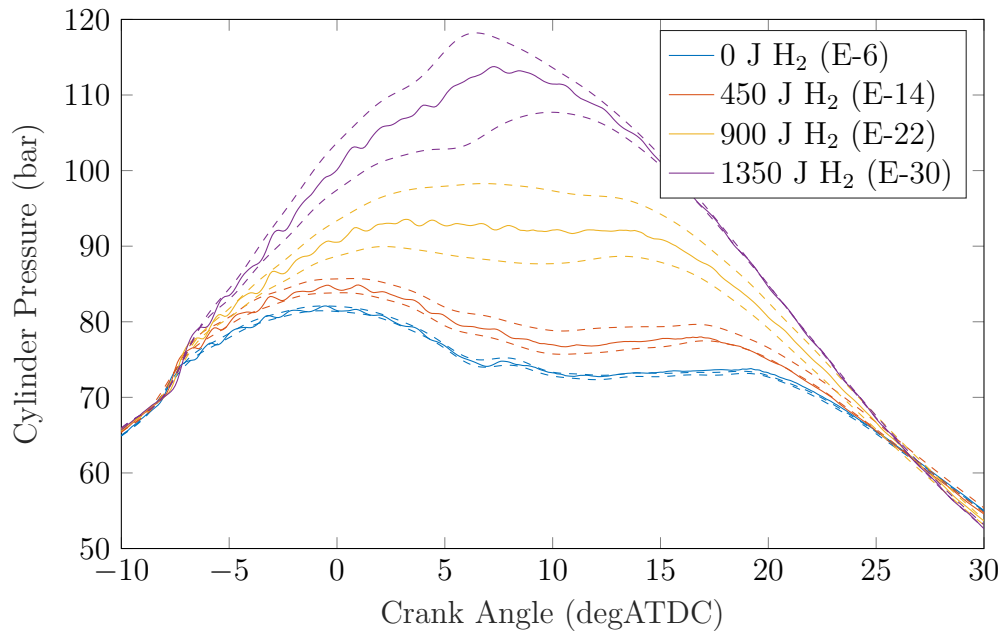


Figure 5.4: Maximum and minimum cylinder pressure traces from selected Bin E trials.

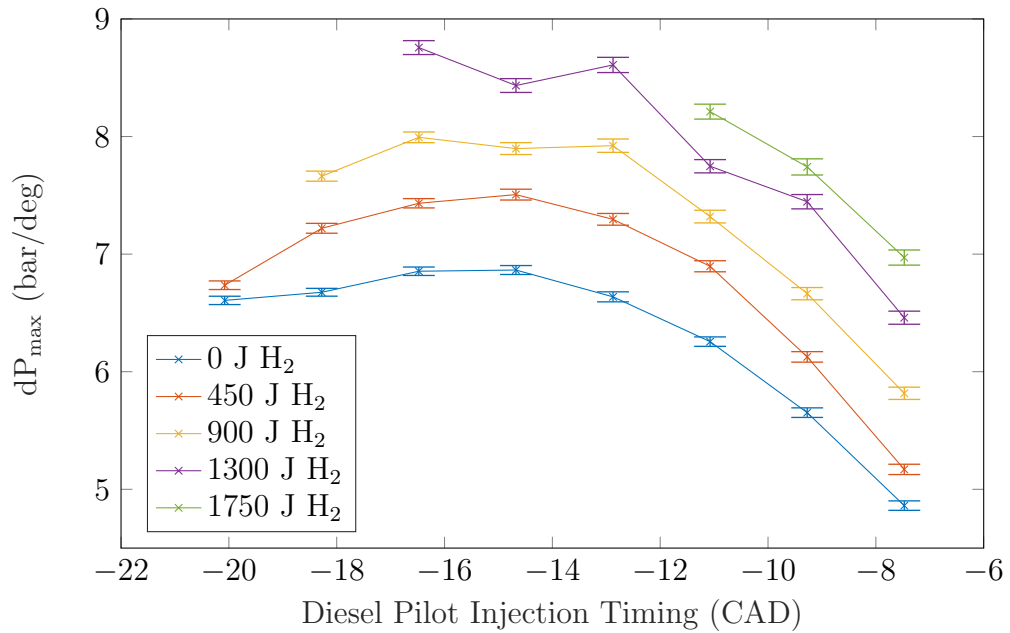


Figure 5.5: MPRR for the Bin F trials.

In order to investigate the stability of the cylinder pressure, plots for the coefficient of variance (CoV) of the engine's IMEP_g are presented in Figures 5.6 and 5.7. At high loads (Figure 5.7), the hydrogen-diesel CoV can be seen to be extremely similar to pure diesel combustion, regardless of the hydrogen replacement energy. This indicates that combustion is stable at high loads, even at operating conditions where the hydrogen mixture is too lean to support premixed flame propagation.

Bin A (Figure 5.6) shows evidence of a different trend: initially, as the hydrogen replacement increases, the CoV increases as compared to diesel. However, as hydrogen replacement reaches its largest values, the CoV begins to retrace towards the diesel CoV (and becomes better than diesel). This pattern would give evidence that the fuel-air equivalence ratio has a significant effect on the CoV of IMEP_g, similar to conventional premixed SI combustion. In SI combustion, mixture too lean to support normal premixed flame propagation result in higher CoV's as the mixture's burned fraction varies significantly cycle-to-cycle [118]. This would explain the pattern evidence in Bin A: initially, as hydrogen is introduced, the CoV becomes worse, as the hydrogen is unable burn with a vigorous premixed flame at a lean air-fuel mixture. However, the hydrogen concentration reaches a crossover point in Bin A at an energy replacement greater than 900 J, and the premixed flame can progress throughout the cylinder normally as the hydrogen mixture passes the lean misfire limit. In the Bins with higher load (Figure 5.7), the diesel can entrain a significant amount of the hydrogen within the cylinder, reducing the effects of non-vigorous premixed flame propagation at lower hydrogen replacement and reducing the magnitude of CoV as compared to the lower load trials.

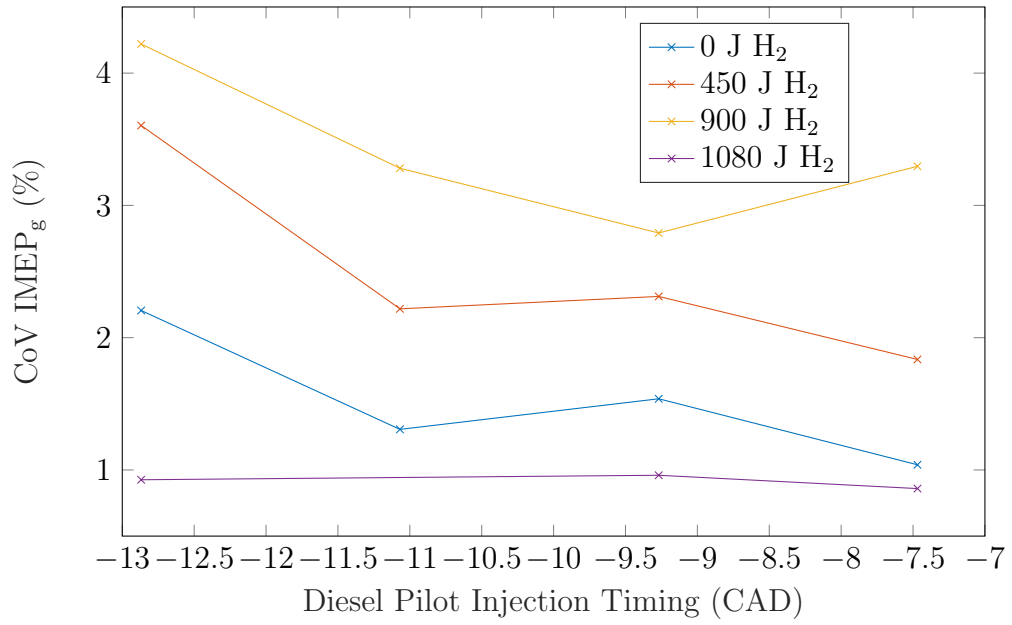


Figure 5.6: CoV of IMEP_g for the Bin A trials.

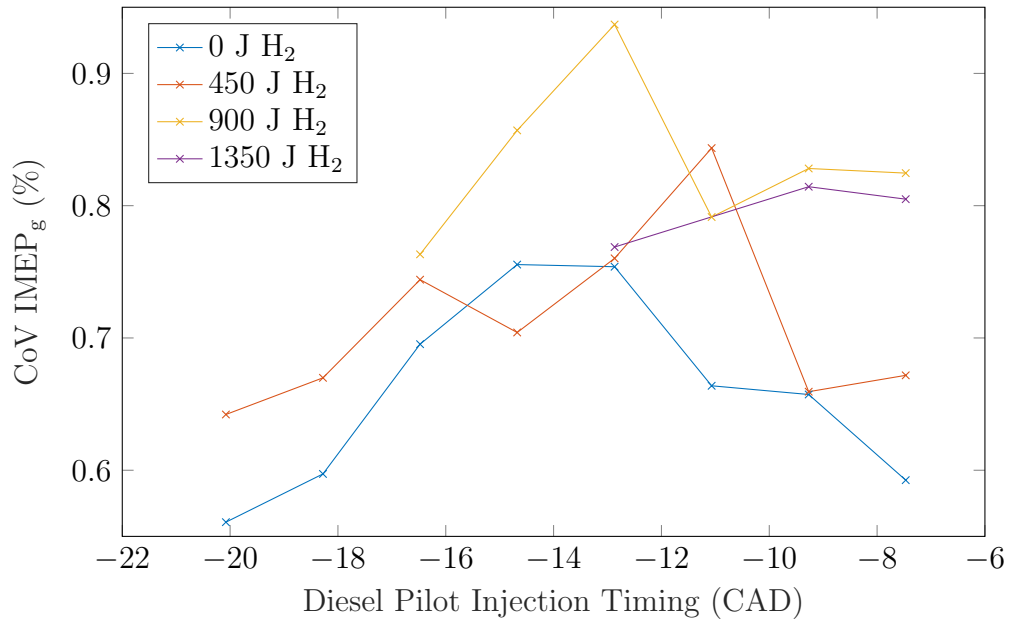


Figure 5.7: CoV of IMEP_g for the Bin H trials.

5.6 Engine Efficiency

In this section, engine efficiencies (include the gross efficiency and combustion efficiencies) are explored. Two examples of the gross cycle efficiency can be seen in Figures 5.8 and 5.9:

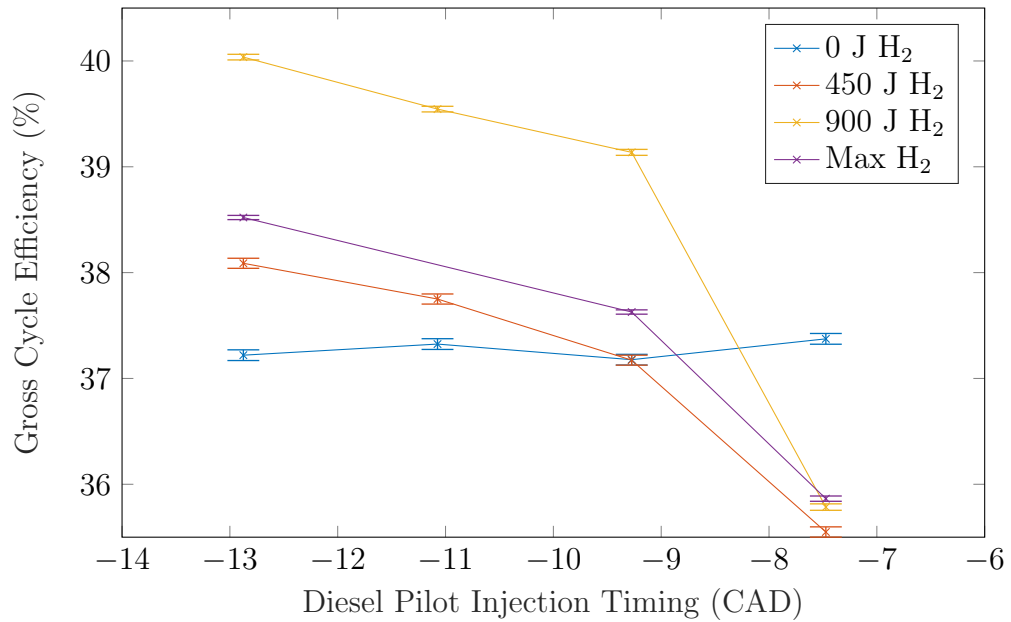


Figure 5.8: Gross engine efficiency of the Bin A trials.

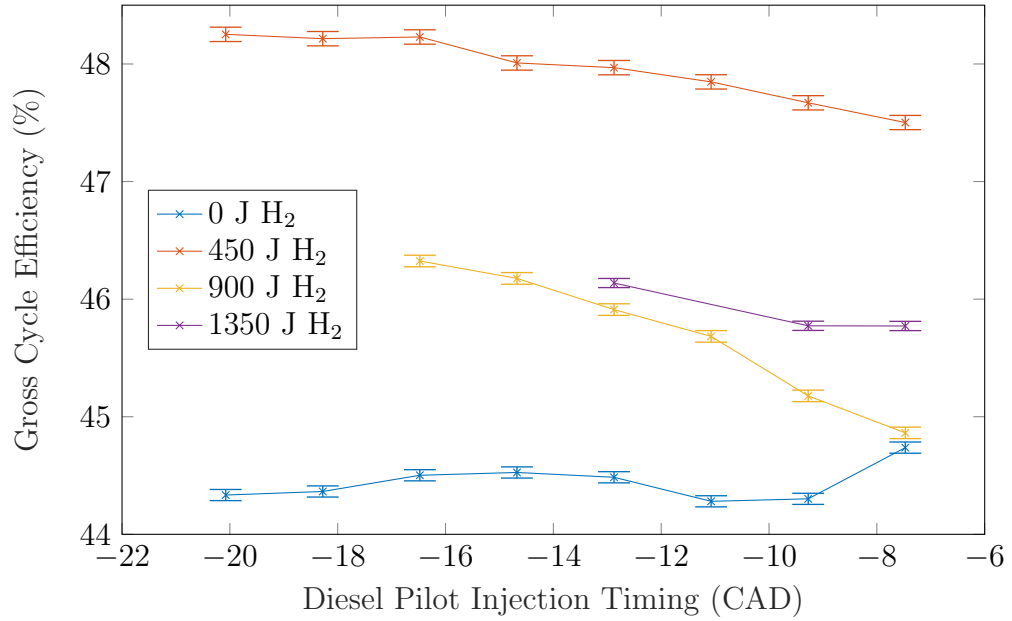


Figure 5.9: Gross engine efficiency of the Bin H trials.

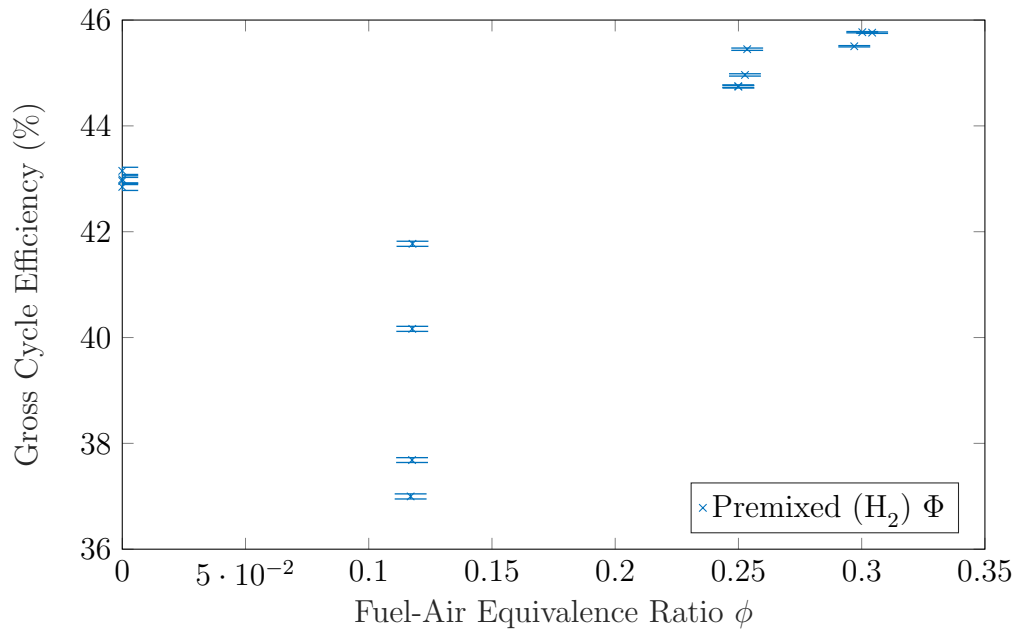


Figure 5.10: Gross engine efficiency of the Bin A trials plotted against the cylinder hydrogen-air equivalence ratio, including pure diesel trials.

Of note is the low gross efficiency at low loads with low hydrogen replacement (Figure 5.8). The efficiency loss is due to high hydrogen slip. This slip is partially driven by the lean premixed air-fuel ratio inherent at low loads, which causes a non-vigorous premixed flame (or at very lean ratios, no premixed flamefront). Once a sufficient amount of hydrogen has been replaced, premixed combustion can occur and the low efficiency trend reverses. For hydrogen combustion, the lower limit for premixed flame propagation is expected to be around $0.2 \leq \phi \leq 0.4$, dependent on cylinder charge turbulence and engine design [119–121]. This limit associates well with the observed premixed equivalence ratio where gross indicated efficiency begins to increase.

When the premixed flamefront cannot progress quickly, the entrainment of hydrogen by the diesel spray becomes more significant to allowing the combustion of hydrogen. However, at low loads the diesel injection is relatively short, and thus less of the hydrogen mixture can be entrained in the spray and combusted. This explains why the low hydrogen replacement tests in the Bin A (Figure 5.8) trials have a low efficiency compared to the Bin H trials (Figure 5.9), despite having similar hydrogen replacement energies. The Bin H diesel injections are significantly longer due to the higher engine load, therefore more of the hydrogen can be entrained by the diesel spray within the cylinder.

The effect that the hydrogen-air equivalence ratio has on the gross efficiency of the Bin B trials is presented in Figure 5.10. Gross efficiency can be seen to fall until $\phi \approx 0.2$ (Max H₂ trials. trials), where an increase in gross efficiency can be seen for all pilot injection cases as compared to the 900 J H₂ trials. This represents a reversal of the trend present from the pure diesel trials to the 900 J trials, where gross efficiency can be seen to fall. This reversal correlates well the hydrogen lean flammability limit.

At lower loads, the lack of heat in the cylinder also allows hydrogen to escape combustion by having a too low temperature for combustion to occur [40]. Mediating these issues could potentially allow for lower amounts of hydrogen to be injected while maintaining gross efficiency, or to allow lower-load engine operation. Both the low cylinder temperature and the overly lean premixed air-fuel ratio could be improved by richening the air-fuel mixture, which would likely be done by throttling as per classical SI engines. Other methods such as increasing the intake charge temperature

or increasing the EGR fraction could also help to increase the initial temperature of the charge [39]. Stratification of the hydrogen charge could also be used to create a local rich zone (thus requiring less or no intake throttling with its associated efficiency loss), however significant stratification requires for hydrogen to be directly injected into the cylinder. Stratified injection strategies allow for lower slip and higher cycle efficiency [122], at the cost of higher NO_x output.

5.6.1 Combustion Efficiencies

The combustion efficiency of an engine is a major contributing factor the engine's indicated efficiency. Combustion efficiencies lower than unity indicate that fuel is able to escape the cylinder without combusting (or only partially oxidized), reducing thermal efficiency. For hydrocarbon-based fuels, fuel in the exhaust stream is also a controlled emission. As such, operating points that maximize combustion efficiency are highly important to operate a clean and efficient engine.

The hydrogen combustion efficiency is plotted below (Figures 5.11 and 5.12). The presented combustion efficiency is purely that of the inducted hydrogen gas, and the diesel combustion efficiency is separated using exhaust gas analysis of the combustion products. Hydrogen combustion efficiency is not only effected by the engine load, but intake pressure/mixture air-fuel ratio. Leaner hydrogen air-fuel mixtures were found to negatively impact efficiency when these mixtures were close to or leaner than the lean flammability limit. This was the most important factor in ensuring high combustion efficiency. Higher loads were found to improve combustion efficiency while operating in this lean mixture range, however the higher load was still unable to compensate for the lack of a premixed flame front and hydrogen combustion efficiency was significantly reduced as compared to cases where a flamefront could be maintained. The correlation of generally higher hydrogen combustion efficiency and higher loads is in agreement with existing literature [33, 40].

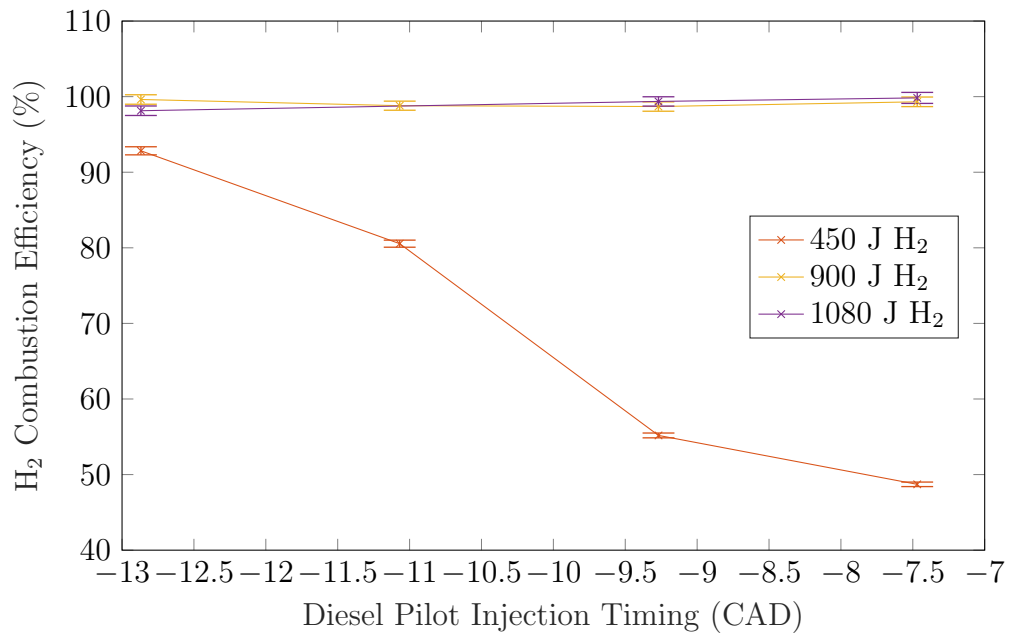


Figure 5.11: H₂ combustion efficiency of the Bin A trials.

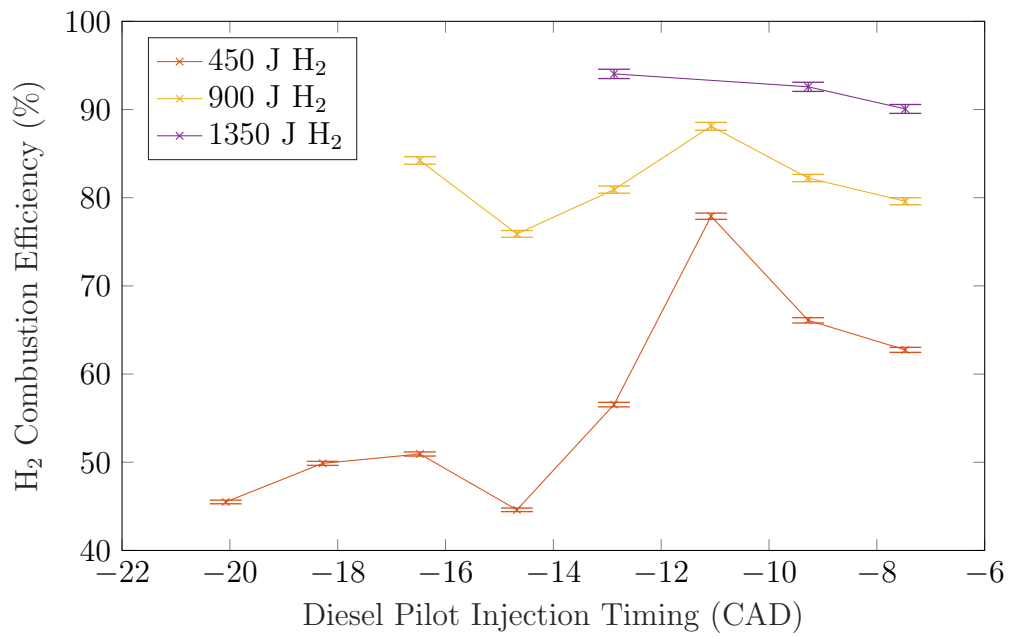


Figure 5.12: H₂ combustion efficiency of the Bin H trials.

At high loads (Bins G and H), the hydrogen combustion efficiency is observed to be above 60% at all points. This indicates that either the diesel spray is able to entrain a significant amount of the mixture at high loads, a premixed flamefront can burn through a significant portion of the mixture (in the cases of the higher replacement tests), or that the temperature within the cylinder is sufficient in order to cause oxidation of more hydrogen. From Bins A and H (Figures 5.11 and 5.12), there is some evidence that higher pilot advancement can result in a greater hydrogen combustion efficiency. For instance, in the 450 J and 1350 J bins, respectively, combustion efficiency can be seen to improve as the pilot injection advances. This would correlate well with existing literature that suggests higher in-cylinder temperatures is helpful to reduce hydrogen slip [39]. Greater pilot advancement would mean an earlier start of combustion, and thus higher cylinder pressures and temperatures near TDC. This would indicate that a higher peak gas temperature in-cylinder is beneficial for increasing hydrogen combustion efficiency, and also gives a relatively simple control method to adjust this temperature. However, pilot advancement is limited by knock and maximum pressure rise rate, so it may not be effective in all circumstances.

The diesel combustion efficiency for Bin F is given below in Figure 5.13. The diesel combustion efficiency was separated from the hydrogen combustion efficiency by exhaust gas analysis of non-oxidized hydrocarbons and partially oxidized species.

At high loads (Bins G and H), the diesel combustion efficiency with hydrogen replacement is observed to remain similar to trials with no hydrogen replacement. However, at low loads (and especially load points where a single diesel injection strategy is used) diesel combustion efficiency is observed to decrease significantly (Bins A and C). It is important to note that instrument measurement instability was reported for the diesel for trials A-13-S through A-15-S and C-17-S through C-20-S, so these low diesel combustion efficiency readings may simply be an artifact from measurement. There is also a decrease in diesel combustion efficiency with high hydrogen replacement as compared to low hydrogen replacement throughout most Bins (which can also be observed in Figure 5.13). Similar results have been reported running dual fuel [123], which attributed lower diesel combustion efficiency to the presence of hydrogen negatively effecting diesel combustion.

The overall combustion efficiency is related to the ratio of the heating value of

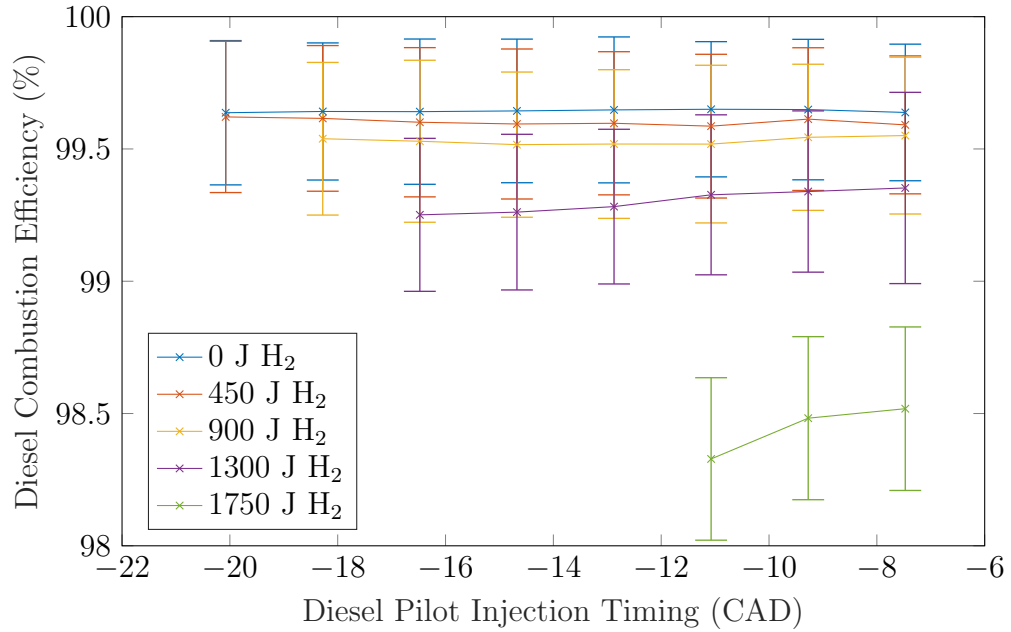


Figure 5.13: Diesel combustion efficiency of the Bin F trials.

the partially and non-oxidized exhaust products to the inputted fuel energy. Thus, points with low hydrogen combustion efficiency may still have an acceptable overall combustion efficiency if the hydrogen replacement was relatively low at that operating point. The overall combustion efficiency for Bin F is shown in Figure 5.14. Overall combustion efficiency can be seen to remain high in Bin F, provided that a high hydrogen replacement value is used. The lower combustion efficiencies with lower replacement correlate to the mixture being unable to support a premixed flame, thus having higher hydrogen slip.

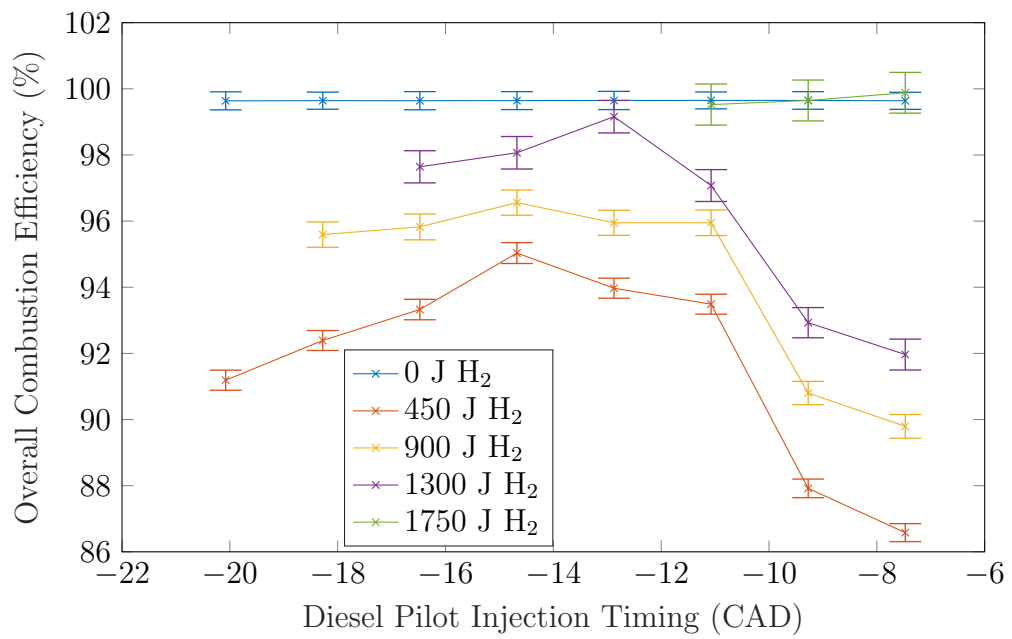


Figure 5.14: Overall combustion efficiency of the Bin F trials.

5.7 Engine Emissions

The engine-out emissions profile was found to be significantly effected by hydrogen. In this section, the NO_x , particulate, CO_2 , CO , and non-methane uHC emissions will be investigated.

5.7.1 NO_x emissions

Oxides of Nitrogen (NO_x) are emissions caused by the oxidation of N_2 under the high temperatures and pressures that are present in-cylinder during combustion. Higher cylinder temperatures result in greater NO_x production. As such, they are expected to be increased by the pressure and temperature rises associated with premixed combustion. However, the stratified combustion of the diesel injection coupled with the homogenous premixed hydrogen combustion makes the combustion process significantly more complicated than an engine undergoing only one of these processes. The NO_x emissions of the engine, for Bins C and F, is provided in Figures 5.15 and 5.16:

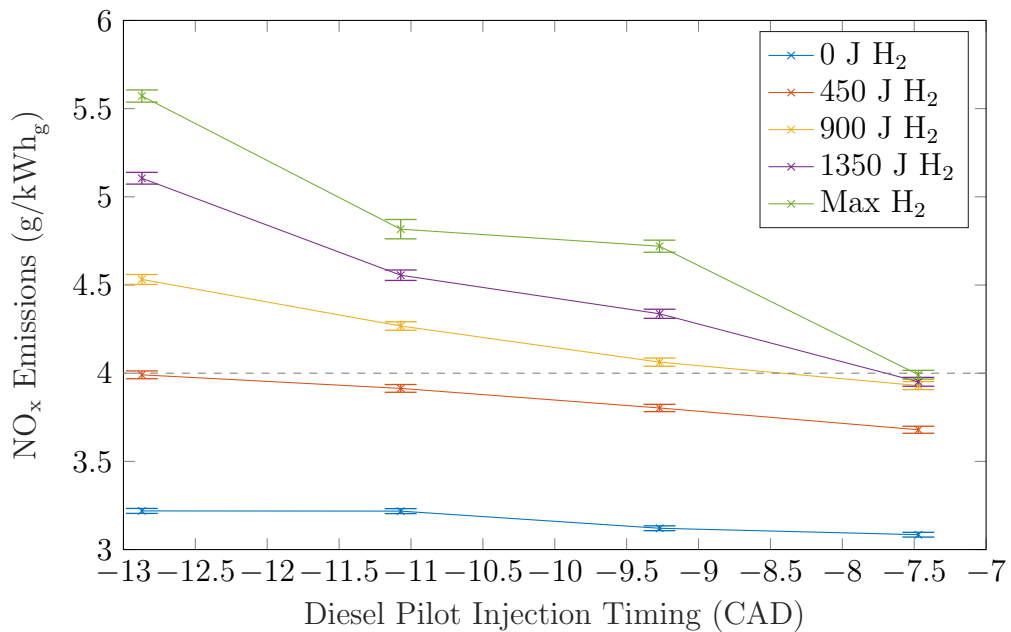


Figure 5.15: NO_x output for the Bin C trials, with EPA Tier 3 Offroad Standard threshold.

Of note is the general trend in each Bin where the NO_x emissions of the engine can be seen to increase with increasing hydrogen addition. The excess air ratio plays

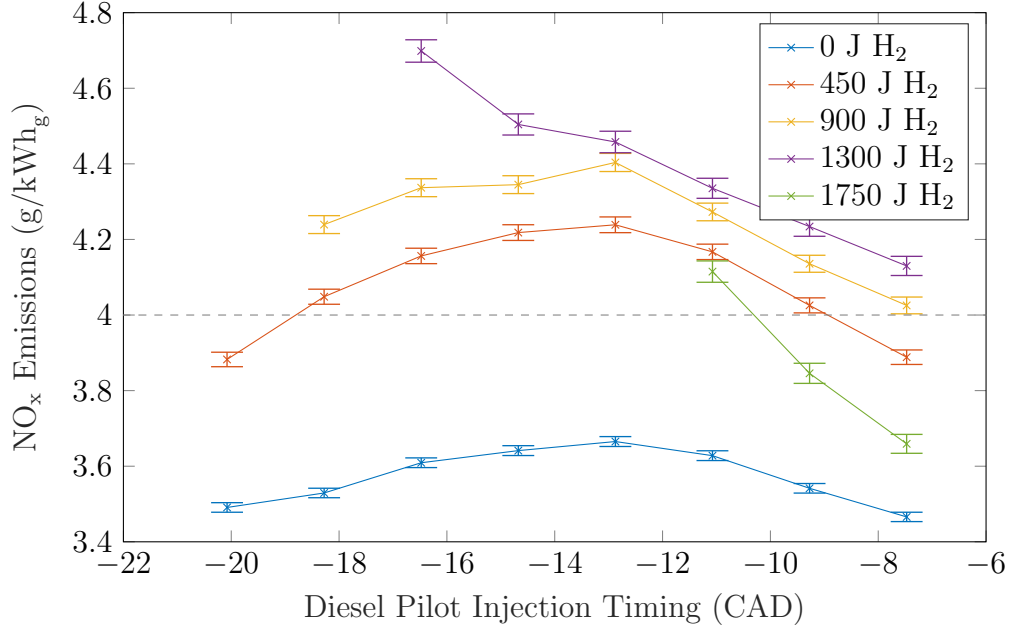


Figure 5.16: NO_x output for the Bin F trials, with EPA Tier 3 Offroad Standard threshold.

a large role in the NO_x emissions, which can clearly be seen in the differences in the emissions between Bins E and F, where the higher intake pressure in Bin F correlates in a reduction in NO_x production across all hydrogen trials compared to Bin E with the same replacement values. This is closely coupled with the in-cylinder temperature, which at temperatures above 1800 K can result in higher NO_x formation [57], and increasing NO_x rates with higher temperatures beyond this [58].

Some outliers from this trend can be seen at high replacement values. For instance, in Bin F (Figure 5.16), the NO_x output of the engine decreases when moving to the highest replacement H₂ trials versus the second highest (however this number is still greater than the pure diesel NO_x output). This phenomena could possibly be explained by a reduction in hotspots, likely due to changes in the diesel injection spray coupled with a relatively lean hydrogen premixed air-fuel ratio. It could also be explained by slow premixed flame propagation, which would result in lower peak temperatures in-cylinder, thus less NO_x formation.

The NO/NO_x molar ratio of the NO_x emissions, on a molar basis from Bin H, is provided in Figure 5.17. NO₂ can be formed by various methods, however its formation is more prevalent with lower combustion temperatures [124]. This means that

NO₂ is generally formed during the expansion stroke of the engine or along the periphery of the diesel spray in conventional diesel engines [125]. NO₂ contributes more to NO_x emissions due to its higher molar mass, however higher NO₂ concentrations are advantageous to diesel aftertreatment and diesel oxidation catalysts are often designed to promote NO₂ formation in the exhaust stream before the DPF and SCR modules [126, 127].

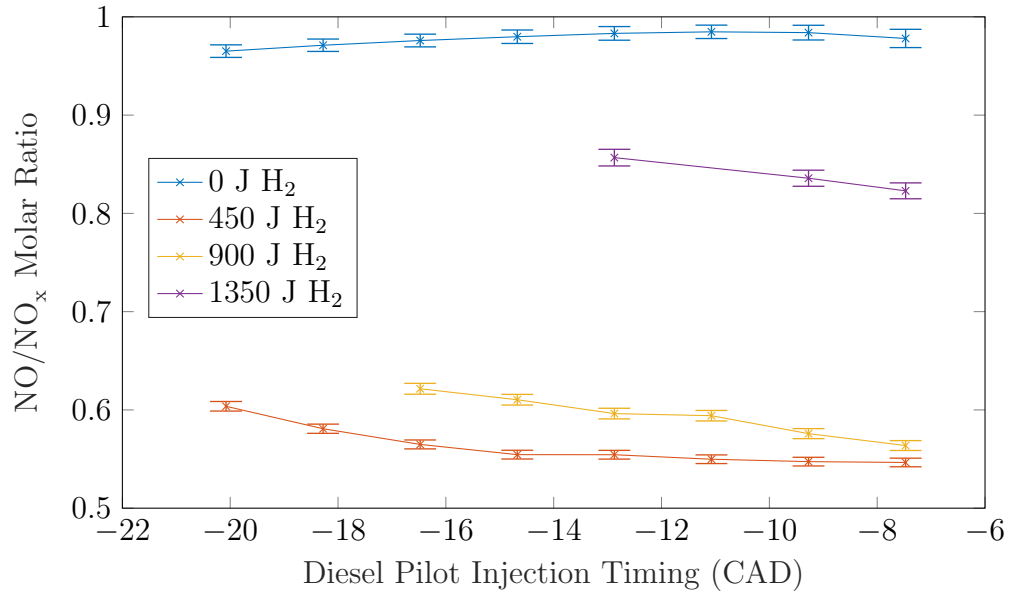


Figure 5.17: NO/NO_x molar ratio from the Bin H trials.

It can be seen from Figure 5.17 that conditions with low premixed air-fuel ratios result in NO to NO₂ ratios closer to unity. This has been seen before in previous hydrogen-diesel engine research [128]. The high NO₂ production can be explained by Hydrogen catalyzing the oxidation of NO to NO₂ via the HO₂ radical mechanism. Leaner air-fuel ratios result in either incomplete combustion or a longer residence time of uncombusted hydrogen in-cylinder due to a slower flame speed and burn rate, thus explaining the relationship. The HO₂ radical mechanism progresses significantly faster at lower temperatures combined with rapid gas cooling [125], meaning that to catalyze the mechanism free hydrogen must exist in the cylinder during the expansion stroke.

The NO/NO₂ ratio is of importance for SCR aftertreatment operation. An even ratio of NO to NO₂ results in the fast NO_x reaction being able to be used to reduce NO_x to atmospheric nitrogen in the SCR, which results in an efficient and rapid reduction of NO_x [129]. Ratios of NO to NO₂ that deviate from this ratio result in NO_x reduction reactions with slower rates and thus lower SCR efficiency. As such, despite hydrogen resulting in greater engine NO_x output, tailpipe NO_x emissions may be reduced compared to pure diesel when running conventional aftertreatment systems. Conventional common-rail diesel engines with aftertreatment often feature a relatively high pilot advance (usually ranging from 20 to 35 CAD), partially to promote a higher fraction of NO₂ in the exhaust stream, as can be seen in Figure 5.17.

In conclusion, running dual-fuel hydrogen-diesel results in higher engine-out NO_x emissions than pure diesel operation. However, a greater fraction of NO₂ is produced as compared to conventional diesel combustion. This may prove useful and reduce NO₂ concentration post-aftertreatment with conventional diesel aftertreatment systems as compared to diesel engines, however more research is required to explore this.

5.7.2 CO₂ Emissions

The CO₂ emissions of the engine, for Bins C and G, is provided in Figures 5.18 and 5.19. CO₂ emissions can be seen to be highly coupled to the hydrogen replacement amount, as hydrogen directly displaces diesel in the combustion process and means

less carbon is introduced to the cylinder. The CO_2 emissions are also related to the cycle efficiency, as a higher cycle efficiency would result in a lower amount of fuel consumed, thus less diesel being required for the same amount of work.

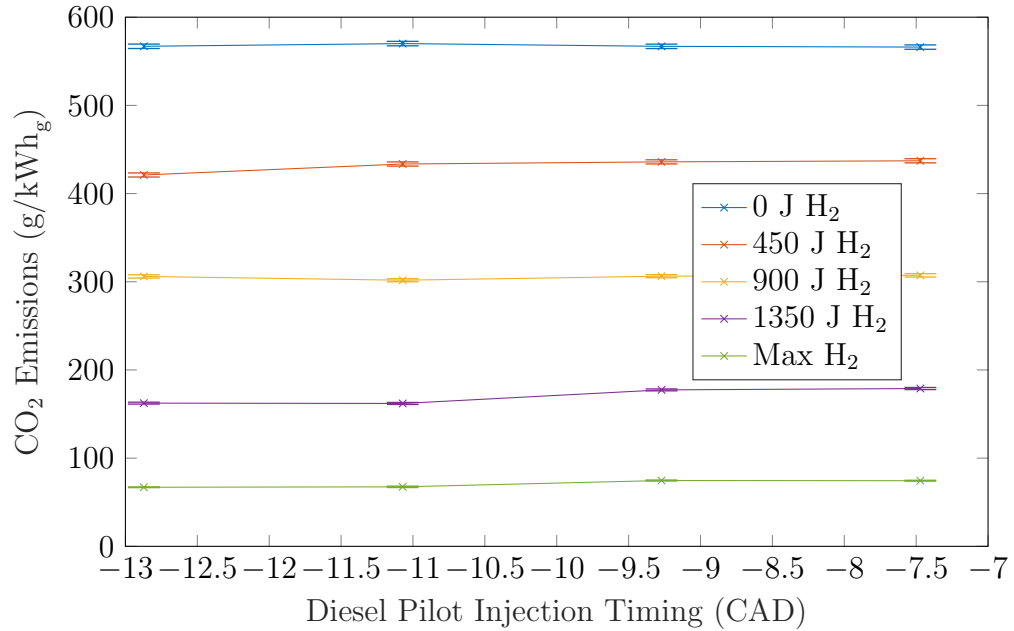


Figure 5.18: CO_2 output for the Bin C trials.

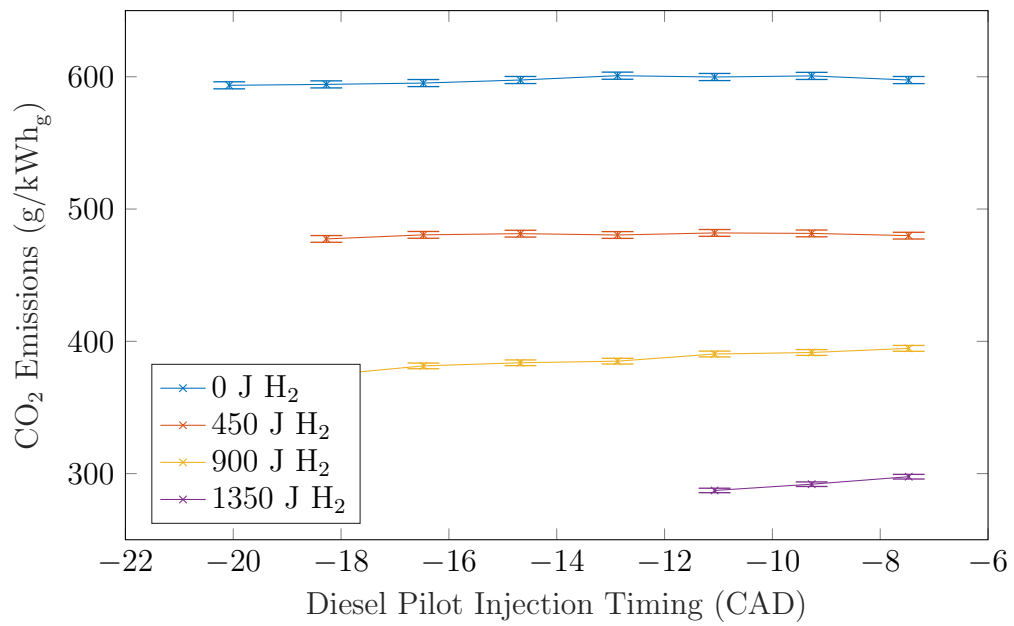


Figure 5.19: CO₂ output for the Bin G trials.

As can be seen, hydrogen replacement is highly effective at offsetting engine out CO₂ emissions. As load increases (Figure 5.19), the maximum CO₂ reduction can be seen to decrease. This was due to the knock and maximum pressure rise rate limits being reached with high hydrogen replacement. The maximum hydrogen induction into the cylinder was limited to 1750 J, with a dependence upon the excess air ratio. This means that as the load increased, the maximum fraction of hydrogen energy to fuel energy decreased. At an engine load of 7.5 bar IMEP (Figure 5.18), a CO₂ output 67 g/kWh was achieved, showing a significant reduction in the greenhouse gas emissions of the engine while running hydrogen. It is possible the exhaust gas recirculation (EGR) may help to further improve the maximum hydrogen replacement value, as EGR has been used in hydrogen engines to improve engine knock resistance at lower excess air ratios, and has been used in dual-fuel hydrogen diesel engines before [39, 63, 130].

5.7.3 Particulate Emissions

A representative example of the engine particulate emissions is provided in Figure 5.20 . Particulate emissions can be seen to drop significantly with increasing hydrogen enrichment. This is expected not only due to the reduction in diesel delivered to the cylinder (physically reducing the amount of fuel able to produce particulates), but also the higher temperature cylinder conditions that are associated with premixed flame propagation.

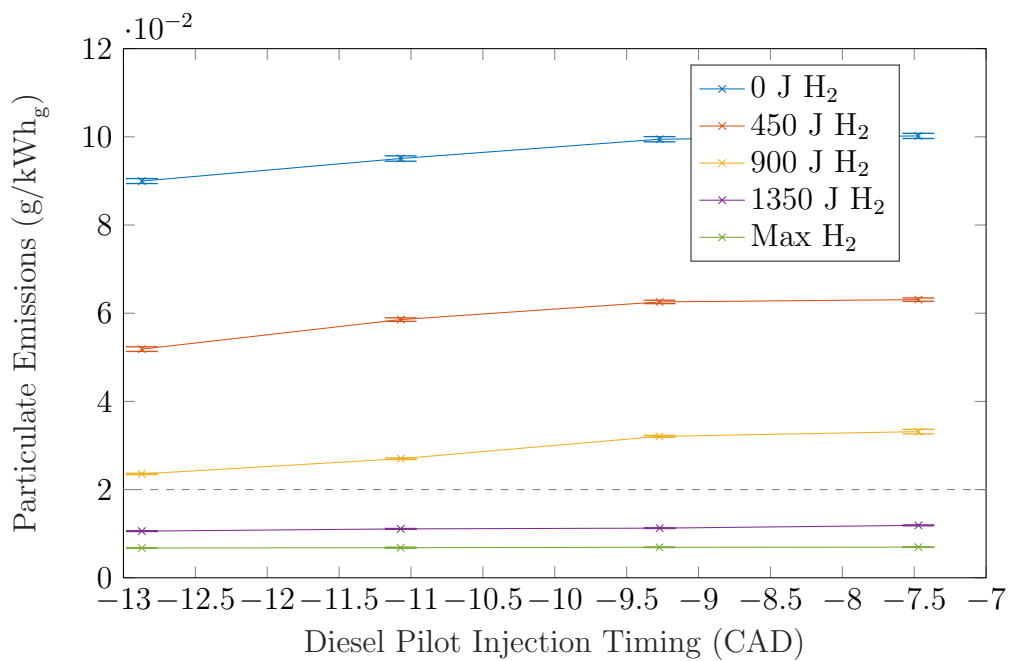


Figure 5.20: Particulate output for the Bin C trials, with EPA Tier 4 Offroad Standard threshold.

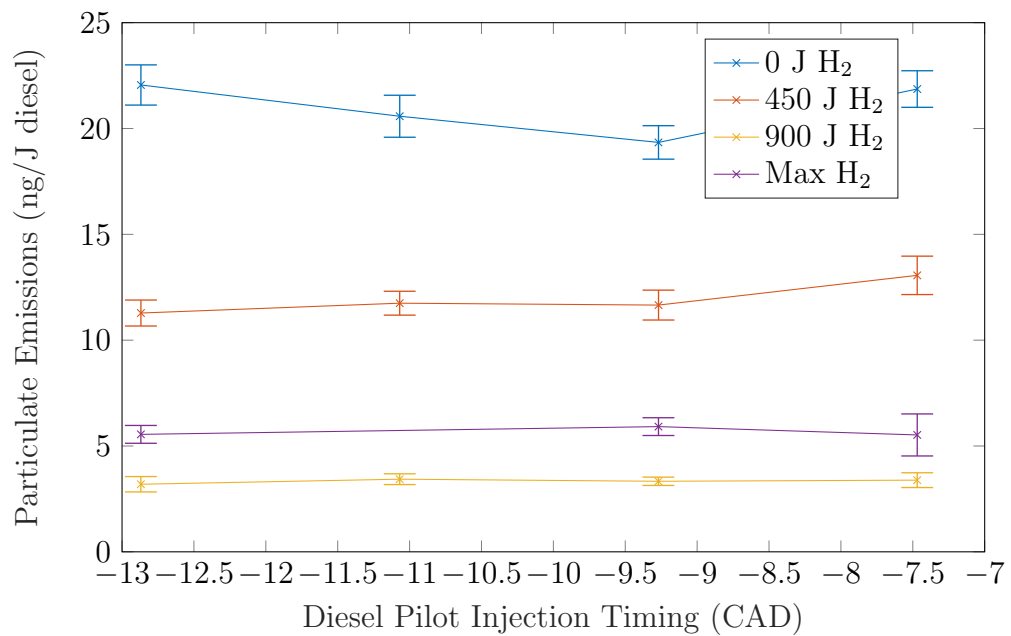


Figure 5.21: Particulate emissions output per Joule of diesel for the Bin C trials. Max H₂ trials are run with a single diesel injection.

The high reduction in particulate output presents an option for pursuing new aftertreatment strategies as compared to conventional diesel engines. At operating points with high hydrogen replacement, EPA Tier 4 Offroad particulate emissions standards of 0.02 g/kWh [131] were able to be met in the test grid. This may mean dual fuel engines could run without particulate aftertreatment and only with an NO_x aftertreatment system, which would help to reduce both engine cost and running costs associated with DPF maintenance. Lower particulate concentrations may also have a net positive effect on engine maintenance by reducing the mass of particulate that is recirculated through the engine via the EGR system, as particulate is known to be a major cause of diesel engine wear [132, 133].

Of note is the impact of the diesel injection duration on particulate formation. At low injection durations, a diesel injection spray pattern may be less atomized due to lower cylinder temperatures and pressures reducing the lean flame out region size [134]. This results in more particulate nucleation sites from fuel-rich droplets in the spray core [134]. When looking at trials that run a single diesel injection, the amount of particulate produced per Joule of diesel injected can be seen to mildly increase as compared to multiple injection tests where more diesel is injected at longer durations (Figure 5.21). This indicates a negative impact in the diesel combustion process either due to low injection duration or interactions with hydrogen gas.

5.7.4 CO Emissions

Although not normally present in significant quantities in diesel exhaust emissions due to high temperatures and high excess air ratios, CO emissions indicate incomplete combustion of hydrocarbons is occurring, and that energy is being lost. Additionally, CO is a highly toxic pollutant which can cause severe harm to human health. The CO emissions for Bin C is provided in Figure 5.22:

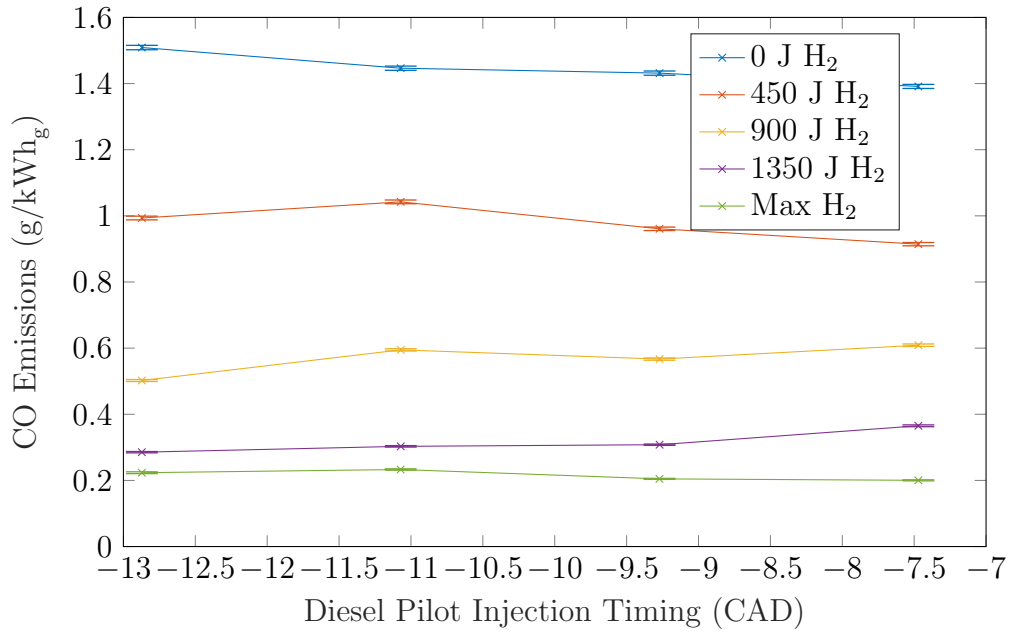


Figure 5.22: CO output for the Bin C trials.

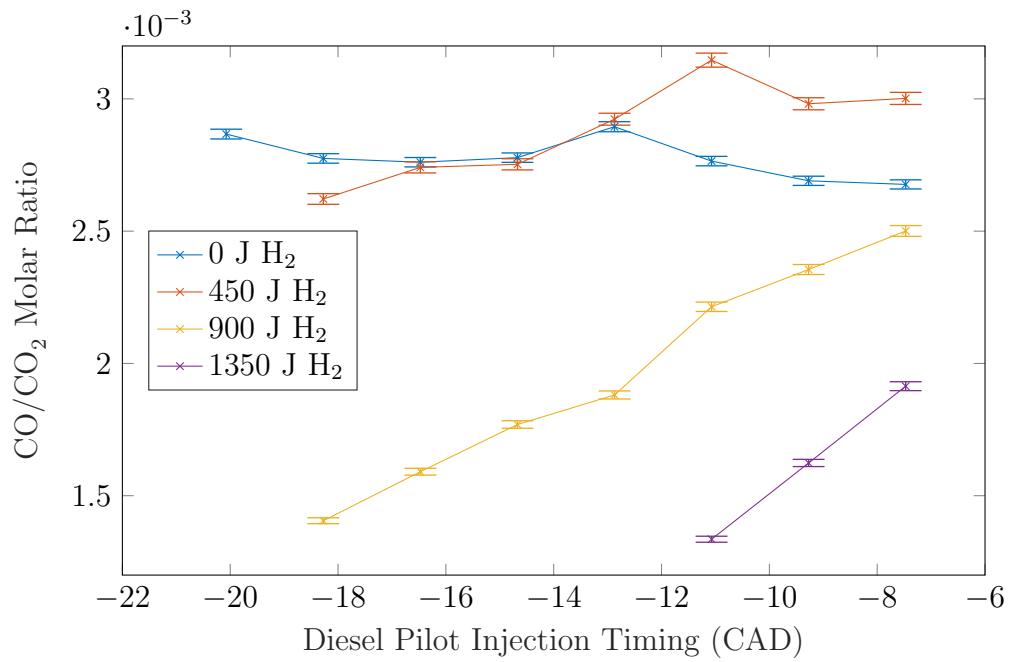


Figure 5.23: Ratio of CO to CO₂ output for the Bin G trials.

CO was seen to fall with increasing hydrogen replacement, as expected due to the reduction in diesel fuel. CO creation is also less preferential than CO₂ when dual fuel combustion is occurring with very high hydrogen replacement rates as compared to pure diesel combustion (Figure 5.23).

5.7.5 Unburnt Hydrocarbon Emissions

The UHC emissions for Bins A and F is provided in Figures 5.24 and 5.25. UHC is presented as non-methane unburnt hydrocarbons (NMHC) for comparison to EPA offroad emissions standards.

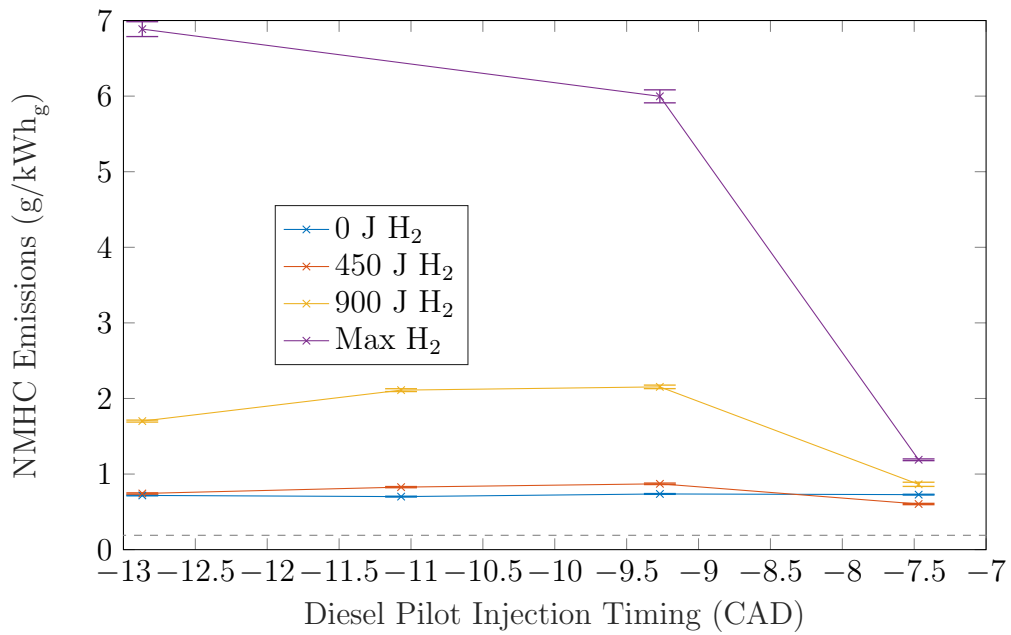


Figure 5.24: NMHC output for the Bin A trials, with EPA Tier 4 Offroad Standard threshold.

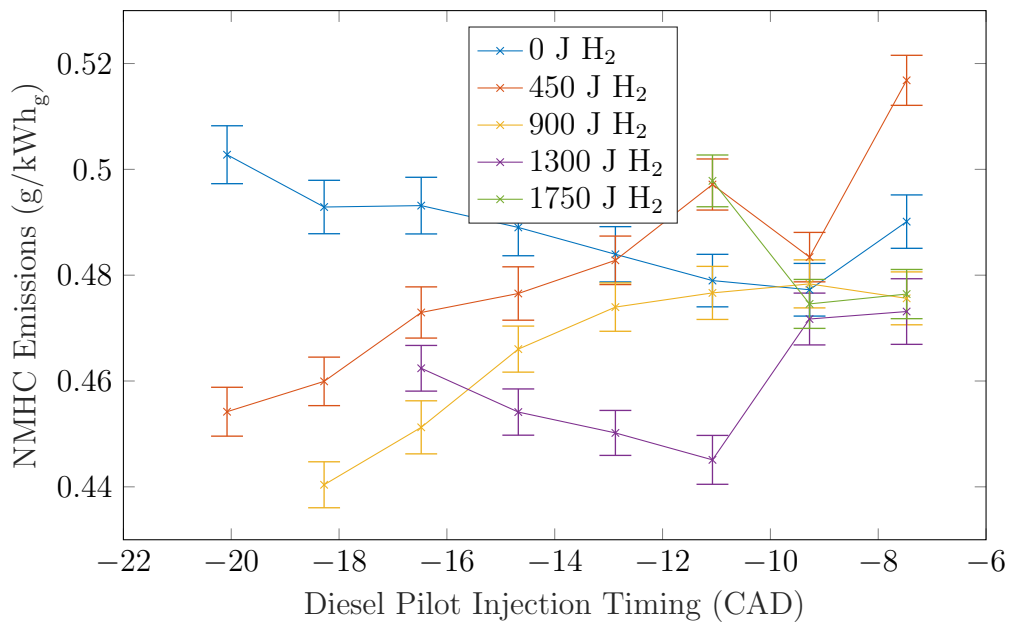


Figure 5.25: NMHC output for the Bin F trials.

UHC was only clearly seen to fall at higher loads (Figure 5.25), while at lower loads the UHC emissions while running hydrogen was either equivalent or higher than the pure diesel UHC emissions. The diesel emissions being equivalent even when the overall diesel fraction is reduced would indicate that more fuel is escaping complete combustion. Similar results have been reported [123], where the higher UHC was thought to be due to hydrogen negatively impacting the combustion process. Notable increases in the NMHC emissions are present in Bin A (Figure 5.24) for the highest hydrogen replacement trials, where the diesel combustion efficiency drops significantly. However, exhaust measurement instability was experienced in these test points, which may explain this large change.

5.8 Heat Release

In this section, the heat release rate traces and its derived metrics (crank angle of mass fraction burned, mass fraction burned crank angle interval) are explored. The heat release rate traces for Bins A and B are presented in Figures 5.26 and 5.27. The most notable difference between pure diesel and high-hydrogen replacement trials is the reduction of the “dual-peak” heat release rate phenomena that is present from the multiple diesel injection events. There is also evidence for which trials undergo premixed combustion and which trials do not. For instance, in the Bin C results (Figure 5.27), premixed combustion only appears to occur once the hydrogen replacement has reached 900 J, as below this the heat release rate drops to near-zero between diesel injection events. In some trials, brief periods of negative heat release rate can be observed. This is due to inaccuracies in the assumed wall heat loss model.

Also notable is that hydrogen increases the peak heat release rate associated with the pilot injection advance. This would correlate well to the increase in the MPRR that was observed with increasing hydrogen replacement, as a greater heat release rate would indicate a higher rise in cylinder pressure and temperature.

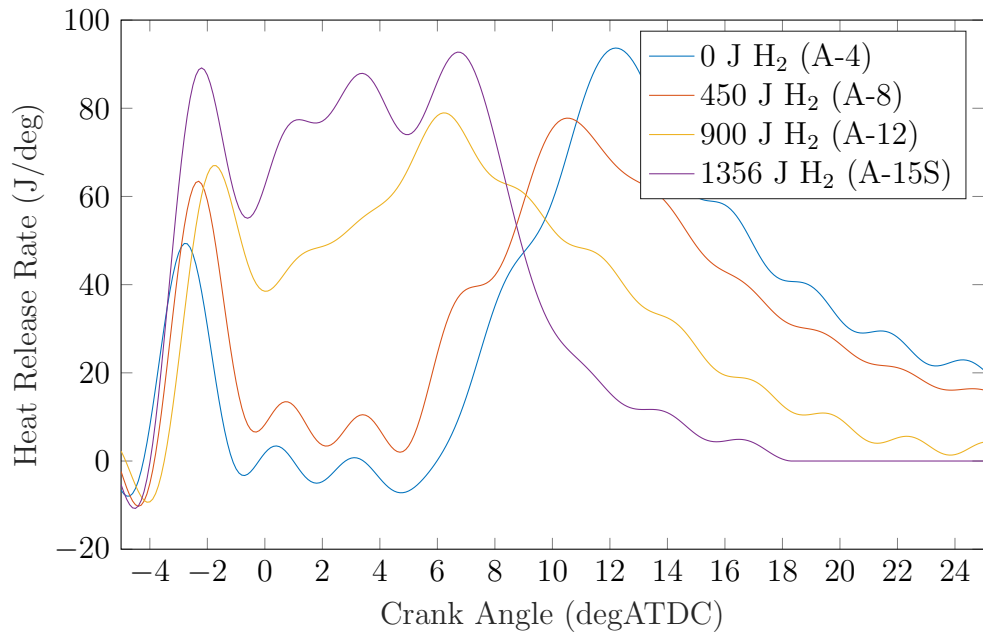


Figure 5.26: Heat release rate traces for Bin A.

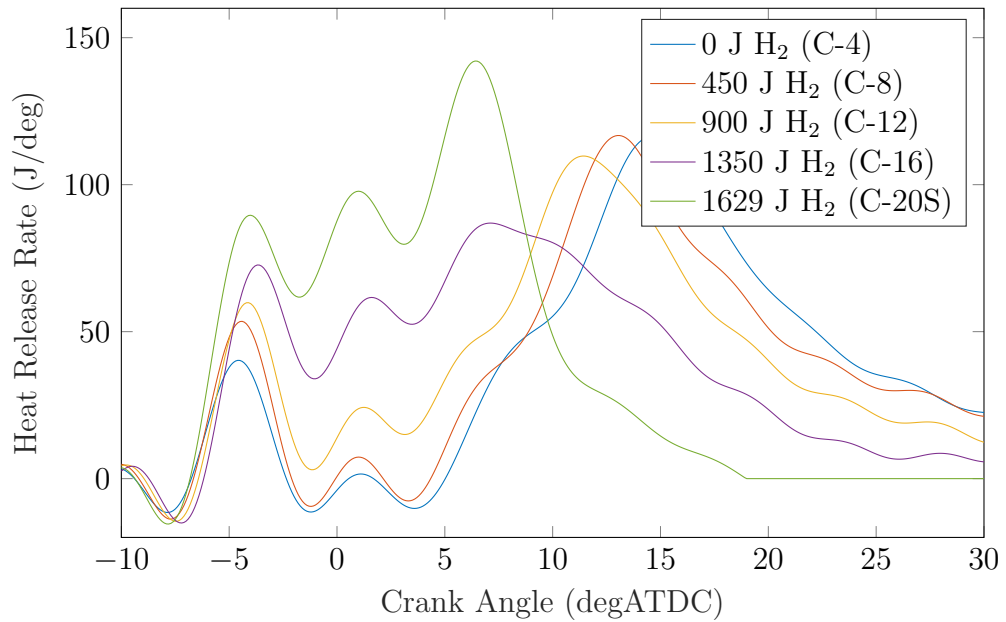


Figure 5.27: Heat release rate traces for Bin C.

CA_x is a measurement of the engine angle at which x fraction of the fuel is burnt. The results for CA_{10} through CA_{90} for Bin F are given below. It can be seen that adding hydrogen causes CA_{10} to advance compared to diesel in all test cases, and both increasing the pilot injection advance and the hydrogen replacement energy causes CA_{10} to further increase. The rate of CA_{10} advance with advanced pilot injection can also be seen to increase with greater hydrogen replacement. This can be explained by the hydrogen combusting in a premixed flame, which is triggered by the initial pilot. As the mixture becomes richer (the hydrogen replacement increases), the premixed flame speed increases, causing further advancement of CA_{10} .

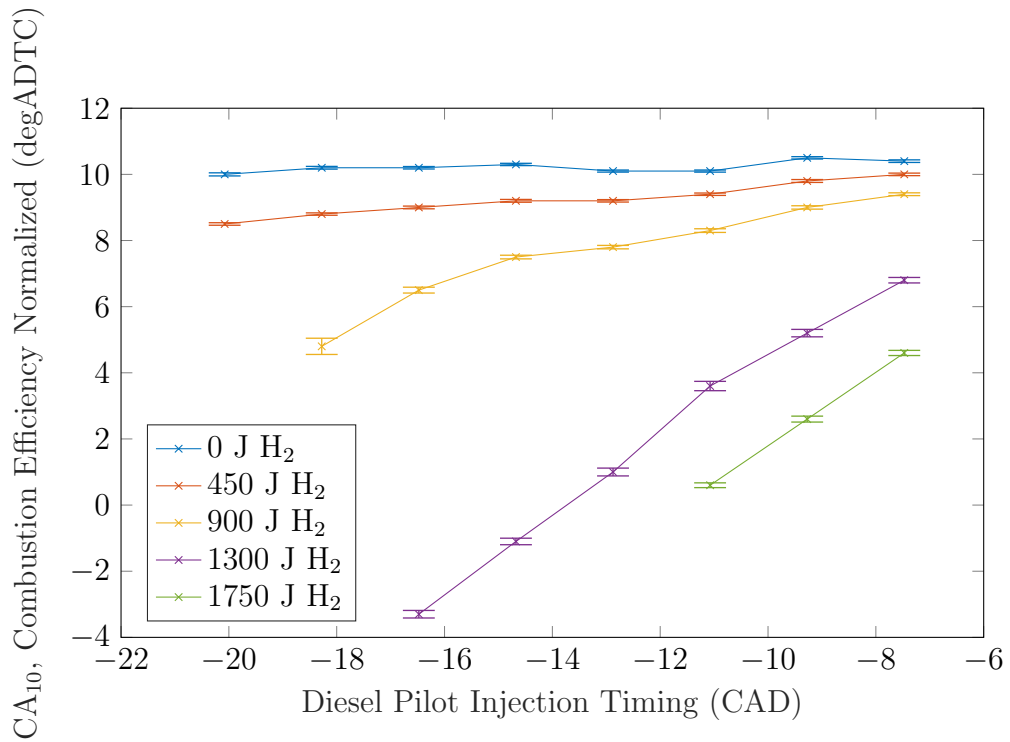


Figure 5.28: CA_{10} for the Bin F trials.

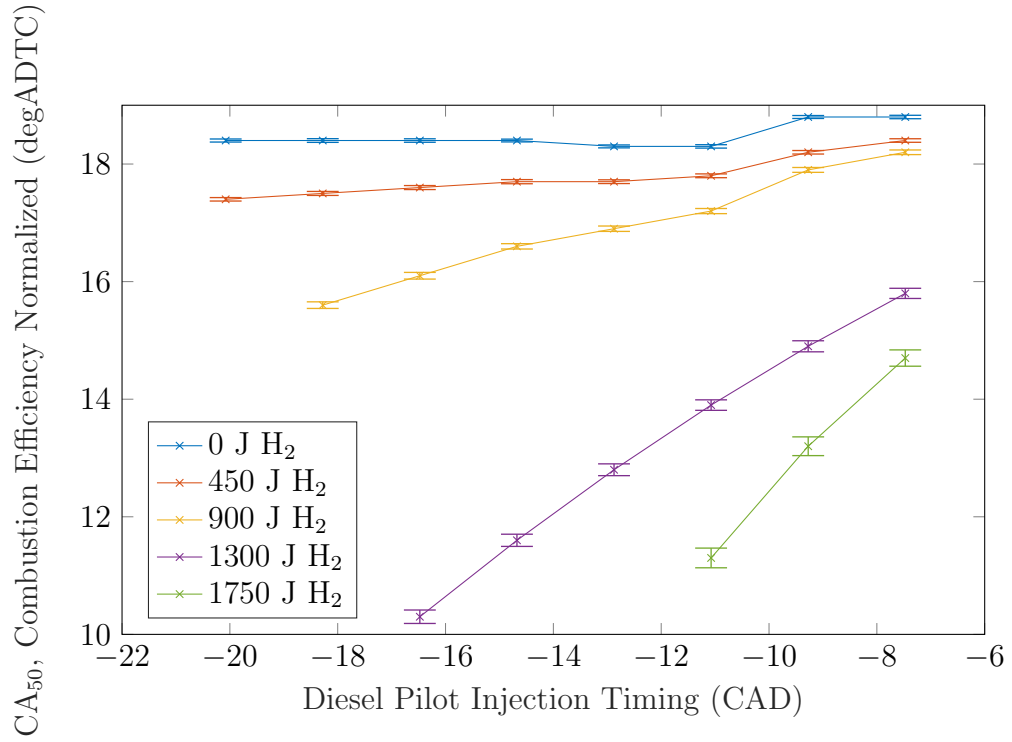


Figure 5.29: CA₅₀ for the Bin F trials.

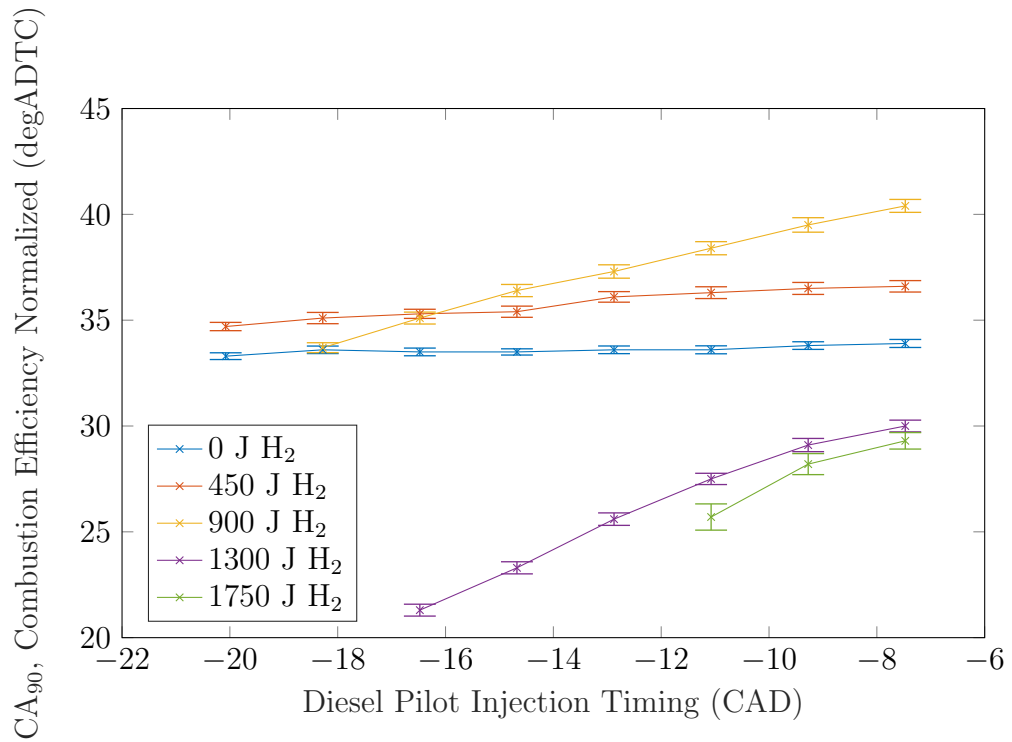


Figure 5.30: CA₉₀ for the Bin F trials.

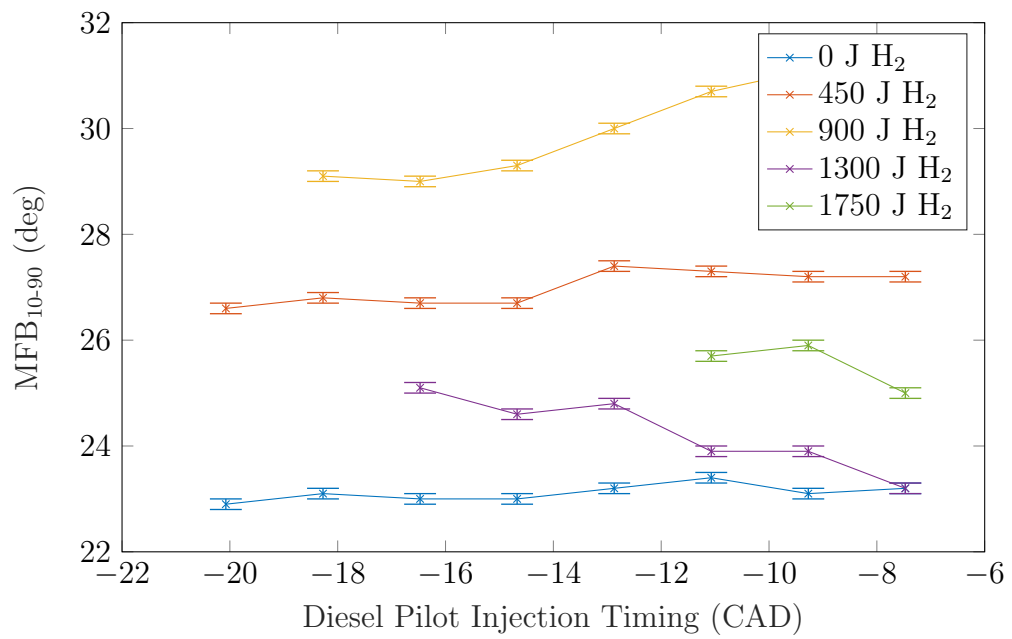


Figure 5.31: MFB_{10-90} for the Bin F trials.

CA_{50} (Figure 5.29) shows a similar trend to CA_{10} , with higher pilot advance and hydrogen replacement causing advancement of CA_{50} . However, CA_{90} (Figure 5.31) shows some deviations from this trend of consistent CA advancement, especially at low hydrogen replacement values. For instance, the lowest replacement hydrogen trials can be seen to have a more retarded CA_{90} as compared to pure diesel combustion. This trend appears to be increased to higher hydrogen replacement in the Bins with higher intake pressures, indicating a relation to the hydrogen air-fuel ratio. When comparing Bin E and Bin F, the 900 J hydrogen trials can be seen to have a more delayed CA_{90} than diesel in Bin F, but not in Bin E. Diesel combustion rate is known to scale positively with increased oxygen partial pressure according to the Arrhenius equation [135], thus more rapid diesel combustion with increased intake pressures is expected.

The retarding in CA_{90} with increasing intake pressure in the hydrogen trials is related to the higher air pressure resulting in a leaner premixed hydrogen air-fuel ratio. Leaner mixture ratios result in lower flame speeds, which would increase the amount of time the flamefront would take to progress across the cylinder if the conditions are rich enough to allow a premixed flamefront to occur. Take, for instance, Bin F (Figure 5.31). The 1300 J and 1750 J H_2 trials result in CA_{90} advancement as compared to diesel. However, the lower hydrogen replacement trials do not. This may indicate that a premixed flamefront is not occurring in these cases, meaning that hydrogen combustion is happening via diesel entrainment, or that the premixed flamefront propagation speed is slow enough to prolong combustion.

MFB (mass fraction burned) is a measurement of the crank angle it takes for a certain fraction of the in-cylinder fuel to combust. The MFB_{10-90} of the Bin F is given in Figure 5.31. A shorter MFB_{10-90} interval indicates that combustion is occurring in a shorter duration, which would allow for improved cycle efficiency by better approximating the instantaneous heat release of the ideal Otto cycle. The MFB_{10-90} values show a similar trend to the CA_{90} values, where only high hydrogen replacement coupled with richer premixed air-fuel ratios can allow for shortening of the combustion duration. Only the greatest hydrogen replacement values coupled with lower intake pressures (Bins A, C, and E) show an improvement over diesel MFB_{10-90} at lower loads, while the higher intake pressure Bins (B, D, and F) show a degradation in MFB_{10-90} with hydrogen replacement as compared to diesel that is

only able to reach diesel-like values with high hydrogen replacement. The high load trials (Bins G and H) show some deviations from this trend, as Bin G shows both the 900 J and 1350 J trials improving the MFB_{10-90} and the Bin H 1350 J trial has an improved MFB_{10-90} at some points. This is partially due to the entrainment of hydrogen by the diesel spray at higher loads, where the longer duration diesel sprays can entrain more hydrogen gas as compared to low loads.

5.8.1 Exhaust Temperatures

Exhaust temperatures are extremely important in order to ensure efficient aftertreatment system operation. Exhaust temperatures that are too low can result in catalysts not being able to reach their optimal operating temperatures, decreasing their efficiency [136]. A less efficient catalyst means more emissions, or more likely a larger, more expensive catalyst to make up for this lower efficiency while still being able to meet emissions regulations. Modern diesel engines often have issues with low exhaust temperatures at low loads, meaning that they have to inject diesel fuel in the exhaust stroke in order to heat the exhaust stream [137]. As such, if hydrogen could improve exhaust temperatures, it may find uses at low loads despite the high slip rate. The exhaust temperatures of the engine during Bin A testing is presented in Figure 5.32:

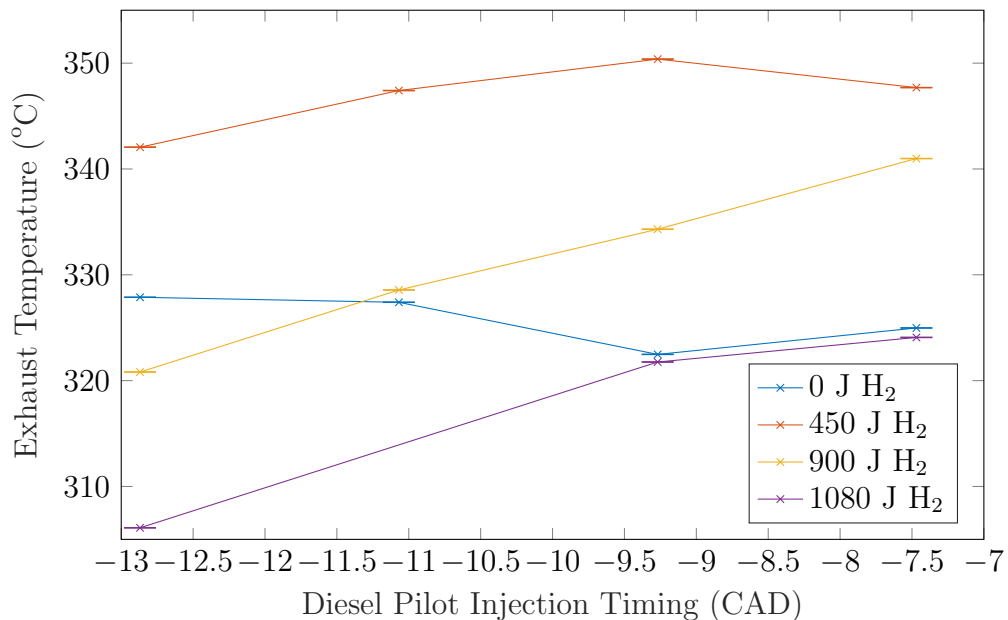


Figure 5.32: Engine exhaust port gas temperatures for the Bin A trials.

As can be seen, at low loads hydrogen generally increases the exhaust temperatures as compared to pure diesel. This is likely tied to the lower cycle efficiency that has been witnessed at these loads. However, as hydrogen replacement and diesel pilot advance increases, the exhaust temperature can be seen to fall. For instance, in Bin A (Figure 5.32), the maximum hydrogen replacement results in a lower exhaust temperature than pure diesel. The reduction in temperature with increasing advance is expected with premixed combustion, as a greater advance means earlier combustion, which means that more energy can be extracted as work — and the higher in-cylinder temperatures means more heat losses to the cooling jacket of the engine. This results in lower exhaust gas temperatures. Importantly, the exhaust gas temperatures are still above 300 °C, which would not negatively effect most diesel aftertreatment system efficiencies [138, 139].

Another factor with hydrogen is its high reactivity and low light-off temperature diesel oxidation catalysts [140]. This means that engine-out uncombusted hydrogen emissions could still be useful in aftertreatment systems, as it could significantly increase the exhaust temperature after passing a diesel oxidative catalyst, and promote oxidation of CO [140]. This may have significant improvements in emissions for cold weather conditions due to the lower light-off temperatures of hydrogen [140], which modern diesel engines often have lesser performance in [141]. It could also mean that the diesel post injection may not be required when running hydrogen in low-load cases, which could help to alleviate the dual-fuel efficiency gap found at low engine loads.

5.9 Best-Case Comparison

The targets for the best-case comparison were taken as the trials within the test grid that resulted in the lowest CO₂ emissions output while running hydrogen. This metric was chosen because of current governmental and social pressures to reduce CO₂ emissions, while other emissions have experienced less pressure on their reduction. Additionally, a secondary metric was maximizing engine efficiency, which would allow for more efficient usage of hydrogen. To find these best-case operating points, the engine load, diesel pilot injection timing, diesel main injection duration, hydrogen

injected mass, and intake pressure were varied. The constraints in operation were the maximum cylinder pressure and maximum cylinder pressure rise rate – as these present issues with engine lifespan if the engine design thresholds are exceeded. The results of this variation are the trials from Table 5.1. The comparisons are present in Figures 5.33 through 5.40.

It is important to note that in a turbocharged engine, as intake pressure increases, the indicated cycle efficiency may not increase in the same manner as the gross indicated cycle efficiency. This is because the turbocharger requires energy from the exhaust stream from the engine in order to drive the compressor. This load results in an efficiency reduction due to the energy required from the exhaust stroke in order to drive the compressor. As such, increasing the intake pressure may not result in an improvement in the brake efficiency at the engine, however this depends heavily upon the design of the turbocharger system and its efficiency at the operating point. This would result in the net efficiency of a turbocharged engine being less than the gross efficiency, and additionally having a higher emissions output (less work can be extracted for the same emissions cost). However, this would negatively affect both the pure diesel and dual fuel operation modes, thus they should still be comparable in a different engine configuration.

The best case comparison ended up with trials in Bins A and B, Bins C and D Bins F and F, and Bins H and H, with the former Bin being the hydrogen trial and the latter Bin being the diesel trial. At low loads, the diesel performed better (better emissions and gross efficiency) with higher IMAP, which is expected as the diesel combustion rate is highly dependent upon the oxygen partial pressure [135]. However, this would mean that theoretically a hydrogen-diesel dual fuel engine would have a lower efficiency penalty if a turbocharger were used to supply the increased intake pressure, as a lower boost pressure was used at the 4.5 bar and 7.5 bar IMEP operating points.

The peak hydrogen energy fraction was found to be 92% of the total input fuel energy, at 7.5 bar IMEP load. The maximum energy fraction at the 4.5 bar and 7.5 bar load points was dependent upon the minimum possible injection length for the diesel injector. As such, with a diesel injector that would be designed for lower flow, higher replacement ratios are conceivable at loads below 7.5 bar IMEP. At the load

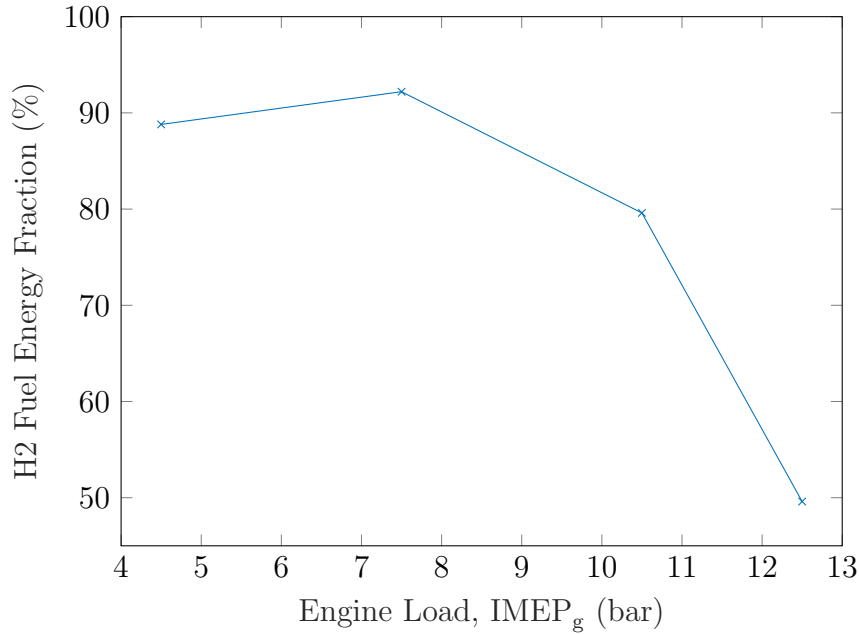


Figure 5.33: Highest hydrogen fractions achieved in trials.

points higher than this, the hydrogen energy fraction was limited by the maximum pressure rise rate. High efficiency and high hydrogen replacement operating points resulted in this constraint being breached with higher hydrogen replacement, thus it was not pursued. The diesel operating points for comparison ended up being the highest efficiency operating points, as these operating points resulted in the lowest CO₂ emissions. Likewise, the hydrogen operating points were also the highest efficiency operating points. At lower loads, dual-fuel operation can be seen to have a higher efficiency than diesel operation. This would prove useful for optimal hydrogen consumption, as the limited storage mass could be used more efficiently.

The CO₂ (Figure 5.35) and particulate (Figure 5.36) emissions for the hydrogen best-cases are significantly reduced compared to pure diesel operation. The peak reduction in CO₂ emissions was found to be 89% at 7.5 bar IMEP, while the peak particulate reduction achieved was 97%, at 4.5 bar IMEP. The hydrogen replacement fraction at the operating point plays a significant role in the maximum reduction of these emissions, with the 4.5 bar and 7.5 bar IMEP operating points having higher reductions than the higher load operating points.

It is apparent from Figure 5.37 and Figure 5.38 that the dual-fuel combustion significantly reduces CO₂ and particulate production versus diesel operation. The lowest

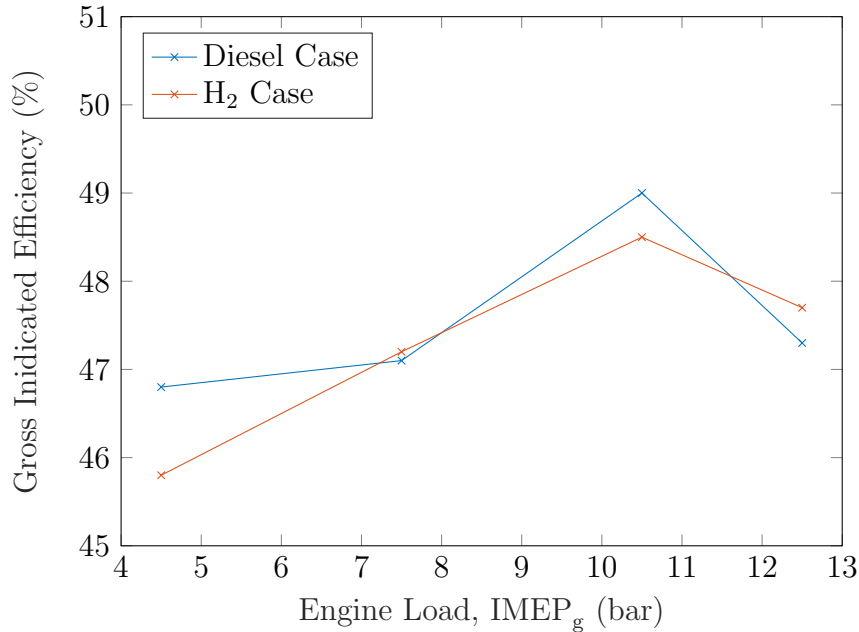


Figure 5.34: Comparison between the best efficiencies for dual-fuel and diesel operation in trials.

CO₂ emission operating point was 67 g/kWh at 7.5 bar IMEP, showing a significant potential for GHG reduction. CO₂ emissions are tied to the reduction of diesel injection, which is related to both the hydrogen energy fraction and the gross indicated efficiency of the engine cycle. From Figure 5.39 it can be seen that the dual-fuel NO_x emissions are elevated as compared to diesel, likely due to elevated production of thermal NO_x because of the higher cylinder pressures and temperatures and the HO₂ radical mechanism. This NO_x production issue presents a major setback to hydrogen-diesel dual fuel combustion, and is an issue that in a real-world application would have to be solved by exhaust gas aftertreatment, lower CO₂ reduction targets, or by using other combustion modes. The overall combustion efficiency can be seen to be diesel-like at operating points other than 12.5 bar IMEP load. The slip at this load is likely driven by a relatively lean mixture at the higher intake pressure, however it still retains efficient operation (likely due to lower cylinder wall heat loss).

The tested loads are only up to 12.5 bar IMEP, while the engine in a stock configuration was capable of generating 17.5 bar IMEP. However, the peak CO₂ reduction occurring at 7.5 bar (approximately 40% engine load) has a benefit due to the average engine's load state. If an engine has an average load under 30%, on average, CO₂

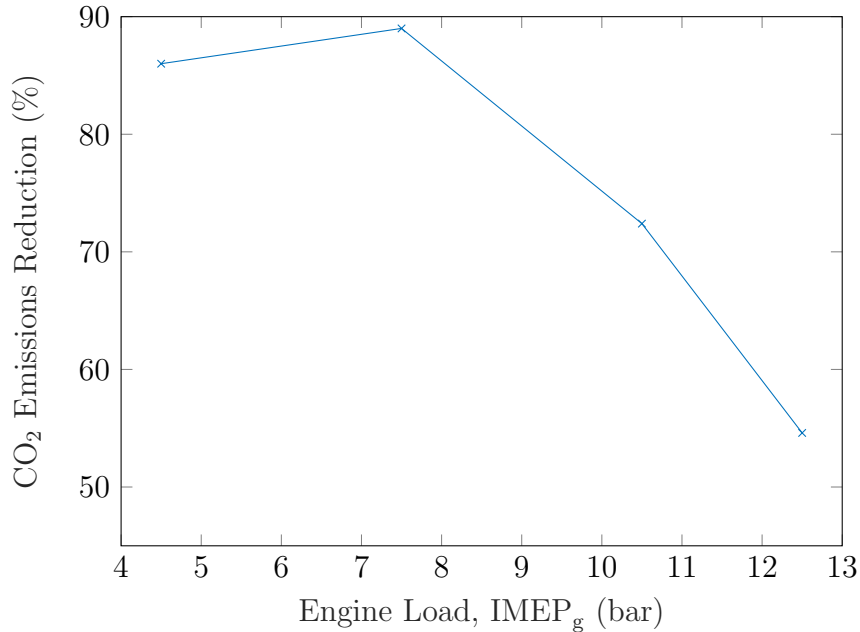


Figure 5.35: CO₂ reduction for the highest hydrogen fraction trials.

reduction could approach the best-case value seen in this work. However, operation at this point with maximum CO₂ reduction as a target would result in approximately 35% greater NO_x emissions before aftertreatment. For a more realistic model, a vehicle and its load pattern would have to be characterized.

It is evident that a vehicle running hydrogen-diesel dual fuel would have to run with some kind of aftertreatment system in order to meet Tier 4 Offroad emissions. NO_x output will require aftertreatment, as the NO_x output from the engine is more than ten times the certification threshold of 0.4 g/kWh [131]. It is also evident that optimization of the engine's operating points to lower engine-out NO_x may have some benefit in meeting these emissions standards, even with aftertreatment. However, without an aftertreatment system model, it is not known what target thresholds for engine-out emissions are required to meet tailpipe emissions. Additionally, uHC emissions will also require catalytic aftertreatment in order to reduce their concentration to certification levels (0.19 g/kWh [131]). However, particulate emissions certification (0.02 g/kWh [131]) could conceivably be reached without particulate aftertreatment while running in a dual-fuel mode. This is of great importance, because simplifying the aftertreatment system could potentially offset the cost of the additional hydrogen fuel system.

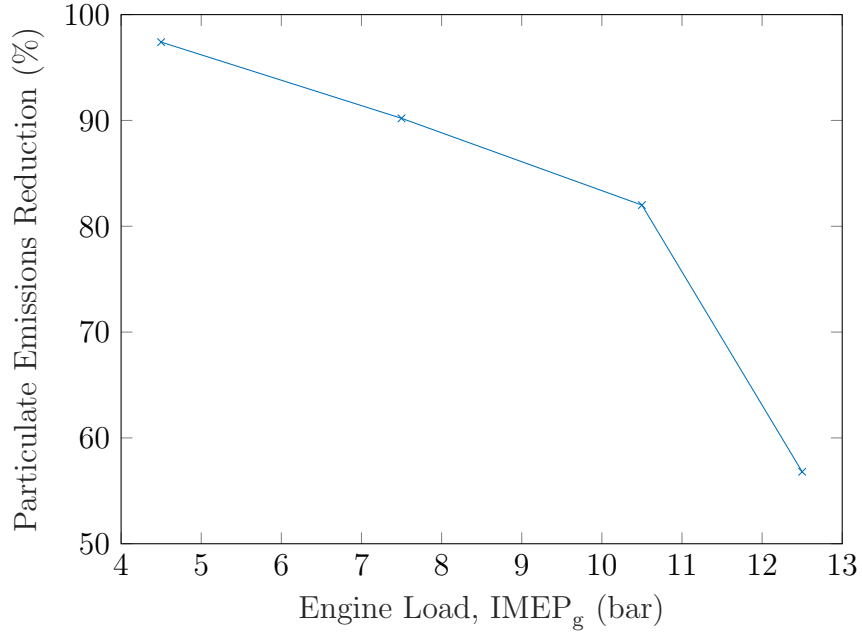


Figure 5.36: Particulate reduction for the highest hydrogen fraction trials.

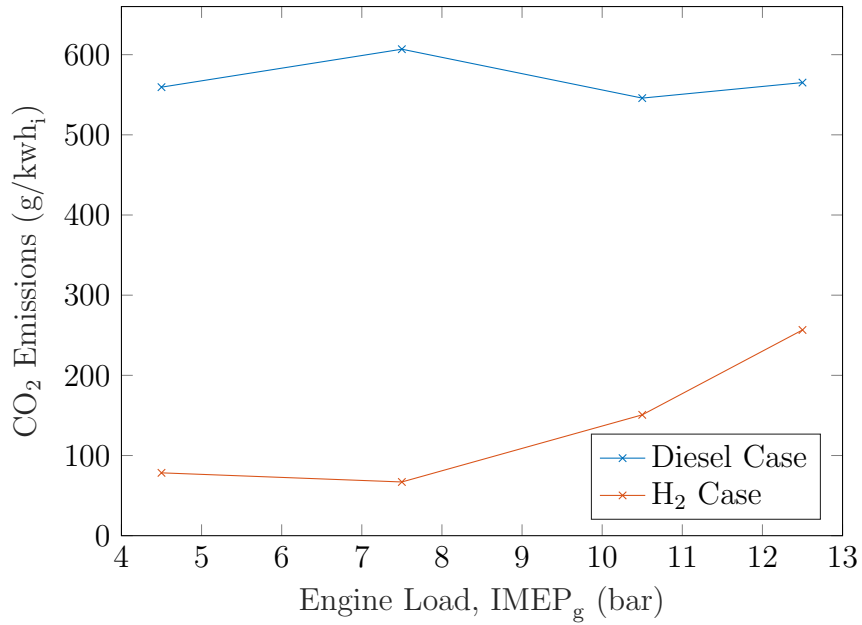


Figure 5.37: Comparison between the CO₂ emissions for dual-fuel and diesel operation in trials.

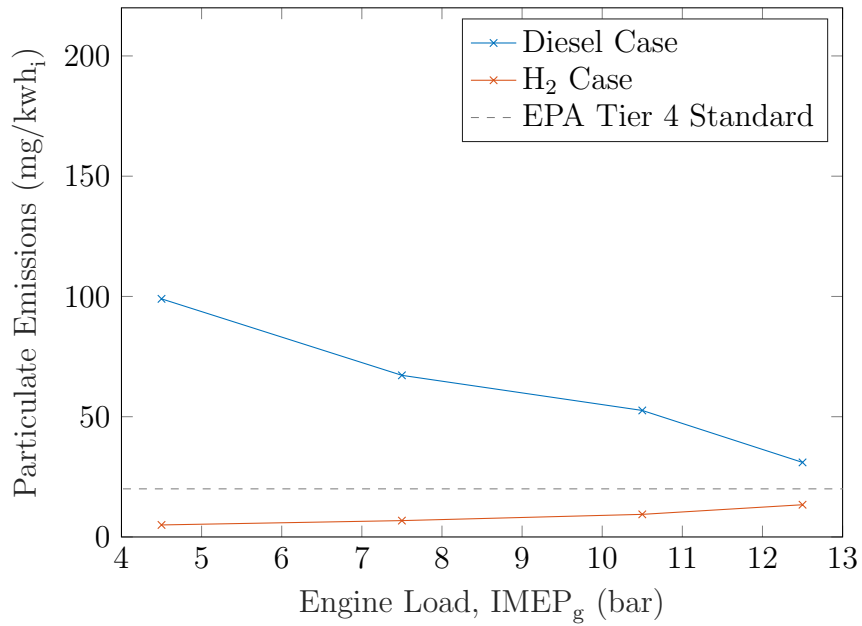


Figure 5.38: Comparison between the particulate emissions for dual-fuel and diesel operation in trials.

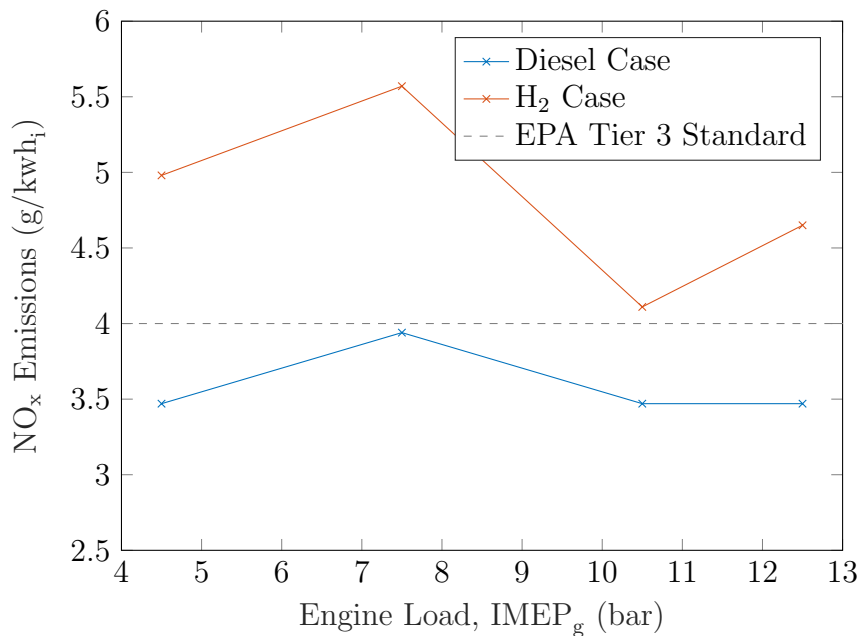


Figure 5.39: Comparison between the NO_x emissions for dual-fuel and diesel operation in trials.

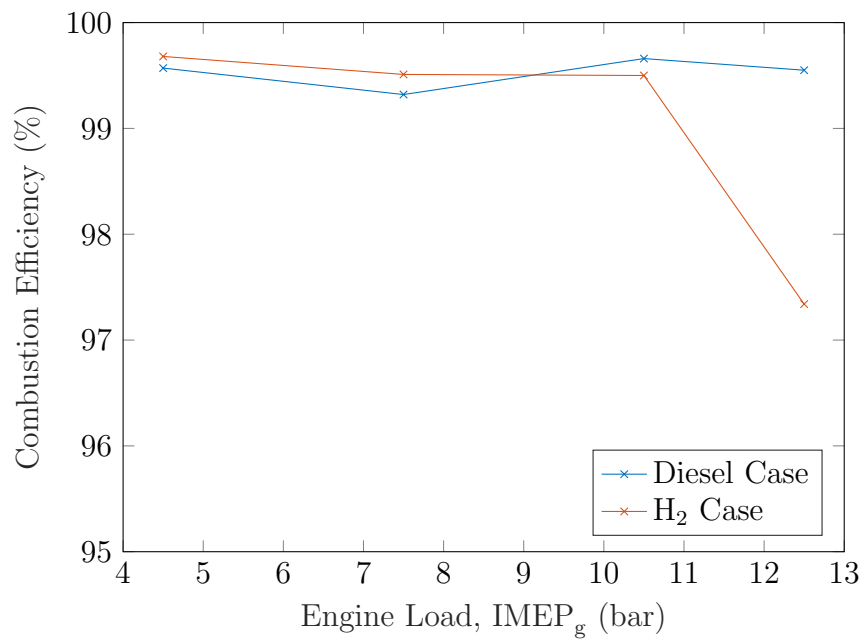


Figure 5.40: Comparison between the overall combustion efficiencies for dual-fuel and diesel operation in trials.

Chapter 6

Conclusion

6.1 Steady State Dual-Fuel Operation

Hydrogen-diesel dual fuel combustion is a potent method to decrease both CO₂ and particulate production as compared to diesel engines. Steady state operation of the engine under hydrogen-diesel dual fuel operation showed that hydrogen was able to reduce CO₂ output by up to 89% at low-load operation, and by approximately 50% at 12.5 bar IMEP, or 70% of rated engine load. Particulate emissions were also able to be reduced by up to 97% at low loads, and 56% at 12.5 bar IMEP. However, NO_x emissions were increased over pure diesel operation, with the magnitude correlating with increasing hydrogen replacement fraction. Up to 85% greater NO_x emissions compared to pure diesel were observed. However, these NO_x emissions had a significantly greater fraction of NO₂ than conventional diesel combustion (approaching a 1:1 ratio of NO to NO₂ at some operating points), which may be useful for engine aftertreatment. The maximum threshold of hydrogen replacement was limited to 1750 J by knock and the maximum pressure rise rate of the engine, which was able to be extended by using increased intake pressure and retarded diesel pilot injection timing. UHC emissions were observed to increase unless the engine is operated at engine loads higher than approximately 10.5 bar IMEP while running dual-fuel hydrogen diesel. Hydrogen combustion efficiency suffers significantly when the hydrogen air-fuel ratio is run beyond its lean flammability limit, which can be alleviated by either increasing the hydrogen fuel-air ratio at the operating point, or with a sufficiently rich mixture advancing the diesel pilot injection timing.

High hydrogen combustion efficiencies were only achievable when premixed stoi-

chiometric mixtures were within hydrogen's flammability range ($\lambda < 5$). With mixtures leaner than this, hydrogen combustion appeared to occur mainly via entrainment within the diesel spray instead of premixed flame propagation, and hydrogen combustion efficiency was impaired. The greatest hydrogen combustion efficiencies were observed with $\lambda < 4$. At higher loads (beyond 10.5 bar IMEP), there appeared to be a limited extension of the lean flammability range to $\lambda \approx 6$.

When a sufficiently rich premixed air-fuel mixture was used, hydrogen was observed to be able to retain similar-to-diesel (within 1%) indicated efficiencies with high hydrogen replacement across all tested loads. If this parameter was not met, the engine indicated efficiency fell significantly compared to baseline diesel operation. However, when diesel operation was constrained to the same lower intake pressures as hydrogen-diesel operation, engine indicated efficiency while running hydrogen was greater than diesel. A maximum improvement of 4.8% in indicated efficiency was found at 4.5 bar IMEP load under this constrained intake pressure condition.

6.2 Future Work

Areas of possible future work to extend the knowledge of this thesis includes:

- Modeling of the dual fuel combustion process is of great importance to be able to simulate high-performance operating points before spending significant effort manually testing operating points. A computational fluid dynamics simulation may help to better understand the dual-fuel combustion process, improve cycle efficiency, and to predict the formation of NO_2 in-cylinder. Particularly, a computational fluid dynamics model may be useful to explain the relatively high hydrogen slip at certain operating points, and to estimate and maximize diesel spray entrainment of hydrogen gas.
- Hydrogen-diesel dual fuel's impact on tailpipe emissions after aftertreatment should be analyzed to gain a rough idea of tailpipe emissions with current emissions reduction technologies. The NO/NO_2 ratio that was closer to unity that pure diesel combustion in Chapter 5 may have a positive effect on the selective catalytic reduction of NO_x , however the magnitude of this effect (or

if it can offset higher engine-out NO_x numbers) in real-world operation is yet to be determined. Other NO_x reduction aftertreatment systems should also be investigated for possibly better performance while running hydrogen.

- Usage of exhaust gas recirculation and intake throttling should be investigated for their effects on emissions and performance gains. From other works, exhaust gas recirculation has been effective for both NO_x reduction and low-load hydrogen slip reduction. Intake throttling may also have a positive effect on engine cycle efficiency at lower loads.
- Investigation of varied pilot injection masses on dual-fuel combustion should be investigated in order to determine the pilot injection's interaction with dual-fuel combustion efficiency and emissions output.
- Control models for controlling the hydrogen-diesel combustion should be investigated to progress implementation of dual-fuel engines. Lambda-based feedback control should be analyzed due to its common usage on on-road vehicles. Non-linear model predictive control could also be investigated for its ability to control and predict the engine's combustion and emissions, and high functionality with complicated systems.
- A multiple-cylinder implementation of dual fuel should be investigated. Using multiple cylinder would allow to see the effects of non-balanced intake air and EGR flow, and determine dual-fuel's sensitivity to differing cylinder-to-cylinder conditions (such as cylinder wall temperatures). A multi-cylinder engine could also be turbocharged so that net IMEP could be investigated. Brake efficiency should be investigated to determine if the higher cylinder pressures associated with hydrogen combustion cause an increase in the frictional losses of the engine.
- Investigation and optimization of low-temperature dual-fuel combustion presents a way to offset the higher NO_x emissions associated with conventional dual fuel combustion. Analysis and modeling of the LTC regime could allow for higher efficiency LTC combustion, thus making it competitive with conventional diesel combustion in a larger load range. EGR's effects on LTC could also be investigated to observe changes in the load limitation boundaries.

- Higher loads, similar to peak loads in current on-road diesel engines (20-25 bar IMEP) should be investigated for hydrogen's performance, emissions impacts and knock limits. Observing the maximum hydrogen replacement throughout an engine's full load range would be useful for modeling vehicle emissions with varying drive cycles.
- The effects of the engine's compression ratio on dual-fuel's performance, emissions and knock limits should be investigated in order to determine an optimal compression ratio that can balance both hydrogen replacement at higher loads and emissions output. This would be critical in maximizing the hydrogen replacement in future engines.

Bibliography

- [1] A. J. Weaver, K. Zickfeld, A. Montenegro, and M. Eby, “Long term climate implications of 2050 emission reduction targets,” *Geophysical Research Letters*, vol. 34, no. 19, 2007. DOI: <https://doi.org/10.1029/2007GL031018>. eprint: <https://agupubs.onlinelibrary.wiley.com/doi/pdf/10.1029/2007GL031018>. [Online]. Available: <https://agupubs.onlinelibrary.wiley.com/doi/abs/10.1029/2007GL031018>.
- [2] G. Mallouppas and E. A. Yfantis, “Decarbonization in shipping industry: A review of research, technology development, and innovation proposals,” *Journal of Marine Science and Engineering*, vol. 9, no. 4, 2021, ISSN: 2077-1312. DOI: [10.3390/jmse9040415](https://doi.org/10.3390/jmse9040415). [Online]. Available: <https://www.mdpi.com/2077-1312/9/4/415>.
- [3] M. Prussi, L. Laveneziana, L. Testa, and D. Chiaramonti, “Comparing e-fuels and electrification for decarbonization of heavy-duty transports,” *Energies*, vol. 15, no. 21, 2022, ISSN: 1996-1073. DOI: [10.3390/en15218075](https://doi.org/10.3390/en15218075). [Online]. Available: <https://www.mdpi.com/1996-1073/15/21/8075>.
- [4] A. Ajanovic and R. Haas, “Economic and environmental prospects for battery electric- and fuel cell vehicles: A review,” *Fuel Cells*, vol. 19, no. 5, pp. 515–529, 2019. DOI: <https://doi.org/10.1002/fuce.201800171>. eprint: <https://onlinelibrary.wiley.com/doi/pdf/10.1002/fuce.201800171>. [Online]. Available: <https://onlinelibrary.wiley.com/doi/abs/10.1002/fuce.201800171>.
- [5] R. Cracknell, S. Ciatti, S. Dorofeev, R. Eggels, K. McManus, and K. Nakata, “Decarbonization of mobility, including transportation and renewable fuels,” *Proceedings of the Combustion Institute*, vol. 39, no. 1, pp. 1–9, 2023, ISSN: 1540-7489. DOI: <https://doi.org/10.1016/j.proci.2023.02.001>. [Online]. Available: <https://www.sciencedirect.com/science/article/pii/S154074892300007X>.
- [6] C. Ledna, M. Muratori, A. Yip, P. Jadun, and C. Hoehne, “Decarbonizing medium-duty and heavy-duty on-road vehicles: Zero-emission vehicles cost analysis,” Mar. 2022. DOI: [10.2172/1854583](https://doi.org/10.2172/1854583). [Online]. Available: <https://www.osti.gov/biblio/1854583>.
- [7] R. C. Samsun, M. Rex, L. Antoni, and D. Stolten, “Deployment of fuel cell vehicles and hydrogen refueling station infrastructure: A global overview and perspectives,” *Energies*, vol. 15, no. 14, 2022, ISSN: 1996-1073. DOI: [10.3390/en15144975](https://doi.org/10.3390/en15144975). [Online]. Available: <https://www.mdpi.com/1996-1073/15/14/4975>.

- [8] J. Alazemi and J. Andrews, “Automotive hydrogen fuelling stations: An international review,” *Renewable and Sustainable Energy Reviews*, vol. 48, pp. 483–499, 2015, ISSN: 1364-0321. DOI: <https://doi.org/10.1016/j.rser.2015.03.085>. [Online]. Available: <https://www.sciencedirect.com/science/article/pii/S1364032115002385>.
- [9] M. Ball and M. Wietschel, “The hydrogen economy: Opportunities and challenges,” 2009.
- [10] P. S. Government of Canada and P. Canada, *2030 emissions reduction plan : Canada’s next steps to clean air and a strong economy.: En4-460/2022e-pdf - government of canada publications - canada.ca*, publications.gc.ca, Jul. 2002. [Online]. Available: <https://publications.gc.ca/site/eng/9.909338/publication.html>.
- [11] E. Eckermann, *World History of the Automobile* (Premiere Series Bks). Society of Automotive Engineers, 2001, ISBN: 9780768008005. [Online]. Available: <https://books.google.ca/books?id=yLZeQwqNmdgC>.
- [12] C. White, R. Steeper, and A. Lutz, “The hydrogen-fueled internal combustion engine: A technical review,” *International Journal of Hydrogen Energy*, vol. 31, no. 10, pp. 1292–1305, 2006, ISSN: 0360-3199. DOI: <https://doi.org/10.1016/j.ijhydene.2005.12.001>. [Online]. Available: <https://www.sciencedirect.com/science/article/pii/S0360319905003721>.
- [13] J. Andrews and B. Shabani, “The role of hydrogen in a global sustainable energy strategy,” *WIREs Energy and Environment*, vol. 3, no. 5, pp. 474–489, 2014. DOI: <https://doi.org/10.1002/wene.103>. eprint: <https://wires.onlinelibrary.wiley.com/doi/pdf/10.1002/wene.103>. [Online]. Available: <https://wires.onlinelibrary.wiley.com/doi/abs/10.1002/wene.103>.
- [14] S. C. Davis and R. G. Boundy, “Transportation energy data book: Edition 39,” Oak Ridge National Lab.(ORNL), Oak Ridge, TN (United States), Tech. Rep., 2021.
- [15] N. B. L. Thermodynamics Research Center, “Nist chemistry webbook: Thermophysical properties of fluid systems, nist standard reference database number 69,” National Institute of Standards and Technology, U.S. Department of Commerce, Tech. Rep., 2023. DOI: <https://doi.org/10.18434/T4D303>.
- [16] R. Schmich, R. Wagner, G. Hörpel, T. Placke, and M. Winter, “Performance and cost of materials for lithium-based rechargeable automotive batteries,” *Nature energy*, vol. 3, no. 4, pp. 267–278, 2018.
- [17] J. Krishnanunni, H. Bhankar, D. Chugh, D. Bhatia, and L. M. Das, “Strategies for stable operation of a h₂ - ICE at high equivalence ratios with use of unburnt and externally injected hydrogen for reducing NO_x emissions,” *International Journal of Hydrogen Energy*, vol. 45, no. 41, pp. 22 125–22 137, 2020. DOI: [10.1016/j.ijhydene.2020.05.212](https://doi.org/10.1016/j.ijhydene.2020.05.212).

- [18] X. Liu, G. Seberry, S. Kook, Q. N. Chan, and E. R. Hawkes, “Direct injection of hydrogen main fuel and diesel pilot fuel in a retrofitted single-cylinder compression ignition engine,” *International Journal of Hydrogen Energy*, vol. 47, no. 84, pp. 35 864–35 876, 2022, ISSN: 0360-3199. DOI: <https://doi.org/10.1016/j.ijhydene.2022.08.149>. [Online]. Available: <https://www.sciencedirect.com/science/article/pii/S0360319922036771>.
- [19] A. Boretta, “A dual fuel ICE diesel-h₂ featuring 1,600 bar cryogenic liquid h₂ injection,” *International Journal of Hydrogen Energy*, vol. 46, no. 36, pp. 19 171–19 179, 2021. DOI: 10.1016/j.ijhydene.2021.03.048.
- [20] P. Rorimpandey *et al.*, “Hydrogen-diesel dual-fuel direct-injection (h₂ddi) combustion under compression-ignition engine conditions,” *International Journal of Hydrogen Energy*, vol. 48, no. 2, pp. 766–783, 2023. DOI: 10.1016/j.ijhydene.2022.09.241.
- [21] S Furuhashi and Y Kobayashi, “Development of a hot-surface-ignition hydrogen injection two-stroke engine,” *International Journal of Hydrogen Energy*, vol. 9, no. 3, pp. 205–213, 1984. DOI: 10.1016/0360-3199(84)90120-4.
- [22] S. S. Goldsborough and P. V. Blarigan, “A numerical study of a free piston IC engine operating on homogeneous charge compression ignition combustion,” in *SAE Technical Paper Series*, SAE International, 1999. DOI: 10.4271/1999-01-0619.
- [23] M. Akif Ceviz, A. K. Sen, A. K. Küleri, and I. Volkan Öner, “Engine performance, exhaust emissions, and cyclic variations in a lean-burn si engine fueled by gasoline–hydrogen blends,” *Applied Thermal Engineering*, vol. 36, pp. 314–324, 2012, ISSN: 1359-4311. DOI: <https://doi.org/10.1016/j.applthermaleng.2011.10.039>. [Online]. Available: <https://www.sciencedirect.com/science/article/pii/S1359431111005916>.
- [24] M Berckmüller *et al.*, “Potentials of a charged si-hydrogen engine,” SAE Technical Paper, Tech. Rep., 2003.
- [25] J. M. Towers and R. L. Hoekstra, “Engine knock, a renewed concern in motorsports—a literature review,” *SAE transactions*, pp. 2329–2343, 1998.
- [26] X. Zhen *et al.*, “The engine knock analysis – an overview,” *Applied Energy*, vol. 92, pp. 628–636, 2012, ISSN: 0306-2619. DOI: <https://doi.org/10.1016/j.apenergy.2011.11.079>. [Online]. Available: <https://www.sciencedirect.com/science/article/pii/S0306261911007859>.
- [27] B. Grandin and I. Denbratt, “The effect of knock on heat transfer in si engines,” *SAE transactions*, pp. 622–630, 2002.
- [28] S. Russ, “A review of the effect of engine operating conditions on borderline knock,” 1996.

- [29] K. Mohiuddin, H. Kwon, M. Choi, and S. Park, "Effect of engine compression ratio, injection timing, and exhaust gas recirculation on gaseous and particle number emissions in a light-duty diesel engine," *Fuel*, vol. 294, p. 120547, 2021, ISSN: 0016-2361. DOI: <https://doi.org/10.1016/j.fuel.2021.120547>. [Online]. Available: <https://www.sciencedirect.com/science/article/pii/S0016236121004233>.
- [30] S. Szwaja, "Dilution of fresh charge for reducing combustion knock in the internal combustion engine fueled with hydrogen rich gases," *International Journal of Hydrogen Energy*, vol. 44, no. 34, pp. 19017–19025, 2019, Selected Papers from the 3rd International Hydrogen Technologies Congress, ISSN: 0360-3199. DOI: <https://doi.org/10.1016/j.ijhydene.2018.10.134>. [Online]. Available: <https://www.sciencedirect.com/science/article/pii/S0360319918333330>.
- [31] M. M. Ibrahim and A. Ramesh, "Experimental investigations on a hydrogen diesel homogeneous charge compression ignition engine with exhaust gas recirculation," *International Journal of Hydrogen Energy*, vol. 38, no. 24, pp. 10116–10125, 2013, ISSN: 0360-3199. DOI: <https://doi.org/10.1016/j.ijhydene.2013.05.092>. [Online]. Available: <https://www.sciencedirect.com/science/article/pii/S0360319913012883>.
- [32] H. Fayaz, R. Saidur, N. Razali, F. Anuar, A. Saleman, and M. Islam, "An overview of hydrogen as a vehicle fuel," *Renewable and Sustainable Energy Reviews*, vol. 16, no. 8, pp. 5511–5528, 2012, ISSN: 1364-0321. DOI: <https://doi.org/10.1016/j.rser.2012.06.012>. [Online]. Available: <https://www.sciencedirect.com/science/article/pii/S1364032112003929>.
- [33] T. Tsujimura and Y. Suzuki, "The utilization of hydrogen in hydrogen/diesel dual fuel engine," *International Journal of Hydrogen Energy*, vol. 42, no. 19, pp. 14019–14029, 2017, Special Issue on The 21st World Hydrogen Energy Conference (WHEC 2016), 13-16 June 2016, Zaragoza, Spain, ISSN: 0360-3199. DOI: <https://doi.org/10.1016/j.ijhydene.2017.01.152>. [Online]. Available: <https://www.sciencedirect.com/science/article/pii/S036031991730318X>.
- [34] F. Poursadegh, M. Brear, B. Hayward, and Y. Yang, "Autoignition, knock, detonation and the octane rating of hydrogen," *Fuel*, vol. 332, p. 126201, 2023, ISSN: 0016-2361. DOI: <https://doi.org/10.1016/j.fuel.2022.126201>. [Online]. Available: <https://www.sciencedirect.com/science/article/pii/S0016236122030253>.
- [35] Y. Li, W. Gao, P. Zhang, Z. Fu, and X. Cao, "Influence of the equivalence ratio on the knock and performance of a hydrogen direct injection internal combustion engine under different compression ratios," *International Journal of Hydrogen Energy*, vol. 46, no. 21, pp. 11982–11993, 2021, ISSN: 0360-3199. DOI: <https://doi.org/10.1016/j.ijhydene.2021.01.031>. [Online]. Available: <https://www.sciencedirect.com/science/article/pii/S0360319921000896>.

- [36] M. A. R. S. Al-Baghdadi, “Development of a pre-ignition submodel for hydrogen engines,” *Proceedings of the Institution of Mechanical Engineers, Part D: Journal of Automobile Engineering*, vol. 219, no. 10, pp. 1203–1212, 2005. DOI: 10.1243/095440705X34883. eprint: <https://doi.org/10.1243/095440705X34883>. [Online]. Available: <https://doi.org/10.1243/095440705X34883>.
- [37] S. Szwaja and J. D. Naber, “Dual nature of hydrogen combustion knock,” *International Journal of Hydrogen Energy*, vol. 38, no. 28, pp. 12 489–12 496, 2013.
- [38] R. Ono and T. Oda, “Spark ignition of hydrogen-air mixture,” *Journal of Physics: Conference Series*, vol. 142, no. 1, p. 012 003, 2008. DOI: 10.1088/1742-6596/142/1/012003. [Online]. Available: <https://dx.doi.org/10.1088/1742-6596/142/1/012003>.
- [39] P. Dimitriou, T. Tsujimura, and Y. Suzuki, “Low-load hydrogen-diesel dual-fuel engine operation – a combustion efficiency improvement approach,” *International Journal of Hydrogen Energy*, vol. 44, no. 31, pp. 17 048–17 060, 2019, ISSN: 0360-3199. DOI: <https://doi.org/10.1016/j.ijhydene.2019.04.203>. [Online]. Available: <https://www.sciencedirect.com/science/article/pii/S0360319919316362>.
- [40] T. Gatts, S. Liu, C. Liew, B. Ralston, C. Bell, and H. Li, “An experimental investigation of incomplete combustion of gaseous fuels of a heavy-duty diesel engine supplemented with hydrogen and natural gas,” *International Journal of Hydrogen Energy*, vol. 37, no. 9, pp. 7848–7859, 2012, 7th Petite Workshop on the Defect Chemical Nature of Energy Materials, 14-17 March 2011, Storaas, Kongsberg, Norway, ISSN: 0360-3199. DOI: <https://doi.org/10.1016/j.ijhydene.2012.01.088>. [Online]. Available: <https://www.sciencedirect.com/science/article/pii/S036031991200184X>.
- [41] J. Duan, F. Liu, and B. Sun, “Backfire control and power enhancement of a hydrogen internal combustion engine,” *International Journal of Hydrogen Energy*, vol. 39, no. 9, pp. 4581–4589, 2014, ISSN: 0360-3199. DOI: <https://doi.org/10.1016/j.ijhydene.2013.12.175>. [Online]. Available: <https://www.sciencedirect.com/science/article/pii/S0360319913031674>.
- [42] T Wang, Z Peng, S.-L. Liu, H.-D. Xiao, and H Zhao, “Optimization of stratification combustion in a spark ignition engine by double-pulse port fuel injection,” *Proceedings of the Institution of Mechanical Engineers, Part D: Journal of Automobile Engineering*, vol. 221, no. 7, pp. 845–857, 2007. DOI: 10.1243/09544070JAUTO376. eprint: <https://doi.org/10.1243/09544070JAUTO376>. [Online]. Available: <https://doi.org/10.1243/09544070JAUTO376>.
- [43] T. Yamato, H. Sekino, T. Ninomiya, and M. Hayashida, “Stratification of in-cylinder mixture distributions by tuned port injection in a 4-valve si gas engine,” SAE Technical Paper, Tech. Rep., 2001.

- [44] M. Garg and R. Ravikrishna, "Effect of port gas injection on in-cylinder stratification in a cng fuelled si engine," *Progress in Computational Fluid Dynamics, an International Journal*, vol. 14, no. 4, pp. 244–258, 2014, PMID: 63865. DOI: 10.1504/PCFD.2014.063865. eprint: <https://www.inderscienceonline.com/doi/pdf/10.1504/PCFD.2014.063865>. [Online]. Available: <https://www.inderscienceonline.com/doi/abs/10.1504/PCFD.2014.063865>.
- [45] M. S. A. Momin, M. Dutta, M. G. Kader, and S. M. Iftakher, "Study of lpg (liquefied petroleum gas) and cng (compressed natural gas) vehicles and it's future aspects," in *International Conference on Mechanical, Industrial and Energy Engineering*, 2016, pp. 26–27.
- [46] S Verhelst, S Verstraeten, and R Sierens, "A comprehensive overview of hydrogen engine design features," *Proceedings of the Institution of Mechanical Engineers, Part D: Journal of Automobile Engineering*, vol. 221, no. 8, pp. 911–920, 2007. DOI: 10.1243/09544070JAUTO141. eprint: <https://doi.org/10.1243/09544070JAUTO141>. [Online]. Available: <https://doi.org/10.1243/09544070JAUTO141>.
- [47] V. Chintala and K. Subramanian, "A comprehensive review on utilization of hydrogen in a compression ignition engine under dual fuel mode," *Renewable and Sustainable Energy Reviews*, vol. 70, pp. 472–491, 2017, ISSN: 1364-0321. DOI: <https://doi.org/10.1016/j.rser.2016.11.247>. [Online]. Available: <https://www.sciencedirect.com/science/article/pii/S1364032116310188>.
- [48] I. E. B. R. E. Coverdill J. E. Kirwan and J. E. Peters, "The effects of throttle body injection on fuel/air distribution in a spark ignition engine," *Combustion Science and Technology*, vol. 66, no. 4-6, pp. 189–198, 1989. DOI: 10.1080/00102208908947149. eprint: <https://doi.org/10.1080/00102208908947149>. [Online]. Available: <https://doi.org/10.1080/00102208908947149>.
- [49] A. Dhar, A. K. Agarwal, and V. Saxena, "Measurement of dynamic lubricating oil film thickness between piston ring and liner in a motored engine," *Sensors and Actuators A: Physical*, vol. 149, no. 1, pp. 7–15, 2009.
- [50] A. L. Miller, C. B. Stipe, M. C. Habjan, and G. G. Ahlstrand, "Role of lubrication oil in particulate emissions from a hydrogen-powered internal combustion engine," *Environmental science & technology*, vol. 41, no. 19, pp. 6828–6835, 2007.
- [51] A. P. Singh, A. Pal, and A. K. Agarwal, "Comparative particulate characteristics of hydrogen, cng, hcng, gasoline and diesel fueled engines," *Fuel*, vol. 185, pp. 491–499, 2016.
- [52] R. Derwent, P. Simmonds, S. O'Doherty, A. Manning, W. Collins, and D. Stevenson, "Global environmental impacts of the hydrogen economy," *International Journal of Nuclear Hydrogen Production and Applications*, vol. 1, no. 1, pp. 57–67, 2006.

- [53] M. Talibi, P. Hellier, R. Morgan, C. Lenartowicz, and N. Ladommatos, “Hydrogen-diesel fuel co-combustion strategies in light duty and heavy duty ci engines,” *International Journal of Hydrogen Energy*, vol. 43, no. 18, pp. 9046–9058, 2018, ISSN: 0360-3199. DOI: <https://doi.org/10.1016/j.ijhydene.2018.03.176>. [Online]. Available: <http://www.sciencedirect.com/science/article/pii/S0360319918310085>.
- [54] H. Koten, “Hydrogen effects on the diesel engine performance and emissions,” *International Journal of Hydrogen Energy*, vol. 43, no. 22, pp. 10 511–10 519, 2018, ISSN: 0360-3199. DOI: <https://doi.org/10.1016/j.ijhydene.2018.04.146>. [Online]. Available: <https://www.sciencedirect.com/science/article/pii/S0360319918313338>.
- [55] H. Li, S. Liu, C. Liew, Y. Li, S. Wayne, and N. Clark, “An investigation on the mechanism of the increased no2 emissions from h2-diesel dual fuel engine,” *International Journal of Hydrogen Energy*, vol. 43, no. 7, pp. 3837–3844, 2018, ISSN: 0360-3199. DOI: <https://doi.org/10.1016/j.ijhydene.2018.01.001>. [Online]. Available: <https://www.sciencedirect.com/science/article/pii/S0360319918300363>.
- [56] S. Sterlepper, M. Fischer, J. Claßen, V. Huth, and S. Pischinger, “Concepts for hydrogen internal combustion engines and their implications on the exhaust gas aftertreatment system,” *Energies*, vol. 14, no. 23, 2021, ISSN: 1996-1073. DOI: 10.3390/en14238166. [Online]. Available: <https://www.mdpi.com/1996-1073/14/23/8166>.
- [57] *Prediction of NOx Emissions*, vol. Volume 2: Coal, Biomass and Alternative Fuels; Combustion and Fuels; Oil and Gas Applications; Cycle Innovations, Turbo Expo: Power for Land, Sea, and Air, Mar. 1981, V002T06A023. DOI: 10.1115/81-GT-119. eprint: <https://asmedigitalcollection.asme.org/GT/proceedings-pdf/GT1981/79627/V002T06A023/2393646/v002t06a023-81-gt-119.pdf>. [Online]. Available: <https://doi.org/10.1115/81-GT-119>.
- [58] A. M. Mellor, J. P. Mello, K. P. Duffy, W. L. Easley, and J. C. Faulkner, “Skeletal mechanism for no x chemistry in diesel engines,” *SAE Transactions*, vol. 107, pp. 786–801, 1998, ISSN: 0096736X, 25771531. [Online]. Available: <http://www.jstor.org/stable/44746494> (visited on 08/11/2023).
- [59] S. Nag, P. Sharma, A. Gupta, and A. Dhar, “Experimental study of engine performance and emissions for hydrogen diesel dual fuel engine with exhaust gas recirculation,” *International Journal of Hydrogen Energy*, vol. 44, no. 23, pp. 12 163–12 175, 2019, ISSN: 0360-3199. DOI: <https://doi.org/10.1016/j.ijhydene.2019.03.120>. [Online]. Available: <https://www.sciencedirect.com/science/article/pii/S0360319919311280>.
- [60] D.-S. Ma and Z. Sun, “Progress on the studies about nox emission in pfi-h2ice,” *International Journal of Hydrogen Energy*, vol. 45, no. 17, pp. 10 580–10 591, 2020, AEM 2018 - Smart Materials for Hydrogen Energy, ISSN: 0360-3199. DOI: <https://doi.org/10.1016/j.ijhydene.2019.11.065>. [Online]. Available: <https://www.sciencedirect.com/science/article/pii/S0360319919342466>.

- [61] G. A. Karim, "Hydrogen as a spark ignition engine fuel," *International Journal of Hydrogen Energy*, vol. 28, no. 5, pp. 569–577, 2003, ISSN: 0360-3199. DOI: [https://doi.org/10.1016/S0360-3199\(02\)00150-7](https://doi.org/10.1016/S0360-3199(02)00150-7). [Online]. Available: <https://www.sciencedirect.com/science/article/pii/S0360319902001507>.
- [62] S. Purayil, M. O. Hamdan, S. Al-Omari, M. Selim, and E. Elnajjar, "Review of hydrogen–gasoline si dual fuel engines: Engine performance and emission," *Energy Reports*, vol. 9, pp. 4547–4573, 2023, ISSN: 2352-4847. DOI: <https://doi.org/10.1016/j.egyr.2023.03.054>. [Online]. Available: <https://www.sciencedirect.com/science/article/pii/S2352484723002913>.
- [63] T. Gatts *et al.*, "An experimental investigation of h₂ emissions of a 2004 heavy-duty diesel engine supplemented with h₂," *International Journal of Hydrogen Energy*, vol. 35, no. 20, pp. 11 349–11 356, 2010, Hyceltec 2009 Conference, ISSN: 0360-3199. DOI: <https://doi.org/10.1016/j.ijhydene.2010.06.056>. [Online]. Available: <https://www.sciencedirect.com/science/article/pii/S0360319910012322>.
- [64] P. Dimitriou, M. Kumar, T. Tsujimura, and Y. Suzuki, "Combustion and emission characteristics of a hydrogen-diesel dual-fuel engine," *International Journal of Hydrogen Energy*, vol. 43, no. 29, pp. 13 605–13 617, 2018, ISSN: 0360-3199. DOI: <https://doi.org/10.1016/j.ijhydene.2018.05.062>. [Online]. Available: <https://www.sciencedirect.com/science/article/pii/S0360319918315775>.
- [65] Y. Suzuki, T. Tsujimura, and T. Mita, "The performance of multi-cylinder hydrogen/diesel dual fuel engine," *SAE International Journal of Engines*, vol. 8, no. 5, pp. 2240–2252, 2015.
- [66] H. L. Yip *et al.*, "A review of hydrogen direct injection for internal combustion engines: Towards carbon-free combustion," *Applied Sciences*, vol. 9, no. 22, p. 4842, 2019. DOI: 10.3390/app9224842.
- [67] J. Gomes Antunes, R. Mikalsen, and A. Roskilly, "An investigation of hydrogen-fuelled hcci engine performance and operation," *International Journal of Hydrogen Energy*, vol. 33, no. 20, pp. 5823–5828, 2008, ISSN: 0360-3199. DOI: <https://doi.org/10.1016/j.ijhydene.2008.07.121>. [Online]. Available: <https://www.sciencedirect.com/science/article/pii/S0360319908009099>.
- [68] M. Mohamed Ibrahim and A. Ramesh, "Investigations on the effects of intake temperature and charge dilution in a hydrogen fueled hcci engine," *International Journal of Hydrogen Energy*, vol. 39, no. 26, pp. 14 097–14 108, 2014, ISSN: 0360-3199. DOI: <https://doi.org/10.1016/j.ijhydene.2014.07.019>. [Online]. Available: <https://www.sciencedirect.com/science/article/pii/S0360319914019740>.
- [69] R. K. Maurya and M. R. Saxena, "Characterization of ringing intensity in a hydrogen-fueled hcci engine," *International Journal of Hydrogen Energy*, vol. 43, no. 19, pp. 9423–9437, 2018, ISSN: 0360-3199. DOI: <https://doi.org/10.1016/j.ijhydene.2018.03.194>. [Online]. Available: <https://www.sciencedirect.com/science/article/pii/S0360319918310279>.

- [70] A. A. Hairuddin, T. Yusaf, and A. P. Wandel, “A review of hydrogen and natural gas addition in diesel hcci engines,” *Renewable and Sustainable Energy Reviews*, vol. 32, pp. 739–761, 2014, ISSN: 1364-0321. DOI: <https://doi.org/10.1016/j.rser.2014.01.018>. [Online]. Available: <https://www.sciencedirect.com/science/article/pii/S136403211400029X>.
- [71] H. Wei, T. Zhu, G. Shu, L. Tan, and Y. Wang, “Gasoline engine exhaust gas recirculation – a review,” *Applied Energy*, vol. 99, pp. 534–544, 2012, ISSN: 0306-2619. DOI: <https://doi.org/10.1016/j.apenergy.2012.05.011>. [Online]. Available: <https://www.sciencedirect.com/science/article/pii/S0306261912003595>.
- [72] B. V. Rajalingam and P. V. Farrell, “The effect of injection pressure on air entrainment into transient diesel sprays,” *SAE Transactions*, vol. 108, pp. 652–660, 1999, ISSN: 0096736X, 25771531. [Online]. Available: <http://www.jstor.org/stable/44743400> (visited on 08/10/2023).
- [73] K. ichi Shimizu and A. Satsuma, “Hydrogen assisted urea-scr and nh3-scr with silver–alumina as highly active and so2-tolerant de-nox catalysis,” *Applied Catalysis B: Environmental*, vol. 77, no. 1, pp. 202–205, 2007, ISSN: 0926-3373. DOI: <https://doi.org/10.1016/j.apcatb.2007.07.021>. [Online]. Available: <https://www.sciencedirect.com/science/article/pii/S0926337307002251>.
- [74] J. Chong, A. Tsolakis, S. Gill, K. Theinnoi, and S. Golunski, “Enhancing the no2/nx ratio in compression ignition engines by hydrogen and reformat combustion, for improved aftertreatment performance,” *International Journal of Hydrogen Energy*, vol. 35, no. 16, pp. 8723–8732, 2010, ISSN: 0360-3199. DOI: <https://doi.org/10.1016/j.ijhydene.2010.06.008>. [Online]. Available: <https://www.sciencedirect.com/science/article/pii/S0360319910011511>.
- [75] V. Praveena and M. L. J. Martin, “A review on various after treatment techniques to reduce nox emissions in a ci engine,” *Journal of the Energy Institute*, vol. 91, no. 5, pp. 704–720, 2018, ISSN: 1743-9671. DOI: <https://doi.org/10.1016/j.joei.2017.05.010>. [Online]. Available: <https://www.sciencedirect.com/science/article/pii/S1743967117300260>.
- [76] P. Braun, J. Gebhard, F.-M. Matysik, and H.-P. Rabl, “Potential technical approaches for improving low-temperature nox conversion of exhaust aftertreatment systems,” *Chemie Ingenieur Technik*, vol. 90, no. 6, pp. 762–773, 2018. DOI: <https://doi.org/10.1002/cite.201700122>. eprint: <https://onlinelibrary.wiley.com/doi/pdf/10.1002/cite.201700122>. [Online]. Available: <https://onlinelibrary.wiley.com/doi/abs/10.1002/cite.201700122>.
- [77] S. Furfori, N. Russo, D. Fino, G. Saracco, and V. Specchia, “No scr reduction by hydrogen generated in line on perovskite-type catalysts for automotive diesel exhaust gas treatment,” *Chemical Engineering Science*, vol. 65, no. 1, pp. 120–127, 2010, 20th International Symposium in Chemical Reaction Engineering—Green Chemical Reaction Engineering for a Sustainable Future, ISSN: 0009-2509. DOI: <https://doi.org/10.1016/j.ces.2009.01.065>. [Online]. Available: <https://www.sciencedirect.com/science/article/pii/S0009250909000943>.

- [78] P. G. Savva and C. N. Costa, “Hydrogen lean-denox as an alternative to the ammonia and hydrocarbon selective catalytic reduction (scr),” *Catalysis Reviews*, vol. 53, no. 2, pp. 91–151, 2011. DOI: 10.1080/01614940.2011.557964. eprint: <https://doi.org/10.1080/01614940.2011.557964>. [Online]. Available: <https://doi.org/10.1080/01614940.2011.557964>.
- [79] A. Väliheikki *et al.*, “Selective catalytic reduction of nox by hydrogen (h2-scr) on wox-promoted cezzr1-zo2 solids,” *Applied Catalysis B: Environmental*, vol. 156-157, pp. 72–83, 2014, ISSN: 0926-3373. DOI: <https://doi.org/10.1016/j.apcatb.2014.03.008>. [Online]. Available: <https://www.sciencedirect.com/science/article/pii/S0926337314001635>.
- [80] S. Salomons, M. Votsmeier, R. Hayes, A. Drochner, H. Vogel, and J. Gieshof, “Co and h2 oxidation on a platinum monolith diesel oxidation catalyst,” *Catalysis Today*, vol. 117, no. 4, pp. 491–497, 2006, Selected papers presented at the 6th International Workshop on Catalytic Combustion, ISSN: 0920-5861. DOI: <https://doi.org/10.1016/j.cattod.2006.06.001>. [Online]. Available: <https://www.sciencedirect.com/science/article/pii/S0920586106003683>.
- [81] S. R. Katare and P. M. Laing, “Hydrogen in diesel exhaust: Effect on diesel oxidation catalyst flow reactor experiments and model predictions,” *SAE International Journal of Fuels and Lubricants*, vol. 2, no. 1, pp. 605–611, 2009, ISSN: 19463952, 19463960. [Online]. Available: <http://www.jstor.org/stable/26273413> (visited on 10/14/2022).
- [82] S. Hemmings and A. Megaritis, “Periodically regenerating diesel particulate filter with a hydrogen/carbon monoxide mixture addition,” *International Journal of Hydrogen Energy*, vol. 37, no. 4, pp. 3573–3584, 2012, International Conference on Renewable Energy (ICRE 2011), ISSN: 0360-3199. DOI: <https://doi.org/10.1016/j.ijhydene.2011.11.062>. [Online]. Available: <https://www.sciencedirect.com/science/article/pii/S0360319911025602>.
- [83] H. L. Yip *et al.*, “A review of hydrogen direct injection for internal combustion engines: Towards carbon-free combustion,” *Applied Sciences*, vol. 9, no. 22, 2019, ISSN: 2076-3417. DOI: 10.3390/app9224842. [Online]. Available: <https://www.mdpi.com/2076-3417/9/22/4842>.
- [84] H. EMS, *H2200 - hana ems co., ltd*, HANA-EN. [Online]. Available: <http://hanaems.com/h2200/> (visited on 04/11/2023).
- [85] G. of Canada, *Can/cgsb-3.517-2020*, Government of Canada Publications, Feb. 2020. [Online]. Available: https://publications.gc.ca/collections/collection_2020/ongc-cgsb/P29-003-517-2020-eng.pdf (visited on 04/22/2023).
- [86] *Fma1600 — mass and volumetric flow meters — omega engineering*, www.omega.ca. [Online]. Available: <https://www.omega.ca/en/flow-instruments/flow-meters/mass-flow-meters/fma1600-series/p/FMA-1611A-V2> (visited on 04/11/2023).
- [87] Pegasor, *Pegasor pps-m brochure*, Pegasor, 2021. [Online]. Available: https://pegasor.fi/site/attachments/Pegasor_PPS_M_web.2.pdf (visited on 04/22/2023).

- [88] N. Instruments, *Pcie-6351 and usb-6351 specifications*, www.ni.com, Mar. 2023. [Online]. Available: <https://www.ni.com/docs/en-US/bundle/pcie-usb-6351-specs/page/specs.html>.
- [89] J. B. Heywood, *Internal combustion engine fundamentals*. McGraw-Hill Education, 2018.
- [90] R. Stone, *Introduction to internal combustion engines*. Springer, 1999, vol. 3.
- [91] A. Bahadori and H. B. Vuthaluru, “Predicting emissivities of combustion gases,” English, *Chemical Engineering Progress*, vol. 105, no. 6, pp. 38–41, Jun. 2009, Copyright - Copyright American Institute of Chemical Engineers Jun 2009; Document feature - Equations; Tables; Graphs; ; Last updated - 2021-09-09. [Online]. Available: <https://login.ezproxy.library.ualberta.ca/login>.
- [92] G. Woschni, “A universally applicable equation for the instantaneous heat transfer coefficient in the internal combustion engine,” SAE Technical paper, Tech. Rep., 1967.
- [93] G. Hohenberg, “Experimentelle erfassung der wandwärme von kolbenmotoren,” 1980.
- [94] J. M. Mattson and C. Depcik, “Emissions-calibrated equilibrium heat release model for direct injection compression ignition engines,” *Fuel*, vol. 117, pp. 1096–1110, 2014, ISSN: 0016-2361. DOI: <https://doi.org/10.1016/j.fuel.2013.10.026>. [Online]. Available: <https://www.sciencedirect.com/science/article/pii/S0016236113009678>.
- [95] J. Mattson, C. Langness, and C. Depcik, “Modified heat release analysis for diesel-assisted cng combustion,” vol. 2015, Apr. 2015. DOI: 10.4271/2015-01-1744.
- [96] D. G. Goodwin, H. K. Moffat, I. Schoegl, R. L. Speth, and B. W. Weber, *Cantera: An object-oriented software toolkit for chemical kinetics, thermodynamics, and transport processes*, <https://www.cantera.org>, Version 2.6.0, 2022. DOI: 10.5281/zenodo.6387882.
- [97] M. Wick, B. Lehrheuer, T. Albin, J. Andert, and S. Pischinger, “Decoupling of consecutive gasoline controlled auto-ignition combustion cycles by field programmable gate array based real-time cylinder pressure analysis,” *International Journal of Engine Research*, vol. 19, no. 2, pp. 153–167, 2018.
- [98] T. X. NguyenThi, J.-P. Bazile, and D. Bessières, “Density measurements of waste cooking oil biodiesel and diesel blends over extended pressure and temperature ranges,” *Energies*, vol. 11, no. 5, 2018, ISSN: 1996-1073. DOI: 10.3390/en11051212. [Online]. Available: <https://www.mdpi.com/1996-1073/11/5/1212>.
- [99] *Hydrogen: Linde formerly praxair*, 2023. [Online]. Available: <https://www.lindedirect.com/resources/gases/hydrogen>.

- [100] H. L. Johnston and D. White, "VII—A Summary of Experimental Determinations of Joule-Thomson Effects in Gases," *Transactions of the American Society of Mechanical Engineers*, vol. 70, no. 6, pp. 651–654, Dec. 2022, ISSN: 0097-6822. DOI: 10.1115/1.4017811. eprint: <https://asmedigitalcollection.asme.org/fluidsengineering/article-pdf/70/6/651/6955887/651\1.pdf>. [Online]. Available: <https://doi.org/10.1115/1.4017811>.
- [101] U. K. Singh and M. Vannice, "Kinetics of liquid-phase hydrogenation reactions over supported metal catalysts — a review," *Applied Catalysis A: General*, vol. 213, no. 1, pp. 1–24, 2001, ISSN: 0926-860X. DOI: [https://doi.org/10.1016/S0926-860X\(00\)00885-1](https://doi.org/10.1016/S0926-860X(00)00885-1). [Online]. Available: <https://www.sciencedirect.com/science/article/pii/S0926860X00008851>.
- [102] S. Bond, R. Alvarez, M. Vollmer, M. Steinbacher, M. Weilenmann, and S. Reimann, "Molecular hydrogen (h₂) emissions from gasoline and diesel vehicles," *Science of The Total Environment*, vol. 408, no. 17, pp. 3596–3606, 2010, ISSN: 0048-9697. DOI: <https://doi.org/10.1016/j.scitotenv.2010.04.055>. [Online]. Available: <https://www.sciencedirect.com/science/article/pii/S0048969710004511>.
- [103] A. L. Randolph, "Methods of processing cylinder-pressure transducer signals to maximize data accuracy," *SAE transactions*, pp. 191–200, 1990.
- [104] K. Lee, M. Yoon, and M. Sunwoo, "A study on pegging methods for noisy cylinder pressure signal," *Control Engineering Practice*, vol. 16, no. 8, pp. 922–929, 2008, Special Section: IFAC Conference on Analysis and Design of Hybrid Systems (ADHS'06), ISSN: 0967-0661. DOI: <https://doi.org/10.1016/j.conengprac.2007.10.007>. [Online]. Available: <https://www.sciencedirect.com/science/article/pii/S096706610700189X>.
- [105] D. J. Timoney, "Problems with heat release analysis in d.i. diesels," in *SAE International Congress and Exposition*, SAE International, 1987. DOI: <https://doi.org/10.4271/870270>. [Online]. Available: <https://doi.org/10.4271/870270>.
- [106] M. A. Theobald and A. C. Alkidas, "On the heat-release analysis of diesel engines: Effects of filtering of pressure data," in *1987 SAE International Fall Fuels and Lubricants Meeting and Exhibition*, SAE International, 1987. DOI: <https://doi.org/10.4271/872059>. [Online]. Available: <https://doi.org/10.4271/872059>.
- [107] F. Payri, P. Olmeda, C. Guardiola, and J. Martín, "Adaptive determination of cut-off frequencies for filtering the in-cylinder pressure in diesel engines combustion analysis," *Applied Thermal Engineering*, vol. 31, no. 14, pp. 2869–2876, 2011, ISSN: 1359-4311. DOI: <https://doi.org/10.1016/j.applthermaleng.2011.05.012>. [Online]. Available: <https://www.sciencedirect.com/science/article/pii/S135943111100264X>.

- [108] J. Cuisano, F. Flores, L. Chirinos, and A. Vaudrey, “In-cylinder pressure statistical analysis and digital signal processing methods for studying the combustion of a natural gas/diesel heavy-duty engine at low load conditions,” *Energy Conversion and Management*, vol. 269, p. 116 089, 2022, ISSN: 0196-8904. DOI: <https://doi.org/10.1016/j.enconman.2022.116089>. [Online]. Available: <https://www.sciencedirect.com/science/article/pii/S0196890422008755>.
- [109] K. NAGASHIMA and K. TSUCHIYA, “65 new indicated mean effective pressure measuring method and its applications,” *SAE Transactions*, vol. 111, pp. 2982–2987, 2002, ISSN: 0096736X, 25771531. [Online]. Available: <http://www.jstor.org/stable/44743310> (visited on 03/21/2023).
- [110] G. McTaggart-Cowan, W. Bushe, P. Hill, and S. Munshi, “A supercharged heavy-duty diesel single-cylinder research engine for high-pressure direct injection of natural gas,” *International Journal of Engine Research*, vol. 4, no. 4, pp. 315–330, 2003.
- [111] M. F. J. Brunt and A. L. Emtage, “Evaluation of imep routines and analysis errors,” *SAE Transactions*, vol. 105, pp. 749–763, 1996, ISSN: 0096736X, 25771531. [Online]. Available: <http://www.jstor.org/stable/44736314> (visited on 03/21/2023).
- [112] J. M. Mattson and C. Depcik, “Emissions-calibrated equilibrium heat release model for direct injection compression ignition engines,” *Fuel*, vol. 117, pp. 1096–1110, 2014.
- [113] D. Bradley and F.-K. Lung, “Spark ignition and the early stages of turbulent flame propagation,” *Combustion and Flame*, vol. 69, no. 1, pp. 71–93, 1987, ISSN: 0010-2180. DOI: [https://doi.org/10.1016/0010-2180\(87\)90022-8](https://doi.org/10.1016/0010-2180(87)90022-8). [Online]. Available: <https://www.sciencedirect.com/science/article/pii/0010218087900228>.
- [114] T. Tanaka, A. Ando, and K. Ishizaka, “Study on pilot injection of di diesel engine using common-rail injection system,” *JSAE Review*, vol. 23, no. 3, pp. 297–302, 2002, ISSN: 0389-4304. DOI: [https://doi.org/10.1016/S0389-4304\(02\)00195-9](https://doi.org/10.1016/S0389-4304(02)00195-9). [Online]. Available: <https://www.sciencedirect.com/science/article/pii/S0389430402001959>.
- [115] P. Carlucci, A. Ficarella, and D. Laforgia, “Effects of pilot injection parameters on combustion for common rail diesel engines,” *SAE Transactions*, vol. 112, pp. 932–943, 2003, ISSN: 0096736X, 25771531. [Online]. Available: <http://www.jstor.org/stable/44741323> (visited on 03/03/2023).
- [116] F. Poursadegh, M. Brear, B. Hayward, and Y. Yang, “Autoignition, knock, detonation and the octane rating of hydrogen,” *Fuel*, vol. 332, p. 126 201, 2023, ISSN: 0016-2361. DOI: <https://doi.org/10.1016/j.fuel.2022.126201>. [Online]. Available: <https://www.sciencedirect.com/science/article/pii/S0016236122030253>.

- [117] C. J. Moreno, O. Stenlaas, and P. Tunestal, “Influence of small pilot on main injection in a heavy-duty diesel engine,” SAE Technical Paper, Tech. Rep., 2017.
- [118] F. A. Ayala and J. B. Heywood, “Lean si engines: The role of combustion variability in defining lean limits,” SAE Technical Paper, Tech. Rep., 2007.
- [119] H. Homan, P. de Boer, and W. McLean, “The effect of fuel injection on nox emissions and undesirable combustion for hydrogen-fuelled piston engines,” *International Journal of Hydrogen Energy*, vol. 8, no. 2, pp. 131–146, 1983, ISSN: 0360-3199. DOI: [https://doi.org/10.1016/0360-3199\(83\)90095-2](https://doi.org/10.1016/0360-3199(83)90095-2). [Online]. Available: <https://www.sciencedirect.com/science/article/pii/S0360319983900952>.
- [120] H. Coward and G. Jones, *Limits of Flammability of Gases and Vapors* (Bulletin (United States. Bureau of Mines) nos. 503-508). U.S. Government Printing Office, 1952. [Online]. Available: https://books.google.ca/books?id=Pz_aKHw03IQC.
- [121] H. Li and G. A. Karim, “Hydrogen Fueled Spark-Ignition Engines Predictive and Experimental Performance,” *Journal of Engineering for Gas Turbines and Power*, vol. 128, no. 1, pp. 230–236, Jul. 2004, ISSN: 0742-4795. DOI: 10.1115/1.2055987. eprint: https://asmedigitalcollection.asme.org/gasturbinespower/article-pdf/128/1/230/5705882/230_1.pdf. [Online]. Available: <https://doi.org/10.1115/1.2055987>.
- [122] X. Liu, G. Seberry, S. Kook, Q. N. Chan, and E. R. Hawkes, “Direct injection of hydrogen main fuel and diesel pilot fuel in a retrofitted single-cylinder compression ignition engine,” *International Journal of Hydrogen Energy*, vol. 47, no. 84, pp. 35 864–35 876, 2022. DOI: 10.1016/j.ijhydene.2022.08.149.
- [123] A. Jamrozik, K. Grab-Rogaliński, and W. Tutak, “Hydrogen effects on combustion stability, performance and emission of diesel engine,” *International Journal of Hydrogen Energy*, vol. 45, no. 38, pp. 19 936–19 947, 2020.
- [124] O. P. Lopatin, “Phenomenology of nitrogen oxides formation in a gas-diesel engine,” *Journal of Physics: Conference Series*, vol. 1515, no. 4, p. 042 009, 2020. DOI: 10.1088/1742-6596/1515/4/042009. [Online]. Available: <https://dx.doi.org/10.1088/1742-6596/1515/4/042009>.
- [125] J. Benajes, J. López, R. Novella, and P. Redón, “Comprehensive modeling study analyzing the insights of the no–no2 conversion process in current diesel engines,” *Energy Conversion and Management*, vol. 84, pp. 691–700, 2014, ISSN: 0196-8904. DOI: <https://doi.org/10.1016/j.enconman.2014.04.073>. [Online]. Available: <https://www.sciencedirect.com/science/article/pii/S0196890414003859>.

- [126] M. AL-Harbi, R. Hayes, M. Votsmeier, and W. S. Epling, “Competitive no, co and hydrocarbon oxidation reactions over a diesel oxidation catalyst,” *The Canadian Journal of Chemical Engineering*, vol. 90, no. 6, pp. 1527–1538, 2012. DOI: <https://doi.org/10.1002/cjce.20659>. eprint: <https://onlinelibrary.wiley.com/doi/pdf/10.1002/cjce.20659>. [Online]. Available: <https://onlinelibrary.wiley.com/doi/abs/10.1002/cjce.20659>.
- [127] A. Arvajová and P. Kočí, “Impact of ptox formation in diesel oxidation catalyst on no2 yield during driving cycles,” *Chemical Engineering Science*, vol. 158, pp. 181–187, 2017, ISSN: 0009-2509. DOI: <https://doi.org/10.1016/j.ces.2016.10.011>. [Online]. Available: <https://www.sciencedirect.com/science/article/pii/S0009250916305401>.
- [128] S. Liu *et al.*, “An experimental investigation of no2 emission characteristics of a heavy-duty h2-diesel dual fuel engine,” *International Journal of Hydrogen Energy*, vol. 36, no. 18, pp. 12 015–12 024, 2011, ISSN: 0360-3199. DOI: <https://doi.org/10.1016/j.ijhydene.2011.06.058>. [Online]. Available: <https://www.sciencedirect.com/science/article/pii/S0360319911015308>.
- [129] M. Koebel, G. Madia, F. Raimondi, and A. Wokaun, “Enhanced reoxidation of vanadia by no2 in the fast scr reaction,” *Journal of Catalysis*, vol. 209, no. 1, pp. 159–165, 2002, ISSN: 0021-9517. DOI: <https://doi.org/10.1006/jcat.2002.3624>. [Online]. Available: <https://www.sciencedirect.com/science/article/pii/S0021951702936249>.
- [130] W. Santoso, R. Bakar, and A. Nur, “Combustion characteristics of diesel-hydrogen dual fuel engine at low load,” *Energy Procedia*, vol. 32, pp. 3–10, 2013, International Conference on Sustainable Energy Engineering and Application (ICSEEA) 2012, ISSN: 1876-6102. DOI: <https://doi.org/10.1016/j.egypro.2013.05.002>. [Online]. Available: <https://www.sciencedirect.com/science/article/pii/S1876610213000040>.
- [131] *Part 1039—control of emissions from new and in-use nonroad compression-ignition engines*, Code of Federal Regulations, 2023. [Online]. Available: <https://www.ecfr.gov/current/title-40/part-1039> (visited on 01/17/2024).
- [132] T.-C. Jao, S. Li, K. Yatsunami, S. J. Chen, A. A. Csontos, and J. M. Howe, “Soot characterisation and diesel engine wear,” *Lubrication Science*, vol. 16, no. 2, pp. 111–126, 2004. DOI: <https://doi.org/10.1002/ls.3010160203>. eprint: <https://onlinelibrary.wiley.com/doi/pdf/10.1002/ls.3010160203>. [Online]. Available: <https://onlinelibrary.wiley.com/doi/abs/10.1002/ls.3010160203>.
- [133] S. Aldajah, O. Ajayi, G. Fenske, and I. Goldblatt, “Effect of exhaust gas recirculation (egr) contamination of diesel engine oil on wear,” *Wear*, vol. 263, no. 1, pp. 93–98, 2007, 16th International Conference on Wear of Materials, ISSN: 0043-1648. DOI: <https://doi.org/10.1016/j.wear.2006.12.055>. [Online]. Available: <https://www.sciencedirect.com/science/article/pii/S0043164807003742>.

- [134] N. A. Henein, “Analysis of pollutant formation and control and fuel economy in diesel engines,” in *Energy and Combustion Science*, Elsevier, 1979, pp. 283–325.
- [135] S.-C. Kong and R. D. Reitz, “Multidimensional modeling of diesel ignition and combustion using a multistep kinetics model,” 1993.
- [136] T. V. Johnson, “Review of selective catalytic reduction (scr) and related technologies for mobile applications,” in *Urea-SCR technology for deNO_x after treatment of diesel exhausts*, Springer, 2014, pp. 3–31.
- [137] C. M. Allen, M. C. Joshi, D. B. Gosala, G. M. Shaver, L. Farrell, and J. McCarthy, “Experimental assessment of diesel engine cylinder deactivation performance during low-load transient operations,” *International Journal of Engine Research*, vol. 22, no. 2, pp. 606–615, 2021.
- [138] M. Hamed, O. Doustdar, A. Tsolakis, and J. Hartland, “Thermal energy storage system for efficient diesel exhaust aftertreatment at low temperatures,” *Applied Energy*, vol. 235, pp. 874–887, 2019, ISSN: 0306-2619. DOI: <https://doi.org/10.1016/j.apenergy.2018.11.008>. [Online]. Available: <https://www.sciencedirect.com/science/article/pii/S0306261918317148>.
- [139] C. Ciardelli *et al.*, “Reactivity of no/no₂-nh₃ scr system for diesel exhaust aftertreatment: Identification of the reaction network as a function of temperature and no₂ feed content,” *Applied Catalysis B: Environmental*, vol. 70, no. 1, pp. 80–90, 2007, Papers presented at the 4th International Conference on Environmental Catalysis (4th ICEC) Heidelberg, Germany, June 05 – 08, 2005., ISSN: 0926-3373. DOI: <https://doi.org/10.1016/j.apcatb.2005.10.041>. [Online]. Available: <https://www.sciencedirect.com/science/article/pii/S0926337306002128>.
- [140] A. V. Karre, R. K. Garlapalli, A. Jena, and N. Tripathi, “State of the art developments in oxidation performance and deactivation of diesel oxidation catalyst (doc),” *Catalysis Communications*, vol. 179, p. 106 682, 2023, ISSN: 1566-7367. DOI: <https://doi.org/10.1016/j.catcom.2023.106682>. [Online]. Available: <https://www.sciencedirect.com/science/article/pii/S1566736723000845>.
- [141] D. Culbertson, M. Khair, J. Pradun, H. G. Petry, and A. Ungermann, “A simulation study of electrically heating diesel exhaust,” SAE Technical Paper, Tech. Rep., 2016.

Appendix A: Engine Operation Procedures

A.1 Operating Manual for 4.5L Cummins Engine

A.1.1 PPE Required

- Hearing protection
- Safety glasses
- Long pants
- Closed toe shoes
- No loose clothing (No ties, sweater strings, necklaces, or anything to get caught in rotating shaft)
- Hair tied back
- Gloves maybe needed if dealing with hot engine parts after running.

A.1.2 Safety Rules

1. Never enter the room when the engine is running at a condition that is higher than 40 Nm of load under the stock controller algorithm.
2. Never enter the room when the hydrogen injection system is enabled or when hydrogen is being injected into the engine.

3. Never stand next to the sides engine or driveshaft when the engine is operating. Being in these regions increases the risk of being hit by debris or scalding fluids if a failure is to occur.
4. Never exceed 30 psi of boost on the input regulators. Exceeding this pressure may cause the engine cylinder pressure to exceed maximum design limits (175 bar) under normal diesel operation.
5. Never cut, pinch or stand on an air line. An energized air line that bursts can cause severe injury. Always check if an air line is energized before interacting with it.

A.1.3 Startup Procedure

1. Turn on room ventilation.
 - Switch three gray ventilation control boxes to “hand”
 - Two control boxes are present on the north wall and one is present on the east wall
 - You should now hear the ventilation system start
2. Check if all exhaust bung plugs or sensing equipment is in place. Ensure the exhaust system is secure and that no items (cables, hoses, anything else) is touching the exhaust pipe or turbo charger.
 - The FTIR is plumbed in via a 1/4 inch swagelock adapter on the top of the cylinder 1 exhaust pipe.
 - The Pegasor is plumbed via two M18 sample and return ports. These ports are the two final ports on the cylinder 1 exhaust pipe before the flexpipe section. The sample port is the one closest to the engine.
 - Other M18 bungs on the cylinder 1 exhaust pipe are used for the UEGO sensor, NOx sensor, hydrogen sensor, or exhaust pressure sensor.

- Ensure hand-valves on the exhaust are closed. One is present on a 1/4 inch sample tube running from the cylinder 1 exhaust pipe. Another is present where the cylinder 1 and cylinders 2-4 exhaust pipes merge.
3. Check engine oil level using dipstick.
 4. Check under engine if any fluids have leaked or if there is any sign of damage.
 5. Check engine coolant level in stainless reservoir tank.
 6. Check drive shaft between engine and dyno for loose bolts or excessive play. Ensure nothing can get caught in the driveshaft.
 7. Power exhaust pressure sensor cooling pump. Located next to the engine exhaust system.
 - Check the contents of the white plastic reservoir if it needs to be filled. Tap water is sufficient for cooling purposes
 - Plug the pump into a 120 V outlet
 - Ensure water is running by checking outlet in reservoir
 8. Turn on the dyno.
 - Turn on cooling water to the dyno. Open the two valves located on the north wall of the lab.
 - Turn on the dyno. This is the small red toggle switch located on the gray box next to the dyno.
 - Ensure dyno oil is at a sufficient level for operation.
 9. Engine cooling:
 - Turn on engine cooling water. The valve is located quite high next to the 4 cylinder GM engine. You should be able to see the red hose going to the engine

- Ensure the water valve on the plate heat exchanger is open about 1/8 to 1/4 of a turn.
10. Check diesel fuel level using the gauge built into the red fuel tank. If fuel is needed see hazard assessment for refuelling.
 11. If using the Pegasor: Power on the Pegasor using the switch present on the power bar located inside its box. The compressor should begin to run, and the sample line should display a flashing light. Consult the Pegasor operating manual for further usage instructions.
 12. If using the FTIR:
 - If the FTIR has not been allowed to reach steady state operation or is unpowered, consult the FTIR operating manual.
 - Ensure the FTIR exhaust line is plumbed into the floor-level ventilation system present on the east wall
 - Check filter integrity of FTIR filter stages before running.
 - Rotate the electrostatic filter's input valve right to sample from the engine, vertical for no flow, or left to sample from the nitrogen bottle.
 13. Power on the Kistler Amplifier that is suspended under the wire conduit via the switch on the rear of the amplifier.
 14. Power on the hydrogen gas pressure sensor, which is a Validyne sensor present in the engine control rack.
 15. Power on the main 12 volt power supply present in the south-east corner of the room in the open server rack. This power supply will also power on the second Kistler amplifier. The MABX and Rapid Pro units along with the NOx sensors should now power on.

16. Power on the 5 volt supplemental power supply for the engine encoder and sensors. Located on the top shelf of the engine control rack.
17. On the 1-26 control PC, start the Kistler SCP software and connect to both amplifiers. Confirm that all used sensors are present in software and reset the amplifiers to start measurement.
18. The engine is now ready for testing, you can return to 1-26 to begin engine testing. The starting and control process will vary as the control software is adapted based on control strategy.

A.1.4 If running with Boosted Intake Pressures

1. THE AIR SYSTEM IS OPERATED AT A SUPPLY PRESSURE OF 100 PSI. OPENING OR CUTTING A PRESSURIZED AIR LINE CAN CAUSE SEVERE INJURY. ENSURE THE SYSTEM IS DE-ENERGIZED BEFORE ADJUSTING AIR CONNECTIONS.
2. Turn both regulators present on the input air handler to 0 psi/shut (fully rotated counter-clockwise) before continuing. If air lines are already hooked up, ensure no hissing noise is heard anywhere along the lines or regulators. If this is the case, the air lines have been energized. Shut all wall valves in this case and proceed to the shutdown procedure.
3. Connect the two 1/2 inch air hoses and the 3/4 inch air hose to the appropriate outlets present in the lab and to the secondary regulator. Use hose clamps on each end over the barbs.
4. After all hoses are connected, ensure regulators are set at 0 psi/shut (fully rotated counter-clockwise)
5. Slightly open an air valve then close it. The system is now energized. The regulator should not be flowing air. If hissing is noticed at any connection

points, fix the leak. If hissing is noticed at the primary regulator (the one without a connected pipe), the secondary regulator is leaking and the primary is relieving the downstream pressure. Check if both regulators are shut. If this is the case, the secondary regulator has failed and testing must be suspended.

6. Connect the 1 inch line to the primary regulator and use the clips to ensure it is locked in place. Move the other end close to the elevator air outlet, but do not connect it yet.
7. Open the three air valves in the lab.
8. Start the engine and allow it to reach operating temperature.
9. Connect the 1 inch line to the elevator output and use the clips to ensure it is locked in place.
10. Slightly open the valve on the elevator output then close it. Check to see if the pressure is dropping. The pressure should drop at a rate of less than 1 psi per second. If this is not the case, the primary regulator is leaking. Check if the primary regulator is completely shut. If this is the case, continue with operation until step 12.
11. To select a boost pressure: GENTLY rotate the SECONDARY REGULATOR first to approximately 5 psi. The tone of the engine should change as the vacuum valve on the input air handler is now closed.
12. If the primary regulator was leaking: GENTLY rotate the PRIMARY REGULATOR to approximately 5 psi then fully shut it. Cycle the valve on the elevator output again. If high leakage persists, the primary regulator has failed and testing must be suspended.
13. GENTLY rotate the PRIMARY REGULATOR to approximately 5 psi. At this point, the target boost pressure can now be freely adjusted on either regulator.

Adjust boost levels while running at low loads, then once all operators have exited the room, run test programs.

A.1.5 If running with hydrogen

1. Ensure that the two hydrogen purge valves are closed. One is located near the engine and the other is located in the ventilated cabinet on the south wall.
2. Ensure hydrogen tank is connected correctly to the system. Perform a leak check using the hydrogen gas “sniffer” located on the top of the gas cabinet.
3. If there are no leaks, slowly open the hydrogen tank. You should now see the tank pressure and the downstream pressure. The downstream pressure should be set to 120 psi.
4. Press the “zero” button on the mass flow controller.
5. Ensure that the two shut off switches are turned on. One on the engine controller rack and one in 1-26 located below the dyno controller.
6. The system will be ready to run. The final signal to enable to the flow of hydrogen will come from the MABX, but the system must have all mechanical and electronic switches positively engaged to flow hydrogen.

A.1.6 Shutdown Procedure

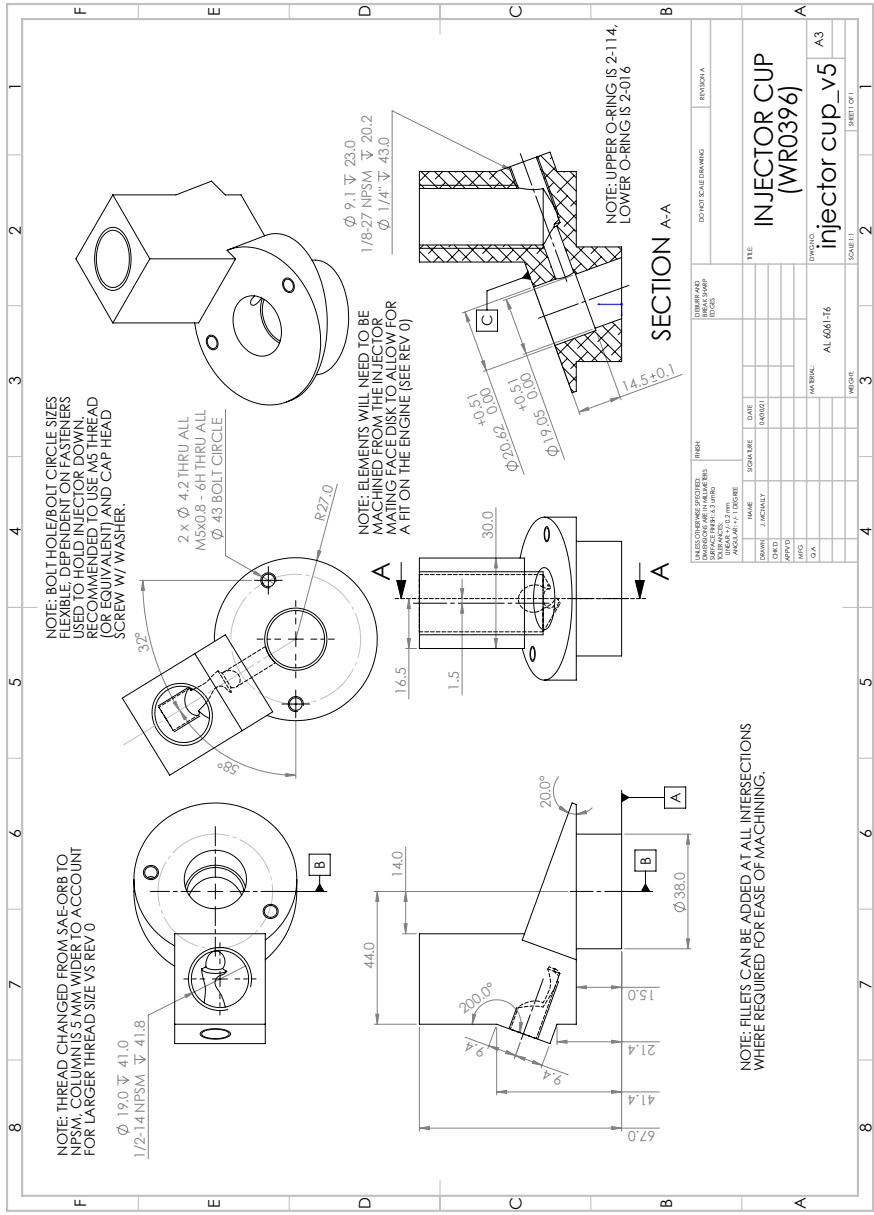
1. The engine and supplementary equipment will now be **HOT**. Please take caution when touching anything near the engine. Wear thick welding gloves if needed.
2. If running with boost:
 - Fully close both of the regulators present on the inlet air handler. The vacuum valve will open and the engine should change pitch.

- Close all 4 of the wall valves. Note that the system is still energized at this point.
 - GENTLY set ONE of the regulators to approximately 5 psi. The vacuum valve should close and eventually open again once the air in the supply line is exhausted. The other regulator should hiss when the vacuum valve is closed. Close the regulator once the vacuum valve opens again.
 - Repeat the previous step for the other regulator. The system is now de-energized.
 - Disconnect the 1 inch line from the elevator air outlet. This air line must be disconnected to prevent pressure surge damage to the upstream regulator. THE SYSTEM MUST BE DE-ENERGIZED BEFORE THIS IS DONE.
 - Other items of the shutdown process can now proceed.
3. Shut down engine following the reverse of the startup procedure.
 4. If running with boost, check if system is de-energized then disconnect and store air lines.

Appendix B: Complete Selection of Steady-State Testing Results Figures

B.1 Injector Cup Design

Figure B.1 contains a design drawing of the injector cup used to hold the hydrogen injector in the intake manifold.



Appendix C: Testing List

C.1 Testing List and their Relation to Files

The following table can be used to cross-reference the more readable test name given in this document with the raw test number:

Table C.1: List of all conventional dual-fuel combustion tests correlated to their file number.

Test	IMEP _g (bar)	IMP (bar)	H2 Energy (J)	H2 Energy Fraction (%)	Pilot Advance (CAD)	Test Number	NMHC (g/kWh)	CO (g/kWh)
A-1	4.5	-11.1	0	0.0	-7.5	346	0.73	2.05
A-2	4.5	-11.1	0	0.0	-9.3	347	0.74	2.16
A-3	4.5	-11.1	0	0.0	-11.1	348	0.70	2.22
A-4	4.5	-11.1	0	0.0	-12.9	349	0.72	2.44
A-5	4.5	-11.1	453	28.2	-7.5	350	0.60	0.90
A-6	4.5	-11.1	455	29.6	-9.3	351	0.87	0.84
A-7	4.5	-11.1	455	30.0	-11.1	352	0.83	0.81
A-8	4.5	-11.1	455	30.3	-12.9	353	0.74	0.80
A-9	4.5	-11.1	918	57.4	-7.5	354	0.86	0.27
A-10	4.5	-11.1	918	63.6	-9.3	355	2.15	0.24
A-11	4.5	-11.1	928	65.1	-11.1	356	2.11	0.23

Table C.1

Test	IMEP _g (bar)	IMP (bar)	H2 Energy (J)	H2 Energy Fraction (%)	Pilot Advance (CAD)	Test Number	NMHC (g/kWh)	CO (g/kWh)
A-12	4.5	-11.1	931	66.5	-12.9	357	1.70	0.22
A-13S	4.5	-11.1	1096	69.6	-7.5	358	1.19	0.21
A-14S	4.5	-11.1	1084	72.9	-9.3	359	6.00	0.20
A-15S	4.5	-11.1	1073	75.0	-12.9	361	6.89	0.22
B-1	4.5	1.5	0	0.0	-7.5	330	0.59	1.67
B-2	4.5	1.5	0	0.0	-9.3	329	0.66	1.89
B-3	4.5	1.5	0	0.0	-11.1	328	0.68	2.03
B-4	4.5	1.5	0	0.0	-12.9	327	0.70	2.27
B-5	4.5	1.5	460	28.8	-7.5	331	0.60	1.00
B-6	4.5	1.5	461	29.0	-9.3	332	0.59	1.01
B-7	4.5	1.5	460	29.2	-11.1	333	0.55	1.00
B-8	4.5	1.5	461	29.7	-12.9	334	0.55	1.02
B-9	4.5	1.5	906	47.8	-7.5	338	0.60	0.51
B-10	4.5	1.5	908	48.4	-9.3	337	0.51	0.46
B-11	4.5	1.5	907	49.3	-11.1	336	0.45	0.39
B-12	4.5	1.5	901	49.9	-12.9	335	0.46	0.37
B-13S	4.5	1.5	1191	65.8	-7.5	342	0.58	0.31
B-14S	4.5	1.5	1153	65.2	-9.3	341	0.50	0.31
B-15S	4.5	1.5	1119	67.8	-11.1	343	0.79	0.26
B-16S	4.5	1.5	1113	68.7	-12.9	344	0.68	0.24
C-1	7.5	1.5	0	0.0	-7.5	306	1.05	1.39
C-2	7.5	1.5	0	0.0	-9.3	307	1.15	1.43

Table C.1

Test	IMEP _g (bar)	IMP (bar)	H2 Energy (J)	H2 Energy Fraction (%)	Pilot Advance (CAD)	Test Number	NMHC (g/kWh)	CO (g/kWh)
C-3	7.5	1.5	0	0.0	-11.1	308	1.20	1.45
C-4	7.5	1.5	0	0.0	-12.9	309	1.10	1.51
C-5	7.5	1.5	458	22.9	-7.5	310	0.70	0.91
C-6	7.5	1.5	458	23.2	-9.3	311	0.72	0.96
C-7	7.5	1.5	459	23.3	-11.1	312	0.78	1.04
C-8	7.5	1.5	466	23.5	-12.9	313	0.77	0.99
C-9	7.5	1.5	905	42.9	-12.9	314	0.99	0.50
C-10	7.5	1.5	899	44.6	-11.1	315	1.23	0.59
C-11	7.5	1.5	928	42.8	-9.3	316	0.65	0.57
C-12	7.5	1.5	925	43.6	-7.5	317	0.81	0.61
C-13	7.5	1.5	1356	59.4	-7.5	318	1.05	0.37
C-14	7.5	1.5	1356	62.4	-9.3	319	1.32	0.31
C-15	7.5	1.5	1357	65.9	-11.1	320	1.85	0.30
C-16	7.5	1.5	1356	69.7	-12.9	321	5.80	0.29
C-17S	7.5	1.5	1677	76.6	-7.5	325	10.31	0.20
C-18S	7.5	1.5	1648	80.2	-9.3	324	5.62	0.20
C-19S	7.5	1.5	1629	85.0	-11.1	322	6.64	0.23
C-20S	7.5	1.5	1621	80.6	-12.9	323	3.41	0.22
D-1	7.5	2.0	0	0.0	-7.5	236	0.43	1.37
D-2	7.5	2.0	0	0.0	-9.3	237	0.43	1.37
D-3	7.5	2.0	0	0.0	-11.1	238	0.44	1.42
D-4	7.5	2.0	0	0.0	-12.9	239	0.45	1.47

Test	IMEP _g (bar)	IMP (bar)	H2 Energy (J)	H2 Energy Fraction (%)	Pilot Advance (CAD)	Test Number	NMHC (g/kWh)	CO (g/kWh)
D-5	7.5	2.0	445	22.3	-7.5	272	0.29	0.92
D-6	7.5	2.0	445	22.3	-9.3	273	0.29	0.92
D-7	7.5	2.0	446	22.4	-11.1	274	0.32	0.93
D-8	7.5	2.0	454	22.9	-12.9	275	0.32	0.94
D-9	7.5	2.0	895	36.3	-7.5	276	0.33	0.74
D-10	7.5	2.0	909	37.1	-9.3	277	0.36	0.73
D-11	7.5	2.0	910	37.6	-11.1	278	0.36	0.72
D-12	7.5	2.0	903	37.8	-12.9	279	0.36	0.69
D-13S	7.5	2.0	1348	55.9	-9.3	283	0.32	0.32
D-14S	7.5	2.0	1349	56.8	-11.1	282	0.33	0.28
D-15S	7.5	2.0	1350	58.3	-12.9	280	0.32	0.25
D-16S	7.5	2.0	1348	59.7	-14.7	281	0.31	0.22
E-1	10.5	1.5	0	0.0	-7.5	383	0.72	1.09
E-2	10.5	1.5	0	0.0	-9.3	384	0.69	1.11
E-3	10.5	1.5	0	0.0	-11.1	385	0.64	1.11
E-4	10.5	1.5	0	0.0	-12.9	386	0.61	1.09
E-5	10.5	1.5	0	0.0	-14.7	387	0.59	1.09
E-6	10.5	1.5	0	0.0	-16.5	396	0.50	1.12
E-7	10.5	1.5	0	0.0	-18.3	397	0.50	1.21
E-8	10.5	1.5	0	0.0	-20.1	398	0.51	1.38
E-9	10.5	1.5	455	17.7	-7.5	388	0.54	0.74
E-10	10.5	1.5	455	17.6	-9.3	389	0.52	0.77

Table C.1

Test	IMEP _g (bar)	IMP (bar)	H2 Energy (J)	H2 Energy Fraction (%)	Pilot Advance (CAD)	Test Number	NMHC (g/kWh)	CO (g/kWh)
E-11	10.5	1.5	453	17.5	-11.1	390	0.52	0.78
E-12	10.5	1.5	454	17.6	-12.9	391	0.50	0.78
E-13	10.5	1.5	453	17.7	-14.7	392	0.48	0.78
E-14	10.5	1.5	453	17.7	-16.5	393	0.47	0.76
E-15	10.5	1.5	456	17.8	-18.3	394	0.47	0.75
E-16	10.5	1.5	454	17.9	-20.1	395	0.46	0.76
E-17	10.5	1.5	921	36.3	-7.5	402	0.49	0.57
E-18	10.5	1.5	931	36.6	-9.3	403	0.46	0.53
E-19	10.5	1.5	927	36.8	-11.1	404	0.46	0.52
E-20	10.5	1.5	925	37.0	-12.9	405	0.46	0.49
E-21	10.5	1.5	928	37.1	-14.7	406	0.45	0.47
E-22	10.5	1.5	930	37.9	-16.5	407	0.44	0.42
E-23	10.5	1.5	933	38.1	-18.3	408	0.41	0.38
E-24	10.5	1.5	938	38.3	-20.1	409	0.39	0.35
E-25	10.5	1.5	1349	54.4	-7.5	410	0.44	0.35
E-26	10.5	1.5	1361	55.5	-9.3	411	0.44	0.34
E-27	10.5	1.5	1366	56.9	-11.1	412	0.44	0.31
E-28	10.5	1.5	1367	58.4	-12.9	413	0.46	0.31
E-29	10.5	1.5	1365	59.1	-14.7	414	0.46	0.28
E-30	10.5	1.5	1363	58.7	-16.5	415	0.44	0.28
F-1	10.5	2.0	0	0.0	-7.5	446	0.49	1.04
F-2	10.5	2.0	0	0.0	-9.3	447	0.48	1.07

Test	IMEP _g (bar)	IMP (bar)	H2 Energy (J)	H2 Energy Fraction (%)	Pilot Advance (CAD)	Test Number	NMHC (g/kWh)	CO (g/kWh)
F-3	10.5	2.0	0	0.0	-11.1	448	0.48	1.09
F-4	10.5	2.0	0	0.0	-12.9	449	0.48	1.11
F-5	10.5	2.0	0	0.0	-14.7	450	0.49	1.16
F-6	10.5	2.0	0	0.0	-16.5	451	0.49	1.23
F-7	10.5	2.0	0	0.0	-18.3	452	0.49	1.39
F-8	10.5	2.0	0	0.0	-20.1	453	0.50	1.64
F-9	10.5	2.0	461	18.3	-7.5	454	0.52	0.84
F-10	10.5	2.0	460	18.4	-9.3	455	0.48	0.81
F-11	10.5	2.0	453	18.1	-11.1	456	0.50	0.83
F-12	10.5	2.0	456	18.2	-12.9	457	0.48	0.82
F-13	10.5	2.0	459	18.4	-14.7	458	0.48	0.81
F-14	10.5	2.0	464	18.7	-16.5	459	0.47	0.84
F-15	10.5	2.0	466	18.7	-18.3	460	0.46	0.89
F-16	10.5	2.0	466	18.8	-20.1	461	0.45	0.99
F-17	10.5	2.0	917	32.4	-7.5	463	0.48	0.67
F-18	10.5	2.0	916	32.5	-9.3	464	0.48	0.67
F=19	10.5	2.0	914	32.7	-11.1	465	0.48	0.67
F-20	10.5	2.0	914	33.0	-12.9	466	0.47	0.64
F-21	10.5	2.0	914	33.4	-14.7	467	0.47	0.62
F-22	10.5	2.0	916	33.8	-16.5	468	0.45	0.59
F-23	10.5	2.0	917	34.2	-18.3	469	0.44	0.56
F-24	10.5	2.0	1363	49.7	-7.5	470	0.47	0.41

Test	IMEP _g (bar)	IMP (bar)	H2 Energy (J)	H2 Energy Fraction (%)	Pilot Advance (CAD)	Test Number	NMHC (g/kWh)	CO (g/kWh)
F-25	10.5	2.0	1363	49.9	-9.3	471	0.47	0.40
F-26	10.5	2.0	1365	50.1	-11.1	472	0.45	0.37
F-27	10.5	2.0	1363	50.5	-12.9	473	0.45	0.33
F-28	10.5	2.0	1369	51.9	-14.7	474	0.45	0.30
F-29	10.5	2.0	1368	52.2	-16.5	475	0.46	0.28
F-30	10.5	2.0	1797	65.5	-7.5	476	0.48	0.26
F-31	10.5	2.0	1802	66.2	-9.3	477	0.47	0.24
F-32	10.5	2.0	1808	67.7	-11.1	478	0.50	0.23
G-1	12.5	1.5	0	0.0	-7.5	424	0.37	1.02
G-2	12.5	1.5	0	0.0	-9.3	425	0.37	1.03
G-3	12.5	1.5	0	0.0	-11.1	426	0.37	1.06
G-4	12.5	1.5	0	0.0	-12.9	427	0.38	1.11
G-5	12.5	1.5	0	0.0	-14.7	428	0.37	1.06
G-6	12.5	1.5	0	0.0	-16.5	429	0.37	1.05
G-7	12.5	1.5	0	0.0	-18.3	430	0.37	1.05
G-8	12.5	1.5	0	0.0	-20.1	431	0.38	1.08
G-9	12.5	1.5	469	15.4	-7.5	432	0.38	0.92
G-10	12.5	1.5	457	14.8	-9.3	433	0.35	0.91
G-11	12.5	1.5	464	15.0	-11.1	434	0.33	0.97
G-12	12.5	1.5	475	15.6	-12.9	435	0.32	0.89
G-13	12.5	1.5	476	15.6	-14.7	436	0.31	0.84
G-14	12.5	1.5	473	15.4	-16.5	437	0.31	0.84

Test	IMEP _g (bar)	IMP (bar)	H2 Energy (J)	H2 Energy Fraction (%)	Pilot Advance (CAD)	Test Number	NMHC (g/kWh)	CO (g/kWh)
G-15	12.5	1.5	466	15.3	-18.3	438	0.31	0.80
G-16	12.5	1.5	915	30.0	-7.5	519	0.34	0.63
G-17	12.5	1.5	915	30.0	-9.3	520	0.34	0.59
G-18	12.5	1.5	914	30.3	-11.1	521	0.36	0.55
G-19	12.5	1.5	916	30.8	-12.9	522	0.33	0.46
G-20	12.5	1.5	914	30.9	-14.7	523	0.34	0.43
G-21	12.5	1.5	914	31.0	-16.5	524	0.33	0.39
G-22	12.5	1.5	913	31.2	-18.3	525	0.32	0.34
G-23	12.5	1.5	1358	45.3	-7.5	526	0.38	0.36
G-24	12.5	1.5	1360	46.3	-9.3	527	0.40	0.30
G-25	12.5	1.5	1360	47.8	-11.1	528	0.41	0.24
H-1	12.5	2.0	0	0.0	-7.5	493	0.70	0.85
H-2	12.5	2.0	0	0.0	-9.3	494	0.68	0.85
H-3	12.5	2.0	0	0.0	-11.1	495	0.67	0.89
H-4	12.5	2.0	0	0.0	-12.9	496	0.64	0.91
H-5	12.5	2.0	0	0.0	-14.7	497	0.63	0.94
H-6	12.5	2.0	0	0.0	-16.5	498	0.61	0.99
H-7	12.5	2.0	0	0.0	-18.3	499	0.61	1.07
H-8	12.5	2.0	0	0.0	-20.1	500	0.60	1.23
H-9	12.5	2.0	466	16.5	-7.5	508	0.50	0.75
H-10	12.5	2.0	466	16.5	-9.3	507	0.51	0.75
H-11	12.5	2.0	465	16.6	-11.1	506	0.50	0.73

Table C.1

Test	IMEP _g (bar)	IMP (bar)	H2 Energy (J)	H2 Energy Fraction (%)	Pilot Advance (CAD)	Test Number	NMHC (g/kWh)	CO (g/kWh)
H-12	12.5	2.0	464	16.6	-12.9	505	0.52	0.74
H-13	12.5	2.0	464	16.7	-14.7	504	0.54	0.77
H-14	12.5	2.0	465	16.8	-16.5	503	0.55	0.79
H-15	12.5	2.0	473	17.1	-18.3	502	0.55	0.81
H-16	12.5	2.0	472	17.1	-20.1	501	0.57	0.85
H-17	12.5	2.0	913	30.7	-7.5	509	0.48	0.63
H-18	12.5	2.0	913	30.9	-9.3	510	0.48	0.61
H-19	12.5	2.0	914	31.1	-11.1	511	0.48	0.62
H-20	12.5	2.0	913	31.6	-12.9	512	0.48	0.57
H-21	12.5	2.0	915	31.7	-14.7	513	0.47	0.56
H-22	12.5	2.0	917	32.1	-16.5	514	0.46	0.53
H-23	12.5	2.0	1352	46.7	-7.5	515	0.46	0.42
H-24	12.5	2.0	1354	46.8	-9.3	516	0.46	0.41
H-25	12.5	2.0	1357	47.9	-12.9	518	0.45	0.37

Appendix D: Selection of Steady-State Testing Results Figures

D.1 Figures from Steady-State Testing Results

The following section contains a complete set of the figures from the steady-state testing results for the cylinder pressure and heat release rate traces.

D.1.1 Cylinder Pressure Traces

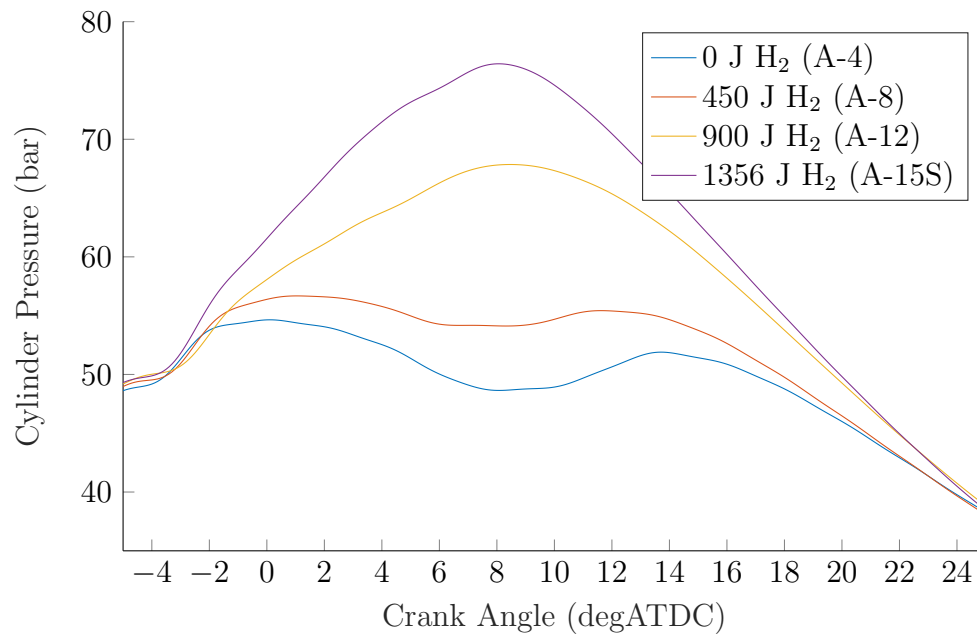


Figure D.1: 600-cycle ensemble average of cylinder pressure traces from Bin A at an injection advance of -11.1 CAD pilot injection advance.

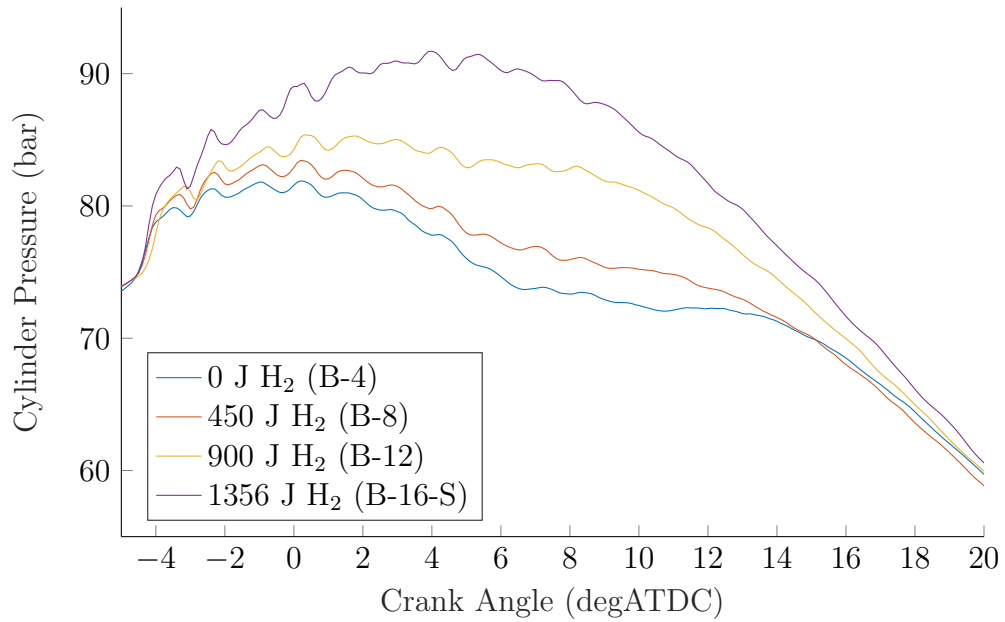


Figure D.2: 600-cycle ensemble average of cylinder pressure traces from Bin B at an injection advance of -9.3 CAD pilot injection advance.

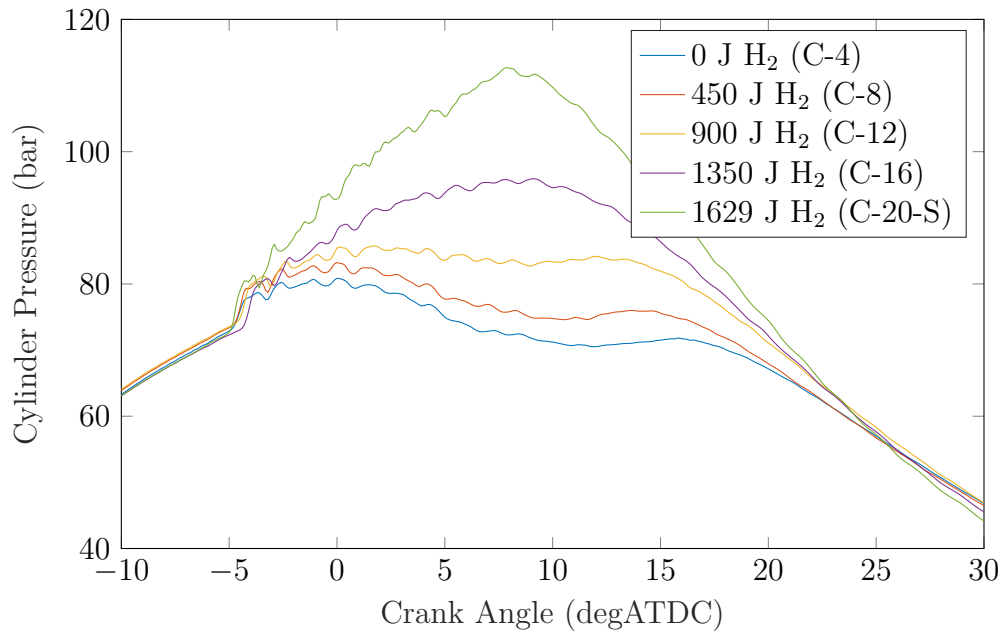


Figure D.3: 600-cycle ensemble average of cylinder pressure traces from Bin C at an injection advance of -11.1 CAD pilot injection advance.

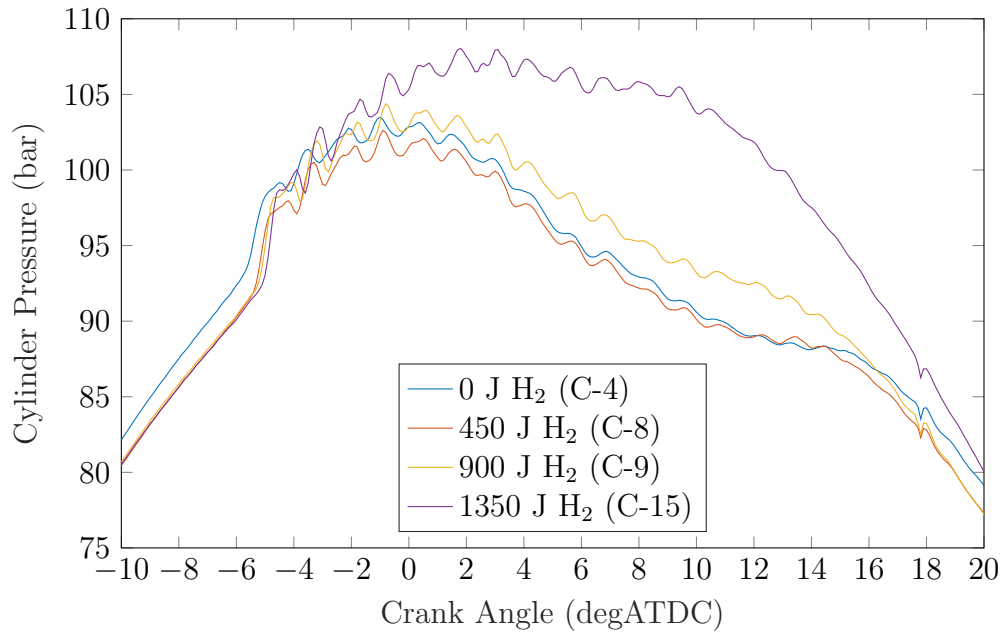


Figure D.4: 600-cycle ensemble average of cylinder pressure traces from Bin D at an injection advance of -11.1 CAD pilot injection advance.

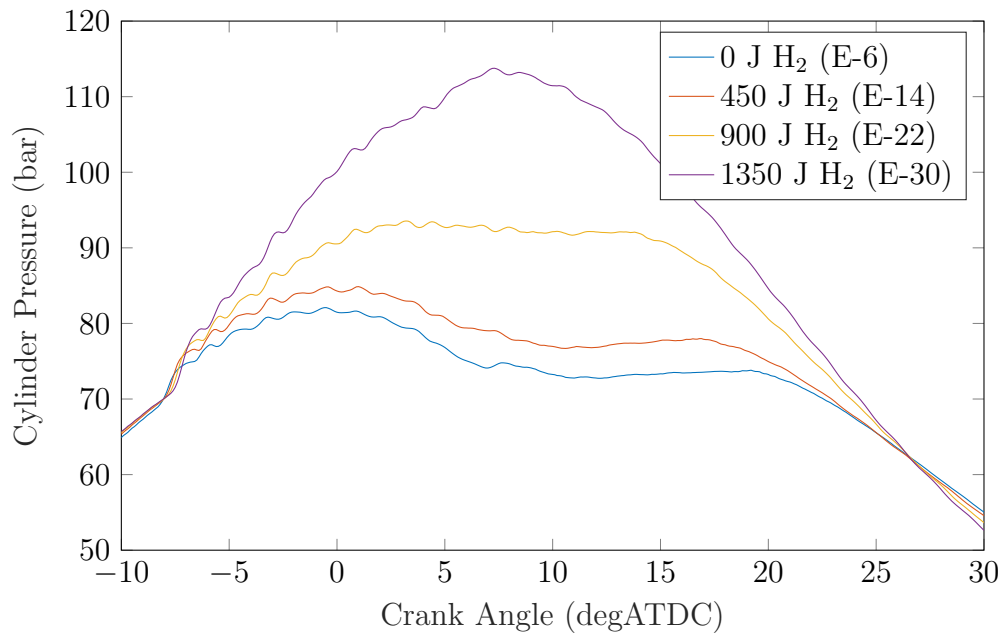


Figure D.5: 600-cycle ensemble average of cylinder pressure traces from Bin E at an injection advance of -16.5 CAD pilot injection advance.

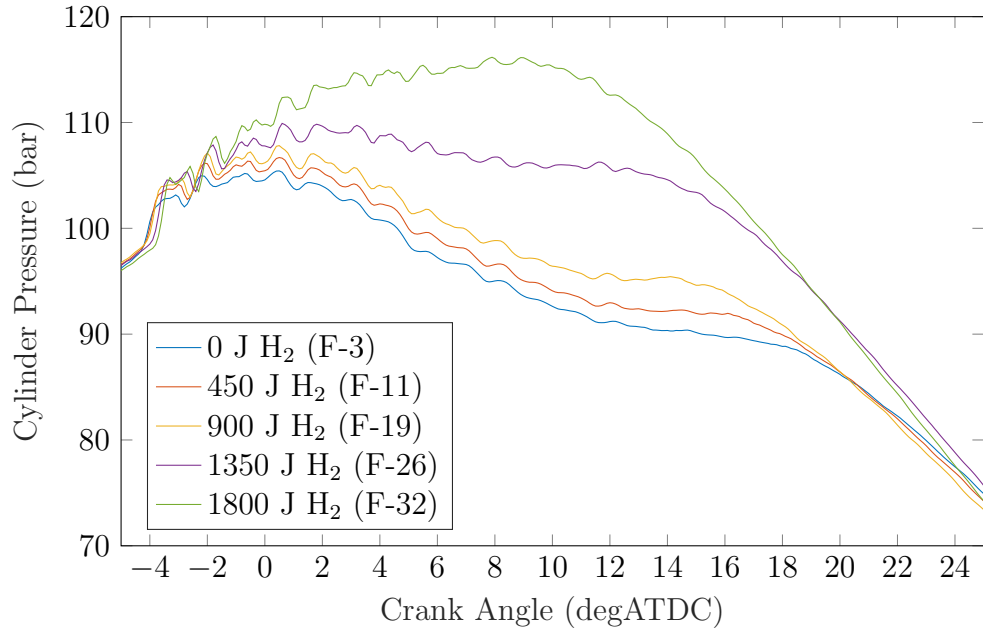


Figure D.6: 600-cycle ensemble average of cylinder pressure traces from Bin F at an injection advance of -9.3 CAD pilot injection advance.

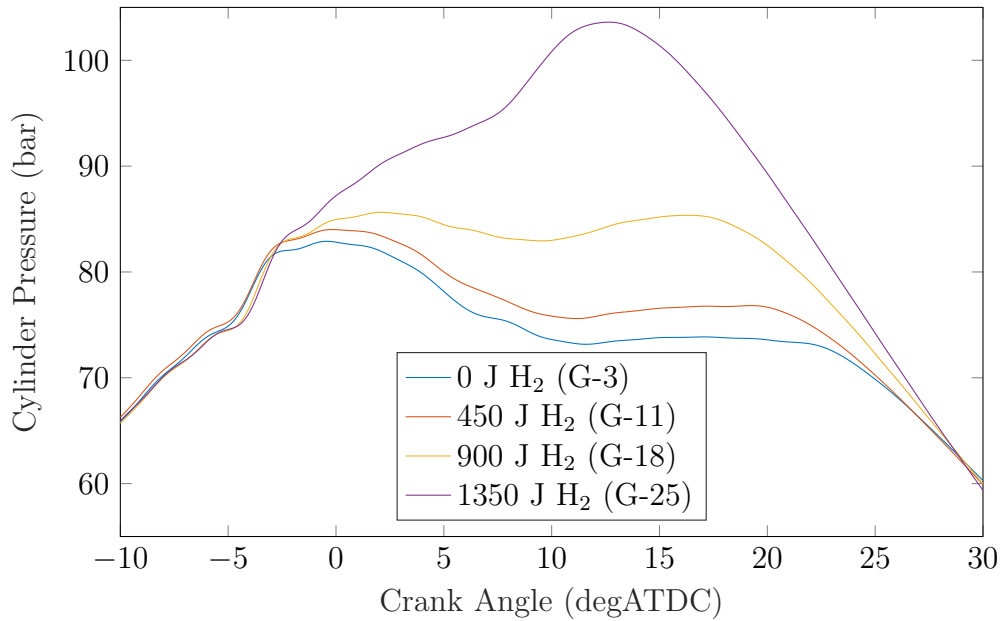


Figure D.7: 600-cycle ensemble average of cylinder pressure traces from Bin G at an injection advance of -9.3 CAD pilot injection advance.

D.1.2 Cylinder Pressure Heat Release Rate Traces

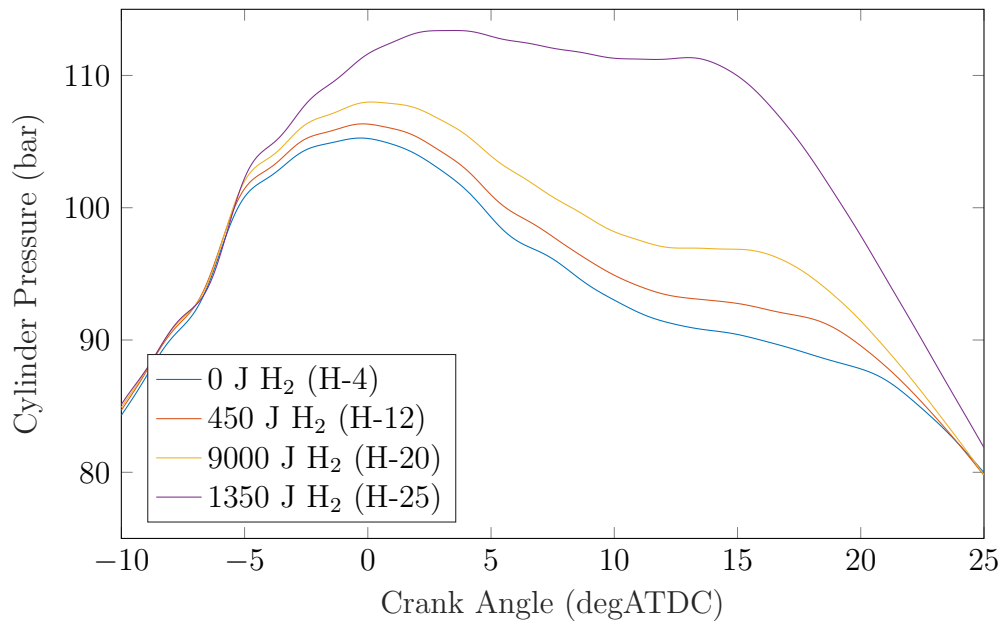


Figure D.8: 600-cycle ensemble average of cylinder pressure traces from Bin H at an injection advance of -11.1 CAD pilot injection advance.

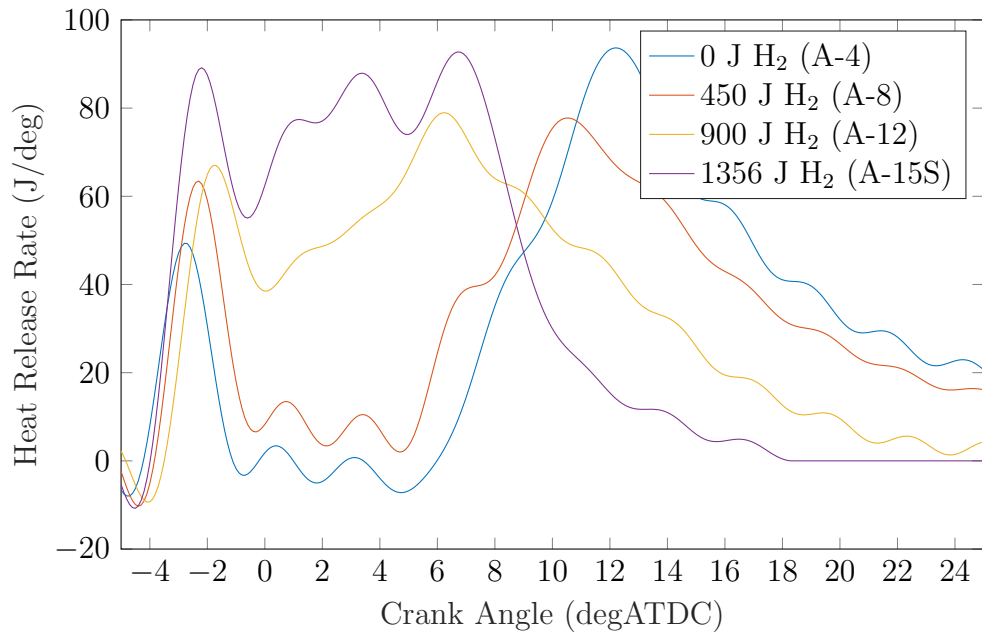


Figure D.9: Heat release rate traces for Bin A.

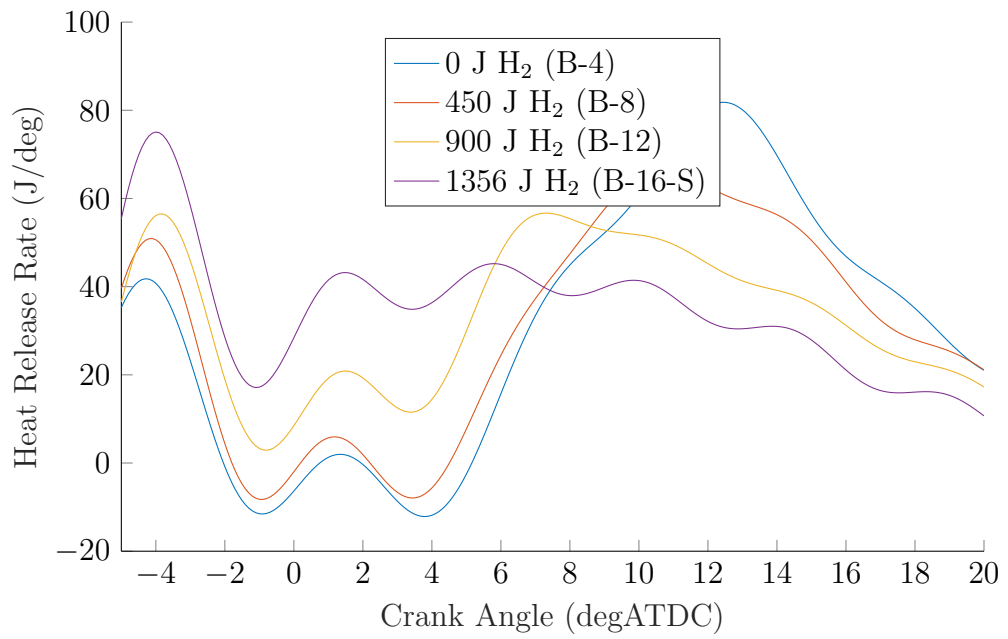


Figure D.10: Heat release rate traces for Bin B.

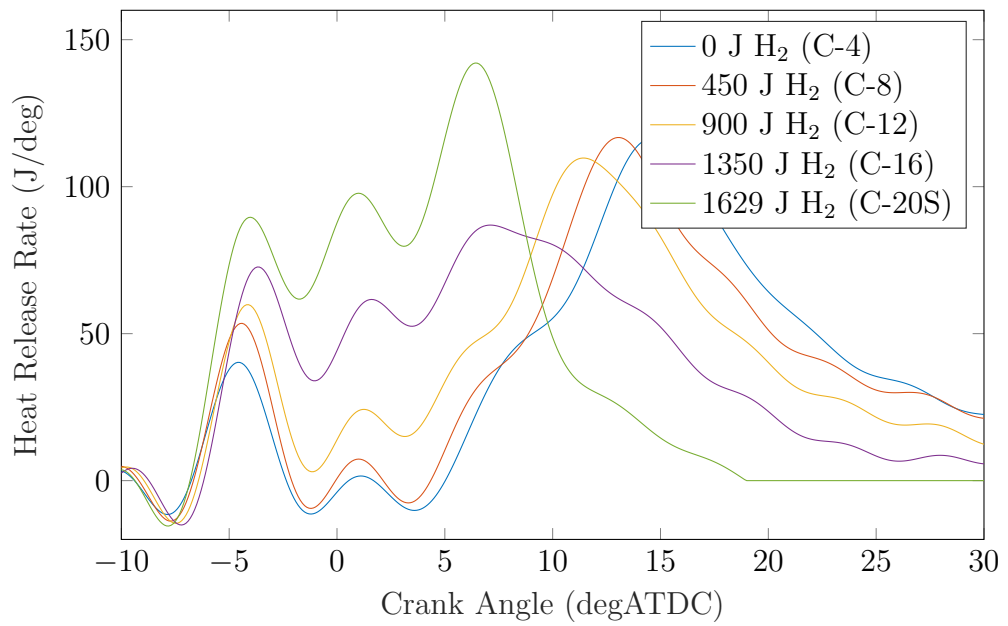


Figure D.11: Heat release rate traces for Bin C.

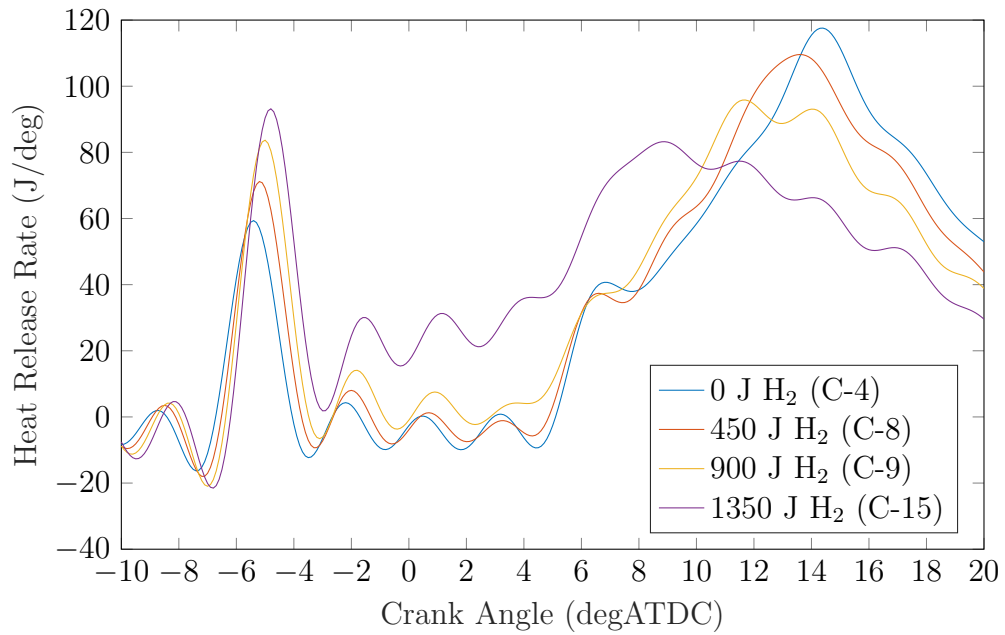


Figure D.12: Heat release rate traces for Bin D.

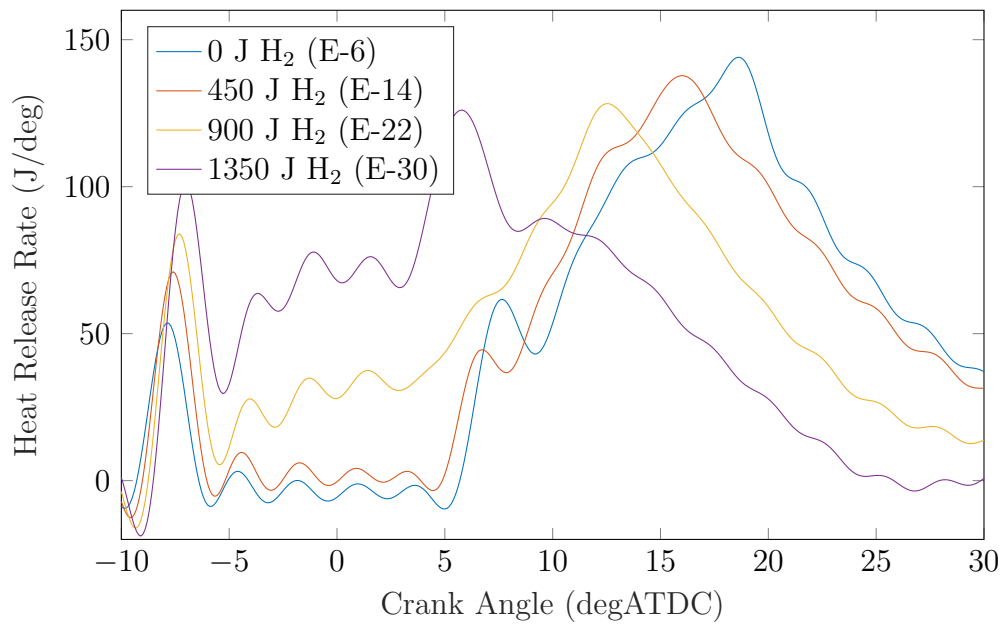


Figure D.13: Heat release rate traces for Bin E.

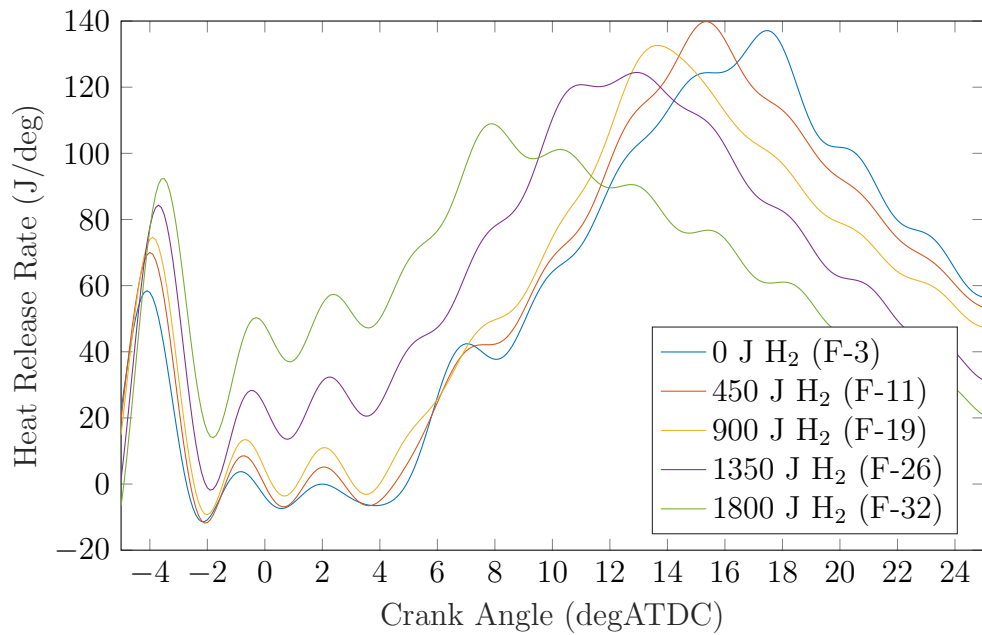


Figure D.14: Heat release rate traces for Bin F.

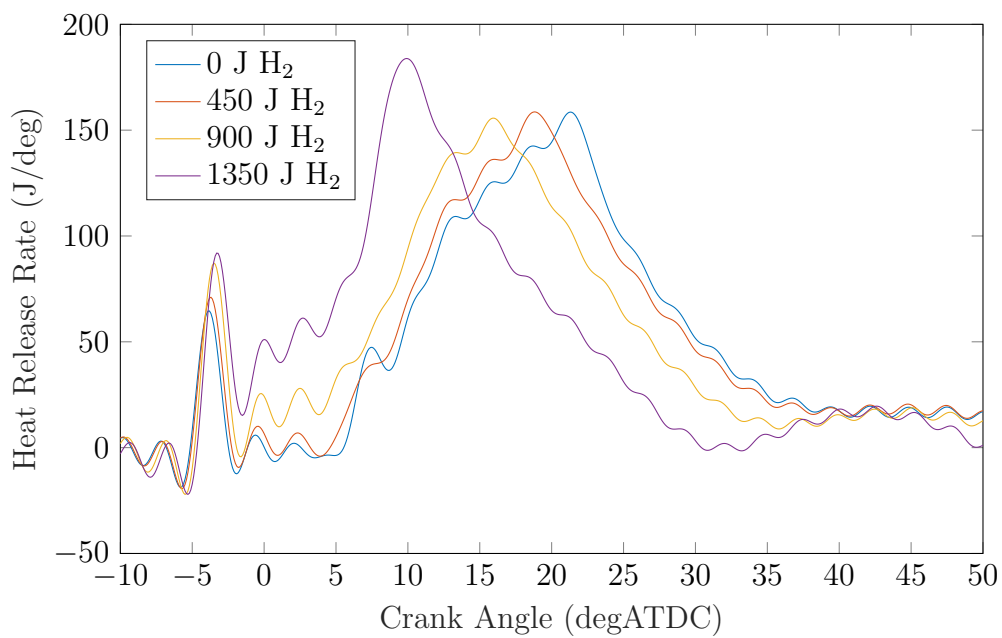


Figure D.15: Heat release rate traces for Bin G.

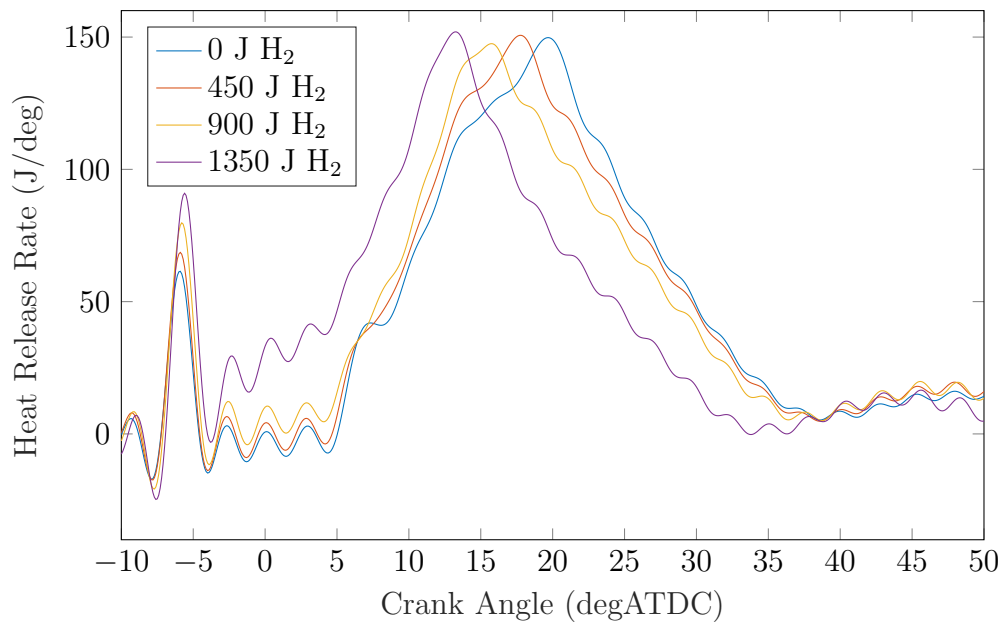


Figure D.16: Heat release rate traces for Bin H.